The volcanic and deformation history, geodynamic setting, and metallogenesis of the Chisel Sequence, Snow Lake, Manitoba, Canada

by

Margaret Signe Stewart

A thesis submitted in partial fulfilment of the requirements for the degree of Doctor of Philosophy (PhD) in Mineral Deposits and Precambrian Geology

The Faculty of Graduate Studies

Laurentian University

Sudbury, Ontario, Canada

THESIS DEFENCE COMMITTEE/COMITÉ DE SOUTENANCE DE THÈSE
Laurentian Université/Université Laurentienne
Faculty of Graduate Studies/Faculté des études supérieures

Title of Thesis Titre de la thèse	The volcanic and deformation history, geodynamic setting, and metallogenesis of the Chisel Sequence, Snow Lake, Manitoba, Canada	
Name of Candidate Nom du candidat	Stewart, Margaret Signe	
Degree Diplôme	Doctor of Philosophy	
Department/Program Département/Programme	Mineral Deposits and Precambrian Geology	Date of Defence Date de la soutenance Nov. 08, 2018

APPROVED/APPROUVÉ

Thesis Examiners/Examinateurs de thèse:

Dr. Harold Gibson
(Co-Supervisor/Co-directeur de thèse)

Dr. Bruno Lafrance
(Co-Supervisor/Co-directeur de thèse)

Dr. Douglas Tinkham
(Committee member/Membre du comité)

Approved for the Faculty of Graduate Studies
Approuvé pour la Faculté des études supérieures
Dr. David Lesbarrères
Monsieur David Lesbarrères
Dean, Faculty of Graduate Studies
Doyen, Faculté des études supérieures

Dr. Thomas Monecke
(External Examiner/Examinateur externe)

Dr. Dean Millar
(Internal Examiner/Examinateur interne)

ACCESSIBILITY CLAUSE AND PERMISSION TO USE

Abstract

The largest Paleoproterozoic VMS district in the world is hosted in the Flin-Flon Glennie Domain of the Trans-Hudson Orogen. Most of the VMS deposits occur within the Flin Flon and Snow Lake arc assemblages of the Flin Flon belt. The Chisel sequence of the ca. 1.89 Ga Snow Lake assemblage is host to six economic VMS deposits; however, its deformation history prior to ca. 1.86 Ga and its ore-forming volcanic environment are poorly constrained. The Photo Lake deposit occurs within the Chisel sequence and exhibits anomalous Au and Cu enrichment when compared to the other Chisel sequence deposits, but the source of this metal enrichment and its stratigraphic position are unknown.

Detailed field mapping, including lithofacies and structural mapping, was completed at 1:2,000 scale, with local detailed areas at 1:100 or 1:200 scale. Core from 20 Hudson Bay Exploration and Development (HBED) drill holes were re-logged and an additional 39 drill holes were examined using whole-rock geochemistry and drill logs provided by HBED to trace the extent of units. Eighty-two outcrop samples and 65 drill core samples, including 32 sulfide samples, were analyzed for whole rock major and trace element geochemistry. Eight of the outcrop samples were also analyzed for whole rock Nd, Hf, and Pb isotopes. Scanning electron microscopy provided the semi-quantitative compositions of mineral phases in least altered and altered samples, and quantitative mineral chemical data for pyrite and pyrrhotite were acquired using an electron microprobe. Trace element maps were produced by laser ablation inductively coupled plasma mass spectrometry (LA-ICP-MS) for individual pyrite grains in four of the sulfide samples.

Detailed field mapping, re-logging of selected drill holes, and whole rock geochemistry completed in this study indicate: 1) the volcanic rocks of the Snow Lake assemblage underwent a folding and thrusting event prior to 1.86 Ga due to intraoceanic accretion or early accretion to the Amisk collage; 2) with the exception of the Threehouse unit, the entire Upper Chisel sequence represents folded and thrust-repeated Lower Chisel sequence strata; 3) the Chisel sequence VMS deposits, including the Photo Lake deposit, formed within a single time-stratigraphic ore interval during a protracted arc-rifting event; 4) Au enrichment in the Photo Lake deposits is syngenetic and can be attributed to a magmatic input; 5) the Anderson VMS deposits formed during widespread arc rifting, whereas the Chisel VMS deposits formed during localized extension above a magma chamber in the extended arc.

Keywords: volcanogenic massive sulfide deposits; Paleoproterozoic; Flin Flon belt; Snow Lake; volcanology; structural geology; metallogeny

Co-authorship statement

The work presented in this dissertation has benefitted from the scientific guidance and supervision of several collaborators, listed as co-authors. This thesis was conceived by Drs. Harold Gibson and Bruno Lafrance as part of a Collaborative Research and Development (CRD) grant between the Natural Sciences and Engineering Research Council (NSERC) of Canada and HudBay Minerals Inc. Drs. Doug Tinkham and Michelle DeWolfe were co-collaborators on the NSERC-CRD grant. All field work, sample collection and preparation, petrography, analytical techniques, interpretation of results, and conclusions are the work of the candidate under the guidance and supervision of Drs. Gibson and Lafrance. Dr. Alan Bailes provided additional geochemical data, drill logs, and internal reports he produced for HudBay Minerals Inc. HudBay Minerals Inc. provided drill logs, mine sections and plans, metal zoning block models, and geochemical and assay data. Discussions with Drs. Bailes and Tinkham contributed to the interpretations made by the candidate. Chapters 2 and 3 are co-authored with Drs. Gibson and Lafrance. Chapter 4 is co-authored with Drs. Gibson, Lafrance, and Bailes. All chapters were edited by Drs. Gibson and Lafrance.

Acknowledgements

First, I thank Dr. Harold Gibson and Dr. Bruno Lafrance for giving me the opportunity to complete this project – I couldn't have asked for a better pair of co-supervisors. Their knowledge, expertise, supervising styles, and boundless positivity complemented each other and made me a more well-rounded geologist. The summers spent in the field with Harold and Bruno have been invaluable to my development as a field geologist and are my fondest memories of this project. Their feedback and reviews of my work have significantly improved the quality of the manuscripts in this thesis and have made me a better researcher. Harold, you have taught me how to ask the right questions, how to lead by example and, most importantly, to never stop learning. Bruno, you have given me an unexpected love of structural geology that I will carry forward with me in my career. I look forward to many future endeavours with Harold and Bruno, now as colleagues.

This project was funded through a Collaborative Research and Development grant between the Natural Sciences and Engineering Research Council (NSERC) of Canada and HudBay Minerals Inc. Additional funding was provided by the NSERC Alexander Graham Bell Scholarship and the Ontario Graduate Scholarship.

Many thanks to Dr. Alan Bailes, who greatly contributed to this thesis through his extensive knowledge of the Snow Lake camp and several helpful field trips and discussions. Thanks to Dr. Doug Tinkham, who patiently answered all of my most basic questions on metamorphic petrology and gave me a new football team to cheer for.

Many thanks to everyone I worked with during my summers in Snow Lake. Thanks to the HudBay crew, including Brian “BJ” Janser, Darren “Zeke” Simms, Karen Wassell Calitis, Craig Taylor, Tim Schwartz, Jason Levers, Kelly Gilmore, and Sarah Bernauer. Thanks to Tom Heine for providing the drill core and data that started this project. Thanks to my field assistants Brett Ferguson, Anthony Valvasori, and Mary Kerr. Thanks to Kate Rubingh for commiserating with me on the complexities of deformation in the Snow Lake camp and for many helpful discussions of her work. Thanks to Antoine Caté for discussions on the Lalor deposit.

The support of my family and close friends has been invaluable throughout this project. Thanks to Carolyn Feeley, Katie Hahn, Jasmine Clancy, and Vanessa Friesen. Thanks to Michelle DeWolfe for being not only a close friend, but also a mentor. A massive thanks to the entire Stewart clan for their unending encouragement and positivity.

I thank my parents, Marilyn and Peter Engelbert, for their support throughout my academic endeavours. From making shoebox dioramas at 2 a.m., to editing papers, also at 2 a.m., I have always been able to count on them. They have instilled in me a sense of curiosity that led me to the sciences and for that I am forever grateful.

Lastly, I thank my husband Craig. His endless support, encouragement, and love has kept me going throughout this project. Craig, you are the best teammate and make me a better person every day, I love you.

Table of Contents

List of Figures

List of Tables

Chapter 1

Introduction to thesis

1.1 Background

Volcanogenic massive sulfide (VMS) deposits form at or near the seafloor in zones of active rifting during short periods of volcanic quiescence (Gibson et al. 1999; Franklin et al. 2005). As a result, these deposits have a strong stratigraphic control, are localized along intervals representing conditions ideal for metal precipitation and accumulation, and are an excellent record of the deformation and metamorphic history of their host rocks. Volcanogenic massive sulfide deposits constitute an important global resource for base metals, but some deposits are also a significant source of other metals, in particular Au. Gold enrichment of some VMS deposits has resulted in classifications that separate VMS deposits into those that are Au enriched from the vast majority that are not (Mercier-Langevin et al., 2011). Gold-enriched VMS deposits occur in modern and ancient submarine oceanic and continental arc settings, forming either early during arc rifting, in back-arc settings, or during evolving arc magmatism (e.g., Hannington et al. 1986; Herzig et al. 1993; Hannington et al. 1999; Moss and Scott 2001; Dubé et al. 2007; de Ronde et al 2011; Mercier-Langevin et al. 2011 and references therein). Of the total metal tonnage in the global VMS record, Precambrian deposits account for approximately 27% Cu, 33% Zn, and 26% Au (Mercier-Langevin et al. 2014, and references therein). These deposits constitute an important global resource for base and precious metals; however, exploration for these deposits is complicated by overprinting deformation events that may affect original deposit geometry, distribution and continuity.

The Flin Flon-Glennie Domain in the Trans-Hudson Orogen hosts the largest Paleoproterozoic VMS district in the world (Syme et al. 1999; Galley et al. 2007). Most of the VMS deposits occur within two of the seven tectono-stratigraphic assemblages of the Flin Flon Belt: the Flin Flon and Snow Lake assemblages. The Snow Lake assemblage is divided into the Anderson, Chisel, and Snow Creek sequences, representing the transition from primitive arc, to mature arc, to arc rift sequences, respectively (Stern et al. 1992, 1995; Bailes and Galley 1999, 2007). Volcanogenic massive sulfide deposits occur in both the Anderson and Chisel sequences, with Cu-rich deposits dominating in the Anderson sequence and Zn-rich deposits dominating in the Chisel sequence (Galley et al. 2007).

Snow Lake is the only assemblage in the Flin Flon belt interpreted to have evolved as a pericratonic arc outboard of the Superior craton rather than as an oceanic arc (Percival et al. 2005; Corrigan et al. 2007, 2009), possibly resulting in a different volcanic, petrogenetic and deformation history than the other assemblages (Stern et al. 1992; David et al. 1996; Lucas et al. 1996). This interpretation is supported by 2.82-2.65 Ga xenocrystic zircons in the 1.892 ±3 Ga Stroud Lake felsic breccia at the base of the Chisel sequence (David et al. 1996) and evolved εNd values of -0.4 to +2.4 (Stern et al. 1992) in the overlying Snell Lake basalt, indicating interaction of the magmas with older (Archean), light REE-enriched lithosphere. None of the volcanic rocks in the Snow Lake assemblage have been successfully age dated and the only age constraints currently available are the U-Pb zircon ages for the synvolcanic Sneath Lake (1886 +17/-9 Ma; Bailes et al. 1991) and Richard Lake (1889 +8/-9 Ma; Bailes et al. 1991) subvolcanic intrusions and the Stroud Lake felsic breccia (1892 ± 3 Ma; David et al. 1996).

The Chisel sequence is divided into a Lower and Upper sequence, with most of its contained Zn-Pb-Cu-Ag-Au VMS deposits occurring at the contact between these sequences (the Chisel Lake, Lost Lake, Ghost Lake, Chisel North, and Lalor deposits). The Photo Lake deposit has been interpreted to occur in a thick section of rhyolite within the Upper Chisel sequence rather than at the contact between the Lower and Upper Chisel sequences (Bailes 1996, 1997; Bailes et al. 1996). The Photo Lake deposit also has higher Au (4.9 g/t versus 0.4 to 2.9 g/t; Galley et al. 2007) and Cu grades (4.58 wt. % versus 0.15 to 1.34 wt. %; Galley et al. 2007) than the other deposits in the Chisel sequence.

The stratigraphy of the Upper Chisel sequence is not defined and is interpreted to be a homoclinal succession that forms the stratigraphic hanging wall to the VMS deposits. It is interpreted to consist of, in ascending order, the Balloch basalt, the Ghost-Photo rhyolite and the Threehouse mafic volcaniclastic rocks and flows, herein referred to as the 'Threehouse unit' (Bailes and Galley 1996, 1999, 2007). The Powderhouse dacite and Chisel rhyolite units are interpreted to occur in the stratigraphic footwall to the deposits, at the top of the Lower Chisel sequence. Volcanogenic massive sulfide deposits occur at the contact between the Chisel rhyolite or Powderhouse dacite and Threehouse unit. At the Lalor deposit, the stratigraphy of the Upper Chisel sequence is more complex and is interpreted to consist of, in ascending order, the North Balloch rhyolite, the Balloch basalt, the Ghost rhyolite, the Threehouse unit, the North Chisel volcaniclastic rocks, and undivided volcaniclastic rocks (Bailes and Galley 1996, 1999, 2007; Bailes et al. 2009, 2013, 2016; Bailes 2014).

Four fold generations (F_1-F_4) associated with three deformation events are recognized in the

Snow Lake district (Kraus and Williams, 1999). Unlike the other tectono-stratigraphic assemblages of the Flin Flon belt, structural evidence for early intraoceanic accretion of arc volcanic rocks within the Snow Lake assemblage has not been recognized. All of the deformation events (D_1-D_4) recorded in the volcanic rocks are also reflected in the Burntwood Group – a package of graywacke, siltstone, and mudstone turbidites that were deposited at about 1.855-1.84 Ga into the Kisseynew Basin (Bailes 1980a, 1980b; Zwanzig 1990; David et al. 1996; Machado et al. 1999) and subsequently structurally interleaved with the Snow Lake arc assemblage. This indicates that all of the recognized deformational events are likely 1.84 Ga or younger and occurred during closure of the Kisseynew basin and terminal continental collision (Ansdell et al. 1995, 1999; Connors et al. 1999).

1.2 Research problems

Structural research in the Snow Lake district has almost exclusively been conducted in the Burntwood Group to date (e.g., Kraus and Williams 1998, 1999; Ansdell et al. 1999; Connors et al. 1999) and a complementary study must be completed in the volcanic rocks. There is structural evidence for intraoceanic accretion in all of the tectono-stratigraphic assemblages of the Flin Flon Belt except for Snow Lake, and this discrepancy must be investigated. Recent work at the Lalor deposit (Bailes et al. 2009, 2016) suggests that the contact between the Lower and Upper Chisel sequences is an overturned thrust fault separating the younger Threehouse mafic volcaniclastic unit in the structural hanging wall from the Powderhouse dacite unit of the Lower Chisel sequence in the structural footwall. This interpretation has major implications for the timing of arc accretion as this fault may represent a deformation event associated with intraoceanic accretion prior to 1.84 Ga. The nature of this contact must be examined in detail

along its strike length in order to determine if this interpreted fault is a significant structure and if it displaced the Upper Chisel sequence and the location of the Lalor VMS deposit.

A detailed structural study of volcanic rocks within the Chisel sequence will provide the context necessary to re-evaluate the stratigraphy of the Upper Chisel sequence. This stratigraphy is more complex above the Lalor deposit than above the other Chisel sequence VMS deposits, and these differences may reflect lateral variations in the volcanic environment, or they may result from thrust repetition and/or folding of units. Better constraints on the stratigraphy of the Upper Chisel sequence are necessary to determine the stratigraphic position of the Photo Lake deposit, which may represent a relatively unexplored productive VMS interval, or it may be a result of structural repetition of the Chisel VMS interval. An understanding of the stratigraphic relationship between the Photo Lake deposit and the other VMS deposits of the Chisel sequence is critical to determine the mechanism(s) responsible for Au and Cu enrichment in the Photo Lake deposit. If the deposit occurs at a separate VMS interval, variations in metal endowment may be related to temporal changes in the mineralizing environment. If the deposit occurs at the same VMS interval, the anomalous enrichment in Au and Cu would suggest that the hydrothermal system or specific processes active at the Photo Lake deposit differed from the other deposits along strike.

An understanding of the stratigraphic relationships between VMS deposits and the processes responsible for selective metal endowment in the Chisel sequence is necessary to reconstruct the volcanic environment at the time of VMS formation. The volcanic reconstruction has implications for the relationship between arc evolution and mineralization, and it will contribute to a new understanding of the volcanic evolution of Paleoproterozoic arc sequences. The

volcanic environment of the Chisel sequence will provide a comparison for the underlying Anderson sequence that will allow a complete re-examination of the metallogenesis of the entire Snow Lake arc. The reconstruction of the Snow Lake arc will provide a comparison for the Flin Flon arc that will contribute to a better understanding of ore-forming environments in disparate Paleoproterozoic volcanic arcs.

1.3 Research objectives

The primary objective of this research is to provide a new understanding of the VMS metallogeny and assembly of the Snow Lake arc assemblage by reconstructing the tectonic, petrogenetic, and volcanic evolution of the Chisel sequence. The following research questions are established to meet the research objectives:

(1) What is the stratigraphy of the Upper Chisel sequence? Does it represent a homoclinal succession or has it been duplicated by thrust faults and/or folds?

(2) What is the pre- and post-Burntwood (1.84 Ga) deformation history of the Snow Lake assemblage and how does it compare with the deformation history of the rest of the Flin Flon belt?

(3) What is the structural and stratigraphic setting of the Photo Lake deposit? Does the Photo Lake deposit occur at the same stratigraphic interval as the other Chisel sequence VMS deposits or does it represent a separate ore interval?

(4) What is the timing and source of Au enrichment in the Photo Lake deposit?

(5) Why is the Photo Lake deposit the only Cu-rich VMS deposit in the Chisel sequence?

(6) What is the internal stratigraphy of the Threehouse unit and does it provide constraints on the volcanic environment and water depths immediately following ore formation in the Chisel sequence?

(7) What is the volcanic environment of the Chisel sequence and what is the petrogenesis of its volcanic rocks?

1.4 Structure of thesis

This dissertation is presented as five chapters. Chapters 2-4 are written as manuscripts intended for publication in refereed scientific journals. For this reason, there is some repetition in the introduction and background sections of these chapters.

Chapter 2 is written as a manuscript entitled **"Early thrusting and folding in the Snow Lake camp, Manitoba: tectonic implications and effects on volcanogenic massive sulfide deposits"** and has been published in the Canadian Journal of Earth Sciences (published 2018, *Canadian Journal of Earth Sciences, vol. 55, p. 935-957*). This chapter documents the earliest deformation event in the volcanic rocks of the Snow Lake arc assemblage. This deformation event was not previously recognized and has repeated several units in the Lower Chisel sequence. A new stratigraphy for the Chisel sequence ore interval and Upper Chisel sequence is proposed and the effects of this early deformation event on the VMS deposits in the Chisel sequence are described. The early deformation event is not documented in the younger turbidite package overlying the volcanic rocks and is interpreted to be related to intraoceanic accretion or early accretion of the Snow Lake arc assemblage to the Flin Flon belt prior to turbidite deposition.

Chapter 3 is written as a manuscript entitled **"The structural and stratigraphic setting, mineralogy, and geochemistry of the Photo Lake VMS deposit, Snow Lake, Manitoba: implications for the timing and source of gold mineralization."** This chapter has been submitted to the journal Economic Geology and is under review. It presents a detailed description of the Photo Lake deposit, including its host rocks, sulfide mineralization, metal zoning, and alteration. This description is used to establish the volcanic history and structural setting of the deposit and determine the timing of Au and processes responsible for Au enrichment. The Photo Lake deposit is interpreted to have formed at the same ore interval as the other VMS deposits in the Chisel sequence, and the Au enrichment is interpreted to be syngenetic, and may have resulted from a magmatic input to the ore-forming hydrothermal system.

Chapter 4 is written as a manuscript entitled **"Petrogenesis and volcanic reconstruction of a VMS-hosting subsidence structure: the Chisel sequence, Snow Lake, Manitoba"** (to be submitted). This chapter documents the lithofacies and geochemistry of the volcanic rocks in the Chisel sequence and provides an interpretation of the volcanic setting for the Chisel sequence within the context of the Snow Lake arc assemblage as a whole. The geodynamic setting of the Snow Lake arc assemblage is compared with that of the Flin Flon arc assemblage in order to contribute to a better understanding of the VMS metallogeny of the Flin Flon belt.

1.5 Statement of original contributions

The following is a summary of original contributions presented by the candidate in this study:

1. A description of a previously unrecognized deformation event in the volcanic rocks of the Snow Lake arc assemblage, which occurred prior to deposition of the Burntwood Group turbidities.
2. A new interpretation for the stratigraphy of the Upper Chisel sequence.
3. The first description of the Photo Lake VMS deposit, including its host rocks, sulfide mineralization, metal zoning, and alteration.
4. A description of four different textural varieties of pyrite in the Photo Lake deposit and their implications for the hydrothermal and metamorphic history of the deposit.
5. A new interpretation for the source of Au and Cu mineralization in the Photo Lake deposit.
6. A description of the internal stratigraphy and lithofacies of the Threehouse unit.
7. A new interpretation for the volcanic evolution of the Chisel sequence and Snow Lake arc assemblage.

1.6 References

Ansdell, K.M., Lucas, S.B., Connors, K., and Stern, R.A. 1995. The Kisseynew Gneiss Belt, Trans-Hudson Orogen, Canada: origin and history of a Paleoproterozoic back-arc sedimentary basin. Geology **23**: 1039-1043.

Ansdell, K.M., Connors, K.A., Stern, R.A., and Lucas, S.B. 1999. Coeval sedimentation, magmatism, and fold-thrust belt development in the Trans-Hudson Orogen: geochronological evidence from the Wekusko Lake area, Manitoba, Canada. Canadian Journal of Earth Sciences **36**: 293-312.

Bailes, A.H. 1980a. Geology of the File Lake area. Manitoba Energy and Mines, Geological Report 78-1.

Bailes, A.H. 1980b. Origin of Early Proterozoic volcaniclastic turbidites, south margin of the Kisseynew sedimentary gneiss belt, File Lake, Manitoba. Precambrian Research **12**: 197-225.

Bailes, A.H. 1996. Setting of Cu-Zn-Au mineralization at Photo Lake (part of NTS 63K16). *In* Report of Activities 1996. Manitoba Energy and Mines, Minerals Division, p. 66-74.

Bailes, A.H. 1997. Geochemistry of Paleoproterozoic rocks in the Photo Lake area, Flin Flon Belt (part of NTS 63K16). *In* Report of Activities 1997. Manitoba Energy and Mines, Minerals Division, p. 61-72.

Bailes, A.H. 2014. Regional geological setting of the Zn- and Au-rich Lalor VMS deposit, Snow Lake, Manitoba, Canada. *In* British Columbia Geophysical Society Lalor Symposium Presentations Listing. Available from http://www.bcgsonline.org/lalor-symposium/ [accessed 10 June 2017].

Bailes, A.H., and Galley, A.G. 1996. Setting of Paleoproterozoic volcanic-hosted massive base metal sulfide deposits, Snow Lake. *In* Bonham-Carter, G.F., Galley, A.G., and Hall, G.E.M., eds., EXTECH 1: A Multidisciplinary Approach to Massive Sulfide Research in the Rusty Lake-Snow Lake Greenstone Belts, Manitoba: Geological Survey of Canada, Bulletin 426, p. 105-138.

Bailes, A.H., and Galley, A.G. 1999. Evolution of the Paleoproterozoic Snow Lake arc assemblage and geodynamic setting for associated volcanic-hosted massive sulfide deposits, Flin Flon Belt, Manitoba, Canada. Canadian Journal of Earth Sciences **36**: 1789-1805.

Bailes, A.H., and Galley, A.G. 2007. Geology of the Chisel-Anderson lakes area, Snow Lake, Manitoba (NTS area 63K16SW and west half of 63J13SE). Manitoba Science, Technology, Energy and Mines, Manitoba Geological Survey, Geoscientific Map MAP2007-1, scale 1:20 000 plus notes.

Bailes, A.H., Hunt, P.A., and Gordon, T.M. 1991. U-Pb dating of possible synvolcanic intrusions in the Flin Flon belt at Snow Lake, Manitoba. *In* Radiogenic Age and Isotopic Studies, Report 4, Geological Survey of Canada, Paper 90-2, pp. 35–43.

Bailes, A.H., Galley, A.G., Skirrow, R.G., and Young, J. 1996. Geology of the Chisel volcanic-hosted massive sulfide area, Snow Lake, Manitoba (part of 63K/16SE). Manitoba Energy and Mines, Open File Report OF95-4, annotated 1:5000 colour map.

Bailes, A.H., Gilmore, K., Levers, J., and Janser, B. 2009. The Lalor deposit – surprise at depth. *In* Manitoba Mineral Resources, Manitoba Mining and Minerals Convention 2009 Proceedings, Winnipeg, Manitoba, November 19-21, pp. 57-58.

Bailes, A.H., Rubingh, K., Gagné, S., Taylor, C., Galley, A., Bernauer, S., and Simms, D. 2013. Volcanic setting of Paleoproterozoic VMS and gold deposits at Snow Lake, Manitoba. Geological Association of Canada – Mineralogical Association of Canada Joint Annual Meeting, Field Trip Guidebook FT-A2. Manitoba Innovation, Energy and Mines, Manitoba Geological Survey, Open File OF2013-3, 63 p.

Bailes, A.H., Galley, A.G., Paradis, S., and Taylor, B.E. 2016. Variations in large synvolcanic alteration zones at Snow Lake, Manitoba, Canada, with proximity to associated volcanogenic massive sulfide deposits. Economic Geology **111** : 933-962.

Connors, K.A., Ansdell, K.M., and Lucas, S.B. 1999. Coeval sedimentation, magmatism, and fold-thrust development in the Trans-Hudson Orogen: propagation of deformation into an

active continental arc setting, Wekusko Lake area, Manitoba. Canadian Journal of Earth Sciences **36**: 275-291.

Corrigan, D., Galley, A.G., and Pehrsson, S. 2007. Tectonic evolution and metallogeny of the southwestern Trans-Hudson Orogen. *In* Mineral Deposits of Canada: A Synthesis of Major Deposit-Types, District Metallogeny, the Evolution of Geological Provinces, and Exploration Methods. *Edited by* W.D. Goodfellow. Geological Association of Canada, Mineral Deposits Division, Special Publication No. 5, p. 881-902.

Corrigan, D., Pehrsson, S., Wodicka, N., and de Kemp, E. 2009. The Palaeoproterozoic Trans-Hudson Orogen: a prototype of modern accretionary processes. Geological Society, London, Special Publications, v. 327, p. 457-479.

David, J., Bailes, A.H., and Machado, N. 1996. Evolution of the Snow Lake portion of the Palaeoproterozoic Flin Flon and Kisseynew belts, Trans-Hudson Orogen, Manitoba, Canada. Precambrian Research, **80**: 107-124.

de Ronde, C.E.J., Massoth, G.J., Butterfield, D.A., Christenson, B.W., Ishibashi, J., Ditchburn, R.G., Hannington, M.D., Brathwaite, R.L., Lupton, J.E., Kamenetsky, V.S., Graham, I.J., Zellmer, G.F., Dziak, R.P., Embley, R.W., Dekov, V.M., Munnik, F., Lahr, J., Evans, L.J., and Takai, K. 2011. Submarine hydrothermal activity and gold-rich mineralization at Brothers Volcano, Kermadec Arc, New Zealand. Mineralium Deposita, **46:** 541-584.

Dubé, B., Mercier-Langevin, P., Hannington, M., Lafrance, B., Gosselin, G., and Gosselin, P. 2007. The LaRonde Penna world-class Au-rich volcanogenic massive sulfide deposit, Abitibi, Québec: mineralogy and geochemistry of alteration and implications for genesis and exploration. Economic Geology, **102:** 633-666.

Franklin, J.M., Gibson, H.L., Jonasson, I.R., and Galley, A.G., 2005, Volcanogenic massive sulfide deposits, in Hedenquist, J.W., Thompson, J.F.H., Goldfarb, R.J., and Richards, J.P., eds., Economic Geology 100th Anniversary Volume, p. 523-560.

Galley, A.G., Syme, R., and Bailes, A.H. 2007. Metallogeny of the Paleoproterozoic Flin Flon Belt, Manitoba and Saskatchewan. *In* Mineral Deposits of Canada: A Synthesis of Major Deposit-Types, District Metallogeny, the Evolution of Geological Provinces, and Exploration Methods. Special Publication No. 5. *Edited by* W.D. Goodfellow, W.D. Geological Association of Canada, Mineral Deposits Division. p. 509-531.

Gibson, H.L., Morton, R.L., and Hudak, G.J., 1999. Submarine volcanic processes, deposits, and environments favorable for the location of volcanic-associated massive sulfide deposits. Reviews in Economic Geology, **8**: 13-51.

Hannington, M.D., Peter, J.M., and Scott, J.D. 1986. Gold in sea-floor polymetallic sulfide deposits. Economic Geology, **81:** 1867-1883.

Hannington, M.D., Poulsen, K.H., Thompson, J.F.H., and Sillitoe, R.H. 1999. Volcanogenic gold in the massive sulfide environment. Reviews in Economic Geology, **8:** 325-356.

Herzig, P.M., Hannington, M.D., Fouquet, Y., von Stackelberg, U., and Petersen, S. 1993. Gold-rich polymetallic sulfides from the Lau back arc and implications for the geochemistry of gold in sea-floor hydrothermal systems of the southwest Pacific. Economic Geology, **88:** 2182-2209.

Kraus, J. and Williams, P.F. 1998. Relationship between foliation development, porphyroblasts growth and large-scale folding in a metaturbidite suite, Snow Lake, Canada. Journal of Structural Geology, **20**: 61-76.

Kraus, J. and Williams, P.F. 1999. Structural development of the Snow Lake Allochthon and its role in the evolution of the southeastern Trans-Hudson Orogen in Manitoba, central Canada. Canadian Journal of Earth Sciences, **36**: 1881-1899.

Lucas, S.B., Stern, R.A., Syme, E.C., Reilly, B.A., and Thomas, D.J. 1996. Intraoceanic tectonics and the development of continental crust: 1.92-1.84 Ga evolution of the Flin Flon Belt, Canada. GSA Bulletin **108**: 602-629.

Machado, N., Zwanzig, H., and Parent, M. 1999. U-Pb ages of plutonism, sedimentation, and metamorphism of the Paleoproterozoic Kisseynew metasedimentary belt, Trans-Hudson Orogen (Manitoba, Canada). Canadian Journal of Earth Sciences **36**: 1829-1842.

Mercier-Langevin, P., Hannington, M.D., Dubé, B., and Bécu, V. 2011. The gold content of volcanogenic massive sulfide deposits. Mineralium Deposita, **46:** 509-539.

Mercier-Langevin, P., Gibson, H.L., Hannington, M.D., Goutier, J., Monecke, T., Dubé, B., and Houlé, M. 2014. A special issue on Archean magmatism, volcanism, and ore deposits: Part 2. Volcanogenic massive sulfide deposits. Economic Geology **109**: 1-9.

Moss, R., and Scott, S.D. 2001. The geochemistry and mineralogy of gold-rich hydrothermal precipitates from the eastern Manus Basin, Papua New Guinea. The Canadian Mineralogist, **39:** 957-978.

Percival, J.A., Whalen, J.B., and Rayner, N. 2005. Pikwitonei-Snow Lake Manitoba transect (parts of NTS 63J, 63O and 63P), Trans-Hudson Orogen-Superior Margin Metallotect Project: new results and tectonic interpretation. *In* Report of Activities 2005. Manitoba Industry, Economic Development and Mines, Manitoba Geological Survey, p. 69-91.

Stern, R.A., Syme, E.C., Bailes, A.H., Galley, A.G., Thomas, D.J., and Lucas, S.B. 1992. Nd-isotopic stratigraphy of Early Proterozoic Amisk group metavolcanic rocks from the Flin Flon Belt, Manitoba and Saskatchewan. *In* Radiogenic age and isotopic studies report 6. Geological Survey of Canada, p. 73-84.

Stern, R.A., Syme, E.C., Bailes, A.H., and Lucas, S.B. 1995. Paleoproterozoic (1.90-1.86 Ga) arc volcanism in the Flin Flon Belt, Trans-Hudson Orogen, Canada. Contributions to Mineralogy and Petrology **119**: 117-141.

Syme, E.C., Lucas, S.B., Bailes, A.H., and Stern, R.A. 1999. Contrasting arc and MORB-like assemblages in the Paleoproterozoic Flin Flon Belt, Manitoba, and the role of intra-arc extension in localizing volcanic-hosted massive sulphide deposits. Canadian Journal of Earth Sciences,**36**: 1767-1788.

Zwanzig, H.V. 1990. Kisseynew gneiss belt in Manitoba: stratigraphy, structure, and tectonic evolution. *In* Lewry, J.F. and Stauffer, M.R., eds., The Early Proterozoic Trans-Hudson Orogen of North America: Geological Association of Canada Special Paper 37, p. 95-120.

Chapter 2

Early thrusting and folding in the Snow Lake camp, Manitoba: tectonic implications and effects on volcanogenic massive sulfide deposits

2.1 Abstract

The Chisel sequence occurs within the Snow Lake arc assemblage (SLA) of the Paleoproterozoic Trans-Hudson Orogen. It is host to six economic volcanogenic massive sulfide (VMS) deposits that formed within a single time-stratigraphic ore interval. The SLA was previously interpreted to share the same deformation history as the ca. 1.86-1.84 Ga Burntwood Group turbidites of the Kisseynew Basin to the north; however, early isoclinal folds identified in the arc assemblage cannot be correlated with structures in the turbidites and therefore developed prior to Burntwood Group deposition. This indicates that the SLA underwent a significant deformation event prior to 1.86 Ga, likely due to intraoceanic accretion to the oceanic Amisk collage during closure of the ancestral Manikewan Ocean. Evidence for this early folding event is recorded in the Chisel sequence deposits where it has influenced the geometry of the deposits and the location of the Chisel sequence ore interval. The deposits are isoclinally folded by these folds, and a major early thrust fault at the Lalor deposit, the Lalor-Chisel fault, displaced the hanging wall rocks of the deposit and the ore interval. Further flattening, transposition, and elongation of the ore lenses occurred during post-1.84 Ga collision of the SLA with the partially hidden Archean Sask craton. Although the VMS deposits are polydeformed and sulfides and precious metals were mechanically and hydrothermally remobilized at the metre scale, their primary base metal zoning remains intact and provides a tool to reconstruct the geometry of the deposits.

2.2 Introduction

Volcanogenic massive sulfide (VMS) deposits form at or near the seafloor in zones of active rifting during short periods of volcanic quiescence (Gibson et al. 1999; Franklin et al. 2005). As a result, these deposits have a strong stratigraphic control and are localized along intervals representing conditions ideal for metal precipitation and accumulation. Of the total metal tonnage in the global VMS record, Precambrian deposits account for approximately 27% Cu, 33% Zn, and 26% Au (Mercier-Langevin et al. 2014, and references therein). These deposits constitute an important global resource for base and precious metals; however, despite their strong stratigraphic control, exploration for these deposits is complicated by overprinting deformation events that may affect original deposit geometry, distribution and continuity.

The Flin Flon-Glennie Complex (FFGC), of the Trans-Hudson Orogen, hosts the largest Paleoproterozoic VMS district in the world (in terms of past production and reserves, estimated at 183 million tonnes; Syme et al. 1999). It is divided into the Glennie Domain in the west and the Flin Flon belt (FFB) in the east, which is further subdivided into the Amisk collage and the Snow Lake arc assemblage (SLA; Fig. 1). Most of the VMS deposits occur within the Flin Flon arc assemblage of the Amisk collage and the SLA (Fig. 1). The Chisel sequence is located in the SLA and hosts five Zn-Pb-Cu-Ag-Au VMS deposits (the Chisel Lake, Lost Lake, Ghost Lake, Chisel North, and Lalor deposits) and one Cu-Zn-Au-Ag deposit (the Photo Lake deposit). The SLA has undergone four major periods of deformation between 1.84 and 1.77 Ga (Kraus and Williams 1999) that have influenced the extent and geometry of the ore interval and may have influenced the current geometry and location of its contained VMS deposits.

The purpose of this study is to determine the structural controls on the present distribution of volcanic strata and VMS deposits in the Chisel sequence and the tectonic significance of these structures. Thus, in this manuscript we: (1) establish the deformation history of the Chisel sequence volcanic rocks; (2) relate this deformation history to the sequence of deformation events previously suggested for the SLA; (3) revise the Upper Chisel sequence stratigraphy; (4) determine how deformation has modified the VMS deposits; and (5) compare the deformation history of the SLA to that suggested elsewhere in the FFGC.

2.3 Regional Geology and Deformation History of the Snow Lake Area

2.3.1 Regional geology

Of the seven ca. 1.92 to 1.88 Ga tectono-stratigraphic assemblages in the FFB, the ca. 1892 Ma SLA (David et al. 1996) is the only assemblage interpreted to have evolved as a pericratonic arc outboard of the Superior craton rather than as an oceanic arc (Percival et al. 2005; Corrigan et al. 2007, 2009). It is divided into the Anderson, Chisel, and Snow Creek sequences, representing the transition from a primitive arc, to mature arc, to rifted arc geodynamic environments, respectively (Bailes and Galley 1996, 1999, 2007). Stratigraphically overlying the volcanic rocks of the SLA are sedimentary rocks of the Kisseynew Basin, which comprise alluvial-fluvial rocks of the Missi Group and turbidites of the Burntwood Group (Bailes 1980a,b; Zwanzig 1990). These rocks were deposited at ca. 1.855-1.84 Ga (David et al. 1996; Machado et al. 1999) and subsequently structurally interleaved with the SLA. With the exception of the Photo Lake deposit, Cu-rich deposits dominate in the Anderson sequence and Zn-rich deposits dominate in the Chisel sequence (Bailes and Galley 1996; Galley et al. 2007).

The Chisel sequence is divided into lower and upper sequences, and the transition between these sequences represents a period of volcanic quiescence and subsidence following rhyolite dome development that coincides with the VMS ore interval (Bailes and Galley 2007; Engelbert et al. 2014a; Gibson et al. 2014; Friesen et al. 2015). The lowermost units of the Lower Chisel sequence are the Stroud breccia, Snell basalt, and Edwards mafic volcaniclastic rocks (Figs. 2, 3a). The stratigraphy of the Lower Chisel sequence immediately below and in the footwall of the VMS deposits consists of the Moore Lake basalt, Powderhouse dacite, and Chisel rhyolite units. The Upper Chisel sequence is interpreted to form the stratigraphic hanging wall to the VMS deposits but its stratigraphy is not well defined. It is interpreted to be a homoclinal succession consisting of, in ascending order, the Balloch basalt, the Ghost-Photo rhyolite and the Threehouse mafic volcaniclastic rocks and flows (Bailes and Galley 1996, 1999, 2007; Figs. 2, 3a). The Threehouse mafic volcaniclastic rocks and flows are herein referred to as the 'Threehouse unit.' Volcanogenic massive sulfide deposits occur at the contact between the Chisel rhyolite or Powderhouse dacite and Threehouse unit. At the Lalor deposit, the stratigraphy of the Upper Chisel sequence is more complex and is interpreted to consist of, in ascending order, the North Balloch rhyolite, the Balloch basalt, the Ghost rhyolite, the Threehouse unit, the North Chisel dacite, and undivided volcaniclastic rocks (Bailes and Galley 1996, 1999, 2007; Bailes et al. 2009, 2013, 2016; Bailes 2014; Figs. 2, 3a). The deposit is located in the footwall to the Lalor-Chisel fault, which juxtaposes steeply dipping strata exposed at surface against the shallowly dipping strata that hosts the deposit (Bailes et al. 2013; Bailes 2014). The Photo Lake deposit is different in terms of its volcanic setting as it sits at the contact between two mineralogically and geochemically distinct rhyolite units that comprise the Photo rhyolite flow complex (Engelbert et al. 2014b). The lower rhyolite unit is characterized by a greater

concentration of amphibole (≤40% amphibole in lower rhyolite versus ≤10% amphibole in upper rhyolite) and lower high field strength element (HFSE) concentrations than the upper rhyolite unit (Engelbert et al. 2014b). The Chisel sequence volcanic rocks are intruded by the synvolcanic Richard intrusive complex, which has been dated at 1889 +8/-6 Ma by U-Pb zircon geochronology (Bailes et al. 1991).

2.3.2 Deformation and metamorphism

Several structural studies have been conducted at Snow Lake, both at the district (Froese and Moore 1980; Galley et al. 1988; Kraus and Williams 1993, 1994, 1998, 1999; Beaumont-Smith and Gagné 2008; Gagné 2009; Rubingh et al. 2012) and deposit scales (Martin 1966; Galley et al. 1993; Tessier 1996, 2000, 2001; Beaumont-Smith and Lavigne 2008; Caté et al. 2014; Caté 2016). Most of the district scale work has been done in turbidites of the Burntwood Group and in the volcanic strata bounded by the McLeod Road and Birch Lake faults north of the area mapped in this study. Little detailed structural work has been completed in the Chisel sequence volcanic rocks. This is due to more restricted accessibility of the Chisel sequence volcanic rocks, as well as better expression of primary and deformation fabrics and structures in the sedimentary rocks than in the volcanic rocks.

Early workers in the Snow Lake area identified two main deformation events in both the Burntwood Group turbidites and the Chisel sequence volcanic rocks (Froese and Moore 1980; Galley et al. 1988; Table 1). The first deformation event (D_1) is characterized by tight, isoclinal folds with a strong penetrative axial planar S_1 foliation that forms the prominent planar fabric in the area and is approximately parallel to S_0. This fabric is defined by biotite and amphibole and

by flattened clasts and mineral aggregates (Froese and Moore, 1980; Galley et al., 1988). These early workers also identified an L_1 mineral stretching lineation moderately plunging to the northeast and defined by stretched clasts. The second deformation event (D_2) consists of megascopic northeast-trending folds that refold S_1 (Froese and Moore, 1980) and cause the large-scale warping of units observed throughout the Snow Lake area (Galley et al., 1988). These F_2 folds, which include the Threehouse synform, have an associated S_2 axial planar cleavage. The S_2 cleavage is defined by biotite and is penetrative in the Missi and Burntwood Groups, less prominent in the felsic volcanic rocks, and rarely observed in the mafic volcanic rocks. Staurolite growth occurred along the S_2 plane. Froese and Moore (1980) also identified an L_2 lineation parallel to F_2 fold axes that is defined by the hinge of crenulations, elongate clasts, and mineral segregations.

The most widely referenced deformation history and tectonic reconstruction of the Snow Lake area is a study by Kraus and Williams (1999; Table 1). This study focused on the Burntwood Group rocks, where the S_1 fabric is expressed as inclusion trails in garnet, biotite, and staurolite porphyroblasts and as a weak slaty cleavage axial planar to rare isoclinal F_1 folds. They described a biotite and staurolite fabric, equivalent to the S_2 fabric of Froese and Moore (1980) and Galley et al. (1988), as the dominant fabric in the Burntwood Group rocks. Kraus and Williams (1998, 1999) correlated this fabric with a generation of isoclinal folds older than the F_2 folds but younger than the F_1 folds of Froese and Moore (1980) and Galley et al. (1988). Therefore, the F_2 folds of Froese and Moore (1980) and Galley et al. (1988) were reclassified as F_3 folds. Kraus and Williams (1998) identified a disjunctive and crenulation S_3 cleavage axial planar to the F_3 folds. Kraus and Williams (1998, 1999) suggested that the tight to isoclinal

southerly-verging F_1 and F_2 folds formed during a progressive D_1-D_2 deformation associated with south- to southwest-directed thrusting and the formation of the McLeod Road and Snow Lake thrust faults, which juxtapose Burntwood turbidites against older volcanic rocks. Deformation in the SLA was due to overthrusting of the Sask craton by the Kisseynew basin and Flin Flon belt followed by collision of the Sask craton with the Superior craton during the Hudsonian orogeny (Stauffer 1984; Ansdell 2005; Corrigan et al. 2007). Peak metamorphism was diachronous and is syn-D_2 in the Snow Lake area (P=4-6 kbar, and T<580°C) and post-D_2 north of the Snow Lake area (P=5-6 kbar, and T=600-800°C) (Kraus and Menard, 1997; Menard and Gordon, 1997; Kraus and Williams, 1999). Although all rocks in the Snow Lake area are metamorphosed, the term "meta" is implicit and this prefix is not used in the text.

2.4 Structures and metamorphic fabrics in the Upper Chisel sequence

Detailed mapping was done in three areas surrounding VMS deposits in the Chisel sequence (Fig. 2): 1) the Photo Lake deposit area; 2) the South Chisel basin area; and 3) the Lalor section. These areas are ideal for structural studies in volcanic rocks due to the strong hydrothermal alteration (e.g., chlorite, sericite) associated with VMS deposit formation. Altered rocks contain abundant micas and therefore record structures and fabrics in rocks that otherwise do not have primary features or mineralogy susceptible to fabric development. These areas are described below and the structures and metamorphic fabrics are shown in Figure 4.

2.4.1 The Photo Lake deposit area

The Photo Lake deposit was mapped underground when it was in production from 1995 to 1998. It consists of two massive sulfide lenses that are tightly folded and transposed parallel to the

axial plane of the folds (Engelbert et al. 2014b). The lenses are flattened and elongated, with a strike and dip of approximately 270°/60° and a plunge and trend of 40° to 45° towards 050° (Tessier, 1996). The surface projections of the folds and the deposit are shown on Figure 5. The folds are well exposed in a quarry, herein named the Photo quarry (Fig. 6), which is along strike of their surface projection. The Photo quarry exposes a large F_1 fold (Photo syncline; Fig. 6) with massive to pillowed flows with flow top breccia younging to the east along its west limb (Fig. 7a) and rhyolite flows overlain by graded mafic volcaniclastic rocks younging to the west along the opposite limb of the fold (Fig. 7b). On the east limb of this fold, an upward transition from massive to lobe facies in the rhyolite flows and rhyolite clasts in the overlying mafic volcaniclastic rocks proximal to the contact provide further evidence of westward younging (Fig. 7c). On an equal-area stereonet plot, the poles to bedding (S_0) define a great circle girdle with a pole (π) plunging 56° and trending 030°. This pole (π) represents the axis of the fold, which, in conjunction with the orientation of the fold axial trace (155° or 335°), defines an axial plane striking 335° and dipping 60° to the northeast (Fig. 6).

The Photo syncline lacks an axial planar cleavage but is transected by a strong spaced cleavage, striking 315° and dipping 46° to the northeast, which is defined by biotite and amphibole and by flattened clasts in the mafic volcaniclastic rocks (Fig. 4a-c). Garnet porphyroblasts are contained within this spaced cleavage but also overgrow it (Fig. 4c). This cleavage varies from weak to strong as a function of the degree of hydrothermal alteration in the rocks, with the most hydrothermally altered rocks exhibiting the best cleavage development. In rocks where hydrothermal alteration is weak to non-existent, the spaced cleavage is an anastomosing fabric defined by aligned amphibole ±biotite that imparts a pseudo-clastic appearance to the coherent

volcanic rocks. Because the cleavage overprints the map-scale fold in Figure 6, it is interpreted as an S_2 fabric overprinting an early F_1 fold. A stretching lineation (L_2) defined by the elongation of the clasts (Fig. 4b), the alignment of amphibole, and pressure shadows around the clasts plunges 41° towards 031° along the plane of the S_2 foliation and roughly parallel to the plunge and trend of the F_1 fold.

A weak S_3 cleavage defined by biotite strikes 010-030° and dips steeply (70-85°) to the east-southeast. In hydrothermally altered rhyolite, the S_3 cleavage is also defined by quartz-filled pressure shadows around garnet porphyroblasts that contain internal inclusion trails parallel to the S_2 cleavage. Biotite laths defining the spaced S_2 cleavage described above are aligned parallel to the S_3 cleavage, which is at a high angle to the spaced cleavage planes (Fig. 4d). The S_3 cleavage is axial planar to open F_3 folds overprinting the S_2 foliation (Fig. 4e) and the map-scale F_1 fold. The poles to the folded S_2 foliation define a great circle girdle which has a pole (π) plunging 44° towards 040°, roughly parallel to the L_2 stretching lineation (Fig. 6). Overprinting relationships between the three generations of structures are observed on an outcrop in the hinge of the F_1 fold, where a mafic dike that has been tightly folded by F_1 is overprinted by the S_2 foliation, the S_3 cleavage, and an F_3 fold (Fig. 8). The F_3 and F_1 folds have similar fold axis orientations indicative of a Type 3 coaxial interference pattern (Ramsey 1967).

2.4.2 The South Chisel basin area

The South Chisel basin area consists of broadly east-west-trending volcanic strata but their orientation is variable due to folding (Fig. 9). This area is host to the Chisel Lake, Chisel North, Lost Lake, and Ghost Lake VMS deposits. The Chisel North deposit is the down-plunge

extension of the Chisel deposit (Galley et al. 1993). Detailed geological and structural mapping (1:100 to 1:2,000 scale) was conducted proximal to the surface projections of these deposits in order to establish the deformation history in this area and determine the effects of deformation on the current geometries and locations of the deposits (Chisel open pit: Fig. 10; Ghost-Lost area: Fig. 11). Detailed structural mapping was also carried out in several critical areas within the Powderhouse dacite unit in order to correlate the structure in the area surrounding the Ghost and Lost deposits with that of the Chisel and Chisel North deposits (Fig. 12).

The earliest fold generation identified in the South Chisel basin area is observed in the Chisel open pit (Fig. 10), where isoclinal folds overprint altered and least altered rhyolite flows. These early folds are overprinted by a strong S_2 foliation, which is defined by flattened clasts and by biotite and amphibole. The S_2 foliation has the same anticlockwise relationship with S_0 on both limbs of the fold, which is defined by the contact between altered and least altered rocks. This is similar to the F_1 fold and overprinting S_2 cleavage relationship at the Photo quarry and indicates that the folds in the Chisel pit are early F_1 folds. South of the Chisel pit, strongly altered rocks associated with the Chisel deposit hydrothermal system preserve the S_2 fabric as quartz inclusion trails in porphyroblasts of garnet and staurolite (Fig. 4f,g).

In the Ghost-Lost area, the Ghost anticline is defined by folded well-bedded mafic and felsic tuff (Fig. 9). Younging is identified on both limbs by normal grading, slumping, and scours (Fig. 7d,e), and younging is towards the west on the west limb and towards the east on the east limb. The bedded tuffs pinch out to the east and cannot be followed any further around the fold, possibly due to termination against a synvolcanic structure (e.g. Gibson et al. 1999; Friesen et al.

2015). The significant volume of intrusions in this area and their strong competency in comparison with the bedded tuffs likely also influenced the geometry of this fold. Detailed mapping through several tight, isoclinal folds revealed that the strong S_2 foliation is axial planar to these folds, which suggests that they are F_2 folds. The map-scale folds, which are best exposed in the Ghost section (Fig. 11) and in the Powderhouse section (Fig. 12), are therefore also interpreted as F_2 folds. On a map scale, bedding is approximately parallel to the S_2 foliation along the limbs of the folds and on an outcrop scale intrafolial folding of the bedding and clasts is observed (Fig. 4h). The poles to bedding in the Ghost section define a great circle girdle with a pole (π) plunging 13° and trending 304° (Fig. 11). This pole is shallower than the fold axis to the Ghost anticline but roughly coaxial (Fig. 11).

Open F_3 folds with an axial planar S_3 cleavage defined by biotite refold the S_2 cleavage and F_1 and F_2 folds in the South Chisel basin area (Figs. 10-12). Quartz pressure shadows surrounding porphyroblasts of garnet and staurolite are also aligned along the S_3 fabric (Fig. 4i). F_3 axial planes and the S_3 cleavage strike northeast and dip steeply to the east-southeast (70-85°). The folds plunge 59° towards 029° as represented by the pole (π) to the great circle defined by the poles to bedding. The F_3 folds have roughly the same orientation as the stretching lineation (L_2) in the map area, which has an average orientation of 32° → 026°.

2.4.3 The Lalor section

The Lalor section exposes a succession of northwest-southeast-trending mafic and felsic flows and heterolithic volcaniclastic rocks that was previously interpreted as a homoclinal volcanic succession with the stratigraphic way-up direction towards the southwest (Bailes and Galley

2007; Bailes et al. 2013; Bailes 2014). Detailed surface mapping of contacts between the volcanic units identified younging reversals throughout the succession indicative of tight, isoclinal folding (Fig. 13). Younging directions were identified by normal-graded bedding, cross-bedding (Fig. 7f), scours (Fig. 7g), truncated bedding, and flow transitions from massive to lobe facies. The upper contacts of rhyolite flows are commonly also marked by monolithic rhyolitic lapilli tuff to tuff breccia interpreted to represent flow top breccia. Where rhyolite flows are in contact with mafic volcaniclastic rocks, clasts of the rhyolite flows occur within the volcaniclastic rocks at the contact and decrease in abundance moving away from the contact (Fig. 7h), indicating that the mafic volcaniclastic rocks overlie the rhyolite flows. Rhyolite clasts were not identified in the mafic volcaniclastic rocks >10 m away from the contact.

The mapping revealed that the Ghost rhyolite (Figs. 2, 13) is stratigraphically below the Balloch basalt and Threehouse mafic volcaniclastic rocks and occupies the core of a map-scale anticline named the Lalor anticline (Figs. 13, 14). An L_2 stretching lineation defined by elongate clasts plunges moderately (30°-50°) to the northeast (Fig. 13). An S_2 foliation, which is defined by biotite, amphibole, and flattened clasts, cuts across both limbs of the fold in clockwise manner. A parasitic fold to the Lalor anticline is present on outcrops of bedded tuffs and lapilli tuffs of the North Chisel dacite, where it is defined by normal grading reversals (Fig. 15). Its axial plane strikes 172°, dips 80° to the east, and its fold axis plunges 20° towards 348°. The S_2 cleavage transects both limbs of the fold on vertical and horizontal surfaces. This suggests that the tight, isoclinal folds along the Lalor section are F_1 folds. As the S_2 cleavage intersects F_1 folds at a very low angle (10-20°), good exposures are required to confidently differentiate F_1 from F_2 folds. For this reason, only folds in the Lalor section that have been identified as F_1 by means of

cross-cutting relationships in the field are labeled as such; all other folds are labeled as F_{1-2} (Fig. 14). This labeling system is maintained throughout the Chisel sequence.

The Lalor section is significant because it is host to the Lalor VMS deposit shown in vertical cross-section in Figure 14. The cross-section builds on previous work by Bailes et al. (2013) and Bailes (2014) through detailed re-logging of selected drill holes combined with drill logs provided by Hudbay Minerals. It shows that a fault (Lalor-Chisel fault) separates the steeply dipping volcanic rocks mapped at surface from the shallowly dipping volcanic rocks hosting the Lalor deposit (Bailes et al. 2013; Bailes 2014; Caté et al. 2014). The fault was intersected in drill holes DUB 172 and 236, where it is characterized by a 10 m-thick metamorphosed breccia (Fig. 16a), and in drill hole DUB 188, where it is defined by a strong, mica-rich foliation and flattened clasts (Fig. 16b). The fault appears to project to surface west of the Lalor cross-section (Fig. 17, 18). Several minor ductile faults were also identified at surface and in cross-section (Figs. 13, 14).

Evidence for large-scale folding of the Lalor-Chisel fault and transposition of the ore lenses in the Lalor deposit is provided by the geometry of the alteration zone and distribution of the host rocks (Fig. 14), detailed underground mapping by Caté et al. (2014), and metal zoning within the ore lenses (Fig. 19; Engelbert et al. 2014c). Volcanogenic massive sulfide deposits are mineralogically and chemically zoned due to differences in temperature-dependent solubility of Pb, Zn, and Cu (Lydon 1984, 1988; Hannington and Scott 1988; Hannington et al. 1995). Zinc is more soluble at lower temperatures than Cu and can thus be transported by lower temperature hydrothermal fluids. Typical VMS deposits therefore have a higher-temperature (300-350°C),

Cu-rich core and stringer zone and lower-temperature (150-200°C), Zn-rich margins (Lydon, 1984, 1988; Hannington and Scott 1988; Hannington et al. 1995). Chalcopyrite and other Cu-bearing mineral phases will also be concentrated along fluid upflow zones where high-temperature fluids migrated upwards. The metal zoning within a deposit as represented by Cu/(Cu + Zn) values (Knuckey et al. 1982) can therefore be useful for identification of primary upflow zones during deposit formation and can aid in determining stratigraphic way up.

Although there is evidence for remobilization of metals within the Lalor deposit (Caté et al. 2014), the deposit-scale primary zoning has been preserved (Duff et al. 2015) and can be used to determine the geometry of the hydrothermal system. The ore lensesin the Lalor deposit are hosted by the Powderhouse dacite and Moore Lake units, which occur at separate stratigraphic intervals; however, the Moore Lake unit consists predominantly of breccia and contains clasts of the overlying Powderhouse dacite (Fig. 14). This indicates that the Moore Lake unit has been resedimented following emplacement of the Powderhouse dacite and occurs at the Chisel sequence ore interval. Therefore, the ore lenses hosted within the Moore Lake breccia occur at the same stratigraphic interval as the lower lenses in the deposit, and the metal zoning within these lenses can be used for the deposit reconstruction.

In the Lalor deposit, metal zoning of the ore lenses indicates that there is a central Cu-rich zone in the deposit, visible in the 10 and 20 lenses (Fig. 19b-e), which is interpreted to be a fluid upflow zone. There is also a Cu-rich zone at the margin of the uppermost sulfide lens (10 lens; Fig. 19b, c). Neither of these Cu-rich zones penetrates through the lower lenses as would be expected if the lenses were originally upright and stacked above an upflow zone; rather, the

lowermost sulfide lenses (30, 31, and 40 lenses) are entirely Zn rich (Fig. 19f, g). The distribution of Zn grades within the deposit indicates that the lenses, including the lowermost Zn-rich lenses, are continuous and folded (Caté 2016). Therefore, the absence of a Cu-rich fluid upflow zone in the lowermost lenses is not a product of stacking by later thrust faulting. This suggests that the lowermost ore lenses are overturned and the ore lenses have been folded about a major anticline (Fig. 14). The current geometry of the ore lenses and host strata suggests that the limbs of the fold have also been offset by a structure parallel to the axial plane of the fold. The metal zoning within the Lalor deposit and identification of isoclinal folding of the lenses can be combined in order to produce a reconstruction of the deposit prior to deformation (Fig. 19h).

2.5 Discussion

2.5.1 Implications for the stratigraphy of the Upper Chisel sequence

Previous work on the hanging wall strata to the Lalor VMS deposit suggested that it represents a homoclinal succession beginning with the North Balloch rhyolite at the base, overlain by the Balloch basalt, Ghost and Photo rhyolites, Threehouse mafic volcaniclastic rocks, and North Chisel dacite (Fig. 3a; Bailes and Galley 2007; Bailes et al. 2013; Bailes 2014). This succession also includes undivided rocks of the Upper Chisel sequence at the northeastern and southwestern extents of the Lalor section that have not been correlated with the Upper Chisel sequence stratigraphy (Figs. 2, 3a; Bailes and Galley, 2007).

Recognition of faulting and early isoclinal folding indicates that the hanging wall succession is not homoclinal, but rather a repetition of the same stratigraphy identified elsewhere in the Chisel basin. Facing reversals indicate that both the North Balloch and Ghost rhyolites occur

immediately below the Balloch basalt and Threehouse mafic volcaniclastic rocks (Figs. 3b, 13, 14), suggesting that the two rhyolites are stratigraphically equivalent. This is further supported by conformable contacts between these rhyolite units and the overlying mafic rocks where the contacts are exposed. The Photo rhyolite is also grouped within this felsic package because Bailes and Galley (1999, 2007) interpreted the Ghost and Photo rhyolites to occur at the same stratigraphic position and they share similar whole rock geochemistry (Bailes 1997). This is further supported by similar contact relationships between the Threehouse unit and the Ghost rhyolite in the Lalor section and between the Threehouse unit and the Photo rhyolite in the Photo quarry. At both contacts, the felsic flows transition upward from massive to lobe facies and are overlain by 5 to 10 m of mafic tuff interbedded with normal graded, well-bedded heterolithic mafic lapilli tuff to tuff breccia. Felsic clasts of the underlying felsic flow occur in the overlying mafic volcaniclastic rocks and decrease in abundance moving upward from this contact. A similar relationship is observed at the upper contact of the North Balloch rhyolite, where it is overlain by undivided mafic volcaniclastic rocks that also contain rhyolite clasts increasing in abundance towards the contact (Fig. 2). Given that this package of undivided mafic volcaniclastic rocks occurs immediately above the North Balloch rhyolite, it is stratigraphically equivalent to the Threehouse unit. This, combined with similarities in clast size, content, and composition between the undivided mafic rocks and the Threehouse unit in the Photo quarry and Lalor section, suggests that the undivided rocks belong to the Threehouse unit (Fig. 17).

Detailed mapping of lithofacies in the North Chisel dacite and Powderhouse dacite has shown that these units are stratigraphically equivalent (Friesen et al. 2015). The North Chisel dacite is now referred to as the Lalor member of the Powderhouse dacite and the Powderhouse dacite

elsewhere in the Chisel sequence is referred to as the Chisel member (Friesen et al. 2015). The undivided unit (Fig. 2; unit indicated by a star in Fig. 17) immediately southwest of the Lalor member in the Lalor section is correlated with the Threehouse mafic volcaniclastic rocks given its similar appearance and stratigraphic position above the Powderhouse dacite (Fig. 17). The undivided unit (Fig. 2; unit indicated by a square in Fig. 17) at the southwestern extent of the Lalor section is interpreted to be equivalent to the Lalor member of the Powderhouse dacite because of its similar appearance, lateral correlations at depth (Fig. 14), and facing reversals indicating that it occurs stratigraphically below the Threehouse unit. Therefore, the units repeated by folding and faulting in the hanging wall to the Lalor deposit are stratigraphically equivalent to the ore interval stratigraphy defined elsewhere in the basin as the transition from Powderhouse dacite, to rhyolite, to Threehouse mafic volcaniclastic rocks (Bailes and Galley 2007; Engelbert et al. 2014a; Fig. 17). However, these units terminate against the Lalor-Chisel fault at depth, and folding, faulting, and erosion may have removed any potential mineralization in the hanging wall to the Lalor deposit.

2.5.2 Relative timing of deformation in the volcanic rocks and Burntwood turbidite sequence

Early isoclinal F_1 folds in the Photo quarry (Photo syncline; Fig. 6), South Chisel basin area (Chisel open pit; Fig. 10), and Lalor section (Lalor anticline; Figs. 13, 14) were not previously recognized. These folds lack an axial planar cleavage and, as they are not recognized in the Burntwood Group turbidites, the associated folding event occurred prior to deposition of the Burntwood Group rocks at ca. 1859-1842 Ma (detrital zircon U/Pb age; David et al. 1996). The earliest cleavage overprinting these folds is a penetrative S_2 foliation defined by biotite, hornblende and flattened clasts. Kraus and Williams (1999) correlated this fabric with the early

S_1 cleavage in the Burntwood Group turbidites (Kraus and Williams 1993, 1994, 1998, 1999), which is preserved as inclusion trails in garnet porphyroblasts. The dominant foliation in the Burntwood Group rocks strikes north-northwest to north-northeast and is defined by biotite wrapping around staurolite and garnet porphyroblasts surrounded by quartz-plagioclase-filled strain shadows. This foliation occurs in the metavolcanic rocks as a weak, north- to northeast-striking cleavage, which can be easily mistaken with a northeast-striking cleavage defined by biotite that is axial planar to the Threehouse syncline (Rubingh et al. 2012). As these two cleavages cannot be differentiated from each other on outcrops where only one of the two cleavages is present, they are grouped together as the S_3 cleavage. The events identified in the current study are correlated with previous studies in Table 1 and the deformation events have been assigned to new generations in order to incorporate the early folding event.

2.5.3 Timing and nature of the Lalor-Chisel fault

The Lalor-Chisel fault is defined in drill core as a zone of heterolithic breccia (Fig. 16a), suggesting that it originated as an early brittle fault. The overprinting S_2 foliation is variably developed along the fault and, where prominent, it is defined by strongly flattened breccia fragments (Fig. 16b). Underground mapping by Caté et al. (2014) also suggested that it formed as an early brittle thrust fault, which was later reactivated and overprinted by S_2.

The Lalor cross-section (Fig. 14) displays the relationships between the Lalor-Chisel fault and the folds in its hanging wall. The fault juxtaposes steeply dipping strata in the hanging wall against shallowly dipping strata in the footwall. The fault cuts across the axial planes of isoclinal F_1 folds in the hanging wall stratigraphy; however, it is folded by recumbent folds at depth in

proximity to the ore lenses (Fig. 14), suggesting that it is an early structure. The Lalor-Chisel fault is therefore interpreted as an early brittle thrust fault that formed later than the F_1 folds in its hanging wall but during the same D_1 deformation event. This interpretation is consistent with that of Caté et al. (2014), who suggested that a significant fault separating altered and least altered rocks at depth had been folded during the D_2 event, but it differs from their interpretation as they interpret this folded fault to be a separate structure from the Lalor-Chisel fault, which they do not project to surface.

Our interpretation suggests that the Lalor-Chisel fault projects to surface beneath the Chisel pluton (Figs. 17, 18). Southwest of the Lalor deposit the fault appears to follow the contact between the Lalor and Chisel members of the Powderhouse dacite formation. Friesen et al. (2015) interpreted the contact between these members to be a major synvolcanic fault separating nested basins within a larger subsidence structure. It is therefore possible that the Lalor-Chisel fault initially formed as a synvolcanic fault that was reactivated during later deformation events. If the Lalor-Chisel fault represents a major synvolcanic structure separating basins, the transition of this structure from steep at surface to shallow at depth (Fig. 18) may be due to the influence of the primary basin structure during later deformation. This would be similar to the structural evolution of the Kisseynew basin margin elsewhere in the Flin Flon belt, where reactivation of normal faults associated with the basin margin during southwest-directed thrusting resulted in the development of a ramp zone and a transition from steep to shallow structures (Lucas et al. 1994; Connors 1996).

Elsewhere in the Chisel basin, Bailes (2014) and Bailes et al. (2016) interpreted the Lalor-Chisel fault to extend to the southwest along the lower contact of the Threehouse unit with the Powderhouse dacite and Chisel rhyolite as opposed to the contact between the Chisel and Lalor members of the Powderhouse dacite as proposed here. However, detailed mapping at surface where this fault has been interpreted to occur indicates that the lower Threehouse contact is conformable with no evidence for a major fault (e.g., Chisel pit, South Chisel basin area; Engelbert et al. 2014a). Detailed cross-sections produced through the Chisel basin by Galley et al. (1993), Bailes (2014), and in this study by building on these earlier sections (Fig. 18) indicate that the Lalor-Chisel fault extends eastward from the Lalor deposit at depth; however it is currently unclear where this fault would project to surface and further work is needed to delineate the fault in this area.

2.5.4 Deformation of the Chisel sequence ore bodies

Structural studies were completed for the Chisel, Chisel North, and Photo Lake deposits while they were in production (Martin 1966; Galley et al. 1993; Tessier, 1996, 2000, 2001). These studies determined that the geometry of the ore bodies and the metal distribution within the deposits were significantly affected by polyphase folding. The deposits are flattened subparallel to the dominant S_2 foliation (Galley et al. 1993; Tessier 1996, 2000, 2001) and are elongated along the L_2 stretching lineation (Galley et al. 1993; Tessier, 1996, 2000, 2001). For example, the Photo Lake deposit is folded around a large fold (Engelbert et al. 2014b) that has no axial planar foliation and is transected by a strong penetrative foliation containing a stretching lineation (Tessier 1996). This is consistent with the F_1/S_2 overprinting relationship observed along strike at the Photo quarry (Fig. 6). Thus, the Photo Lake deposit was deformed by an early F_1 fold during

the D_1 event and underwent further flattening parallel to the S_2 cleavage and was elongated parallel to the L_2 stretching lineation during the D_2 event.

The Chisel North and Chisel Lake deposits are interpreted to have formed from the same synvolcanic hydrothermal system and to have been later deformed into a series of folded sulfide lenses (Galley et al. 1993). The Chisel Lake deposit is interpreted to be more intensely deformed than the Chisel North deposit. The host rhyolite to the Chisel Lake deposit is tightly folded and the ore lenses are located within the rootless, isoclinal fold hinges and attenuated boudinaged limbs of these folds (Galley et al. 1993). The ore lenses are transposed parallel to the S_2 cleavage and elongated parallel to the L_2 stretching lineation (Galley et al. 1993). The ore lenses have been mined and are no longer exposed at surface in the half-flooded Chisel open pit; however, discordant synvolcanic alteration zones associated with mineralization are overprinted by F_1 folds and transected by the S_2 cleavage (Fig. 10). This suggests that the ore deposits were first folded by F_1 folds and were then flattened and transposed parallel to the S_2 cleavage.

The Lalor deposit is currently in production and underground workings active in 2014 have been the focus of a detailed structural study by Caté et al. (2014). Older structures and lithological contacts are transposed parallel to a strong foliation and volcanic clasts are flattened parallel to this foliation, which corresponds to the S_2 foliation mapped at surface. The ore lenses underwent a comparable style of deformation and they are folded and transposed parallel to the S_2 foliation and elongated parallel to the L_2 stretching lineation (Caté et al. 2014; Caté 2016).

In summary, the geometry of the VMS deposits in the Snow Lake camp results from overprinting by early F_1 folds followed by flattening and transposition of these folds and folding of the ore deposits into discontinuous stacked lenses striking parallel to the S_2 foliation and plunging parallel to the L_2 stretching lineation. Mechanical and hydrothermal remobilization of sulfides and precious metals occurred during deformation (Menard and Gordon 1995; Caté et al. 2014; Engelbert et al. 2014b). Syntectonic hydrothermal remobilization of precious metals (Au, Ag) occurred on the centimetre to metre scale at both the Lalor and Photo Lake deposits as indicated by Au-bearing veinlets cutting across sulfide mineralization and least altered host rocks to the ore lenses (Menard and Gordon 1995; Caté et al. 2014; Engelbert et al. 2014b). Mechanical remobilization of sulfide minerals also occurred on similar scales at the Lalor, Photo Lake, and Chisel deposits as indicated by the ductile flow of sulfide minerals in dike boudin necks, in fold hinges, and along the overprinting cleavage, and by the presence of sulfide bands in the deformed lenses (Tessier 1996; Caté et al. 2014). On a grain scale, mechanical sulfide remobilization is indicated by the presence of chalcopyrite, sphalerite, pyrrhotite and galena in intra-granular fractures, strain shadows surrounding cataclastic pyrite, and fractures in metamorphic magnetite (Engelbert et al. 2014b). In spite of the strong deformation and transposition of the deposits and mechanical and hydrothermal remobilization of the sulfides and precious metals, primary metal zoning was preserved at the deposit scale and can be used to reconstruct the original geometry of the deposit, as exemplified by the Lalor deposit (Fig. 19h).

Open, NE-trending F_3 folds with an axial planar S_3 cleavage affected all deposits (Martin 1966; Galley et al. 1993; Tessier 1996, 2000, 2001; Caté et al. 2014) and resulted in the warping of the

ore lenses. Otherwise these folds and the D_3 deformation event had little effect on the geometry of the deposits.

2.5.5 Implications for the tectonic evolution of the Snow Lake arc assemblage

Recognition of a deformation event that pre-dates deposition of the Burntwood Group turbidites has significant implications for the tectonic evolution of the Snow Lake segment of the FFGC. The earliest deformation event previously recognized in the Snow Lake area is bracketed by the maximum age for Burntwood Group deposition at ca. 1859-1842 Ma (David et al. 1996) and the age of calc-alkaline plutons that cut early folds at ca. 1837 Ma (David et al. 1996; Bailes 1992; Table 1). The presence of isoclinal folds that predate Burntwood deposition therefore indicates that the SLA underwent an orogenic event prior to 1859 Ma. There are three possible tectonic settings that can account for this early deformation event: (1) early collision with the Superior craton; (2) early collision with the Amisk collage prior to development of the Kisseynew Basin; (3) intraoceanic accretion with other tectono-stratigraphic assemblages. These possibilities are sequentially considered in detail below.

Early collision between rocks of the Reindeer Zone (internal section of the Trans-Hudson Orogen) and the Superior craton to the east may have begun as early as 1864 Ma (Ansdell 2005). It is therefore possible that early collision with the Superior craton was responsible for the formation of F_1 folds in the Snow Lake area. However, most workers have suggested that collision of the Reindeer Zone with the Superior craton was much later at ca. 1.84-1.79 Ga (e.g., Machado 1990; Bleeker et al. 1995; Kraus and Williams 1999; Connors et al. 2002; White et al. 2002; Corrigan et al. 2007) based on the age of granitoids emplaced during initial collision with

the Superior craton. Therefore, early collision with the Superior craton is unlikely to be the cause of D_1 deformation in the SLA, as this occurred too late to produce a deformation event in the volcanic rocks without affecting the Burntwood Group turbidites.

Collision of the Snow Lake arc with the Amisk collage may have resulted in the formation of the F_1 folds. The contact between the SLA and the Amisk collage is defined by the Morton Lake thrust fault (Fig. 1; Syme et al. 1995). The timing of this fault is interpreted to be post-Burntwood (<1.84 Ga) because it contains a thrust imbricate of Burntwood rocks (Syme et al. 1995), and it is interpreted to be the same age as the Loonhead Lake fault, which thrusts Kisseynew basin rocks over the Flin Flon belt (Syme et al. 1995; Connors 1996). Furthermore, older 1.87 to 1.845 Ga successor arc plutons located in the Flin Flon arc assemblage are absent in the Snow Lake area (David et al. 1996), suggesting that the evolutions of the SLA and Amisk collage remained separate until at least 1.845 Ga. However, a suite of intrusions known as the Josland Lake sills cut this fault (Syme et al. 1995), and these intrusions have been dated at 1886 ± 3 Ma (Zwanzig et al. 2001), bringing into question whether this suture zone formed before or after development of the Kisseynew basin. One possibility to explain this discrepancy in fault timing was presented by Connors (1996), who suggested that the turbidites in this fault zone represent klippen preserved by fold interference patterns resulting from later folding. This interpretation allows for collision of the SLA with the Amisk collage prior to thrusting of the Kisseynew basin and explains the crosscutting relationship of the Josland Lake sills.

Early deformation in the Amisk collage has been attributed to intraoceanic accretion of arc and ocean floor assemblages (Lucas et al. 1996), but this type of deformation has not previously been

recognized in the SLA. Immediately to the west of the SLA is the Northeast Reed assemblage (Fig. 1), which is an extensive sequence of pillowed basalt interpreted to represent an ocean floor assemblage (Syme et al. 1995). It is possible that collision with this assemblage resulted in the D_1 deformation observed at Snow Lake; however, the boundary between these two assemblages is masked by the <1.84 Ga Reed Lake and Ham plutons (Syme et al. 1995; David et al. 1996). Furthermore, screens of Burntwood turbidites are observed within the Reed Lake pluton, and it is possible that this area also represents an imbricate thrust slice of Burntwood turbidites (Syme et al. 1995). Farther south, the Reed Lake pluton entirely masks the contact between the Northeast Reed and Snow Lake assemblages, and it is possible that this contact represents an early structure; however, this cannot be confirmed. Collision with volcanic assemblages to the east is also ruled out as a cause of D_1 deformation because these assemblages are also separated from Snow Lake by thrust imbricates of Burntwood turbidites (Ansdell et al. 1999; Connors et al. 1999).

Therefore, given the currently available information, none of the three tectonic interpretations proposed to explain the formation of early D_1 structures at Snow Lake can account for all of the data and observations. However, we suggest that the most plausible causes for D_1 deformation are intraoceanic accretion or early collision with the Amisk collage prior to Kisseynew basin development, assuming that the thrust imbricate of Burntwood turbidites in the Morton Lake fault represents an infolded klippen as proposed by Connors (1996). This also requires that the screens of Burntwood turbidites separating the Snow Lake and Northeast Reed assemblages are infolded klippen. It is also plausible that intraoceanic accretion and collision with the Amisk collage occurred during progressive strain in the same kinematic frame. Furthermore, the

Kisseynew basin is interpreted to have formed in a back-arc setting behind the Glennie-Hanson-Flin Flon arc (Ansdell et al. 1995). Southwest-directed thrusting of the Kisseynew basin rocks over the Flin Flon belt occurred along the Loonhead Lake fault (Fig. 1), which is correlated along strike with the Snow Lake fault (Connors 1996; Kraus and Williams 1999). This fault represents the ancestral margin of the Kisseynew basin, which promoted development of a footwall ramp zone and imbrication of the hanging wall rocks (Lucas et al. 1994; Connors 1996). This requires that the SLA be accreted to the Amisk collage prior to Kisseynew basin development. This is consistent with the tectonic evolution of the SLA as determined by Kraus and Williams (1999), which requires that the Snow Lake arc allochthon be accreted to the Amisk collage prior to 1.84 Ga.

Early accretion of the Snow Lake allochthon to the Amisk collage suggests that it shares a similar tectonic history with the Amisk collage from approximately 1859 Ma onwards. This is consistent with previous interpretations for the tectonic evolution of the Snow Lake allochthon (Kraus and Williams 1999), the Wekusko Lake area to the east (Connors et al. 1999, 2002; Ansdell et al. 1999), and the File Lake area to the west (Connors 1996). These tectonic interpretations suggest that the D_2 event is related to SW-directed thrusting associated with prograde metamorphism as a result of collision of the Flin Flon belt with the Sask craton (Ansdell et al. 1995; Ansdell 2005). This is supported by SW-verging D_2 fabrics and structures observed in the volcanic rocks at Snow Lake (Kraus and Williams 1999; Connors et al. 2002; this study) and metamorphic mineral growth that postdated development of the S_2 foliation (Fig. 4f,g). The timing of onset of the D_2 deformation event is constrained by the maximum age of the Burntwood turbidites in the Kisseynew basin at ca. 1859 Ma (Gordon et al. 1990) and the age of

the Tramping Lake pluton at ca. 1837 Ma (David et al. 1996), which crosscuts F_2 folds (Bailes 1992). Peak metamorphic conditions are associated with late D_2 deformation and were not reached until ca. 1812 Ma (David et al. 1996; Kraus and Williams 1998, 1999; Connors 1996), indicating that the D_2 event lasted for up to 25 Ma. The D_3 event occurred soon after peak metamorphism (Connors 1996; Kraus and Williams 1998, 1999) and is related to collision of the Flin Flon belt with the Superior craton, causing NW-SE sinistral transpressional shortening (Connors et al. 1999). This is reflected by the style and orientation of F_3 folds in the volcanic rocks at Snow Lake. F_2 and F_3 folds are interpreted to be coaxial due to progressive reorientation of F_2 axes during D_3 tectonic transport (Kraus and Williams 1999; Connors et al. 2002). We propose that the early F_1 folds and coaxial F_2 folds were rotated towards the transport direction during thrusting and collision of the Flin Flon belt with the Sask craton, and were refolded by F_3 folds during collision of the Flin Flon belt with the Superior craton.

2.6 Conclusions

Detailed geological mapping, re-logging of drill holes, and structural analysis indicate that the volcanic rocks of the SLA experienced a period of deformation prior to deposition of the Burntwood Group turbidites. This differs from previous structural interpretations for the Snow Lake area that did not identify deformation events prior to Burntwood Group deposition. This early deformation event may have resulted from one or a combination of intraoceanic accretion or pre-1.86 Ga accretion of the Snow Lake allochthon to the Amisk collage. This suggests that the Snow Lake allochthon shares a more protracted tectonic history with the rest of the Flin Flon belt than previously thought.

This early deformation event has had a significant influence on the current geometry and location of the Chisel sequence VMS deposits. Most of the Chisel sequence VMS deposits show evidence for deposit-scale F_1 folding, which has resulted in thickening of the ore bodies and a reduction in the size of the deposit footprints. A new stratigraphy for the Upper Chisel sequence has emerged through recognition of this early deformation event and indicates that folding and faulting repeat the Chisel sequence ore interval. The Lalor-Chisel fault is a major D_1 structure that has displaced the hanging wall rocks to the Lalor deposit and crosscuts units of the VMS ore interval. This is significant because D_1 faulting may have displaced or removed mineralization elsewhere in the SLA. The early deformation event has therefore affected the geometry and distribution of the Chisel sequence ore interval and must be considered during future VMS exploration in the Snow Lake district.

2.7 References

Ansdell, K.M. 2005. Tectonic evolution of the Manitoba-Saskatchewan segment of the Paleoproterozoic Trans-Hudson orogen, Canada. Canadian Journal of Earth Sciences **42**: 741-759.

Ansdell, K.M., Lucas, S.B., Connors, K., and Stern, R.A. 1995. Kisseynew metasedimentary gneiss belt, Trans-Hudson orogeny (Canada): back-arc origin and collisional inversion. Geology **23**: 1039-1043.

Ansdell, K.M., Connors, K.A., Stern, R.A., and Lucas, S.B. 1999. Coeval sedimentation, magmatism, and fold-thrust belt development in the Trans-Hudson Orogen: geochronological evidence from the Wekusko Lake area, Manitoba, Canada. Canadian Journal of Earth Sciences **36**: 293-312.

Bailes, A.H. 1980a. Geology of the File Lake area. Manitoba Energy and Mines, Geological Report 78-1.

Bailes, A.H. 1980b. Origin of Early Proterozoic volcaniclastic turbidites, south margin of the Kisseynew sedimentary gneiss belt, File Lake, Manitoba. Precambrian Research **12**: 197-225.

Bailes, A.H. 1992. Wekusko Lake (north) project (NTS 63J/13SW). *In* Report of Activities 1992. Manitoba Energy and Mines, Minerals Division, p. 55-64.

Bailes, A.H. 1997. Geochemistry of Paleoproterozoic rocks in the Photo Lake area, Flin Flon Belt (part of NTS 63K16). *In* Report of Activities 1997. Manitoba Energy and Mines, Minerals Division, p. 61-72.

Bailes, A.H. 2014. Regional geological setting of the Zn- and Au-rich Lalor VMS deposit, Snow Lake, Manitoba, Canada. *In* British Columbia Geophysical Society Lalor Symposium Presentations Listing. Available from http://www.bcgsonline.org/lalor-symposium/ [accessed 10 June 2017].

Bailes, A.H., and Galley, A.G. 1996. Setting of Paleoproterozoic volcanic-hosted massive base metal sulfide deposits, Snow Lake. *In* Bonham-Carter, G.F., Galley, A.G., and Hall, G.E.M., eds., EXTECH 1: A Multidisciplinary Approach to Massive Sulfide Research in the Rusty Lake-Snow Lake Greenstone Belts, Manitoba: Geological Survey of Canada, Bulletin 426, p. 105-138.

Bailes, A.H., and Galley, A.G. 1999. Evolution of the Paleoproterozoic Snow Lake arc assemblage and geodynamic setting for associated volcanic-hosted massive sulfide deposits, Flin Flon Belt, Manitoba, Canada. Canadian Journal of Earth Sciences **36**: 1789-1805.

Bailes, A.H., and Galley, A.G. 2007. Geology of the Chisel-Anderson lakes area, Snow Lake, Manitoba (NTS area 63K16SW and west half of 63J13SE). Manitoba Science, Technology, Energy and Mines, Manitoba Geological Survey, Geoscientific Map MAP2007-1, scale 1:20 000 plus notes.

Bailes, A.H., Hunt, P.A., and Gordon, T.M. 1991. U-Pb dating of possible synvolcanic intrusions in the Flin Flon belt at Snow Lake, Manitoba. *In* Radiogenic Age and Isotopic Studies, Report 4, Geological Survey of Canada, Paper 90-2, pp. 35–43.

Bailes, A.H., Galley, A.G., Skirrow, R.G., and Young, J. 1996. Geology of the Chisel volcanic-hosted massive sulfide area, Snow Lake, Manitoba (part of 63K/16SE). Manitoba Energy and Mines, Open File Report OF95-4, annotated 1:5000 colour map.

Bailes, A.H., Simms, D., Galley, A.G., and Young, J. 1997. Geological setting of the Photo Lake volcanic-hosted massive sulfide deposits, Snow Lake, Manitoba (part of 63K/16SE). Manitoba Energy and Mines, Open File Report OF97-5, annotated 1:5000 colour map.

Bailes, A.H., Gilmore, K., Levers, J., and Janser, B. 2009. The Lalor deposit – surprise at depth. *In* Manitoba Mineral Resources, Manitoba Mining and Minerals Convention 2009 Proceedings, Winnipeg, Manitoba, November 19-21, pp. 57-58.

Bailes, A.H., Rubingh, K., Gagné, S., Taylor, C., Galley, A., Bernauer, S., and Simms, D. 2013. Volcanic setting of Paleoproterozoic VMS and gold deposits at Snow Lake, Manitoba. Geological Association of Canada – Mineralogical Association of Canada Joint Annual Meeting, Field Trip Guidebook FT-A2. Manitoba Innovation, Energy and Mines, Manitoba Geological Survey, Open File OF2013-3, 63 p.

Bailes, A.H., Galley, A.G., Paradis, S., and Taylor, B.E. 2016. Variations in large synvolcanic alteration zones at Snow Lake, Manitoba, Canada, with proximity to associated volcanogenic massive sulfide deposits. Economic Geology **111** : 933-962.

Beaumont-Smith, C.J. and Gagné, S. 2008. Structural geology of the Snow Lake-Squall Lake area, Manitoba (parts of NTS 63K16, 63J13). Manitoba Science, Technology, Energy and Mines, Manitoba Geological Survey, Preliminary Map PMAP2008-1, scale 1:20 000.

Beaumont-Smith, C.J. and Lavigne, J. 2008. Structural geology and gold metallogenesis of the New Britannia mine area, Snow Lake, Manitoba (NTS 63K16). *In* Report of Activities 2008. Manitoba Innovation, Energy and Mines, Manitoba Geological Survey, p. 7-17.

Bleeker, W., Nägerl, P., and Machado, N. 1995. The Thompson Nickel Belt, Manitoba: some new U-Pb ages. Geological Association of Canada, Program with Abstracts, **20**: A8.

Caté, A. 2016. Geology of the Paleoproterozoic Zn-Cu-Au Lalor volcanogenic massive sulfide deposit and its gold-rich lenses, Snow Lake, Manitoba. / Géologie du gisement de sulfures massifs volcanogène Paléoprotérozoïque à Zn-Cu-Au de Lalor et de ses lentilles riches en or, Snow Lake, Manitoba. Ph.D. thesis, Université du Québec, Institut national de la recherche scientifique, Québec, Québec, 430 p.

Caté, A., Mercier-Langevin, P., Ross, P.-S., and Simms, D. 2014. Structural controls on geometry and ore distribution in the Lalor auriferous VMS deposit, Snow Lake, west-central Manitoba (part of NTS 63K16): preliminary results from underground mapping. *In* Report of Activities 2014. Manitoba Mineral Resources, Manitoba Geological Survey, p. 104-155.

Connors, K.A. 1996. Unraveling the boundary between turbidites of the Kisseynew belt and volcano-plutonic rocks of the Flin Flon belt, Trans-Hudson Orogen, Canada. Canadian Journal of Earth Sciences **33**: 811-829.

Connors, K.A., Ansdell, K.M., and Lucas, S.B. 1999. Coeval sedimentation, magmatism, and fold-thrust development in the Trans-Hudson Orogen: propagation of deformation into an active continental arc setting, Wekusko Lake area, Manitoba. Canadian Journal of Earth Sciences **36**: 275-291.

Connors, K.A., Ansdell, K.M., and Lucas, S.B. 2002. Development of a transverse to orogen parallel extension lineation in a complex collisional setting, Trans-Hudson Orogen, Manitoba, Canada. Journal of Structural Geology **24**: 89-106.

Corrigan, D., Galley, A.G., and Pehrsson, S. 2007. Tectonic evolution and metallogeny of the southwestern Trans-Hudson Orogen. *In* Mineral Deposits of Canada: A Synthesis of Major Deposit-Types, District Metallogeny, the Evolution of Geological Provinces, and Exploration Methods. *Edited by* W.D. Goodfellow. Geological Association of Canada, Mineral Deposits Division, Special Publication No. 5, p. 881-902.

Corrigan, D., Pehrsson, S., Wodicka, N., and de Kemp, E. 2009. The Palaeoproterozoic Trans-Hudson Orogen: a prototype of modern accretionary processes. Geological Society, London, Special Publications, v. 327, p. 457-479.

David, J., Bailes, A.H., and Machado, N. 1996. Evolution of the Snow Lake portion of the Palaeoproterozoic Flin Flon and Kisseynew belts, Trans-Hudson Orogen, Manitoba, Canada. Precambrian Research, **80**: 107-124.

Duff, S., Hannington, M.D., Caté, A., Mercier-Langevin, P., and Kjarsgaard, M. 2015. Major ore types of the Paleoproterozoic Lalor auriferous volcanogenic massive sulfide deposit,

Snow Lake, Manitoba. *In* Targeted Geoscience Initiative 4: Contributions to the Understanding of Volcanogenic Massive Sulfide Deposit Genesis and Exploration Methods Development, (ed.) J.M. Peter and P. Mercier-Langevin, Geological Survey of Canada, Open File 7853, pp. 147-170.

Engelbert, M.S., Friesen, V., Gibson, H.L., and Lafrance, B. 2014a. Volcanic reconstruction of the productive VMS ore interval in the Paleoproterozoic Chisel sequence, Snow Lake, Manitoba. *In* Geological Association of Canada – Mineralogical Association of Canada Joint Annual Meeting Abstracts Listing, Fredericton, 2014, Abstract Volume, pp. 83-84.

Engelbert, M.S., Gibson, H.L., and Lafrance, B., 2014b, Geologic setting, mineralogy, and geochemistry of the Paleoproterozoic Photo Lake VMS deposit, Snow Lake, Manitoba [abs.]: Geological Association of Canada – Mineralogical Association of Canada Joint Annual Meeting, Fredericton, 2014, Abstract Volume 37, p. 84.

Engelbert, M.S., Lafrance, B., and Gibson, H.L. 2014c. Structural controls on volcanogenic massive sulfide deposits in the Paleoproterozoic Chisel sequence, Snow Lake, Manitoba. 2014 Geological Society of America Annual Meeting, Vancouver, British Columbia, Abstracts Listing, Paper 64-8.

Franklin, J.M., Gibson, H.L., Jonasson, I.R., and Galley, A.G., 2005, Volcanogenic massive sulfide deposits, in Hedenquist, J.W., Thompson, J.F.H., Goldfarb, R.J., and Richards, J.P., eds., Economic Geology 100th Anniversary Volume, p. 523-560.

Friesen, V.C., Engelbert, M., DeWolfe, Y.M., and Gibson, H.L. 2015. Volcanic reconstruction of the Powderhouse dacite in the Paleoproterozoic VMS hosting Chisel sequence, Snow Lake, Manitoba. *In* AGU-GAC-MAC-CGU 2015 Joint Assembly Abstracts Listing, pp. 276.

Froese, E. and Moore, J.M. 1980. Metamorphism in the Snow Lake area, Manitoba. Geological Survey of Canada, Paper 78-27.

Gagné, S. 2009. Geology of the McLeod Road-Birch Lake allochthon, Herblet Lake (Southeast Bay), Snow Lake area, Manitoba (part of NTS 63J13). Manitoba Science, Technology, Energy and Mines, Manitoba Geological Survey, Preliminary Map PMAP2009-1, scale 1:10 000.

Galley, A.G., Ames, D.E., and Franklin, J.M. 1988. Geological Setting of Gold Mineralization, Snow Lake, Manitoba. Geological Survey of Canada, Open File 1700.

Galley, A.G., Bailes, A.H., and Kitzler, G. 1993. Geological setting and hydrothermal evolution of the Chisel Lake and North Chisel Zn-Pb-Cu-Ag-Au massive sulfide deposits, Snow Lake, Manitoba. Exploration and Mining Geology **2**: 271-295.

Galley, A.G., Syme, E.C., and Bailes, A.H. 2007. Metallogeny of the Paleoproterozoic Flin Flon Belt, Manitoba and Saskatchewan. *In* Mineral deposits of Canada: a synthesis of major deposit types, district metallogeny, the evolution of geological provinces and exploration methods. *Edited by* G.D. Goodfellow. Geological Association of Canada, Mineral Deposits Division. Special Publication No. 5, pp. 509–531.

Gibson, H.L., Morton, R.L., and Hudak, G.J. 1999. Submarine volcanic processes, deposits, and environments favorable for the location of volcanic-associated massive sulfide deposits. Reviews in Economic Geology, **8:** 13-51.

Gibson, H.L., Engelbert, M., Lafrance, B., Friesen, V., DeWolfe, M., Tinkham, D., and Bailes, A., 2014, Reconstruction of the ore interval and environment for the Paleoproterozoic Lost and Ghost Lake VMS deposits, Snow Lake, Manitoba. *In* Geological Association of

Canada – Mineralogical Association of Canada Joint Annual Meeting, Fredericton, 2014, Abstract Volume, p. 102.

Gordon, T.M., Hunt. P.A., Bailes, A.H., and Syme, E.C. 1990. U-Pb ages of the Flin Flon and Kisseynew domains, Manitoba: chronology of crust formation at an Early Proterozoic accretionary margin. *In* The Early Proterozoic Trans-Hudson Orogen of North America. *Edited by* J.F. Lewry and M.R. Stauffer. Geological Association of Canada, Special Paper 37, pp. l77-l99.

Hannington, M.D. and Scott, S.D. 1988. Mineralogy and geochemistry of a hydrothermal silica-sulfide-sulfate spire in the caldera of Axial Seamount, Juan de Fuca Ridge. Canadian Mineralogist **26**: 603-625.

Hannington, M.D., Tivey, M.K., Larocque, A.C.L., Petersen, S., and Rona, P.A. 1995. The occurrence of gold in sulfide deposits of the TAG Hydrothermal Field, Mid-Atlantic Ridge. Canadian Mineralogist **33**: 1285-1310.

Knuckey, M.J., Comba, C.D.A., and Riverin, G. 1982. Structure, metal zoning and alteration at the Millenbach deposit, Noranda, Quebec. *In* Precambrian Sulphide Deposits. *Edited by* R.W. Hutchinson, C.D. Spence, and J.M. Franklin. Geological Association of Canada Special Paper 25. pp. 297-318.

Kraus, J. and Menard, T. 1997. A thermal gradient at constant pressure: implications for low- to medium-pressure metamorphism in a compressional tectonic setting, Flin Flon and Kisseynew Domains, Trans-Hudson Orogen, central Canada. The Canadian Mineralogist **35**: 1117-1136.

Kraus, J. and Williams, P.F. 1993. Structural studies along the northern margin of the Flin Flon-Snow Lake greenstone belt, Snow Lake. *In* Report of Activities 1993. Manitoba Energy and Mines, Minerals Division, p. 117-118.

Kraus, J. and Williams, P.F. 1994. Structure of the Squall Lake area, Snow Lake (NTS 63K/16). *In* Report of Activities 1994. Manitoba Energy and Mines, Minerals Division, p. 189-193.

Kraus, J. and Williams, P.F. 1998. Relationship between foliation development, porphyroblasts growth and large-scale folding in a metaturbidite suite, Snow Lake, Canada. Journal of Structural Geology, **20**: 61-76.

Kraus, J. and Williams, P.F. 1999. Structural development of the Snow Lake Allochthon and its role in the evolution of the southeastern Trans-Hudson Orogen in Manitoba, central Canada. Canadian Journal of Earth Sciences, **36**: 1881-1899.

Lucas, S.B., White, D., Hajnal, Z., Lewry, J., Green, A., Clowes, R., Zwanzig, H., Ashton, K., Schledewitz, D., Stauffer, M., Norman, A., Williams, P.F., and Spence, G. 1994. Three-dimensional collisional structure of the Trans-Hudson Orogen, Canada. Tectonophysics **232**: 161-178.

Lucas, S.B., Stern, R.A., Syme, E.C., Reilly, B.A., and Thomas, D.J. 1996. Intraoceanic tectonics and the development of continental crust: 1.92-1.84 Ga evolution of the Flin Flon Belt, Canada. GSA Bulletin **108**: 602-629.

Lydon, J.W. 1984. Ore deposit models – 8. Volcanogenic massive sulphide deposits part 1: a descriptive model. Geoscience Canada, **11**: 195-202.

Lydon, J.W. 1988. Ore deposit models #14. Volcanogenic massive sulphide deposits part 2: genetic models. Geoscience Canada, **15**: 43-65.

Machado, N. 1990. Timing of collisional events in the Trans-Hudson Orogen: evidence from U-Pb geochronology for the New Quebec Orogen, the Thompson Belt, and the Reindeer Zone (Manitoba and Saskatchewan). *In* The early Proterozoic Trans-Hudson Orogen of North America. *Edited by* J.F. Lewry and M.R. Stauffer. Geological Association of Canada. Special Paper 37, pp. 433-441.

Machado, N., Zwanzig, H., and Parent, M. 1999. U-Pb ages of plutonism, sedimentation, and metamorphism of the Paleoproterozoic Kisseynew metasedimentary belt, Trans-Hudson Orogen (Manitoba, Canada). Canadian Journal of Earth Sciences **36**: 1829-1842.

Martin, P.L. 1966. Structural analysis of the Chisel Lake orebody. Canadian Institute of Mining and Metallurgy, Transactions, **69**: 208–214.

Menard, T., and Gordon, T.M. 1995. Syntectonic alteration of VMS deposits, Snow Lake, Manitoba. *In* Report of Activities 1995. Manitoba Energy and Mines, Minerals Division, p. 164-167.

Menard, T., and Gordon, T.M. 1997. Metamorphic P-T paths from the eastern Flin Flon belt and Kisseynew Domain, Snow Lake, Manitoba. The Canadian Mineralogist **35**: 1093-1115.

Mercier-Langevin, P., Gibson, H.L., Hannington, M.D., Goutier, J., Monecke, T., Dubé, B., and Houlé, M. 2014. A special issue on Archean magmatism, volcanism, and ore deposits: part 2. Volcanogenic massive sulfide deposits. Economic Geology **109**: 1-9.

Percival, J.A., Whalen, J.B., and Rayner, N. 2005. Pikwitonei-Snow Lake Manitoba transect (parts of NTS 63J, 63O and 63P), Trans-Hudson Orogen-Superior Margin Metallotect Project: new results and tectonic interpretation. *In* Report of Activities 2005. Manitoba Industry, Economic Development and Mines, Manitoba Geological Survey, p. 69-91.

Ramsey, J.G. 1967. Folding and fracturing of rocks: New York, McGraw-Hill, 568 p.

Rubingh, K.E., Lafrance, B., and Gibson, H.L. 2012. Lithostratigraphy and structural geology of the McLeod Road-Birch Lake thrust panel, Snow Lake, west-central Manitoba (parts of NTS 63K16, 63J13). *In* Report of Activities 2012. Manitoba Innovation, Energy and Mines, Manitoba Geological Survey, p. 104-114.

Stauffer, M.R. 1984. Manikewan: An early Proterozoic ocean in central Canada: Its igneous history and orogenic closure. Precambrian Research **25**: 257-281.

Syme, E.C., Bailes, A.H., and Lucas, S.B. 1995. Geology of the Reed Lake area (Parts of 63K/9 and 63K/10). *In* Report of Activities 1995. Manitoba Energy and Mines, Minerals Division, p. 42-60.

Syme, E.C., Lucas, S.B., Bailes, A.H., and Stern, R.A. 1999. Contrasting arc and MORB-like assemblages in the Paleoproterozoic Flin Flon Belt, Manitoba, and the role of intra-arc extension in localizing volcanic-hosted massive sulphide deposits. Canadian Journal of Earth Sciences, **36**: 1767-1788.

Tessier, A.C. 1996. Secondary structural controls of the mineralization at the Photo Lake Mine; Snow Lake, Manitoba. Internal report for Hudson Bay Mining and Smelting Co., Ltd., 42 p. with additional figures.

Tessier, A.C. 2000. Structural complexities of the Chisel North deposit: Preliminary observations. Internal report for Hudson Bay Mining and Smelting Co., Ltd., 21 p.

Tessier, A.C. 2001. Structural controls of the mineralization at the Chisel North deposit; Snow Lake, Manitoba: Interim report #2. Internal report for Hudson Bay Mining and Smelting Co., Ltd., 27 p.

White, D.J., Lucas, S.B., Bleeker, W., Hajnal, Z., Lewry, J.F., and Zwanzig, H.V. 2002. Suture-zone geometry along an irregular Paleoproterozoic margin: The Superior boundary zone, Manitoba, Canada. Geology **30**: 735-738.

Whitney, D.L. and Evans, B.W. 2010. Abbreviations for names of rock-forming minerals. American Mineralogist **95**: 185-187.

Zwanzig, H.V. 1990. Kisseynew gneiss belt in Manitoba: stratigraphy, structure, and tectonic evolution. *In* Lewry, J.F. and Stauffer, M.R., eds., The Early Proterozoic Trans-Hudson Orogen of North America: Geological Association of Canada Special Paper 37, p. 95-120.

Zwanzig, H.V., Bailes, A.H., and Böhm, C.O. 2001. Josland Lake sills: U-Pb age and tectonostratigraphic implications (parts of NTS 63K and 63N). *In* Report of Activities 2001. Manitoba Industry, Trade, and Mines Manitoba Geological Survey, p. 28-32.

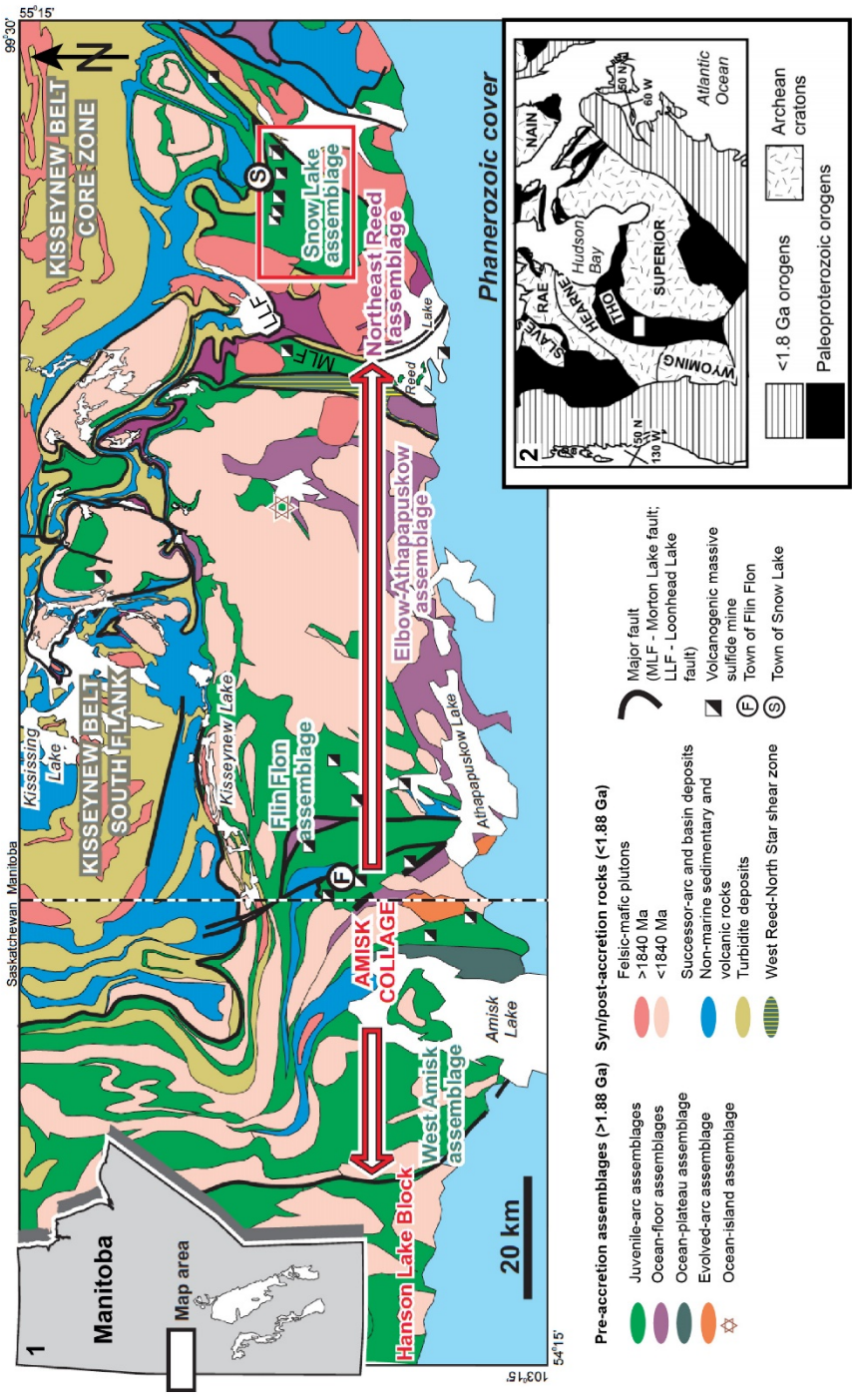

Figure 2-1. Tectono-stratigraphic assemblages of the Flin Flon belt, Manitoba, Canada (modified after Syme et al. 1999). Red box indicates location of the Snow Lake arc assemblage. Inset map 1 shows Manitoba with location of the Flin Flon belt map area. Inset map 2 shows location of Flin Flon belt within the Trans-Hudson Orogen (modified after Syme et al. 1999).

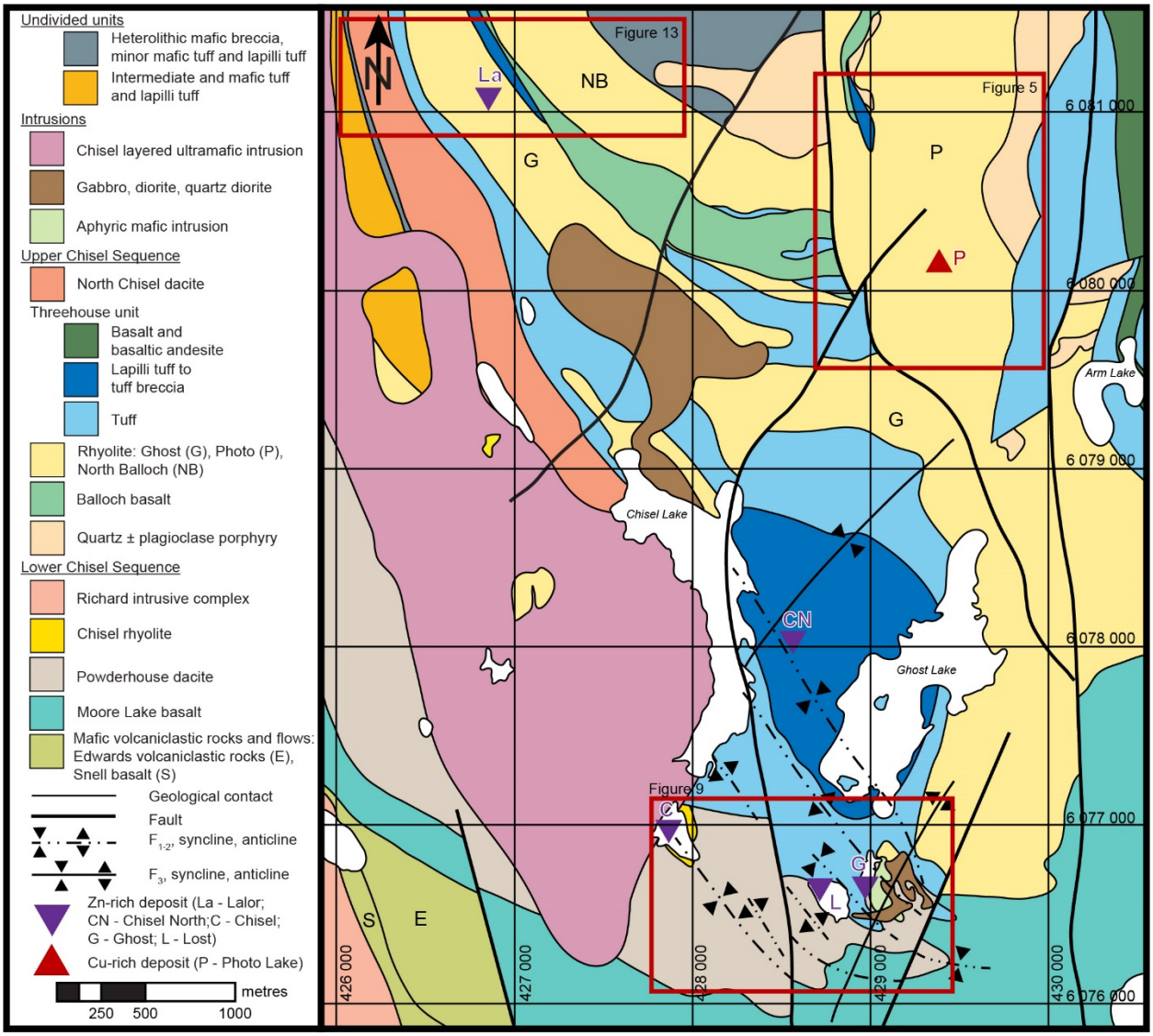

Figure 2-2. Simplified geological map of the Chisel sequence of the Snow Lake arc assemblage (modified after Bailes and Galley 2007; Bailes et al. 2013). Map datum is NAD83 UTM Zone 14. Boxes indicate map areas for Figures 5, 9, 13, representing the Photo Lake deposit area, the South Chisel basin area, and the Lalor section, respectively.

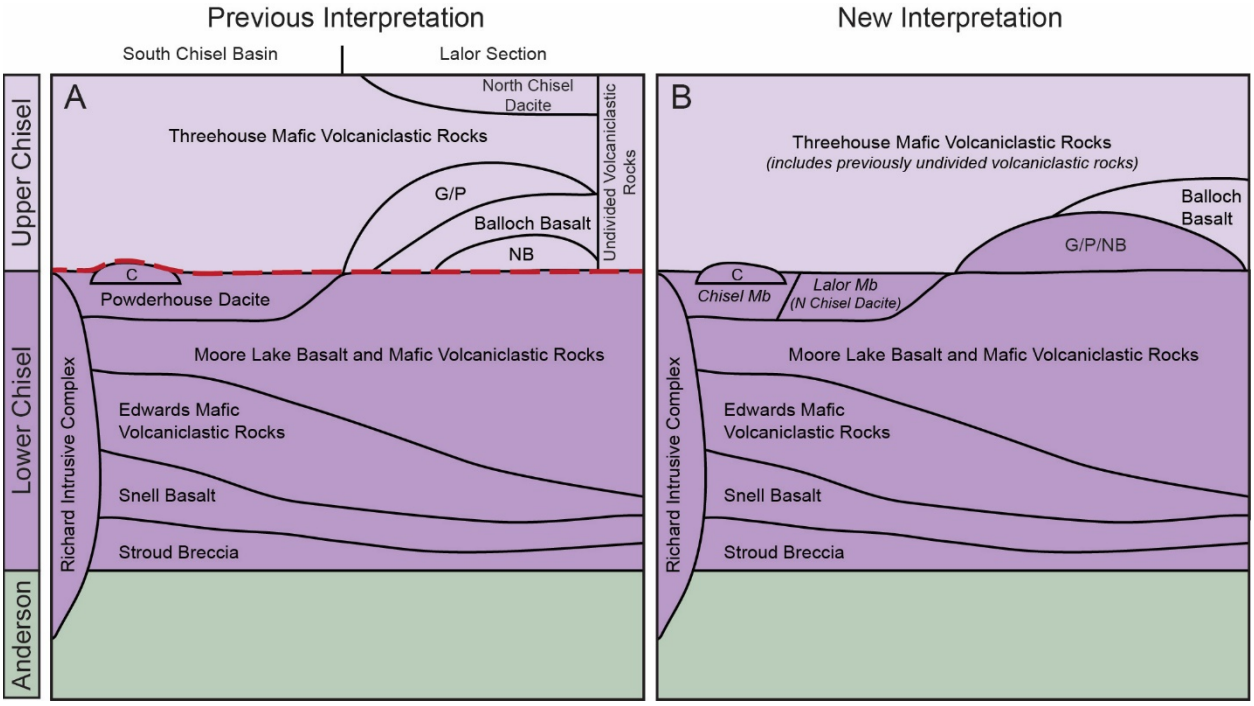

Figure 2-3. Stratigraphy of the Snow Lake arc assemblage showing (a) previous interpretation of Bailes and Galley (1999, 2007), Bailes et al. (2013, 2016), and Bailes (2014); and (b) the interpretation based on the current study. Modified after Bailes and Galley (1999, 2007), Bailes (2014) and Bailes et al. (2013, 2016). Unit and sequence thicknesses not to scale. Red dashed line in (a) represents Lalor-Chisel fault. Abbreviations: C – Chisel rhyolite; G/P – Ghost and Photo rhyolites; NB – North Balloch rhyolite. Chisel Mb and Lalor Mb refer to the Chisel and Lalor members, respectively, of the Powderhouse dacite based on the study by Friesen et al. (2015).

A
S2
B
L2
S2
F3
C
S2
D
500 µm
E
S2
F3
F
500 µm
G
S2
S3
H
F2/S2
I
S2
S3
MERC
Mineral Exploration Research Centre
Laurentian University

Figure 2-4. Representative photographs of fabrics in the Chisel sequence rocks. Photo card for scale (9 cm in length), except for photomicrographs 4d and 4f. (a) Field photograph showing S_2 developed as a spaced cleavage in felsic volcanic rocks. (b) Field photograph showing flattened and stretched clasts in volcaniclastic rocks defining the S_2 fabric and L_2 lineation. Clasts are overprinted by F_3 folds. (c) Field photograph showing garnet porphyroblasts contained within the S_2 spaced cleavage. (d) Plane-polarized light (PPL) photomicrograph showing biotite laths defining the S_2 spaced cleavage. The long axes of the biotite laths are oriented perpendicular to S_2 cleavage planes, defining the S_3 fabric. (e) Field photograph showing open F_3 folds refolding the S_2 fabric defined by flattened clasts. (f) PPL photomicrograph showing quartz inclusion trails in staurolite (right side of image) aligned with the S_2 fabric defined by quartz in the chlorite-rich matrix (left side of image). (g) Field photograph showing inclusion trails of quartz in garnet aligned with the S_2 fabric defined by biotite. S_3 fabric is defined by pressure shadows surrounding garnet and by a weak biotite fabric. (h) Field photograph showing isoclinal rootless F_2 folds in a volcaniclastic rock. (i) Field photograph showing quartz pressure shadows around garnet oriented along the S_3 fabric.

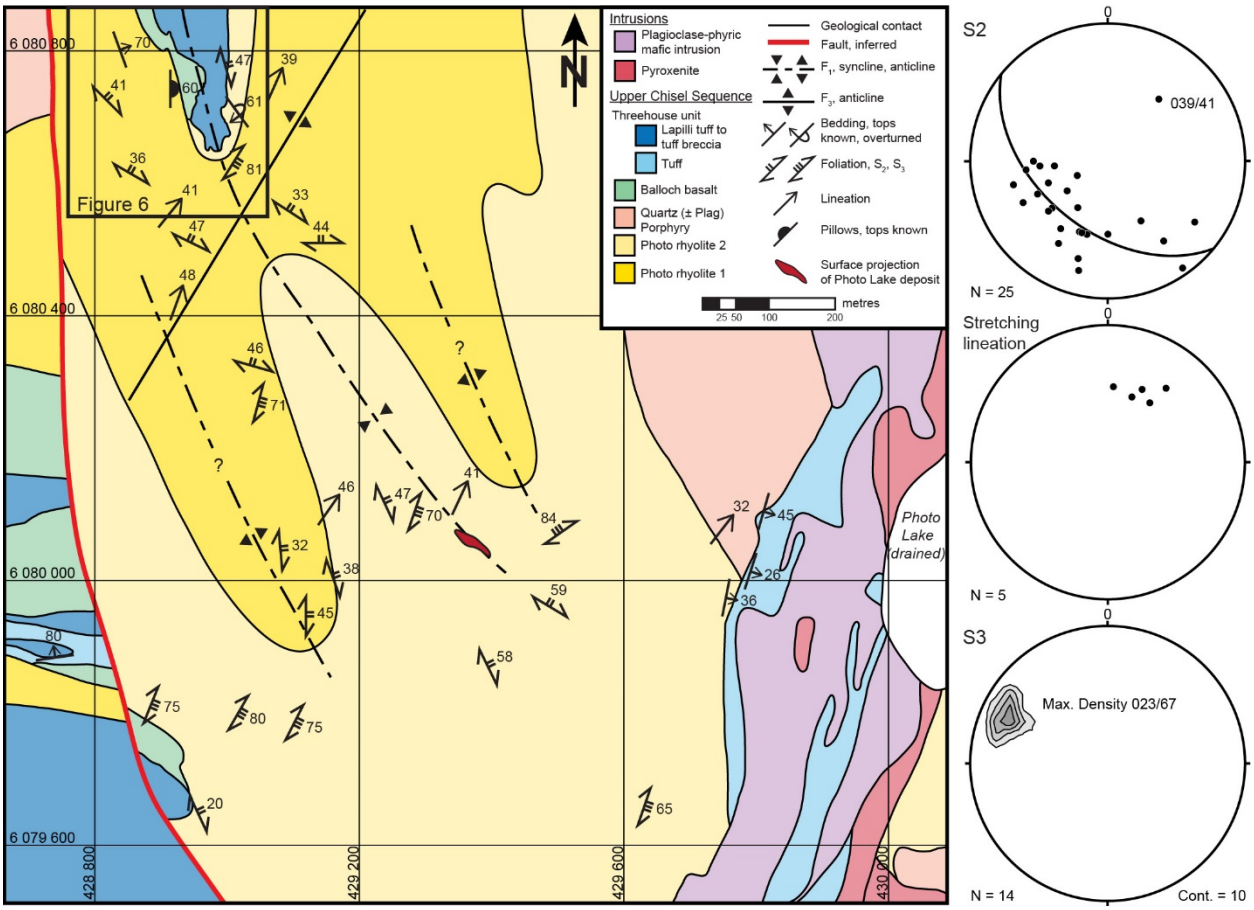

Figure 2-5. Geological map of the Photo Lake area (modified after Bailes et al. 1997) and equal-area, lower hemisphere projections of structural measurements. Number of measurements (N) at bottom of equal-area projections. Map datum is NAD83 UTM Zone 14. Planar features (e.g. bedding, foliations) are plotted as poles. Contours are calculated as percent of total number of data points per 1% area and "Cont." refers to the contour interval. "Max. Density" refers to the average strike/dip and trend/plunge of planes and lineations, respectively. Surface projection of deposit is composite view of both lenses. Box indicates map area for Figure 6.

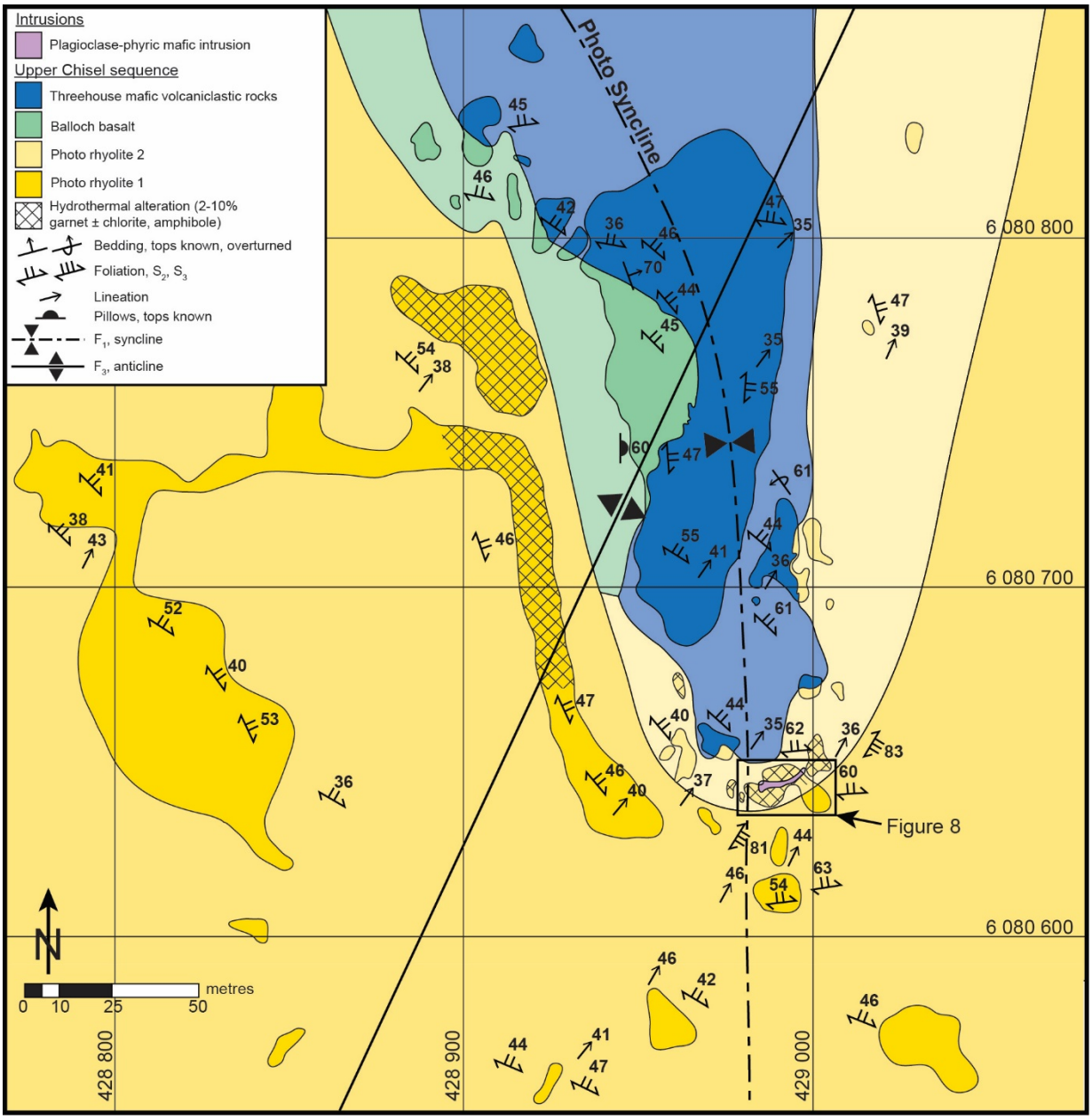
Intrusions
Plagioclase-phyric mafic intrusion
Upper Chisel sequence
Threehouse mafic volcaniclastic rocks
Balloch basalt
Photo rhyolite 2
Photo rhyolite 1
Hydrothermal alteration (2-10% garnet ± chlorite, amphibole)
Bedding, tops known, overturned
Foliation, S2, S3
Lineation
Pillows, tops known
F1, syncline
F3, anticline
Photo Syncline
6 080 800
6 080 700
6 080 600
428 800
428 900
429 000
metres
0 10 25 50
Figure 8

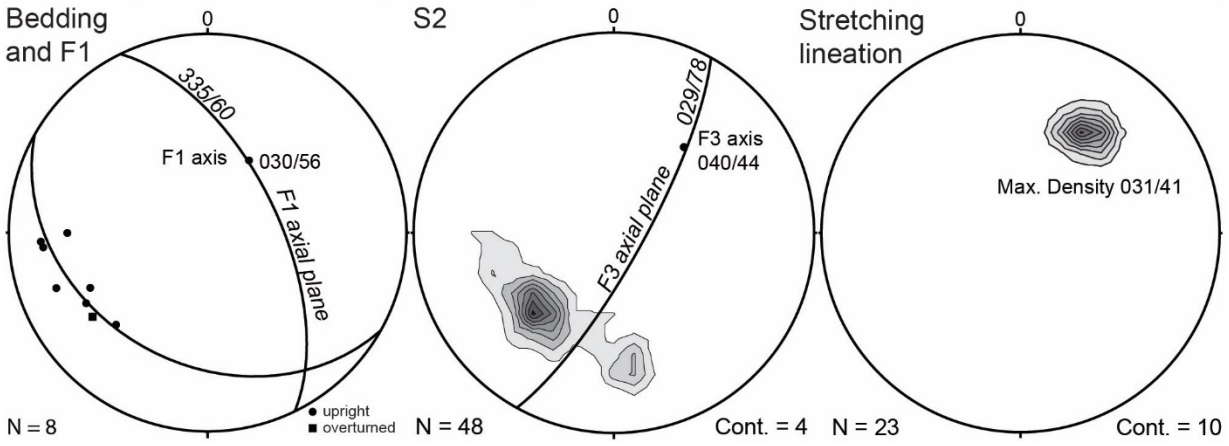
Bedding and F1
335/60
F1 axis
030/56
F1 axial plane
upright
overturned
N = 8
S2
029/78
F3 axis
040/44
F3 axial plane
N = 48
Cont. = 4
Stretching lineation
Max. Density 031/41
N = 23
Cont. = 10

Figure 2-6. Geological map of the Photo quarry area and equal-area, lower hemisphere projections of structural measurements. Map datum is NAD83 UTM Zone 14. Number of measurements (N) at bottom of equal-area projections. Planar features (e.g. bedding, foliations) are plotted as poles. Contours are calculated as percent of total number of data points per 1% area and “Cont.” refers to the contour interval. “Max. Density” refers to the average strike/dip and trend/plunge of planes and lineations, respectively. Black box indicates location of outcrop in Figure 8.

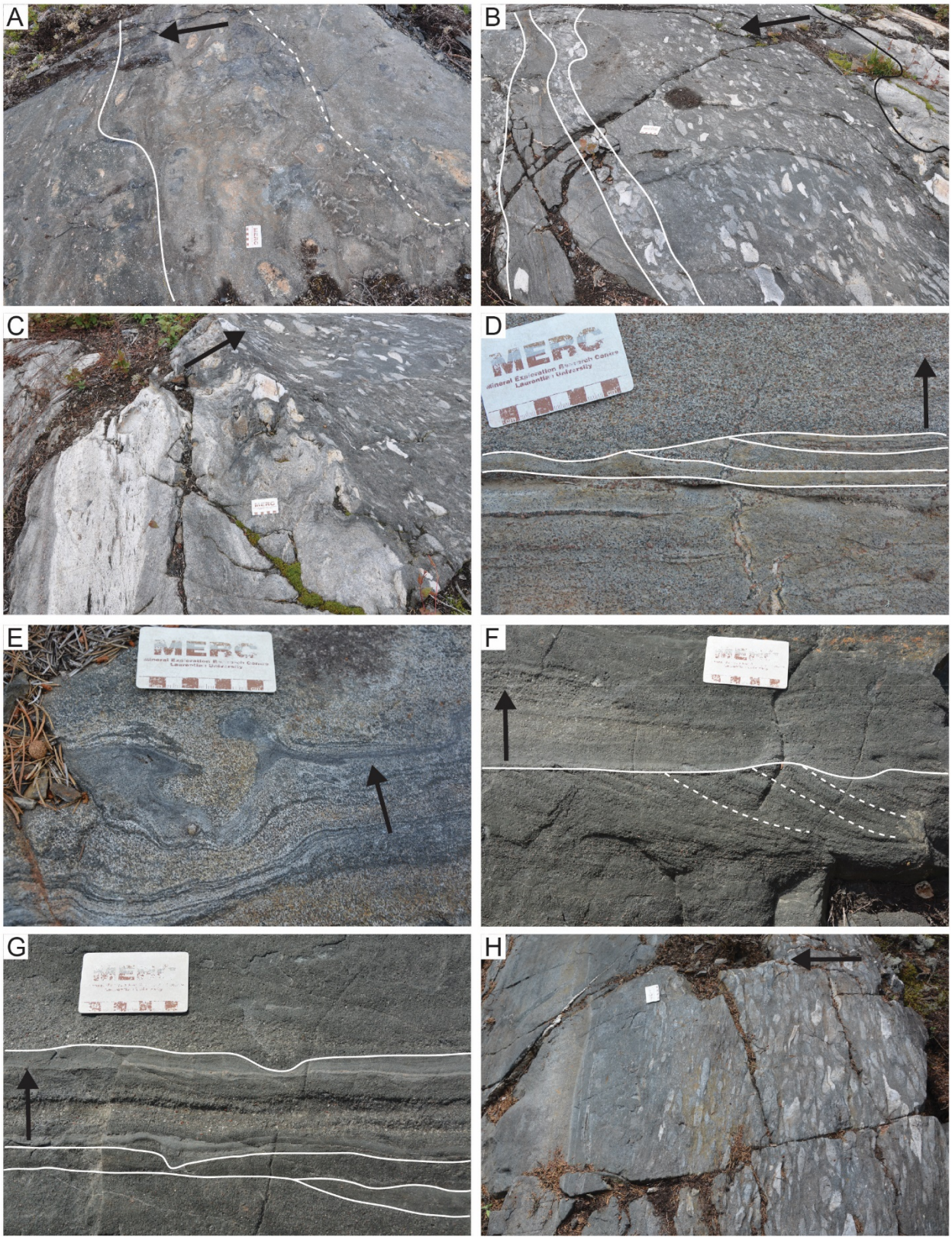
A
B
C
D
MERC
E
MERC
F
G
H

Figure 2-7. Representative field photographs of younging criteria. Photo card for scale (9 cm in length). Black arrow indicates younging direction. (a) Flow transition from massive to pillowed lithofacies (white dotted line) in the Photo quarry. Pillows are in sharp contact with overlying massive flow (white solid line). (b) Rhyolite lobes in the Photo quarry overlain by heterolithic volcaniclastic rocks containing rhyolite clasts that decrease in abundance moving away from the contact. Contact indicated by black solid line. White solid lines indicate sharp bedding contacts. Lowermost bed exhibits normal grading with respect to clast size and content. (c) Contact between rhyolite lobe and overlying heterolithic mafic volcaniclastic rocks in the Photo quarry. Clasts from the margins of the rhyolite lobe are incorporated into the overlying volcaniclastic rocks. (d) Bedded tuffs in the Lost member of the Powderhouse dacite in the Ghost-Lost area. Bedding surfaces outlined in white. Scour truncates underlying beds. (e) Slumping in bedded tuffs of the Lost member of the Powderhouse dacite in the Ghost-Lost area. (f) Cross-bedding in bedded tuffs of the Threehouse unit in the Lalor section. Cross-beds indicated by dotted white lines and overlying planar bed indicated by solid white line. (g) Small scours in bedded tuffs of the Threehouse unit in the Lalor section. Beds used to establish younging direction outlined in white. (h) Heterolithic volcaniclastic rocks at the contact between the Ghost rhyolite and the Threehouse unit in the Lalor section. Rhyolite is not visible in this photograph but is located to the right of this outcrop. Rhyolite clasts are most abundant at this contact and significantly decrease in abundance moving away from the contact. The volcaniclastic rocks exhibit normal grading with respect to clast size and content.

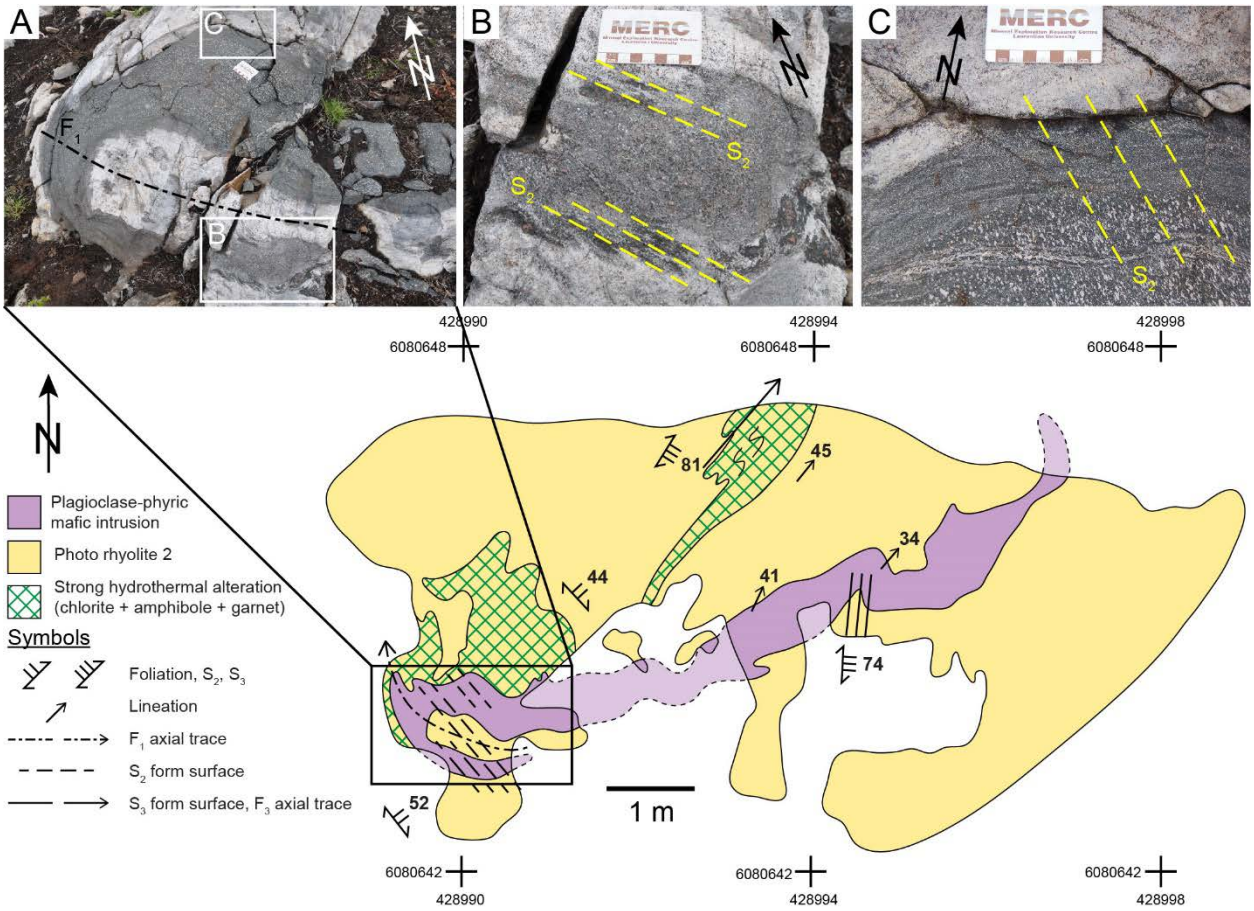

Figure 2-8. Detailed map of an outcrop in the Photo quarry area showing the relationship between D_1, D_2, and D_3 structures and field photographs of the outcrop features with photo card for scale (9 cm in length). (a) Mafic dike folded by a small-scale F_1 fold. (b) Lower limb of the fold in (a) transected by the S_2 cleavage defined by biotite, amphibole, and flattened plagioclase phenocrysts. (c) Upper limb of the fold in (a) transected by the S_2 cleavage defined by flattened plagioclase crystals.

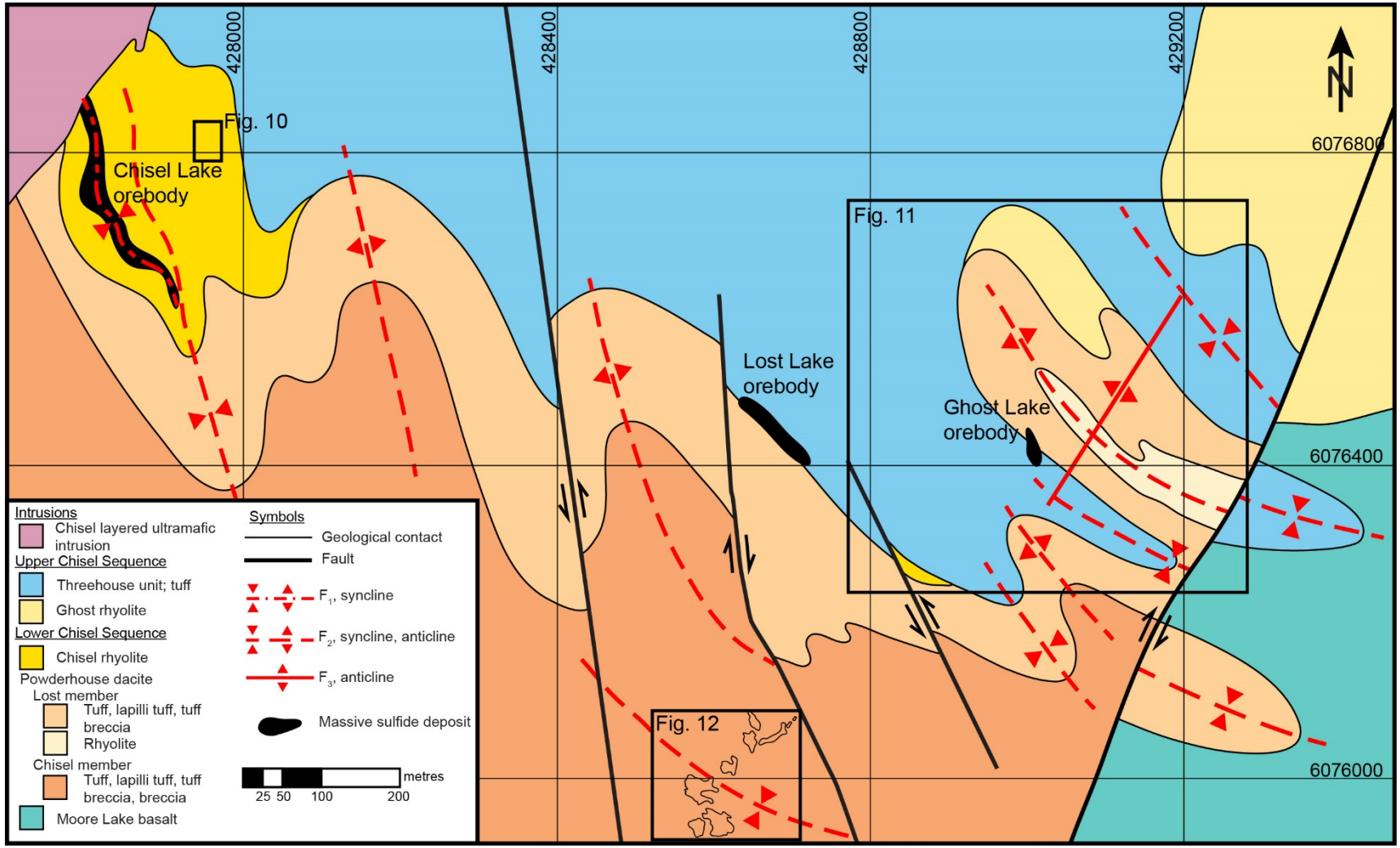
428000
428400
428800
429200
N
6076800
6076400
6076000
Fig. 10
Chisel Lake orebody
Fig. 11
Lost Lake orebody
Ghost Lake orebody
Fig. 12
Intrusions
Chisel layered ultramafic intrusion
Upper Chisel Sequence
Threehouse unit; tuff
Ghost rhyolite
Lower Chisel Sequence
Chisel rhyolite
Powderhouse dacite
Lost member
Tuff, lapilli tuff, tuff breccia
Rhyolite
Chisel member
Tuff, lapilli tuff, tuff breccia, breccia
Moore Lake basalt
Symbols
Geological contact
Fault
F1, syncline
F2, syncline, anticline
F3, anticline
Massive sulfide deposit
metres
25 50 100 200

Figure 2-9. Geological map of the South Chisel basin area, modified after Bailes et al. 1996, Bailes and Galley 2007, and Friesen et al. 2015. Map datum is NAD83 UTM Zone 14. Intrusions and lakes not shown for simplicity. Boxes indicate detailed map areas for Figures 10, 11, and 12.

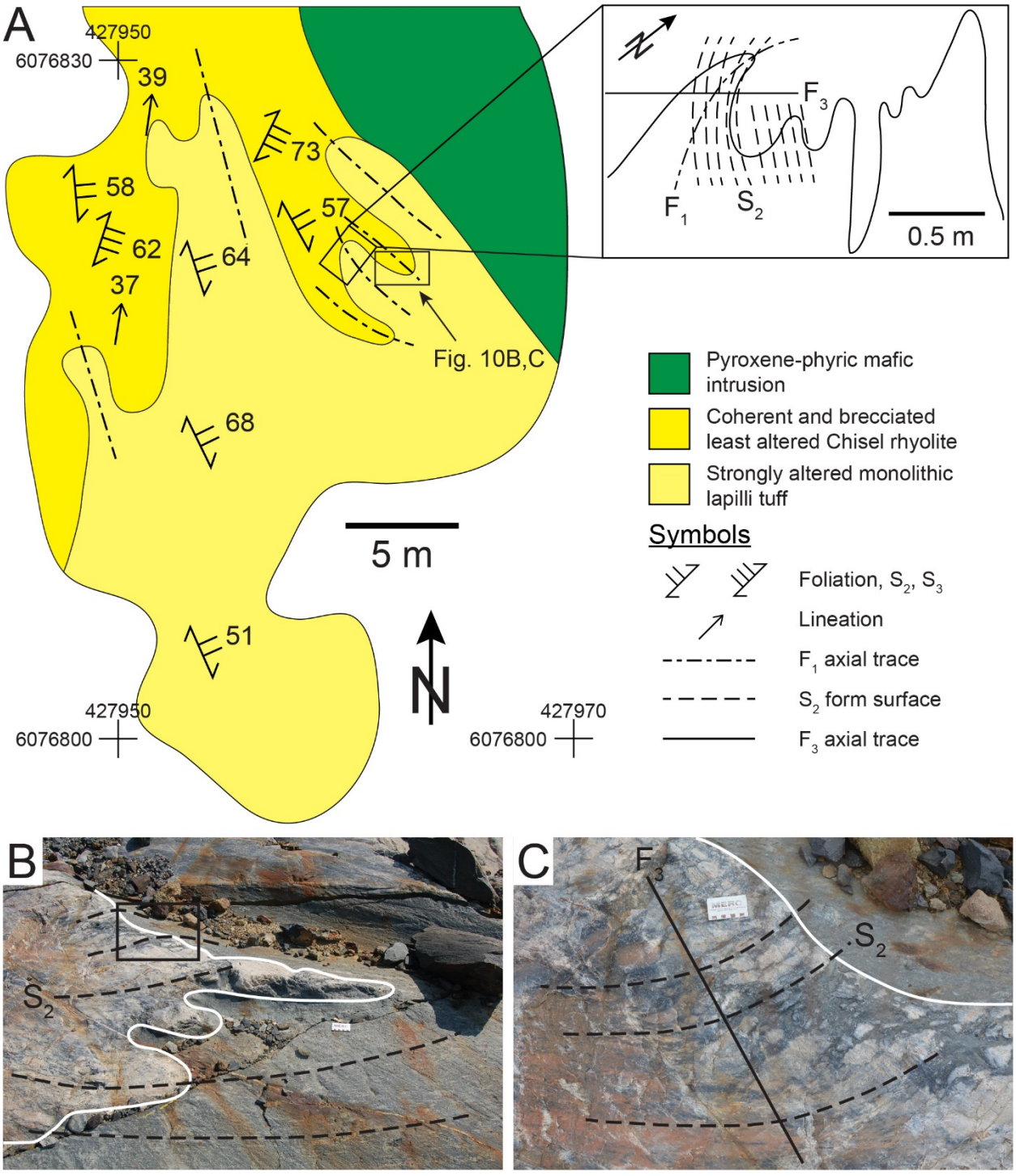

Figure 2-10. Detailed outcrop map within the Chisel open pit. S_0 is the contact between altered and least altered rocks. (a) Folded contact between least altered and strongly altered felsic volcanic rocks. Inset sketch shows that the penetrative S_2 foliation crosscuts the folds, indicating

that they are F_1 folds. (b) One of the parasitic folds observed in the Chisel open pit. The white line delineates the contact between least altered and strongly altered rhyolite that is folded by F_1. Least altered brecciated felsic volcanic rocks core the fold on the left side of the image and strongly altered felsic volcaniclastic rocks surround the fold on the right side of the image. The black box shows the location of the image in (c). (c) Detailed view of a parasitic fold showing the S_2 foliation crosscutting one of the limbs of the F_1 fold at a high angle. The S_2 foliation is refolded by F_3. The white line shows the contact between least altered and strongly altered rhyolite. Photo card (9 cm in length) for scale.

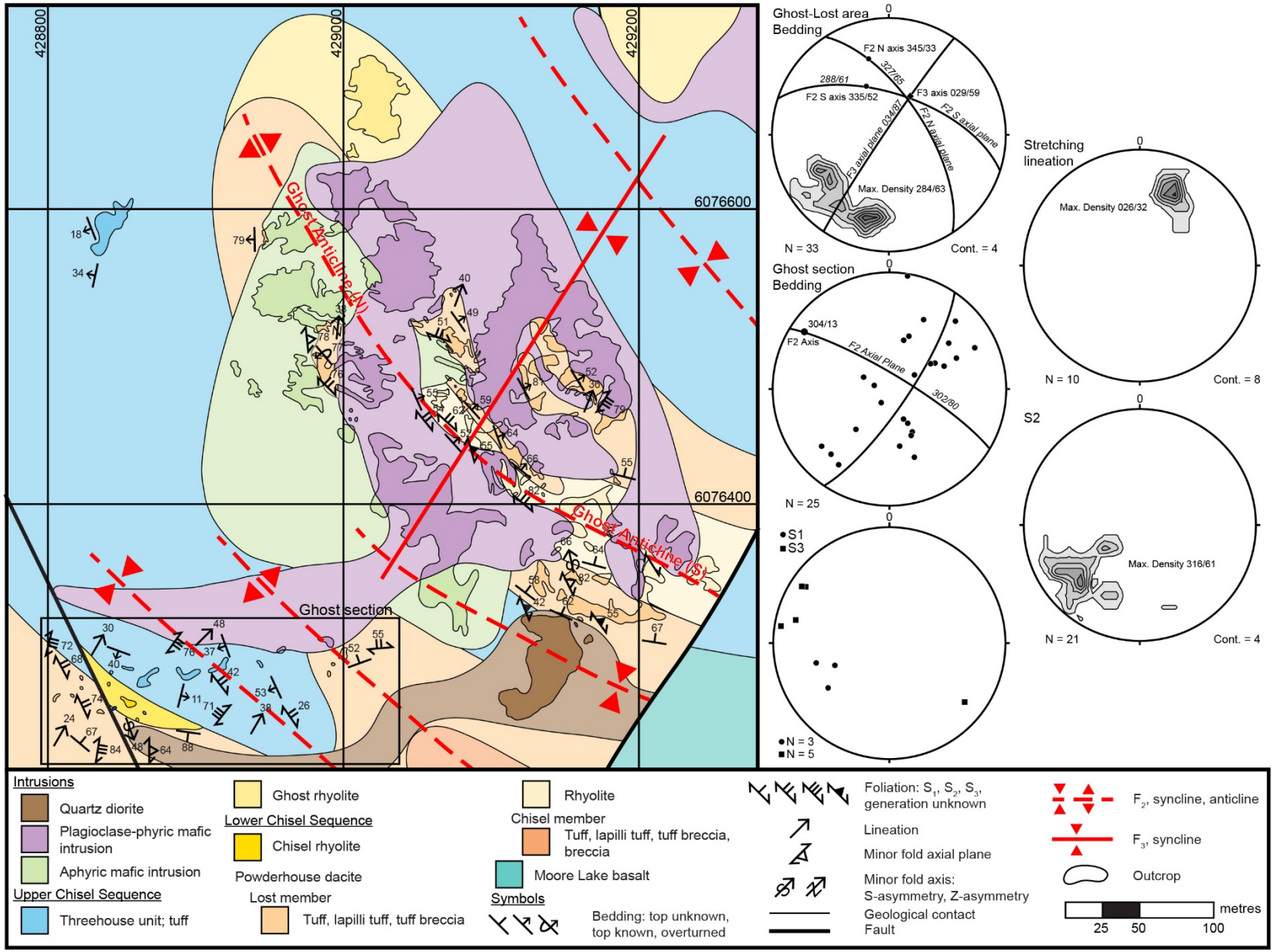
428800
429000
429200
6076600
6076400
Ghost Anticline (N)
Ghost Anticline (S)
Ghost section
Ghost-Lost area
Bedding
F2 N axis 345/33
327/65
288/61
F2 S axis 335/52
F3 axis 029/59
F3 axial plane 034/87
F2 N axial plane
F2 S axial plane
Max. Density 284/63
N = 33
Cont. = 4
Ghost section
Bedding
304/13
F2 Axis
F2 Axial Plane
302/80
N = 25
S1
S3
N = 3
N = 5
Stretching
lineation
Max. Density 026/32
N = 10
Cont. = 8
S2
Max. Density 316/61
N = 21
Cont. = 4
Intrusions
Quartz diorite
Plagioclase-phyric mafic intrusion
Aphyric mafic intrusion
Upper Chisel Sequence
Threehouse unit; tuff
Ghost rhyolite
Lower Chisel Sequence
Chisel rhyolite
Powderhouse dacite
Lost member
Tuff, lapilli tuff, tuff breccia
Rhyolite
Chisel member
Tuff, lapilli tuff, tuff breccia, breccia
Moore Lake basalt
Symbols
Bedding: top unknown, top known, overturned
Foliation: S1, S2, S3, generation unknown
Lineation
Minor fold axial plane
Minor fold axis: S-asymmetry, Z-asymmetry
Geological contact
Fault
F2, syncline, anticline
F3, syncline
Outcrop
metres
25 50 100

Figure 2-11. Detailed map of the Ghost-Lost area and equal-area, lower hemisphere projections of structural measurements. Number of measurements (N) at bottom of equal-area projections. Map datum is NAD83 UTM Zone 14. Planar features (e.g. bedding, foliations) are plotted as poles. Contours are calculated as percent of total number of data points per 1% area and “Cont.” refers to the contour interval. “Max. Density” refers to the average strike/dip and trend/plunge of planes and lineations, respectively. Ghost section shown in black box.

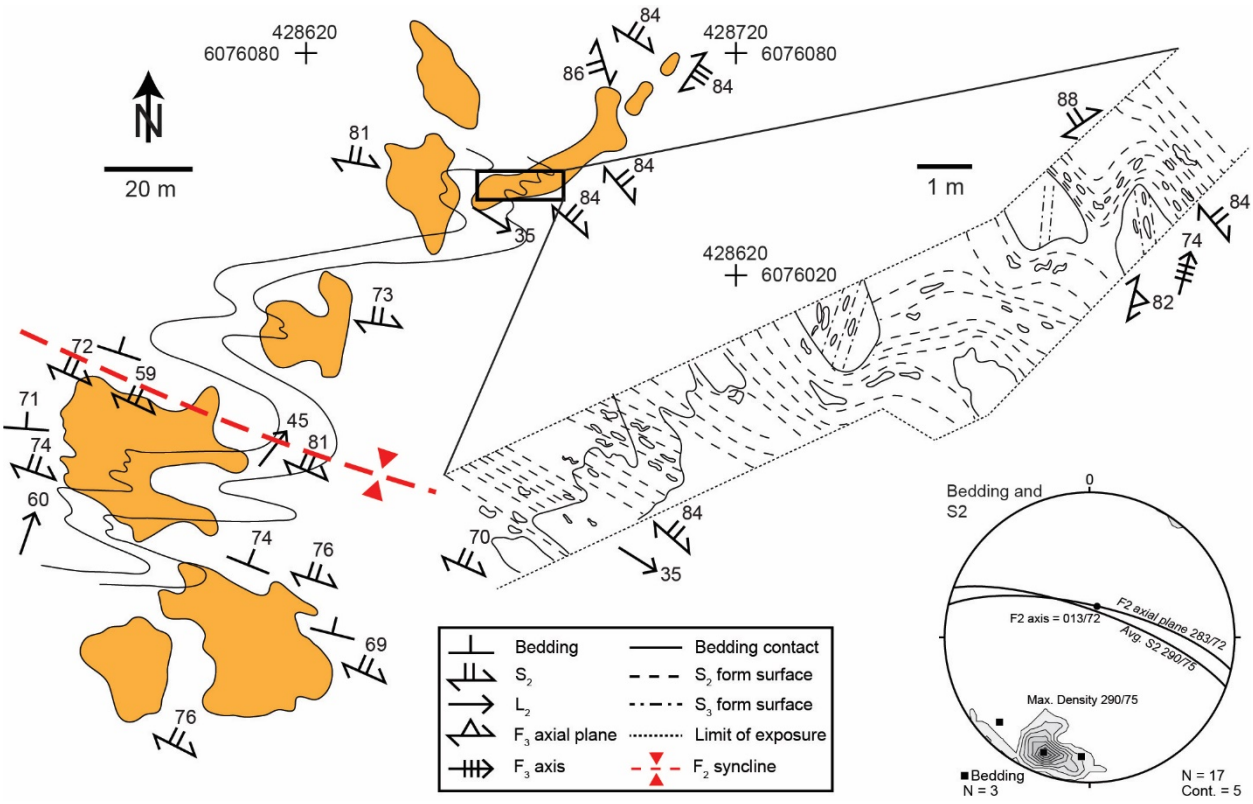

Figure 2-12. Outcrop map of the Powderhouse dacite southwest of the Ghost area showing tight $F_{1\text{-}2}$ folding and equal-area, lower hemisphere projection of structural measurements. Number of measurements (N) at bottom of equal-area projections. Planar features (e.g. bedding, foliations) are plotted as poles. Contours are calculated as percent of total number of data points per 1% area and "Cont." refers to the contour interval. "Max. Density" refers to the average strike/dip and trend/plunge of planes and lineations, respectively.

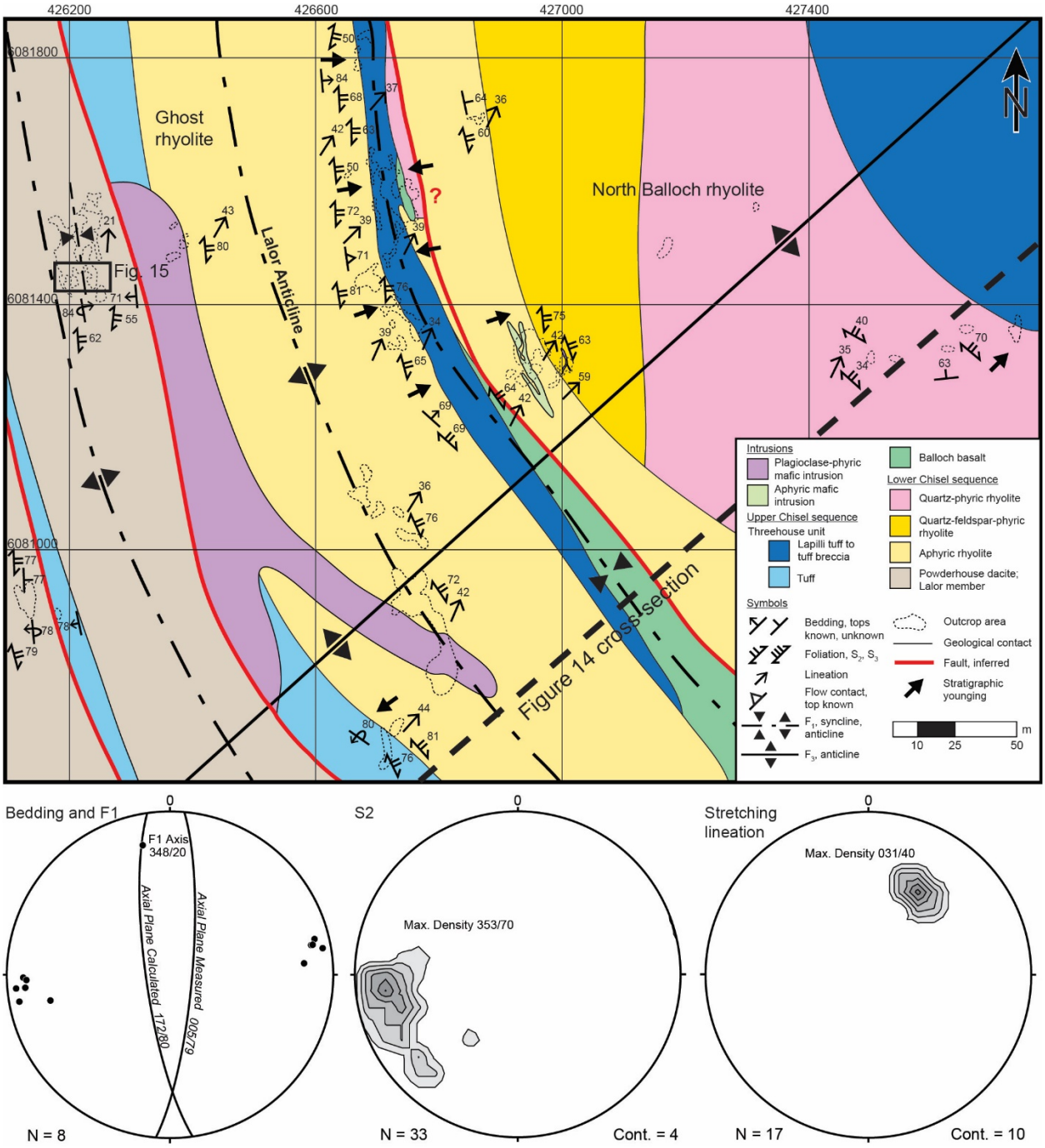

Figure 2-13. Geological map of the Lalor section and equal-area, lower hemisphere projections of structural measurements. Map datum is NAD83 UTM Zone 14. Black box indicates location of parasitic fold in Figure 15. Number of measurements (N) at bottom of equal-area projections.

Planar features (e.g. bedding, foliations) are plotted as poles. Contours are calculated as percent of total number of data points per 1% area and “Cont.” refers to the contour interval. “Max. Density” refers to the average strike/dip and trend/plunge of planes and lineations, respectively.

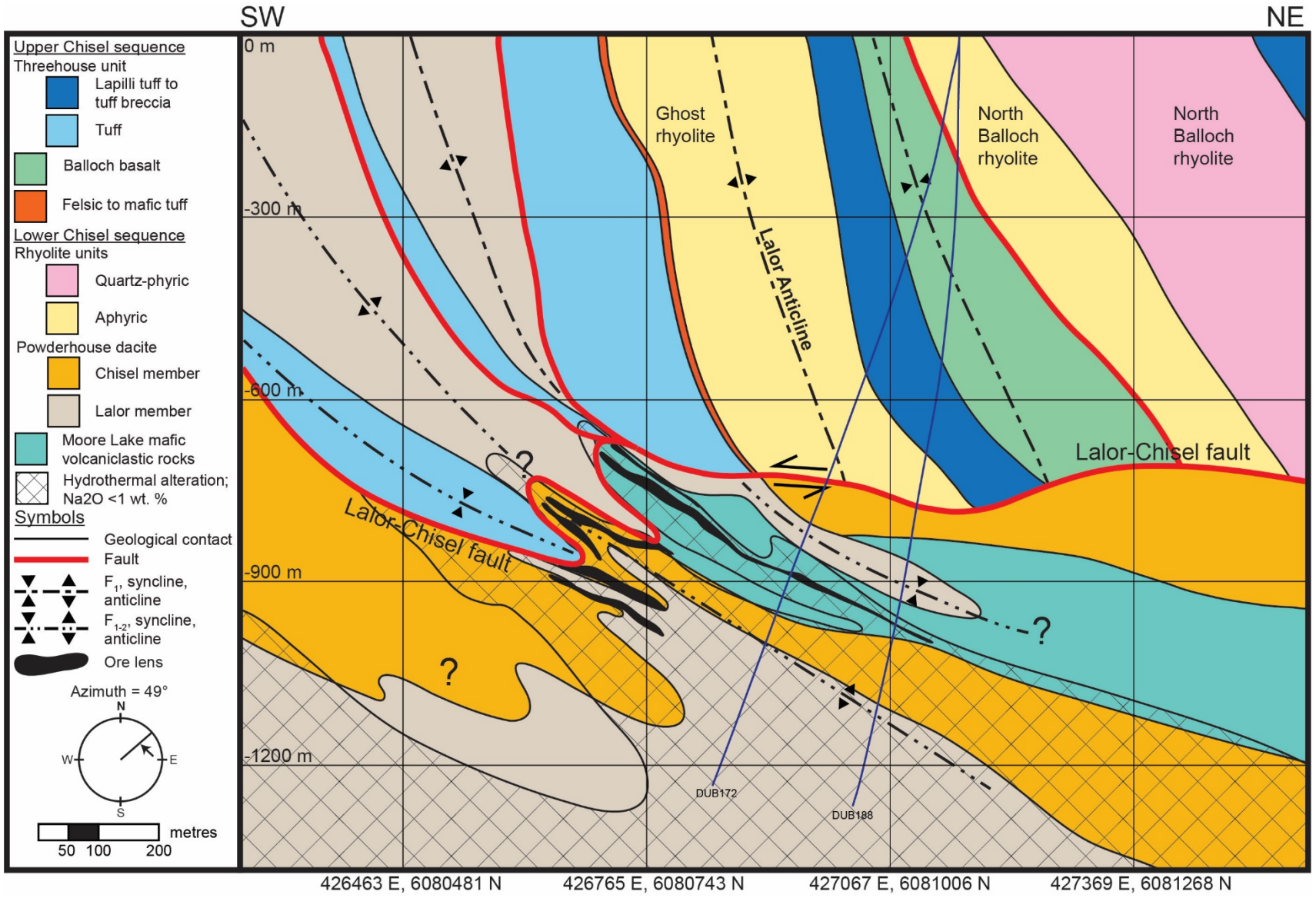
SW
NE
Upper Chisel sequence
Threehouse unit
Lapilli tuff to tuff breccia
Tuff
Balloch basalt
Felsic to mafic tuff
Lower Chisel sequence
Rhyolite units
Quartz-phyric
Aphyric
Powderhouse dacite
Chisel member
Lalor member
Moore Lake mafic volcaniclastic rocks
Hydrothermal alteration; Na2O <1 wt. %
Symbols
Geological contact
Fault
F1, syncline, anticline
F1-2, syncline, anticline
Ore lens
Azimuth = 49°
N
W
E
S
metres
50 100 200
0 m
-300 m
-600 m
-900 m
-1200 m
Ghost rhyolite
North Balloch rhyolite
North Balloch rhyolite
Lalor Anticline
Lalor-Chisel fault
Lalor-Chisel fault
DUB172
DUB188
426463 E, 6080481 N
426765 E, 6080743 N
427067 E, 6081006 N
427369 E, 6081268 N

Figure 2-14. Cross-section through the Lalor section stratigraphy. Cross-section builds on previous work by Bailes et al. (2013), Bailes (2014), and Caté (2016). Refer to Figures 13 and 17 for surface trace of section. Only 2 of 15 drill holes logged shown for reference for images in Figure 16. Map datum is NAD83 UTM Zone 14.

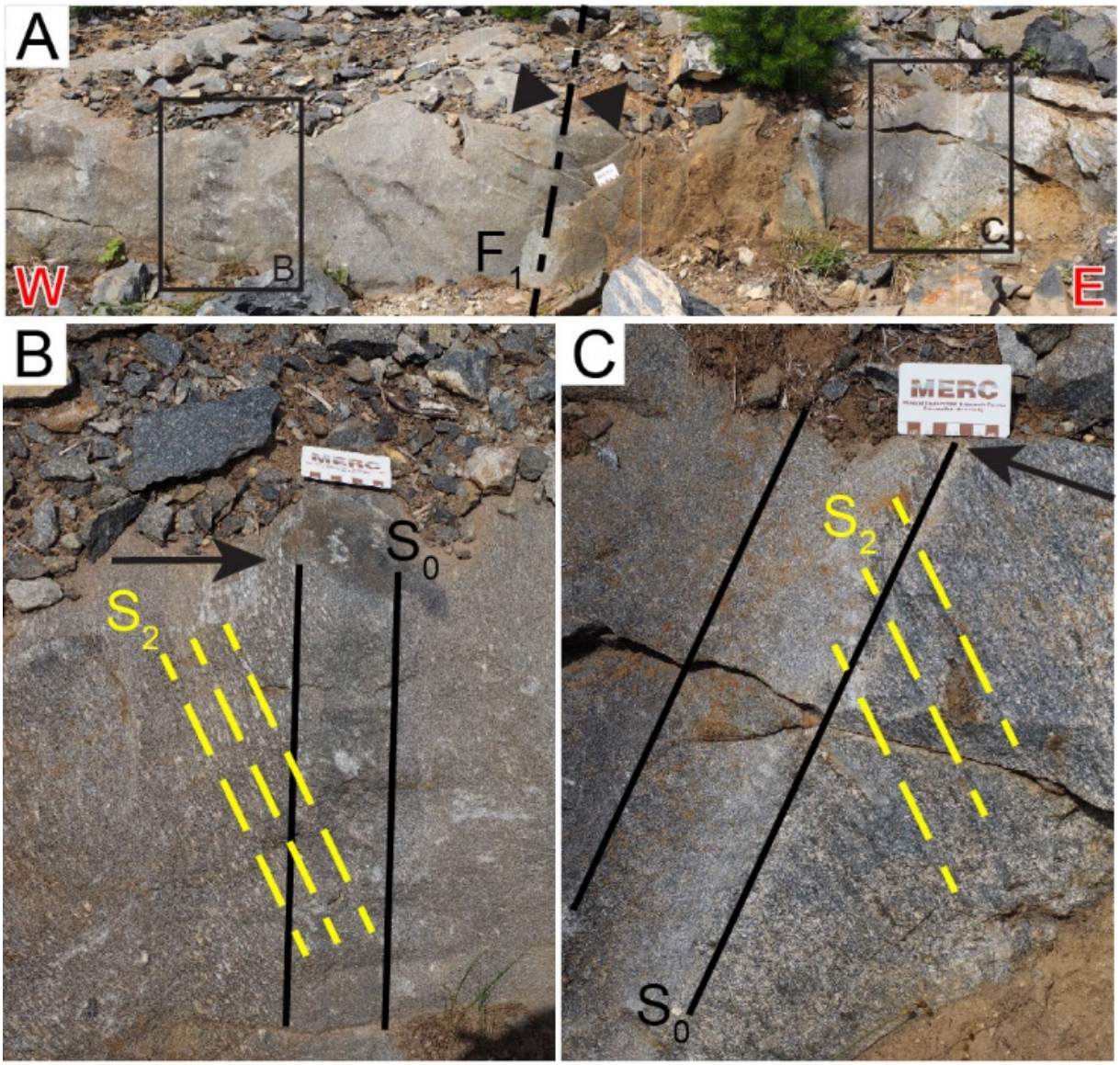

Figure 2-15. Field photographs of a parasitic F_1 fold in rocks of the North Chisel dacite unit located in the Lalor section. Fold location shown on Figure 13. (a) Overall view of fold. (b) West limb and (c) east limb of fold showing anticlockwise relationship of S_2 to bedding on both limbs, indicating that the fold is early and is overprinted by the cleavage. Arrows indicate younging directions defined by normal graded bedding. Photo card (9 cm in length) for scale.

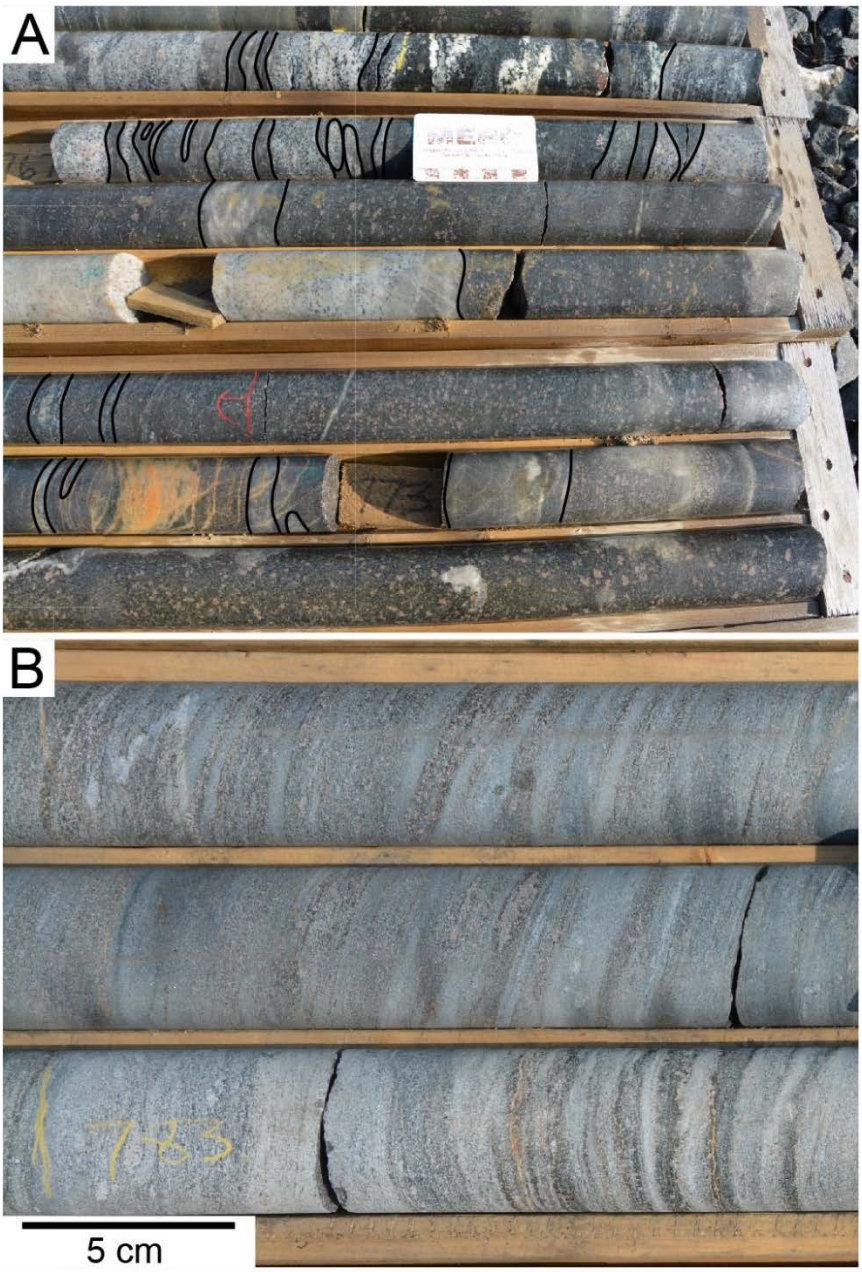

Figure 2-16. Geological characteristics of the Lalor-Chisel fault in drill holes (a) DUB 172 and (b) DUB 188. Drill core size is NQ/47.6 mm in diameter. Photo card (9 cm in length) for scale. (a) Strongly altered breccia zone within the Lalor-Chisel fault. Where clast margins can be identified they are outlined with black lines. (b) Strong foliation in fault zone defined by phyllosilicate alignment and flattened clasts.

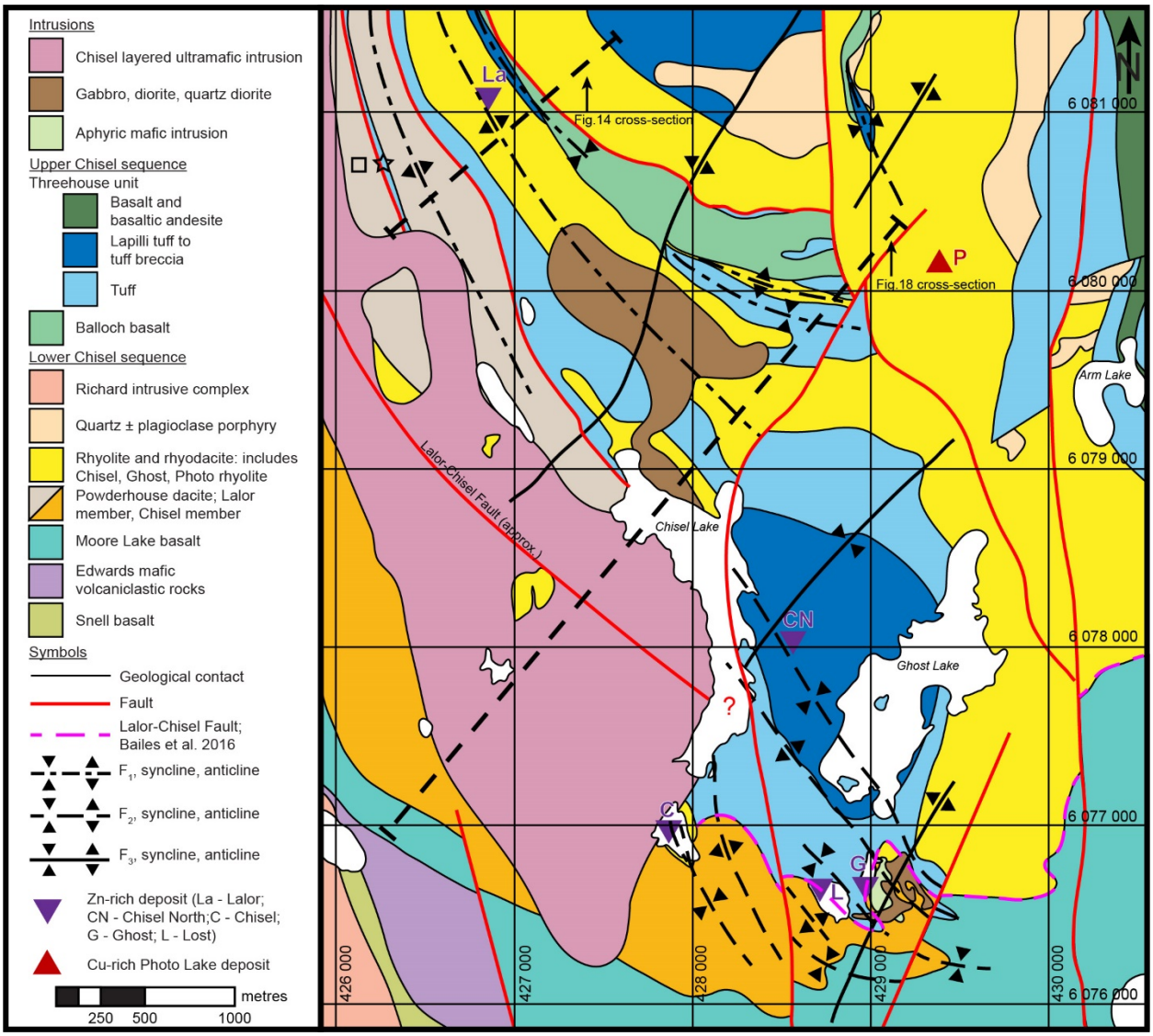

Figure 2-17. Simplified geology of the Chisel sequence incorporating new structural and stratigraphic interpretations from this study (modified after Bailes and Galley 2007). Map datum is NAD83 UTM Zone 14. Cross-section lines shown for Figures 14 and 18.

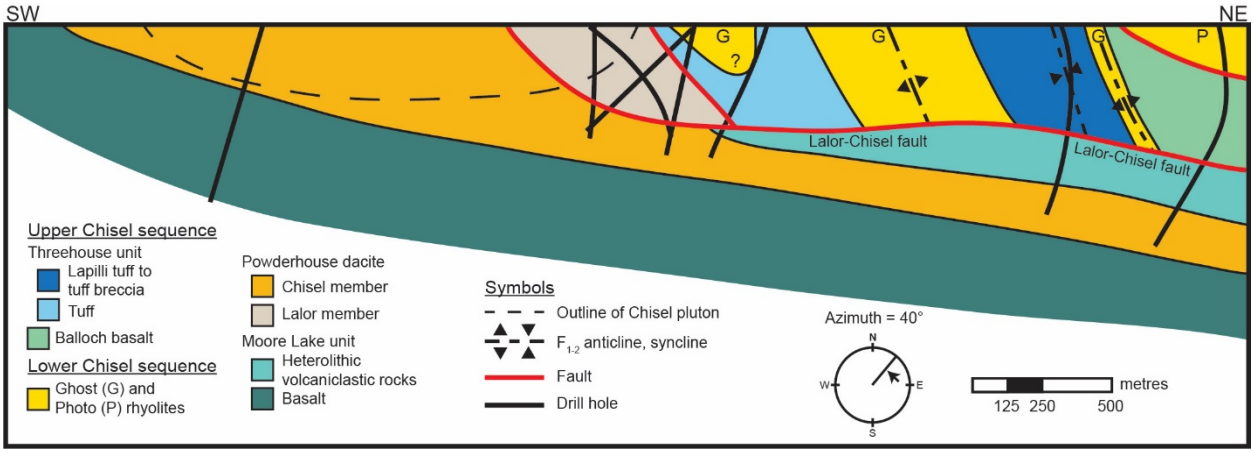

Figure 2-18. SW-NE cross-section along the line in Figure 17 showing the Lalor-Chisel fault as a major structure beneath the Chisel pluton.

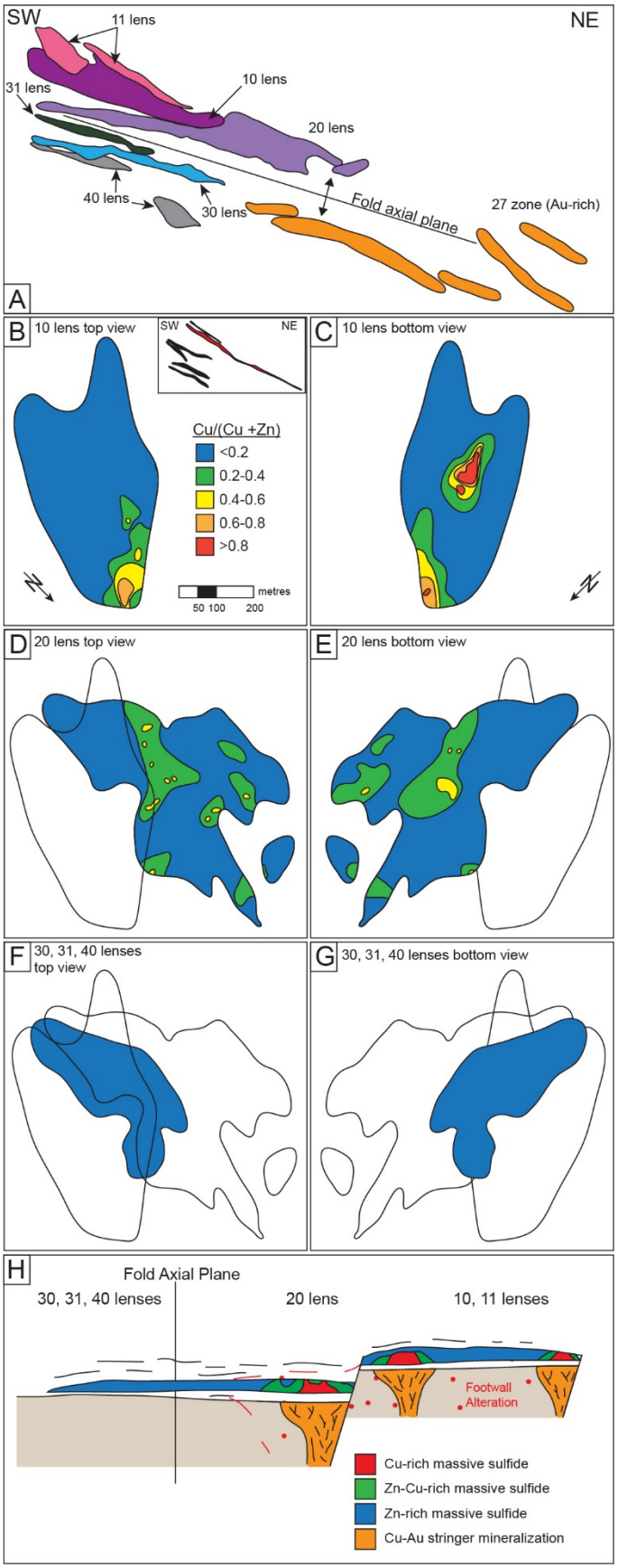
SW
NE
11 lens
10 lens
31 lens
20 lens
40 lens
30 lens
Fold axial plane
27 zone (Au-rich)
A
B
10 lens top view
SW
NE
Cu/(Cu +Zn)
<0.2
0.2-0.4
0.4-0.6
0.6-0.8
>0.8
metres
50 100 200
C
10 lens bottom view
D
20 lens top view
E
20 lens bottom view
F
30, 31, 40 lenses
top view
G
30, 31, 40 lenses bottom view
H
Fold Axial Plane
30, 31, 40 lenses
20 lens
10, 11 lenses
Footwall
Alteration
Cu-rich massive sulfide
Zn-Cu-rich massive sulfide
Zn-rich massive sulfide
Cu-Au stringer mineralization

Figure 2-19. Metal zoning plots for the Lalor deposit and deposit reconstruction. Metal zoning intervals in 0.2 (Cu / Cu+Zn). Metal zoning data and ore lens outlines provided by Hudbay Minerals Inc. Top view refers to the view from above and images the upper surface of the lens, whereas the bottom view refers to the view from below and images the lower surface of the lens. Lens cross-sections in (b), (d), and (f) taken from geological cross-section in Figure 12. (a) Cross section showing all ore lenses in the deposit. (b, c) 10 lens. (d, e) 20 lens. (f, g) Composite view of 31, 30, 40 lenses. (h) Conceptual reconstruction of the Lalor deposit prior to deformation.

TABLE 1. Summary of deformation events in the Snow Lake district (mineral abbreviations according to Whitney and Evans, 2010).

Froese and Moore (1980)	**Galley et al. (1988)**	**Kraus and Williams (1993, 1994, 1998, 1999)**	**This study**
D_3 Refolding of F_2 folds due to emplacement of gneiss domes and related diapirism	D_3 A series of small N-trending sinistral faults that offset the Nor Acme ore body	F_4 E-W-trending F_4 folds that occur locally in N-S trending domains; development of kink bands in unfavourably oriented domains	
		F_3 NE-trending open to tight F_3 folds – Threehouse synform; S_3 is a crenulation cleavage only preserved on E limb of Threehouse synform; S_2 rotated into appearing axial planar to F_3 on W limb of Threehouse synform	D_3 NE-trending open to tight F_3 folds – Threehouse synform; N- to NE-trending, steeply E- to SE-dipping axial planar S_3 cleavage
D_2 Megascopic, NE-trending F_2 folds – McLeod Lake synform, Threehouse synform; axial planar S_2 cleavage – penetrative in Missi and Burntwood, defined by oriented Bt flakes in volcanics; L_2 stretching lineation parallel to F_2 fold axes and defined by crenulations, mica edges, elongate clasts and mineral segregations	D_2 NNE-trending F_2 folds; axial planar S_2 cleavage defined by Bt alignment and St growth in the S_2 plane; oblique sinistral reactivation of the McLeod Road Fault and Birch Lake fault; formation of N- to NE-trending, moderately dipping faults – Howe Sound Fault (?)	F_2 Isoclinal F_2 folds only observed in Burntwood Group turbidites – McLeod Lake syncline, Nor-Acme anticline; S_2 foliation defined by alignment of coarse Bt and pulled-apart St – penetrative and dominant fabric in Burntwood Group, only locally developed in volcanic rocks; formation of McLeod Road Fault and Snow Lake Fault	
---------- Intrusion of calc-alkaline plutons at ca. 1837 to 1830 Ma (Tramping Lake, Wekusko Lake, Ham Lake plutons) -------			
D_1 Megascopic F_1 folds – Nor-Acme anticline, Anderson Lake anticline, Ghost Lake syncline; S_1 foliation defined by orientation of Bt and Amp and by flattened clasts and mineral aggregates – overgrown by St and Grt; L_1 likely exists but is very close in orientation to L_2; McLeod Road Fault pre-dates or is synchronous with D_1	D_1 Isoclinal F_1 folds – Nor-Acme anticline; strong penetrative axial planar S_1 cleavage defined by orientation of Bt and Amp and by flattened clasts; NE-plunging stretching lineation; formation of McLeod Road Fault and Birch Lake Fault	F_1 Micro- to macroscopic isoclinal F_1 folds; S_1 cleavage defined by Bt and Amp alignment and inclusion trails in porphyroblasts; S_1 is rare in Burntwood Group rocks; L_1 stretching lineation sub-parallel to F_1 fold axes	D_2 NW- to NNW-trending isoclinal F_2 folds; axial planar S_2 cleavage defined by orientation of Bt and Amp and by flattened clasts; NE-plunging stretching lineation; tightening of NW-trending F_1 folds
---------- Deposition of Burntwood Group at ca. 1859 to 1842 Ma ----------			
			D_1 N- to NW-trending isoclinal F_1 folds – Photo syncline, Lost anticline, Lalor anticline; W-directed, NW-striking faults; formation of Lalor-Chisel fault
			D_0 synvolcanic faults

Chapter 3

The structural and stratigraphic setting, mineralogy, and geochemistry of the Photo Lake VMS deposit, Snow Lake, Manitoba: implications for the timing and source of gold mineralization

3.1 Abstract

The Photo Lake volcanogenic massive sulfide (VMS) deposit, located in Snow Lake, Manitoba, is a Cu-Zn-Au-Ag deposit that occurs in the Paleoproterozoic Chisel sequence of the Trans-Hudson Orogen. With average Au and Cu grades of 4.87 g/t and 4.58 wt. %, respectively, it is significantly enriched with respect to the five other VMS deposits in the Chisel sequence. Detailed mapping indicates that the Photo Lake deposit, unlike other Chisel sequence VMS deposits, is located at the contact between two distinct rhyolite units within a large, shield-like rhyolitic complex but formed at the same productive ore interval as the other deposits. The strong correlation of Au with Cu, as indicated by deposit-scale metal zonation, coupled with the early timing of Au, as indicated by laser ablation inductively coupled plasma mass spectrometry (LA-ICP-MS) analysis of pyrite, suggests that the anomalous Cu and Au grades result from syngenetic enrichment. Mineral and chemical associations suggest that the anomalous Au and Cu enrichment is due to a magmatic input into the ore system, and the Au and Cu metal distribution within the deposit is a product of boiling of the hydrothermal fluids in the subseafloor.

3.2 Introduction

Volcanogenic massive sulfide (VMS) deposits are traditionally mined for base metals (e.g., Cu, Zn, Pb: Franklin et al., 2005; Galley et al., 2007a), but some VMS deposits are also a significant source of other metals, in particular Au. Gold enrichment of some VMS deposits has resulted in classifications that separate VMS deposits into those that are Au enriched from the vast majority that are not (Poulsen and Hannington, 1995; Mercier-Langevin et al., 2011). Gold-enriched VMS deposits occur in modern and ancient submarine oceanic and continental arc settings, forming either early during arc rifting, in back-arc settings, or during evolving arc magmatism (e.g., Hannington et al., 1986; Herzig et al., 1993; Hannington et al., 1999; Moss and Scott, 2001; Dubé et al., 2007; de Ronde et al. 2011; Mercier-Langevin et al., 2011 and references therein). In modern volcanic settings, sampling of hydrothermal fluids at active vent sites and geochemical analyses of the sulfides precipitating from these fluids allow for direct measurements of the fluid compositions and conditions at the time of venting. The results of these studies indicate that fluid chemistry and temperature are critical for mobilizing Au in hydrothermal fluids (e.g., Hannington et al., 1986; Huston and Large, 1989), and fluid boiling can influence these factors (e.g., Drummond and Ohmoto, 1985; Bischoff and Rosenbauer, 1987; Butterfield et al., 1990; Monecke et al., 2014). There is also strong evidence in modern hydrothermal systems to suggest a correlation between Au enrichment and a magmatic fluid contribution (e.g., de Ronde et al., 2001, 2005, 2011; Moss and Scott, 2001; Moss et al., 2001; Hannington et al., 2005). The geodynamic environment and host rocks are also interpreted to influence the precious metal contents of modern seafloor massive sulfide (SMS) deposits (e.g., Hannington et al., 1999, 2005; Moss et al., 2001). In ancient VMS deposits, it is not possible to measure the venting hydrothermal fluids, and the sulfides are overprinted by later deformation and metamorphism.

Evidence for the processes responsible for Au enrichment in ancient deposits is therefore largely circumstantial and relies on proxies rather than direct measurements, such as correlations between Au and the epithermal suite of elements (e.g., Ag, As, Bi, Mo, Sb, Sn, Te; Hedenquist and Lowenstern, 1994; White and Hedenquist, 1995; Sillitoe et al., 1996; Williams-Jones and Heinrich, 2005; de Ronde et al., 2011) to indicate a magmatic input (e.g., Hannington et al., 1999, 2005; Dubé et al., 2007; Mercier-Langevin et al., 2007; Brueckner et al., 2014; Gill et al., 2016). However, as our understanding of modern seafloor hydrothermal systems advances, so too does our understanding of their ancient analogues, and it is possible to develop a better understanding of Au enrichment in ancient deposits through comparisons with modern processes.

The Paleoproterozoic Photo Lake VMS deposit, located 5 km west of the town of Snow Lake, Manitoba, is a high-grade, low-tonnage deposit that was discovered in 1994 and mined from 1995 to 1998 (689,885 tonnes of 4.58% Cu, 6.35% Zn, 4.87 g/t Au, 29.49 g/t Ag: Galley et al., 2007b). It is one of six VMS deposits (Chisel Lake, Lost Lake, Ghost Lake, Chisel North, and Lalor) that are associated with felsic flow/dome complexes at the contact between felsic and mafic volcaniclastic rocks of the mature arc Chisel sequence (Bailes and Galley, 2007). With Au grades >3.46 g/t, the Photo Lake deposit is classified as auriferous and belongs to a restricted group of deposits displaying such elevated Au grades (Mercier-Langevin et al., 2011).

Recent structural work indicates that the host rocks to the Photo Lake deposit occur within the Chisel sequence ore interval, placing all six VMS deposits at the same stratigraphic position (Stewart et al., 2018); however the anomalous Au- and Cu-rich character of the Photo Lake deposit (4.9 g/t Au versus 0.4 to 2.9 g/t Au; 4.58 wt. % Cu versus 0.15 to 1.34 wt %; Table 1)

differs from the other Chisel sequence VMS deposits. This enrichment in Au and Cu suggests that the hydrothermal system and/or processes active at Photo Lake differed from deposits along strike at the time of VMS formation. Thus, the Photo Lake deposit provides an excellent opportunity to isolate and study Au enrichment processes operative in a Paleoproterozoic submarine volcanic arc setting. Moreover, given its small tonnage and complete excavation, it is possible to study the deposit in its entirety, which is more difficult in larger deposits currently in production. This is especially relevant now, as recognition of the Au enrichment processes at Photo Lake may help to understand more localized Au enrichment at the recently discovered Lalor deposit, which has a total estimated tonnage of 25.6 Mt at 4.88 wt. % Zn, 0.74 wt. % Cu, 3.08 g/t Au and 26.34 g/t Ag (combined reserves, resources, and exploited ore; Caté, 2016), and 1.46 Mt at 0.30 wt. % Zn, 4.24 wt. % Cu, 6.7 g/t Au, and 22.2 wt. % Ag in the Cu-Au zones (Bailes et al. 2016).

In this paper we present evidence and arguments for the timing of Au enrichment in the Photo Lake deposit and identify the process(es) responsible for this enrichment. However, since its discovery, academic research conducted on the Photo Lake deposit has been limited despite its very unusual Au grades. The geology of the Photo Lake area is summarized in maps (1:5,000 and 1:20,000 scales; Bailes et al., 1996, 1997; Bailes and Galley, 2007) and two open file reports by the Manitoba Geological Survey (Bailes 1996, 1997); however, these publications focus on the overall geology of the surrounding area and do not provide a detailed description of the Photo Lake deposit. The only detailed study of the deposit is a structural study completed by Hudson Bay Exploration and Development (HBED) and Hudson Bay Mining and Smelting (HBMS) while the mine was operational (Tessier, 1996). Therefore, we must first describe the deposit,

including its host rocks, sulfide mineralization, metal zoning, and alteration, and establish the volcanic history and structural setting of the deposit. The timing of Au and processes responsible for Au enrichment are then assessed within the context of the deposit description. The results have implications not only for Au enrichment at Snow Lake, but for VMS districts globally.

3.3 Regional geology and geology of the Snow Lake area

3.3.1 Regional geology

The Chisel sequence is in the Snow Lake arc assemblage of the Paleoproterozoic Flin Flon-Glennie Complex (Fig. 1). This complex is located in the Reindeer Zone of the Trans-Hudson Orogen and comprises the Flin Flon Belt in the east and the Glennie Domain in the west. The Flin Flon Belt is a collage of five tectono-stratigraphic assemblage types: juvenile arc, evolved arc, juvenile ocean floor, oceanic plateau, and Archean crustal slices (Lucas et al., 1996). The Snow Lake arc assemblage is the easternmost of the seven 1.92 to 1.88 Ga tectono-stratigraphic assemblages in the Flin Flon Belt. The Flin Flon-Glennie Complex hosts the largest Paleoproterozoic VMS district in the world (Syme et al., 1999; Galley et al., 2007b), with most of the VMS deposits located in the Flin Flon and Snow Lake arc assemblages. The Flin Flon arc assemblage is classified as a bimodal mafic lithotectonic setting and the Snow Lake arc assemblage is classified as a bimodal felsic setting according to the VMS classification scheme by Franklin et al. (2005).

Of the seven tectono-stratigraphic assemblages in the Flin Flon Belt, Snow Lake is the only assemblage interpreted to have evolved as a pericratonic arc outboard of the Superior craton, rather than as an oceanic arc (Percival et al., 2005; Corrigan et al., 2007, 2009), possibly

resulting in a different volcanic and petrogenetic history than the other assemblages (Stern et al., 1992; David et al., 1996; Lucas et al., 1996). This interpretation is supported by 2.82-2.65 Ga xenocrystic zircons in the 1.892 ± 3 Ma Stroud Lake felsic breccia at the base of the Chisel sequence (David et al., 1996) and evolved ε_{Nd} values of -0.4 to +2.4 (Stern et al., 1992) in the overlying Snell Lake basalt, indicating interaction of the magmas with older (Archean), light REE-enriched lithosphere. None of the volcanic rocks in the Snow Lake assemblage have been successfully dated and the age constraints available are U-Pb zircon ages for the synvolcanic Sneath Lake (1886 +17/-9 Ma; Bailes et al., 1991) and Richard Lake (1889 +8/-9 Ma; Bailes et al., 1991) subvolcanic intrusions and the Stroud Lake felsic breccia.

3.3.2 Geology of the Snow Lake Area

The Snow Lake arc assemblage is divided into the Anderson, Chisel, and Snow Creek sequences, representing the transition from primitive arc, to mature arc, to arc rift, respectively (Bailes and Galley, 2007). Volcanogenic massive sulfide deposits occur in both the Anderson and Chisel sequences, with Cu-rich deposits dominating in the Anderson sequence and Zn-rich deposits dominating in the Chisel sequence.

The Chisel sequence is divided into lower and upper successions, with the contact between these successions represented by a period of quiescence in explosive and effusive volcanism that coincides with the Chisel VMS ore interval. The lower Chisel sequence comprises mafic and felsic flows and abundant volcaniclastic rocks (Fig. 2; Bailes and Galley, 1996, 1999, 2007; Bailes et al., 1996, 1997). The upper Chisel sequence has been interpreted as comprising a younger, homoclinal succession consisting of, in ascending order, the Balloch basalt, the Ghost

and Photo rhyolites, the Threehouse mafic volcaniclastic rocks and flows (Threehouse unit), and the North Chisel dacite (Bailes and Galley, 1996, 1999, 2007; Bailes, 2014; Bailes et al., 2016). This succession also included undivided rocks of the upper Chisel sequence that were not correlated with the upper Chisel sequence stratigraphy (Bailes and Galley, 2007). However, recent work suggests that, with the exception of the Threehouse unit and Balloch basalt, this succession represents folded and thrust-repeated lower Chisel sequence strata (Fig. 2; Stewart et al., 2018). The North Chisel dacite is interpreted to be the stratigraphic equivalent to the Powderhouse dacite (Friesen et al., 2015), and this is supported by detailed structural work (Stewart et al., 2018). The North Balloch, Ghost, and Photo rhyolites are interpreted to be stratigraphically equivalent and were emplaced prior to the Balloch basalt, which occurs at the same stratigraphic interval as the Threehouse unit (Stewart et al., 2018). Therefore, only the Threehouse unit and Balloch basalt occur in the upper Chisel sequence (Stewart et al., 2018). The contact between the lower and upper Chisel sequences is conformable (Stewart et al., 2018). The ore interval is bounded by the Powderhouse dacite in the footwall and the Threehouse unit and Balloch basalt in the hanging wall and is defined by felsic flows and domes and volcaniclastic deposits (Bailes and Galley, 2007; Engelbert et al., 2014a; Gibson et al., 2014). Volcanogenic massive sulfide deposits occur at the contact between localized rhyolite domes and the Threehouse unit (e.g. Chisel Lake deposit) and, where rhyolite domes are not present, between the Powderhouse dacite and the Threehouse unit (e.g., Lost Lake deposit; Fig. 2). The Photo Lake deposit is the only deposit known to occur within a sequence of voluminous felsic flows (Bailes, 1996, 1997).

3.3.3 Deformation and metamorphism

Four main deformation events are recognized in the Snow Lake district (Froese and Moore, 1980; Galley et al., 1988; Kraus and Williams, 1993, 1994, 1998, 1999; Stewart et al., 2018). The earliest event, D_1, was recently recognized in the Chisel sequence volcanic rocks by Stewart et al. (2018) and has not been identified in the Burntwood Group turbidites. It is characterized by tight to isoclinal F_1 folds without a preserved axial planar S_1 cleavage. The D_2 deformation event is recognized in both the Burntwood Group turbidites and the volcanic rocks of the Snow Lake arc assemblage and is characterized by tight to isoclinal F_2 folds, a pervasive axial planar S_2 cleavage that is the dominant fabric in the area, and a strong L_2 stretching lineation (Kraus and Williams 1998, 1999; Rubingh et al., 2012; Stewart et al. 2018). S_2 has been preserved as straight inclusion trails in kyanite, staurolite, garnet, and biotite porphyroblasts (Kraus and Williams, 1999; Stewart et al., 2018). D_3 is characterized by upright, open to closed NE-striking F_3 folds that refold F_1 and F_2 folds and D_1 and D_2 faults (Kraus and Williams, 1999; Rubingh et al., 2012; Stewart et al., 2018). F_1 and F_2 fold axes were progressively reoriented during D_3 tectonic transport (Kraus and Williams, 1999). D_4 produced approximately east-west-trending F_4 folds that overprint $F_{1\text{-}2}$ and F_3 structures but only occur locally in approximately north-south-trending domains (e.g. west limb of the Threehouse synform; Kraus and Williams, 1999). Peak, middle almandine-amphibolite facies (~5-6 kbar, 550-600°C) metamorphism occurred syn- to post-D_2 but prior to D_3 (Menard and Gordon, 1997; Caté, 2016). In hydrothermally altered volcanic rocks at Photo Lake this metamorphism is reflected by a peak assemblage of staurolite + garnet + biotite and kyanite + chlorite (Menard and Gordon, 1997). The term “meta” is implicit for all rock types at Snow Lake and is not used as a prefix in the text.

3.4 Analytical techniques

3.4.1 Field techniques

Field mapping (1:2000 and 1:200 scales) and sampling was carried out from 2012 to 2014. Core from eight drill holes through the deposit was logged and sampled to determine the distribution and contact relationships of the ore lenses, host rocks, and alteration zone at depth. Thirty-six samples from three of these drill holes with exceptionally high Au were selected for petrography and whole rock geochemical analyses to be representative of different metal concentrations: (1) high Au (>7 g/t), high Cu (>6.5 wt %), high Zn (>10 wt %); (2) low Au, high Cu, low Zn; (3) high Au, high Cu, low Zn; (4) high Au, low Cu, high Zn; and (5) low Au, low Cu, high Zn.

3.4.2 Petrography

Petrographic analysis included 24 least altered and 12 altered samples from the Photo Lake host rocks, along with 36 samples collected from the economic ore lenses. Sixteen sulfide samples were examined using a JEOL 6400 scanning electron microscope (SEM) connected to an energy-dispersive spectrometer (EDS) at the Central Analytical Facility (CAF) at Laurentian University (Sudbury, Ontario) to identify Au and acquire backscattered electron (BSE; acceleration voltage of 20 kV) images of Au and associated minerals. Scanning electron microscopy provided the semi-quantitative chemistries and composition of mineral phases in least altered and altered samples.

Quantitative mineral chemical data for pyrite and pyrrhotite were acquired using a JEOL JXA-8230 electron microprobe equipped with 5 tunable wavelength dispersive (WD) spectrometers at the University of Ottawa. Operating conditions were 40 degree takeoff angle, beam energy of 20

keV, beam current of 50 nA, and beam diameter of 1 µm. The count time was 16 seconds for Ti and 40 seconds for all other elements, with an off-peak count time of 40 seconds for all elements. The standards used were Bi_2Se_3 (MM-1) for Se, cochromite (HM-1) for Co, cubanite (SM-1) for Cu, rutile (MM-1) for Ti, GaAs (MM-1) for As, Sphalerite (MM-1) for Zn, pentlandite (MM-1) for Ni, and pyrite (Pyrite-48230) for S and Fe. Detection limits for all elements are on the order of 0.015 wt. % or lower. Quantitative microprobe data is provided in Table 2 and images of minerals analyzed are provided in Figure 3.

3.4.3 Geochemistry

To characterize the Photo Lake VMS deposit four sample suites were analyzed: (1) 21 outcrop and drill core samples of least altered felsic volcanic rocks; (2) 32 drill core samples from the economic ore lenses; (3) 12 drill core samples from the discordant footwall alteration zone; and (4) 21 drill core samples selected to provide geochemical coverage of the deposit at depth.

Suites 1, 2, and 3 were crushed in a steel jaw-crusher and pulverized in an agate mill at the Ontario Geoscience Laboratories (OGL; Sudbury, Ontario). Samples from suites 1 and 3 were dissolved by closed vessel multi-acid (hydrofluoric, hydrochloric, nitric, and perchloric) digestion and analyzed for total abundances of trace elements by inductively coupled plasma – mass spectrometry (ICP-MS) at OGL. Splits of the pulverized samples were analyzed by X-ray fluorescence (XRF) fusion for total abundances of major oxides at Activation Laboratories (ActLabs; Ancaster, Ontario). Samples were roasted at 1000°C for 2 hours to determine the loss on ignition (LOI). After roasting, the samples were mixed with a combination of lithium

metaborate and lithium tetraborate with lithium bromide as a releasing agent and fused in Pt crucibles to produce the fusion disk.

Samples from suite 2 were also dissolved and analyzed at OGL to obtain metal and trace metal concentrations of the mineralization at the Photo Lake deposit. Samples underwent an open vessel multi-acid (hydrofluoric, hydrochloric, nitric, and perchloric) digestion in order to dissolve most of the silicate phases present. The samples were then analyzed for total abundances of select major and trace elements by ICP – atomic emission spectrometry (ICP-AES) and for Cu, Pb, and Zn by atomic absorption spectroscopy – flame (AAS-Flame). The samples from suite 2 were also analyzed for total abundances of the trace elements by ICP-MS following an aqua regia digestion consisting of a combination of cold concentrated hydrochloric and nitric acid followed by a 1 hour digestion at 100°C in order to dissolve the labile elements from silicate and sulfide phases. Gold and Ag were pre-concentrated using a lead-based flux and separated by cupellation before being measured by gravimetric finish. Finally, sulfur and total carbon as CO_2 were measured by infrared absorption spectroscopy following combustion of the samples in an oxygen-rich environment.

Sample suite 4 was crushed in a steel jaw-crusher and pulverized in a mild steel mill at ActLabs. The samples were then prepared for major oxide and trace element analysis by lithium metaborate-tetraborate fusion and weak nitric acid digestion. The samples were analyzed by ICP – optical emission spectrometry (ICP-OES) for total abundances of major oxides and by ICP-MS for total abundances of trace elements. Splits of the pulverized samples were dissolved by closed

vessel multi-acid (hydrofluoric, hydrochloric, nitric, and perchloric) digestion and analyzed for Ag, Cd, Cu, Ni, Pb, S, and Zn by ICP-MS at ActLabs.

With the exception of Bi, Cr and Sn, the relative standard deviations (%RSD) calculated for replicate analyses and standards are <10% for ICP-MS determinations of least altered and altered samples. Precision of the data for the mineralized samples was variable. The results of AAS-Flame (Cu, Pb, Zn) and infrared absorption (S, CO_2) produced %RSD <10% but the results of ICP-AES and ICP-MS varied depending on the element analyzed. Tables 3 and 4 summarize the data with the best precision for sample suites 1 and 3, respectively, normalized to 100%.

New results collected by this study were supplemented with data from the Hudson Bay Exploration and Development (HBED) geochemistry and assay database compiled from drill core samples collected during exploration and mining of the Photo Lake deposit from 1994 to 1996. All HBED data was analyzed at X-Ray Assay Laboratories (XRAL; now SGS Minerals Services) by X-ray fluorescence (XRF) for total abundances of major oxides and by atomic absorption spectroscopy (AAS) for total abundances of Au and Cu, Zn, Au, and Ag. Lead-fire assay techniques were used to concentrate Au and Ag prior to analysis.

3.4.4 LA-ICP-MS

Trace element maps were produced by laser ablation inductively coupled plasma mass spectrometry (LA-ICP-MS) for individual pyrite grains in four of the sulfide samples (12-145S-004-1, 12-145S-004-7B, 12-145S-005-2, 12-146S-002-3). These grains were analyzed for Ag, As, Au, Bi, Co, Cu, Fe, Hg, Mo, Ni, Pb, Pd, Pt, Sb, Se, Sn, and Te. The maps were produced at

the Geo-Fingerprinting Lab at Laurentian University and the OGL in Sudbury, Ontario, Canada using a ThermoScientific XSeries2 quadrupole ICP-MS equipped with an ArF excimer (193 nm) laser-ablation system (RESOlution M-50). The total acquisition time for each map varied from 2-6 hours depending on the size of the map. An appropriate spot size was selected for each individual pyrite grain and ranged from 10-14 µm. The scan rate, repetition rate, and fluence (laser energy density) all varied for each map and were 4-7 µm/s, 7-8 Hz, and 5-6 J/cm^2, respectively. After every 10 lines reference materials (NIST 610, BHVO2G, MASS) were analyzed and the internal reference used was Fe. On the mass spectrometer, each isotope was analyzed for 10 ms per cycle. Before each map was produced, the mass spectrometer was tuned while ablating reference material NIST 612 to optimize the signal output of the detector while minimizing oxide formation (<0.3%).

3.5 Geology of the Photo Lake Deposit Area

3.5.1 Stratigraphy

The Photo Lake deposit is hosted by the Photo rhyolite (informal unit of Bailes and Galley 2007), which is conformably overlain by the Balloch basalt and Threehouse unit (Bailes and Galley 2007; Stewart et al., 2018). The Photo rhyolite was interpreted as a coherent felsic unit with no internal subdivisions (Bailes, 1996, 1997; Bailes and Galley, 2007); however, detailed field mapping, petrography, and geochemistry indicate that the Photo rhyolite consists of two distinct felsic units that are referred to as Photo rhyolite 1 (PR1) and 2 (PR2) herein (Table 5). The distribution of PR1 and PR2 is shown in Figures 4 and 5 and the differences between these units are summarized in Table 5.

Photo rhyolite 1 consists dominantly of a massive coherent facies (Fig. 6A) that transitions into a lobe facies with monolithic in situ and clast-supported breccias developed towards the upper contact (Fig. 6B, C). The lobes are typically less than a metre in diameter. Flow banding defined by biotite-amphibole-rich layers alternating with quartz-feldspar-rich layers occurs towards the top of the unit (Fig. 6D). Quartz- and calcite-filled amygdules (1-3%) occur throughout the unit, but are concentrated towards the top.

Photo rhyolite 2 consists of massive coherent and lobe facies (Fig. 7A, B). Lobes occur internally to the unit, where they are up to several metres in diameter, as well as at the margins of the unit, where they are typically less than a metre in diameter. At the upper contact with the overlying Threehouse unit, the flow lobes are brecciated along their margins (Fig. 7B, C) and are in contact with highly altered zones approximately 5-30 cm thick that consist of chlorite + calcic amphibole ± garnet. Amygdules (1-3%) occur along the margins of the internal flow lobes and are typically filled with quartz and lesser calcite. Large gas cavities up to 2 cm in diameter (Fig. 7D) and incipient columnar jointing occur locally.

The contact between PR1 and PR2 is not exposed, but outcrop exposures within a few centimetres on either side of the contact suggest that it is sharp. In these exposures, PR1 typically grades from a massive coherent facies to a lobe facies towards the contact, with well-developed flow banding increasing towards the top of PR1. Overprinting alteration, deformation, and metamorphism have destroyed any microscopic primary textures that may have been present in the felsic volcanic rocks, and the rocks exhibit, to a variable extent, textures indicative of deformation and metamorphism, including subgrain boundaries, undulatory extinction, and

granoblastic polygonal textures. Key mineralogical textural and compositional attributes that distinguish PR1 and PR2 are summarized in Table 5 and in Figures 6E, 6F, 7E, and 7F.

3.5.2 Photo rhyolite geochemistry

Geochemical classification of Snow Lake felsic volcanic rocks is challenging due to their anomalous low HFSE and REE concentrations, which result in samples plotting as andesites and basaltic andesites on the Nb/Y vs. Zr/Ti classification diagram of Pearce (1996). Furthermore, due to major element mobility during alteration and metamorphism, the felsic rocks cannot be reliably classified on major element classification diagrams (e.g. SiO_2 versus $Na_2O + K_2O$ diagram of Le Maitre et al., 1989). For this reason, historically used terms such as 'rhyolite,' 'rhyodacite,' and 'dacite' are only retained where they refer to existing informal stratigraphic units, and otherwise the term felsic is used herein.

Hydrothermal alteration and overprinting peak middle almandine-amphibolite facies metamorphism have affected all the felsic volcanic rocks to variable degrees. To assess the primary geochemical characteristics of the Photo rhyolite, altered samples with the following geochemical criteria were rejected: loss on ignition (LOI) > 4.5 wt.%, Na_2O < 1 wt.%, Al_2O_3/Na_2O > 10 (Spitz and Darling, 1978), and chlorite-carbonate-pyrite index (CCPI) > 85, and Ishikawa Alteration Index (AI) > 65.

Element mobility was evaluated using X-Y binary diagrams. Zirconium was determined to be the best immobile element monitor (MacLean, 1990; Barrett and MacLean, 1994), and other trace

elements such as Nb, Hf, and Th and the REE exhibited the least amount of scatter relative to Zr, with correlation coefficients of 0.74, 1.0, 0.97 and 0.50 – 0.91, respectively.

Using least altered samples, plots of TiO_2 (Fig. 8A), Al_2O_3 (Fig. 8B), TiO_2 (Fig. 8C), $Fe_2O_{3(total)}$ (Fig. 8D), P_2O_5 , Co, Sc and V versus Zr define two geochemical clusters that separate PR1 from PR2. Of the major oxides, ratios of Al_2O_3 to Zr have the least amount of scatter, with correlation coefficients of 0.78, whereas TiO_2, Fe_2O_3, P_2O_5 and SiO_2 exhibit scatter indicating some element mobility.

Photo rhyolite 1 and PR2 have tholeiitic affinities (Fig. 8E) and trace element contents characteristic of volcanic arc rocks (Fig. 8F). Photo rhyolite 1 and PR2 fall within the FII rhyolite field of the Hart et al. (2004) rhyolite classification diagram (Fig. 8G) and plot dominantly within the andesite/basaltic andesite field on the Zr/Ti versus Nb/Y discrimination diagram of Pearce (1996; Fig. 8H). Both felsic units exhibit similar primitive mantle-normalized patterns characterized by LREE enrichment (La/Sm_{PM} = 1.9-2.8; Table 3; Fig. 9A) and strong negative Nb (Nb/Th_{PM} = 0.21-0.32) and Ti anomalies (Fig. 9A, B). Element ratios that effectively discriminate the two Photo rhyolite units are summarized in Table 5, which also contains a summary of the important geochemical characteristics of the two felsic units. Whole rock geochemical data for both felsic units are summarized in Table 3.

3.5.3 Threehouse Unit and Balloch Basalt

The Threehouse unit consists of mafic volcaniclastic and coherent rocks (Bailes et al., 1994, 1996, 1997; Bailes and Galley, 2007; Gibson et al., 2014). Volcaniclastic deposits are the

fragmental products of explosive or effusive volcanism that are either deposited directly from volcanic eruptions or have been redeposited from non-lithified volcanic deposits (Fisher, 1966; Gibson et al., 1999; White and Houghton, 2006). In this study, volcaniclastic rocks are classified using granulometric terms proposed by Fisher (1961, 1966) and White and Houghton (2006); however, the terms are used in a non-genetic sense. The Threehouse unit conformably overlies the Photo rhyolite east of the deposit (Fig. 4), and is best exposed in a rock quarry ('Photo quarry'), where it occupies an F_1 fold ('Photo syncline'; Figs. 4, 5). It also occurs south of the Photo Lake area in a large elliptical structure called the Chisel basin (Fig. 2; Bailes et al., 1996). The field characteristics of the Threehouse unit indicate that it is the product of explosive pyroclastic and effusive eruptions (Bailes and Galley, 2007; Gibson et al., 2014) and are described below.

In the Photo quarry, massive and pillowed basalt flows of the Balloch basalt conformably overlie PR1 and pinch out to the south. The flows contain phenocrysts of plagioclase (up to 20%) and amphibole after pyroxene (up to 8%) and have well-developed flow top breccias, with the uppermost flow top marked by 3-5 cm of hyaloclastite. These basalt flows are conformably overlain by poorly sorted to weakly bedded heterolithic mafic lapilli tuff to tuff breccia. Where basalt flows are missing, PR1 and PR2 are overlain by approximately 5 to 10 m of mafic tuff interbedded with normal-graded, well-bedded heterolithic mafic lapilli tuff to tuff breccia. The remainder of the Threehouse unit consists of the same poorly sorted to weakly bedded heterolithic mafic lapilli tuff to tuff breccia. The upper contact of the Threehouse unit is not observed, and the mafic volcaniclastic and coherent rocks are the least altered rocks in the map area.

In the Chisel basin (Fig. 2) and east of the Photo rhyolite (Fig. 4), the Threehouse unit consists predominantly of bedded tuffs that exhibit features indicative of variations in water depth from shallow water to below storm wave base (i.e., >200 m; Bailes and Galley, 2007; Gibson et al., 2014). Shallow-water features include scour channels, convolute bedding, hummocky and trough cross-bedding, pebble lags, and volcanic bombs (Bailes and Galley, 2007; Gibson et al., 2014). Symmetrical ripple marks with mud drapes indicate that the unit was locally deposited in a tidal environment and accretionary lapilli may indicate that this environment was locally subaerial or that the eruption column breached the surface of the water (Gibson et al., 2014). These shallow-water features alternate with thin-bedded to laminated and medium- to thick-bedded or massive tuffs and crystal tuffs indicative of deeper water, below storm wave base conditions (Gibson et al., 2014).

3.5.4 Structure

The Photo Lake VMS deposit was interpreted to occur within a single massive felsic unit (Bailes, 1996, 1997). However, detailed mapping, re-logging, and geochemistry indicate that the Photo deposit occurs at the contact between PR1 and PR2, and that this contact defines isoclinal folds (Fig. 10). Thus, the Photo Lake sulfide lenses occur along the limbs of a parasitic synclinal isoclinal fold, where PR2 occupies the core of this syncline (Fig. 10). The axial plane of this fold trends approximately northwest and dips to the east-northeast.

At surface, the projected axial trace of the Photo Lake deposit fold extends to the north where it defines the axial plane to the Photo syncline (Figs. 4, 5). The axial plane of this fold strikes northwest and dips to the east-northeast and the axis plunges moderately (56°) to the northeast.

An axial planar cleavage was not identified (Fig. 5). This fold represents the earliest deformation event identified in the Photo Lake area and is an F_1 fold (Stewart et al., 2018). This fold is overprinted by a strong S_2 spaced cleavage defined by biotite and amphibole (Figs. 6A, 7A) and by flattened clasts. The spaced cleavage is much better developed in PR1 than in PR2 due to the higher abundance of biotite and amphibole in the more altered PR1 rocks. A weak S_3 cleavage is defined by biotite, and a composite L_2/L_3 lineation is defined by the elongation of clasts, amphiboles, and plagioclase phenocrysts. At the map scale the F_1 Photo syncline is refolded by an F_3 fold (Fig. 4; Stewart et al., 2018). Parasitic open F_3 folds are observed at the outcrop scale and fold lithological contacts and the S_2 cleavage.

A north-south-trending fault truncates the host rocks to the Photo Lake deposit west of the surface projection of the deposit (Fig. 2). This fault was initially interpreted as a late brittle fault (Bailes and Schledewitz, 1999); however, later mapping determined that it merges with the early Snow Lake thrust fault to the north (Bailes et al., 2011; Gagné, 2011). At depth, this fault brings stratigraphically older Photo rhyolite over younger Balloch basalt (Bailes, 2014), which is consistent with the fault being a thrust. The fault was identified in drill core during the current study and is characterized by an approximately 30-50 m-thick section of foliated heterolithic mafic and felsic lapilli tuff to tuff breccia. This is an S_2 foliation and is defined by biotite and flattened clasts. The fault cuts the east-west trending volcanic succession to its west (Fig. 2). This succession is interpreted to have been isoclinally folded during D_1 (Stewart et al., 2018), suggesting that the fault is late D_1 or early D_2. The fault truncates the Photo rhyolite at depth (Bailes, 1996; Bailes and Schledewitz, 1999; Gagné, 2011), and the nature of the lower contact of the Photo rhyolite is therefore unknown.

3.6 The Photo Lake Deposit

The Photo Lake deposit consists of two economic ore lenses that are subparallel and elongated, with a strike and dip of approximately 270°/60° (Tessier, 1996). The lenses are elongated along the prominent regional L_2 stretching lineation, with the #1 lens having a trend and plunge of 44°→ 049° and the #2 lens having a trend and plunge of 41° → 050° (Fig. 10; Tessier, 1996). Down-plunge of the ore lenses, the alteration zone below the #2 lens merges with the alteration zone surrounding the #1 lens, coincident with a third massive sulfide lens that was uneconomic (Heine and Prouse, 1998). The Cu-rich #1 lens subcropped and contained 336,063 tonnes of ore at 5.71% Cu, 2.95% Zn, 5.14 g/t Au, and 29.66 g/t Ag (Tessier, 1996). The Zn-rich #2 lens contained 157,694 tonnes of ore at 4.06% Cu, 10.98% Zn, 4.73 g/t Au, and 48.65 g/t Ag (Tessier, 1996).

3.6.1 Sulfide assemblages

The dominant sulfide minerals are, in decreasing order of abundance, pyrite, sphalerite, chalcopyrite, pyrrhotite, galena, and arsenopyrite, with a higher modal abundance of chalcopyrite and pyrrhotite in the Cu-rich #1 lens and a higher modal abundance of sphalerite in the Zn-rich #2 lens. Arsenopyrite is only identified in the #2 lens and magnetite is only identified in the #1 lens. Galena is dominantly found in the #2 lens, but it also occurs as inclusions in magnetite in the #1 lens.

The #2 lens consists of massive sulfides with sparse intervals of host rock. Intervals of disseminated and fine stringer mineralization also extend for up to 10s of metres into the

footwall rocks and down plunge of the sulfide lens. The massive sulfide lens is dominated by sphalerite, but pyrite and chalcopyrite are dominant within the discontinuous zones along the periphery of the lens. Locally, sphalerite is cut by veinlets of chalcopyrite and pyrite or has a banded texture with pyrite and/or chalcopyrite (Fig. 11A). Chalcopyrite disease (Barton and Bethke, 1987) in sphalerite is common. Massive sphalerite is typically coarsely recrystallized with crystals up to 1 cm in size (Fig. 11B). Anhedral massive chalcopyrite, sphalerite, and pyrrhotite are observed surrounding brittle-deformed, corroded, and annealed pyrite (Fig. 11C, D). Galena occurs in veins that crosscut other minerals, as inclusions, and along mineral grain boundaries (Fig. 11E, F). Flow-textured galena, characterized by the absence of triangular pits that are typically observed in unstrained grains (Taylor et al., 2010), surrounds annealed pyrite (Fig. 11E). Galena is often Se-bearing, and in some areas clausthalite is observed (PbSe; solid solution with galena). Gudmundite (FeSbS), and cassiterite (SnO_2) occur as euhedral to subhedral crystals or in crosscutting veins, inclusions, and along mineral grain boundaries (Fig. 11G, H). Along mineral grain boundaries, an unidentified Ag-Se mineral phase forms framboid-like shapes that consist of individual euhedral crystals (Fig. 11I). Arsenopyrite occurs as subhedral to euhedral individual crystals (Fig. 11J) that can contain inclusions of recrystallized pyrite (Fig. 11K).

The #1 lens is dominated by chalcopyrite but contains a significant amount of pyrrhotite and pyrite. The sulfides are much less continuous than those of the #2 lens and are typical of a VMS footwall stringer zone. Altered host rock alternates with sulfide intervals, and intervals of disseminated and fine stringer mineralization extend for up to 10s of metres into the footwall and hanging wall. Pyrrhotite and pyrite occur as veinlets and pods within chalcopyrite (Fig. 11L) and

pyrite also occurs as coarsely recrystallized individual crystals up to 2.5 cm in size. Magnetite occurs as euhedral to subhedral individual crystals and less commonly in small crystal clusters (Fig. 11M) and as rims on carbonate minerals, often where the carbonate minerals are in contact with pyrrhotite. Fractures within magnetite contain chalcopyrite, sphalerite, and pyrrhotite. Where present, hematite is closely associated with magnetite and forms acicular polycrystalline aggregates cut by chlorite or amphibole and rimmed by magnetite (Fig. 11N). The hematite aggregates appear to have replaced an earlier mineral phase with a cubic crystal habit (e.g., pyrite). Mercurian electrum (Au-Ag-Hg alloy) occurs in both sulfide lenses (Fig. 11I, O).

3.6.2 Pyrite

Pyrite in the Photo lake deposit is unique relative to other sulfide minerals because it displays four distinct textural varieties identified through petrographic and SEM analysis: (1) concentric (Py1); (2) spongy (Py2); (3) pitted (Py3); and (4) crystalline (Py4; Fig. 12). Concentric pyrite (Py1) occurs as rounded to elliptical spheroids, where alternating bands of fine pitted pyrite and an iron-oxide-sulfide phase define a concentric structure (Fig. 12A, B). Pyrite is the dominant phase within the core of concentric pyrite and the concentration of the iron-oxide-sulfide phase increases towards the rim (Fig. 3, 12A, B; Table 2). At the microscopic scale, blades of pyrite are oriented perpendicular to the concentric surfaces (Fig. 12C). Concentric pyrite (Py1) is typically spatially associated with pyrrhotite and is more abundant in the #2 lens than in the #1 lens. Spongy pyrite (Py2) occurs as anhedral individual grains that are heavily pitted and often contain inclusions of hematite (Fig. 12D-F). Pitted pyrite (Py3) occurs as individual euhedral to subhedral grains (Fig. 12G) or as annealed masses (Fig. 11D). Crystalline pyrite (Py4) is typically inclusion-free and dominantly occurs as rims on pitted euhedral to subhedral pyrite

grains (Fig. 12H), as individual euhedral grains (Fig. 12I), as zones within annealed pyrite masses, or as annealed subhedral grains with 120° dihedral grain boundaries (Fig 12J). Crystalline pyrite also forms a skeletal or pseudo-skeletal texture with sphalerite and chalcopyrite (Fig. 12K).

Concentric pyrite is crosscut by the other three textural varieties of pyrite (Fig. 12L). Spongy pyrite is found in close spatial association with concentric pyrite (Fig. 12E, F), and there are often inclusions of an iron oxide phase in spongy pyrite with a similar chemistry to the oxidized bands of concentric pyrite. Pitted pyrite crosscuts spongy pyrite (Fig. 12E). Crystalline pyrite occurs as rims on pitted pyrite and crosscuts all three of the other textural varieties (Fig. 12H, L).

3.6.3 LA-ICP-MS of pyrite

Element maps produced by LA-ICP-MS for the different textural varieties of pyrite define compositional differences that may trace the primary chemical evolution of the Photo Lake deposit during its formation and subsequent deformation (Figs. 13, 14, 15). Pyrite was selected for this purpose because of its refractory nature (Craig and Vokes, 1993, 1998).

Concentric pyrite (Fig. 13) has a rim that is compositionally distinct from the core. The rim is enriched in Cu and Mo relative to the core, whereas the core is enriched in Co and Ni relative to the rim. Selenium is slightly enriched in areas of the rim, but this distribution is not uniform. Arsenic and Bi are enriched in fracture-controlled inclusions cutting the pyrite grain. Gold is hosted in inclusions that are concentrated in the rim of the pyrite grain and are located in fractures that cut the interior of the grain.

Spongy pyrite (Fig. 14) exhibits a more uniform trace element distribution. Nickel and Se are relatively evenly distributed throughout the grain, and there is no appreciable amount of As, Au, Co, or Cu. Bismuth and Mo are hosted in inclusions and along fractures cutting the spongy pyrite grain.

The trace element distribution in pitted pyrite (Fig. 14, 15) is controlled by inclusions hosted in the pits. Arsenic, Au, Bi, and Cu are all concentrated within inclusions in the pyrite grain. There are no appreciable amounts of Co, Mo, or Ni. Selenium has a relatively even distribution throughout the grain.

Crystalline pyrite (Figs. 14, 15) exhibits a relatively even distribution of As and Co. Bismuth and Ni are inclusion controlled and share a spatial relationship. There are no appreciable amounts of any other elements in crystalline pyrite.

Element maps produced by LA-ICP-MS also display distinct chemical differences between the textural varieties of pyrite. The concentric and spongy pyrite textural varieties are both enriched in Se relative to crystalline pyrite. The trace element composition of pitted pyrite is variable relative to concentric and spongy pyrite, with both enrichments and depletions of Se. Concentric and pitted pyrite both contain Au as inclusions and up to several weight percent Cu, which exhibits a spatial relationship with Au and Mo. Crystalline pyrite is depleted in all trace elements relative to concentric, spongy, and pitted pyrite except for Co and As.

3.6.4 Gold occurrence and distribution

Gold in the Photo Lake deposit occurs as mercurian electrum. The electrum fineness (fineness = 1000 x Au/Au+Ag; Au and Ag measured as concentrations in electrum) ranges from 470 to 730 in the #1 lens and from 100 to 580 in the #2 lens. When a gold-silver alloy has a fineness less than 200, it is referred to as silver rather than electrum (Morrison et al., 1991). Trace element concentrations within electrum differ between the ore lenses. In the #1 lens, electrum contains small amounts of Nb and Te, whereas electrum in the #2 lens contains small amounts of Bi, Nb, Sb, and Se.

Electrum occurs as inclusions in pyrite and magnetite, along pyrite and arsenopyrite grain boundaries, and crosscutting pyrite, arsenopyrite, and magnetite (Fig. 16). Larger electrum grains (>100 μm) occur interstitially to pyrite grains (Fig. 16A, B). Electrum also has a close spatial relationship with chalcopyrite. Cassiterite, galena – clausthalite, and gudmundite are restricted to #2 lens where they are associated with electrum (Fig. 16C) and occur crosscutting other minerals, as inclusions, and along mineral grain boundaries. In the #1 lens electrum is mostly closely associated with magnetite (Figs. 11M, 16D).

3.6.5 Base and precious metal zonation

Metal zoning cross-sections through the Photo Lake deposit indicate a strong positive correlation between Cu and Au (Fig. 17). Gold is concentrated in some areas with high Zn grades (5 to >10 wt. %), but these areas are usually associated with high Cu grades (4 to >8 wt. %). There is a clear spatial separation between Cu and Zn, and Zn is concentrated towards the centre and top of the #2 lens (Fig. 17A). These metal zoning patterns are consistent with primary zonation in VMS

deposits that formed due to zone refining processes (e.g., Eldridge et al., 1983; Lydon, 1984, 1988; Large, 1992; Ohmoto, 1996; Franklin et al., 2005) and support the interpretation that the #2 lens is upright and the #1 lens is overturned (Fig. 10).

3.6.6 Sulfide geochemistry

Whole rock geochemical data for the sulfide lenses and calculated correlation coefficients for selected elements reveal two distinct metal groups based on positive correlation coefficients: 1) Au, Cu, Se, Bi, Te, and Fe; and 2) Hg, Mo, Ni, Sb, and Zn. Silver exhibits a good positive correlation with Au, but its relationship with the other metals of group 1 is unclear. Group 1 metals exhibit a negative correlation with some of the group 2 metals and no correlation with others (Table 6). There is a relative enrichment of group 1 metals in the #1 lens and of group 2 metals in the #2 lens. The #1 lens is also enriched in Ba and CO_2 relative to the #2 lens, and the #2 lens is enriched in Ag, As, Cd, Co, Ga, Tl, and S relative to the #1 lens. These chemical variations, particularly the enrichments in Cu and Au in the #1 lens and in Zn and Pb in the #2 lens, are consistent with the mineralogical differences between the two lenses. Whole rock analysis of the sulfides does not indicate a strong correlation between Sn and either the group 1 or group 2 metals.

3.6.7 Alteration

Alteration associated with the Photo Lake deposit is characterized by the mineral assemblages chlorite + biotite + garnet ± staurolite ± actinolite and sericite + quartz ± magnetite ± kyanite. The alteration is broadly discordant to strata and occurs predominately in PR1, where it surrounds most of the #1 lens and is below the #2 lens (Fig. 10). Locally, the alteration extends

into the felsic (PR2) stratigraphic hanging wall of both lenses (Fig. 10). This distribution is consistent with the synclinal fold interpretation, where the #1 lens is overturned and the #2 lens is upright (Fig. 10).

Chlorite and biotite are the dominant minerals in the alteration zone and occur proximal to the ore lenses as well as down-plunge of the lenses. Sericite is less pervasive and localized proximal to the sulfide lenses. Chlorite is more pervasive proximal to the #1 lens and sericite and biotite are more pervasive proximal to the #2 lens. The primary alteration assemblage has been overprinted by peak, middle almandine-amphibolite facies (~5-6 kbar, 550-600°C) metamorphism (Menard and Gordon, 1997; Caté, 2016). Therefore, the biotite observed in the alteration zone is likely the metamorphic product of chlorite, and much of the chlorite now present may be retrograde, formed through replacement of biotite. Staurolite and garnet porphyroblasts occur throughout the alteration zone. Garnet ranges from trace amounts up to 50 modal percent of the rock and has a composition of almandine-spessartine with up to several weight percent Ca. Staurolite is less common and occurs locally in the immediate vicinity of the ore lenses.

Least altered and altered samples display a clear trend towards chlorite on an alteration box plot (Fig. 18A), as is expected for typical proximal VMS-style alteration (e.g., Riverin and Hodgson, 1980; Large et al., 2001; Franklin et al., 2005; Galley et al., 2007a). On a plot of the Ishikawa alteration index (AI) versus the advanced argillic alteration index (AAAI), the altered samples display a trend towards muscovite and show no indication of the pyrophyllite trend typical of advanced argillic alteration (Fig. 18B).

3.7 Discussion

3.7.1 Deformation and stratigraphic reconstruction of the Photo Lake deposit

The Photo Lake deposit is strongly tectonized and has been affected by several deformation events. The map-scale fold pattern indicates that the F_1 syncline in the Photo Lake deposit can be correlated with the Photo syncline in the Photo quarry (Fig. 4). This stratigraphic and structural interpretation places the Photo Lake deposit at the contact between the PR1 and PR2 felsic units, which conformably underlie the Threehouse mafic unit and Balloch basalt. The Threehouse unit is an excellent marker of the upper boundary of the productive Chisel sequence ore interval because it is geochemically and visually distinct, laterally extensive throughout the Chisel basin, and occurs in the immediate hanging wall to many of the Chisel sequence VMS deposits (Bailes and Galley, 2007). This reconstruction indicates that the Photo Lake deposit and its host rocks formed within the same time-stratigraphic interval as the other VMS deposits in the Chisel sequence and not at a younger stratigraphic interval as was previously interpreted (Bailes, 1996, 1997).

3.7.2 Tectonic setting and volcanic reconstruction

The two Photo rhyolite units exhibit the same primitive mantle-normalized trace element patterns characterized by negative Nb and Ti anomalies (Fig. 9B), consistent with an arc setting (e.g., Pearce and Peate, 1995). The felsic rocks define two distinct geochemical trends on immobile incompatible vs. compatible element diagrams (Fig. 8A-D), but share identical primitive mantle-normalized REE profiles (Fig. 9A). Variations in Fe, Mg, and Ca are consistent with fractionation of plagioclase and amphibole from the same parental magma, and this is supported by the mineralogical differences observed between the two felsic units. These geochemical

characteristics suggest that PR1 and PR2 were produced through fractionation of the same parental magma. Photo rhyolite 2 is slightly enriched in incompatible elements relative to PR1 (e.g. Zr, Th, Y, Yb, Hf), which is consistent with the stratigraphic relationship identified through mapping.

Previous workers interpreted differences in ε_{Nd} values for mafic (ε_{Nd} = -0.4 to +3.2) and felsic (+3.3, +3.7) volcanic rocks to indicate the felsic and mafic rocks were derived from separate sources and are not related through fractionation (Stern et al., 1992, 1995; Bailes and Galley, 1996, 1999). They proposed that the felsic volcanic rocks were derived through partial melting of a hydrated, mafic crustal source during rifting and mafic volcanism. This interpretation, and the association with VMS deposits, is consistent with a rifted arc setting for the Chisel Sequence as proposed by Bailes and Galley (1999). The large variation in ε_{Nd} values, negative ε_{Nd} values reported for the mafic volcanic rocks, and presence of 2.82-2.65 Ga xenocrystic zircons in the 1.892 ± 3 Ma Stroud Lake felsic breccia at the base of the Chisel sequence (David et al., 1996) are interpreted to be the result of variable contamination by older Archean crust (Stern et al., 1992). The Photo Lake VMS deposit formed within a proximal felsic volcanic centre defined by PR1 and PR2, which are collectively referred to as the Photo Rhyolite complex herein. Photo rhyolite 1 and PR2 were erupted on the seafloor as lobe hyaloclastite flows as evidenced by flow interiors characterized by massive rhyolite, large lobes with amygdules along their margins but lacking hyaloclastite, and flow margins marked by the development of smaller lobes with altered hyaloclastite and monolithic felsic breccia (e.g., Gibson et al., 1999).

The Photo Lake deposit formed within the Photo Rhyolite complex during the interval between eruption of PR1 and PR2. This interval, or hiatus in volcanism, is not represented by volcaniclastic or sedimentary rocks. However, the more pronounced alteration of PR1 relative to PR2 indicates that the hydrothermal system was at its peak during and immediately following the eruption of PR1 and in its waning stages during the eruption of PR2. An unknown amount of time separated these felsic eruptions. Mafic volcanic flows and volcaniclastic rocks of the Threehouse unit conformably overlie PR2 and, where the latter is absent, directly overlie PR1 (Fig. 5). The lack of VMS-related alteration within the Threehouse unit indicates that VMS hydrothermal activity had ended prior to mafic volcanism. The combined results from field mapping, drill hole logging, and structural analysis to determine the present distribution of the host rocks and alteration zone and unravel the pre-deformation geometry of the deposit are summarized in a deposit reconstruction in Figure 19.

3.7.3 Paragenesis of sulfide minerals

In order to establish the timing of Au mineralization it is critical to determine the paragenetic sequence of the sulfide and oxide minerals in the two ore lenses. Determination of the primary paragenetic sequence is complicated by remobilization and replacement of sulfide and oxide minerals during zone refining of the sulfide lenses and by subsequent remobilization of sulfide and oxide minerals during deformation and peak, middle almandine-amphibolite facies metamorphism. Textures indicative of sulfide remobilization include flow-textured galena and anhedral chalcopyrite and sphalerite surrounding recrystallized and brittle-deformed pyrite (Fig. 11D, E) and chalcopyrite, sphalerite, and pyrrhotite filling fractures in metamorphic magnetite. Pyrite has accommodated deformation and metamorphism through brittle deformation, as

indicated by heavily fractured grains, and recrystallization, as indicated by annealed grain boundaries (Fig. 11D, E; Fig. 12J). Although some primary textures may be preserved, it is virtually impossible to determine the complete paragenesis of these sulfide phases prior to metamorphism and deformation. However, the syn- to post-metamorphic paragenesis can be determined and is important for understanding how Au was remobilized during metamorphism and deformation.

The primary paragenetic sequence for the two ore lenses is summarized in Figure 20 and assumes that the primary sequence of mineral deposition approximates that of a typical VMS deposit during its thermal evolution and zone refining (Eldrige et al., 1983; Lydon, 1984, 1988). Pyrite, sphalerite, chalcopyrite, pyrrhotite, and galena are common primary minerals in VMS deposits and these minerals are all assumed to have formed during the Photo Lake VMS-forming hydrothermal event. In VMS deposits, sphalerite and galena typically precipitate from lower temperature hydrothermal fluids and are replaced by chalcopyrite and pyrrhotite during higher temperature zone refining (Eldridge et al., 1983; Lydon, 1984, 1988). Features such as massive sphalerite cut by veinlets of chalcopyrite, and chalcopyrite cut by veinlets of pyrrhotite are consistent with primary zone refining but could also be the result of mechanical or fluid-assisted remobilization of chalcopyrite during deformation (e.g., Tomkins, 2007). Chalcopyrite disease observed in sphalerite suggests that chalcopyrite formation followed sphalerite precipitation (Barton and Bethke, 1987). The timing of galena-clausthalite is less certain; however, its occurrence in interstitial spaces between subhedral to euhedral pyrite crystals, as small inclusions in large recrystallized masses of pyrite, or as inclusions with sphalerite in individual pyrite crystals suggests that it was precipitated during the VMS-forming hydrothermal event – possibly

with sphalerite – and was later remobilized. Arsenopyrite, cassiterite, and gudmundite crosscut all other mineral phases and often occur as subhedral to euhedral individual crystals, indicating that these minerals formed late in the sulfide paragenesis and may be the products of metamorphism. Arsenopyrite also contains inclusions of recrystallized pyrite (Fig. 11K), further supporting a metamorphic origin. Where magnetite is observed as subhedral to euhedral individual crystals it cuts all other mineral phases, and where it forms rims on carbonate minerals and hematite aggregates the rims appear to be reaction rims. Both of these relationships indicate that magnetite is a late mineral phase. The hematite aggregates replace an earlier mineral phase with a cubic crystal habit such as pyrite, and the occurrence of pyrite within hematite supports that timing relationship.

3.7.4 Primary versus metamorphic pyrite

Textural and compositional variations in pyrite are extremely useful in recording the geochemical evolution of metamorphosed VMS deposits. Due to its high thermal stability and physical strength pyrite is highly refractory and stable well into amphibolite grades of metamorphism (Craig and Vokes, 1993, 1998). It is therefore possible for primary pyrite textures to be preserved at the metamorphic conditions of the Photo Lake deposit. For example, Parr (1994) documented primary pyrite textures, including colloform banding, preserved at granulite facies metamorphic conditions. The timing of the four textural varieties of pyrite are considered below.

A texture similar to concentric pyrite has been documented at Benson Mines (de la Cruz, 1968; Hagni et al., 1969) and in the Adirondack pyrrhotite-pyrite deposits (O'Leary, 1967). In these

deposits, the concentric texture is interpreted as a reaction rim between pyrrhotite and pre-existing pyrite, and a remnant pyrite core is observed. Iron-oxide phases are also distributed in radial elongate patches (de la Cruz, 1968), as is observed in the concentric pyrite at Photo Lake. In the Photo Lake deposit, concentric pyrite is typically spatially related to or surrounded by pyrrhotite (Figs. 12A, B, E, F). The cores of concentric pyrite are stoichiometric (Table 2), supporting its formation by reaction of pre-existing pyrite with later pyrrhotite. Concentric pyrite is surrounded by a rim that becomes increasingly oxidized moving outwards (Table 2) and is typically spatially associated with carbonate, which is consistent with reaction in an oxidizing environment, as is inferred for the Benson Mines and Adirondack pyrrhotite-pyrite deposits (O'Leary, 1967; de la Cruz, 1968; Hagni et al., 1969). Concentric pyrite is therefore either a primary texture that formed during deposit development, or it is a metamorphic texture. If it is metamorphic, concentric pyrite is likely an early prograde feature, as metamorphic pyrrhotite development has been documented to form during prograde metamorphism due to increased sulfur activity (Craig and Vokes, 1993). Furthermore, concentric pyrite is cut by recrystallized metamorphic pyrite (Fig. 12L), suggesting that it formed prior to peak metamorphism. Regardless of the timing of development of the reaction rim, the pyrite at the core of the concentric structure must be primary. Spongy pyrite is often cross cut by prograde pyrrhotite, suggesting that it was present prior to metamorphism or it formed during the early stages of metamorphism. Compositional variations within individual grains and the anhedral nature of spongy pyrite are atypical of metamorphic pyrite, which is usually euhedral and chemically homogenous (Craig and Vokes, 1993, 1998; Huston et al., 1995). Pitted pyrite also exhibits chemical variations and trace element concentrations inconsistent with metamorphic pyrite,

which may suggest that it has a primary origin; however, the annealed nature suggests that it was recrystallized during metamorphism and deformation.

Crystalline pyrite is interpreted to be a product of metamorphic recrystallization because it is often euhedral, forms as overgrowths on early pyrite, is typically inclusion-free and exhibits minimal chemical zonation. Metamorphic recrystallization has been found to remove inclusions and nonstoichiometric lattice substitutions from pyrite (Huston et al., 1995). Crystalline pyrite is enriched in Co and Ni, both of which occur as stoichiometric substitutions for Fe and are not readily removed through metamorphic recrystallization (Huston et al., 1995). It is also enriched in As, which has been shown to occur as a lattice substitution for S (Cook and Chryssoulis, 1990; Huston et al., 1995). Furthermore, the skeletal or pseudo-skeletal texture of crystalline pyrite associated with sphalerite and chalcopyrite (Fig. 12K) has been interpreted at the Archean Kidd Creek and Lemoine deposits to have formed by metamorphic recrystallization of pyrite around early, porous pyrite followed by selective replacement of the early pyrite during metamorphism (Hannington et al., 1999a; Mercier-Langevin et al., 2014b).

3.7.5 Timing of gold mineralization

The source and timing of gold enrichment in VMS deposits is debated. Recent research on ancient and active VMS systems has shown that syngenetic gold emplacement is common (e.g., 1806 zone of the Ming Mine: Brueckner et al., 2014; Pilote et al., 2017; Horne: Kerr and Gibson, 1993; Eskay Creek: Roth et al., 1999; LaRonde Penna and Bousquet 2-Dumagami: Dubé et al., 2007, 2014; Westwood: Yergeau et al., 2015; Brothers Volcano: de Ronde et al., 2011; Axial Seamount and southern Explorer Ridge: Hannington et al., 1986; TAG Hydrothermal Field:

Hannington et al., 1995) and results from various processes active at different scales and times in an ore-forming system (Hannington et al., 1999b; Huston, 2000; Monecke et al., 2014; Mercier-Langevin et al., 2015). This is further complicated for ancient VMS deposits that have undergone significant metamorphism and deformation because precious metals can be remobilized (e.g., Tomkins et al., 2004; Tomkins, 2007; Caté, 2016), often obscuring the primary mineral and elemental associations with gold and the sequence of mineralizing events. The gold in some VMS deposits is also interpreted to be epigenetic, resulting from either an orogenic (e.g., Mount Gibson, Western Australia: Yeats and Groves, 1998), or a magmatic or intrusion-related (e.g., Urals VMS deposits: Prokin and Buslaev, 1999) overprint.

At the Photo Lake deposit, the deposit architecture, gold distribution, alteration, and metal zoning indicate that gold is syngenetic and was introduced into the hydrothermal system during the VMS mineralizing event. The deposit reconstruction produced through combined field mapping, drill hole logging, and detailed structural analysis indicates that the deposit consists of a concordant zone of massive to semi-massive sulfides (#2 lens) underlain by a discordant footwall stringer zone (#1 lens; Fig. 19), which is consistent with typical VMS deposit architecture (Franklin et al., 2005). Intrusion-related deposits are spatially associated with an intrusion (e.g., Hart, 2007), and this is not the case for the Photo Lake deposit.

The alteration assemblages in the Photo Lake deposit are identical to those described for other Chisel sequence VMS deposits by Galley et al. (1993), Caté et al. (2014a, 2015), Mercier-Langevin et al. (2014a), Bailes et al. (2016), and Caté (2016), who interpreted them to be the metamorphosed equivalents of greenschist facies chlorite and sericite alteration assemblages

typical of many VMS alteration zones (Franklin et al., 2005). The distribution of alteration around the sulfide lenses at Photo Lake is similar to that of the Chisel and Chisel North deposits, where the sericite is localized proximal to the sulfide lenses and the chlorite and biotite zones form a broader halo below the zone of mineralization (Galley et al., 1993). There is no evidence for overprinting alteration at the Photo Lake deposit, and it does not display alteration suggestive of an orogenic (e.g., shear zone-hosted iron carbonate alteration: Dubé and Gosselin, 2007) or intrusion-related (e.g., vein selvages consisting of K-feldspar or carbonate replacement: Hart, 2007) overprint. Disseminated carbonate occurs within both ore lenses and is interpreted to be a late overprinting feature because early carbonate is not likely to have survived middle almandine-amphibolite facies metamorphism. However, this carbonate is not restricted to the deposit and is also observed in barren rocks at surface, suggesting that it represents a barren metasomatic event associated with metamorphism and is not associated with an Au overprint on the deposit. Where it is associated with Au in the Photo Lake deposit, it occurs along fractures and crosscutting porphyroblasts (Fig. 16D), suggesting that it is associated with remobilization of pre-existing Au. A similar style of metasomatism is documented in the Lalor deposit (Caté, 2016), where it is also interpreted to be associated with metamorphism and not an orogenic Au overprint.

Metal zoning within the sulfide lenses of the Photo Lake deposit (Fig. 17) and within pyrite grains (Figs. 13, 14, 15) indicates a strong positive chemical and spatial correlation between Au and Cu. Metal zoning is not observed in orogenic deposits (Goldfarb et al., 2005), but the Cu-Au association is common in Au-rich VMS deposits (Huston and Large, 1989; Hannington et al., 1999b) and indicates that Au is genetically associated with Cu. Given the paragenetic sequence

of sulfide mineralization (Fig. 20) and the typical VMS architecture and alteration of the Photo Lake deposit, Cu is interpreted to have been deposited during the VMS mineralizing event, implying that Au was also deposited during VMS formation.

At the deposit scale, Au is disseminated throughout the two ore lenses, as is expected for syngenetic Au, and is not hosted by cross-cutting veins, as would be expected for orogenic or intrusion-related Au deposits (e.g., Groves et al., 1998; Goldfarb et al., 2005; Dubé and Gosselin, 2007; Hart, 2007). Gold in late structural sites has been documented in the Photo Lake deposit and the nearby Lalor deposit; however, this Au is interpreted as having a syngenetic origin and was remobilized by late metasomatism associated with deformation (Menard and Gordon, 1995; Tinkham, 2013; Caté et al., 2014b, 2015; Duff et al., 2015; Duff, 2016; Caté, 2016). The Au fineness in the Photo Lake deposit (100 to 730) is also atypical of orogenic Au deposits, in which Au fineness averages 920 to 940 and falls within a narrower range than VMS deposits (Morrison et al., 1991; Goldfarb et al., 2005).

At a microscopic scale, Au is hosted in inclusions within pitted pyrite (Py3) that is rimmed by metamorphic crystalline pyrite (Py4; Figs. 14, 15) and within magnetite and arsenopyrite porphyroblasts, suggesting that Au was present prior to metamorphism. It also occurs as inclusions in concentric pyrite (Py1; Fig. 13), which is interpreted to have formed by reaction of primary hydrothermal pyrite with hydrothermal or metamorphic pyrrhotite. The pyrrhotite surrounding concentric pyrite contains very little to no Au (Fig. 13; Table 2), suggesting that the Au is associated with the primary pyrite and was not introduced later with the pyrrhotite. In spite of the syngenetic origin of Au, there is evidence that it has been remobilized during deformation

and metamorphism, as it crosscuts pyrite, arsenopyrite, and magnetite porphyroblasts and occurs interstitially to recrystallized pyrite grains (Fig. 16). Where Au surrounds recrystallized pyrite but is not associated with late fractures, it may have been liberated from the pyrite crystal structure during metamorphism (e.g., Wagner et al., 2007).

3.7.6 Gold enrichment processes

Syngenetic gold enrichment in VMS deposits is generally attributed to one or a combination of the following: (1) boiling of the hydrothermal fluids in the subseafloor (e.g., Butterfield et al., 1990; Herzig et al., 1993; Hannington et al., 1999b; Huston, 2000; Hannington et al. 2017); (2) a magmatic input to the hydrothermal system (e.g., Hannington et al., 1999b; Huston, 2000; de Ronde et al., 2011; Mercier-Langevin et al., 2007b); and (3) geodynamic and petrogenetic conditions favourable for Au enrichment (e.g., Huston, 2000; Mercier-Langevin et al., 2007b). In ancient VMS deposits, interpretations on the source of Au are speculative, because it is not possible to measure venting hydrothermal fluids and the primary mineral and chemical relationships in the sulfide lenses are overprinted by later deformation and metamorphism. Modern hydrothermal systems, where the active processes and primary relationships can be observed, must therefore be used as analogues for ancient systems.

The average Au grades of all the Chisel sequence VMS deposits are relatively high (Table 1), with all but the Chisel North deposit having an average Au grade above the 0.76 g/t arithmetic mean for VMS deposits (Mercier-Langevin et al., 2011). This may suggest that there is a district-scale source of Au enrichment in the Chisel sequence deposits, such as the geodynamic setting or a source-rock control (Caté, 2016); however, this does not account for the uniquely high Au

concentration in the Photo Lake deposit, which is more than double the average grade for the Chisel sequence deposits (4.87 g/t Au at Photo Lake versus 2.23 g/t average; Table 1). Therefore, a magmatic input and boiling are considered as potential sources of selective Au enrichment in the Photo Lake deposit. These processes are considered below.

3.7.6.1 Boiling

Boiling is an efficient mechanism for metal deposition in VMS and epithermal ore systems because it results in a decrease in the hydrothermal fluid temperature (Butterfield et al., 1990; Gibson et al., 1999; Hannington et al., 1999b), causing precipitation of highly temperature-dependent metals such as Cu and Au and separation of these metals from Zn, Pb, and Ag (Hannington et al., 1999b). Boiling hydrothermal fluids are documented at several modern vent sites (e.g., Butterfield et al., 1990; Charlou et al., 1996; Gallant and Von Damm, 2006; de Ronde et al., 2011).

The geometry and pronounced metal zoning of the Photo Lake deposit, where Cu and Au are largely restricted to the discordant stringer mineralization of the #1 lens and Zn is restricted to the seafloor massive sulfides of the #2 lens, suggests that the ore-forming fluids underwent boiling. The coherent, impermeable nature of the host rocks to the deposit would have limited the amount of seawater-hydrothermal fluid mixing in the subseafloor (e.g., Franklin et al., 2005), thus maintaining high fluid temperatures. The majority of the sulfide accumulation should therefore have been proximal to or at the seafloor, with minimal subseafloor precipitation; however, the Photo Lake deposit has a well-developed stringer zone, which constituted 68% of the total tonnage of the deposit (336,063 tonnes of ore in the #1 lens versus 157,694 tonnes of

ore in the #2 lens; Tessier, 1996). Therefore, an alternative mechanism to seawater-hydrothermal fluid mixing must have been responsible for sulfide precipitation in the subseafloor, and, given the extensive vertical stockwork beneath the Photo Lake deposit, this mechanism is most likely to have been boiling (e.g., Hannington et al., 1999b).

Enrichment in lower temperature elements, such as Ag, Hg, and Sb within the Zn-rich #2 lens is an expected consequence of boiling, as these elements are deposited at lower temperatures. Boiling and the associated fluid temperature decrease would provide an effective mechanism to separate these elements from the Au and Cu in the underlying stockwork, and to concentrate them above the boiling zone within the massive sulfide zone (Hannington et al., 1999b).

3.7.6.2 Magmatic input

Magmatic fluid contributions to VMS hydrothermal systems have been proposed by several authors in modern (e.g., Hedenquist and Lowenstern, 1994; Herzig et al., 1998; Moss et al., 2001; de Ronde et al., 2011) and ancient (e.g., Lydon, 1996; Sillitoe et al., 1996; Hannington et al., 1999b; Huston, 2000; Mercier-Langevin et al., 2007b) systems. In these systems, metal-rich fluids are exsolved from high-level magma chambers beneath a VMS deposit and incorporated into the ore-forming hydrothermal system. Evidence to support a magmatic input of Au in the Photo Lake deposit is outlined below.

(1) The strong correlation between Cu and Au and Se, Bi, and Te, which is well documented in high-temperature VMS deposits where the Au is interpreted to be a direct magmatic contribution (e.g., Tennant Creek: Huston et al., 1993; Lemoine deposit: Mercier-Langevin et al., 2014b; Westwood deposit: Yergeau et al., 2015).

(2) The Nb, Te, Bi, and Se content of electrum, and the spatial association between cassiterite (SnO_2) and Mo-bearing galena (PbS) and clausthalite (PbSe) with Au in the #2 lens, support a relationship between Au and the magmatic suite of elements (Sn, Te, Mo, Bi, Se; Hedenquist and Lowenstern, 1995; Williams-Jones and Heinrich, 2005; Huston et al., 2011; de Ronde et al., 2011).

(3) Trace element concentrations in pyrite strongly suggest a syngenetic magmatic input to the Photo Lake deposit. In concentric pyrite, there is a good correlation between Cu and Mo in the rim, where Au inclusions are concentrated (Fig. 13). In pitted pyrite, Au, Cu, Bi, and Se exhibit a strong correlation (Figs. 14, 15).

(4) The high Se content (≥1000 ppm; Figs. 13-15) measured for concentric, spongy, and pitted pyrite is not inclusion-controlled, suggesting that Se was incorporated into the pyrite structure, likely as a stoichiometric substitution for S (Huston et al., 1995). High Se concentrations in pyrite have been linked to a magmatic input in other systems. For example, in the Cu-rich Mount Lyell deposit, Se concentrations in pyrite of 90-900 ppm are reported to be consistent with a fluid that has a magmatic component of >50% at 300°C (Huston et al., 1995).

For some Au-rich VMS deposits, the presence of advanced argillic alteration and high sulfidation assemblages (e.g., kaolinite, pyrophyllite, alunite, enargite, tennantite, bornite) and their metamorphosed equivalents has been cited as evidence of alteration by a fluid with an anomalously low pH due to either very low-T conditions or direct magmatic input of volatiles to the system, the latter process having been considered more likely (e.g., Sillitoe et al., 1996; Hannington et al., 1999; Dubé et al., 2007, 2014; Mercier-Langevin et al., 2013; Beaudoin et al.,

2014). These deposits and their associated alteration zones are compared to high sulfidation epithermal gold deposits, where Au has a magmatic origin (Hedenquist and Lowenstern, 1994). The compositional changes associated with the Photo Lake alteration assemblages are characterized by gains in Fe_2O_3, MgO, and K_2O and losses in Na_2O, CaO, and SiO_2, which are consistent with gains and losses documented by Galley et al. (1993), Bailes et al. (2016) and, Caté et al. (2015) for the Chisel, Chisel North, Lost, Ghost, and Lalor deposits. Argillic or advanced argillic-style alteration associated with some large Au-rich VMS deposits (e.g., Bousquet 2-Dumagami: Tourigny et al., 1993; Dubé et al., 2014; LaRonde Penna: Dubé et al., 2007; Boliden: Mercier-Langevin et al., 2013, 2015) is therefore not present at Photo Lake (Fig. 18B), nor is it present in other Au-rich VMS deposits (e.g., Horne: Kerr and Gibson, 1993; Estrades: Welch, 1995; Lemoine: Mercier-Langevin et al., 2014b; Lalor: Caté, 2016).

Recent work at the hydrothermally active Brothers Volcano, Kermadec Arc (de Ronde et al., 2005, 2011) has documented changes in the physico-chemical parameters of the hydrothermal system that result mainly from episodic contributions of magmatic fluids to the larger seawater-dominated hydrothermal system. Large volumes of seawater overprint the effects of magmatic fluids; however, the isotopic composition and elemental signatures (Mo, Bi, Se, Co, Au) of the sulfides are preserved and indicate a magmatic contribution (de Ronde et al., 2011). This is consistent with what is observed in ancient systems that lack the mineral assemblages typically associated with magmatic systems but that have strong chemical evidence for a magmatic input. Such is the case for the Photo Lake deposit, where the trace element signature of the sulfides and the mineral and elemental associations with Au suggest a magmatic input. Furthermore, at Brothers Volcano, the intervals during which the hydrothermal fluids retained their most

magmatic signature correlate with the highest Au grades (de Ronde et al., 2011), indicating that a magmatic input may be critical for Au enrichment in VMS systems in arc and backarc settings.

3.7.7 Implications for Au enrichment in the Photo Lake deposit

The ore lens and alteration zone geometry, metal zoning, and trace element signatures of the ore lenses suggest that boiling and a magmatic input contributed to deposit development. A selective magmatic input to the Photo Lake deposit may be explained by its volcanic setting and location. The large volume of the Photo Rhyolite complex (minimum 1.5 km^3) and its location at the margin of a subsidence structure hosting the Powderhouse dacite unit (Fig. 2; Friesen et al., 2015) suggest proximity to a major synvolcanic structure. This structure is interpreted to have been a magma conduit for the fissure-fed Photo rhyolite flows and a hydrothermal fluid conduit during formation of the Photo Lake deposit. This deep-penetrating structure may have also allowed fluids derived from a high-level magma chamber beneath the deposit to ascend to the seafloor.

Selective development of a concentrated Cu-Au stringer zone due to boiling in the Photo Lake deposit may be the result of water depth variations along the Chisel sequence ore interval. Boiling is dependent on fluid salinity, temperature, and pressure, with the latter expressed by water depth in VMS systems (Butterfield et al., 1990). All the Chisel sequence VMS deposits formed at the same time-stratigraphic interval and are products of the same large-scale hydrothermal system. However, volcanic lithofacies, bedforms and structures within volcaniclastic units of the Chisel sequence ore interval and the immediately overlying Threehouse unit indicate variations in water depth during and after VMS formation, from

emergent to below storm wave base (Engelbert et al., 2014a; Gibson et al., 2014; Friesen et al., 2015). It is therefore probable that Chisel sequence VMS deposits formed at different water depths, resulting in variable boiling conditions along the ore interval. Assuming the deposits formed from a common fluid with consistent metal content, salinity and temperature, variations in water depth may account for localized boiling and Cu enrichment in the footwall to the Photo Lake deposit. At a water depth significantly shallower than that required to suppress boiling of an ascending fluid, temperature-dependent metals such as Cu (±Au) would precipitate over a larger interval deeper in the subseafloor. At greater water depths, where boiling is suppressed or confined to the immediate subseafloor, a more concentrated Cu (±Au) stringer zone would be expected, such as in the Photo Lake deposit. This is consistent with the relationship between metal endowment and water depth documented in modern seafloor hydrothermal systems, where Cu-rich deposits are generally restricted to water depths >1,000 m, and deposits containing >5% Zn commonly form at water depths <1,000 m (Monecke et al., 2014). These water depth controls on base metal concentrations have been attributed, in part, to subseafloor boiling during hydrothermal fluid ascent and the attendant decrease in fluid temperature, causing precipitation of Cu at depth within a subseafloor stockwork zone (Monecke et al., 2014). Furthermore, recent work on modern hydrothermal systems suggests that variable Au grades in hydrothermal systems may the product of localized boiling, with deep boiling vents exhibiting a strong Cu-Au association (Hannington et al., 2017), as is observed in the Photo Lake deposit.

Variations in water depth and boiling only explain the greater overall enrichment of Cu and Au in the stringer zone to the Photo Lake deposit and not the higher overall Cu and Au content of

the deposit. Therefore, we favor an interpretation that involves a localized and direct magmatic fluid component to explain the high Cu and Au enrichment in the Photo Lake deposit.

Differences in the primary permeability of the footwall strata to the Photo Lake deposit and other Chisel sequence deposits may also have played a role in metal endowment (e.g., Bailes and Galley, 1999; Gibson et al., 1999). The location of the Photo Lake deposit within a coherent and less permeable felsic lava-dome complex may have minimized cold seawater advection, helping to maintain the temperature of ascending fluids at shallow levels in the subseafloor where boiling could occur. Conversely, other Chisel sequence deposits are underlain by more permeable volcaniclastic rocks of the Powderhouse dacite unit (Lost, Chisel North, and Lalor deposits) and brecciated felsic flows (Chisel and Ghost deposits; Bailes and Galley, 1999, 2007). The more permeable volcaniclastic strata would have facilitated cold seawater infiltration into the footwall and resulted in cooling of an ascending hydrothermal fluid by mixing or conduction.

3.8 Conclusions

The stratigraphic and volcanic reconstruction, sulfide mineralogy and chemistry, metal zonation, and geochemistry demonstrate the following:

1. The Photo Lake deposit formed in a felsic, vent-proximal lobe-hyaloclastite flow complex. The deposit formed at the contact between two geochemically and visually distinct felsic flows (PR1 and PR2).
2. The Photo Lake deposit formed at the same productive ore interval as the other Chisel sequence VMS deposits and does not represent a separate VMS-forming event.

3. The Photo Lake deposit has been folded by an isoclinal F_1 fold that has transposed the Cu-Au stringer zone (#1 lens) into sub-parallelism with the Zn-rich massive sulfide lens (#2 lens).
4. Gold occurs as mercurian electrum and occupies a late position with respect to the post-metamorphic paragenesis of the ore lenses, indicating that it was locally remobilized syn- to post-peak metamorphism and deformation. The deposit architecture, gold distribution, alteration, and metal zoning indicate that gold is syngenetic and was introduced into the hydrothermal system during the VMS mineralizing event.
5. Gold and Cu enrichment is interpreted to be the product of a magmatic input to enrich the hydrothermal fluids in Au and Cu followed by boiling of the hydrothermal fluids to facilitate efficient precipitation of these metals into a Cu-and Au-rich subseafloor stringer zone and Zn- and Au-rich seafloor massive sulfide lens. Variations in water depth and variable magmatic fluid input along the Chisel sequence ore interval may have resulted in the variable Cu and Au metal endowment of the Chisel sequence VMS deposits.
6. The metamorphosed alteration assemblages in the Photo Lake deposit are consistent with amphibolite grade metamorphism of typical VMS-style alteration. Advanced argillic assemblages or their metamorphic equivalents that are associated with some Au-rich VMS deposits are not present at Photo Lake.
7. The lack of a high sulfidation mineral assemblage typically representative of a magmatic input indicates either that the hydrothermal system was strongly overprinted by seawater or that the magmatic fluid mixed with the hydrothermal fluid in the subseafloor, masking the magmatic signature. Mixing with seawater and associated fluid buffering may also explain the absence of advanced argillic alteration.

8. Future exploration in the study area should be directed at the contact between PR1 and PR2 as this interval was not previously recognized and is relatively unexplored.

3.10 References

Allen, R.L., Weihed, P., and Svensson, S.-A., 1996, Setting of Zn-Cu-AU-Ag massive sulfide deposits in the evolution and facies architecture of a 1.9 Ga marine volcanic arc, Skellefte district, Sweden: Economic Geology, v. 91, p. 1022-1053.

Bailes, A.H., 1996, Setting of Cu-Zn-Au mineralization at Photo Lake (part of NTS 63K16): Manitoba Energy and Mines, Minerals Division, Report of Activities 1996, p. 66-74.

Bailes, A.H., 1997, Geochemistry of Paleoproterozoic volcanic rocks in the Photo Lake area, Flin Flon Belt (part of NTS 63K16): Manitoba Energy and Mines, Minerals Division, Report of Activities 1997, p. 61-72.

Bailes, A.H., and Galley, A.G., 1996, Setting of Paleoproterozoic volcanic-hosted massive base metal sulphide deposits, Snow Lake, in Bonham-Carter, G.F., Galley, A.G., and Hall, G.E.M., eds., EXTECH 1: A Multidisciplinary Approach to Massive Sulphide Research in the Rusty Lake-Snow Lake Greenstone Belts, Manitoba: Geological Survey of Canada, Bulletin 426, p. 105-138.

Bailes, A.H., and Galley, A.G., 1999, Evolution of the Paleoproterozoic Snow Lake arc assemblage and geodynamic setting for associated volcanic-hosted massive sulphide deposits, Flin Flon Belt, Manitoba, Canada: Canadian Journal of Earth Sciences, v. 36, p. 1789-1805.

Bailes, A.H., and Galley, A.G., 2007, Geology of the Chisel-Anderson lakes area, Snow Lake, Manitoba (NTS area 63K16SW and west half of 63J13SE): Manitoba Science,

Technology, Energy and Mines, Manitoba Geological Survey, Geoscientific Map MAP2007-1, scale 1:20 000 plus notes.

Bailes, A.H., Hunt, P.A., and Gordon, T.M., 1991, U-Pb zircon dating of possible synvolcanic plutons in the Flin Flon belt at Snow Lake, Manitoba: Geological Survey of Canada, Radiogenic age and isotopic studies report 4, p. 35-43.

Bailes, A.H., Chackowsky, L.E., Galley, A.G., and Connors, K.A., 1994, Geology of the Snow Lake – File Lake area, Manitoba (parts of NTS 63 K/16 and 63 J/13): Manitoba Energy and Mines, Open File Report OF94-4 and Map, 1:50 000 scale.

Bailes, A.H., Galley, A.G., Skirrow, R.G., and Young, J., 1996, Geology of the Chisel volcanic-hosted massive sulphide area, Snow Lake, Manitoba (part of 63K/16SE): Manitoba Energy and Mines, Open File Report OF95-4 and colour map, 1:5000 with marginal notes.

Bailes, A.H., Simms, D., Galley, A.G., and Young, J., 1997, Geological setting of the Photo Lake volcanic-hosted massive sulphide deposits, Snow Lake, Manitoba (part of 63K/16SE): Manitoba Energy and Mines, Open File Report OF97-5, annotated 1:5000 colour map.

Bailes, A.H., Galley, A.G., Paradis, S., and Taylor, B.E., 2016, Variations in large synvolcanic alteration zones at Snow Lake, Manitoba, Canada, with proximity to associated volcanogenic massive sulfide deposits: Economic Geology, v. 111, p. 933-962.

Barrett, T.J., and MacLean, W.H., 1994, Chemostratigraphy and hydrothermal alteration in exploration for VHMS deposits in greenstones and younger volcanic rocks, in Lentz, D.R., ed., Alteration and alteration processes associated with ore-forming systems: Geological Association of Canada, Short Course Notes 11, pp. 433–467.

Barrie, C.D., Boyce, A.J., Boyle, A.P., Williams, P.J., Blake, K., Ogawara, T., Akai, J., and Prior, D.J., 2009, Growth controls in colloform pyrite: American Mineralogist, v. 94, p. 415-429.

Barton, P.B. and Bethke, P.M., 1987, Chalcopyrite disease in sphalerite: pathology and epidemiology: American Mineralogist, v. 72, p. 451-467.

Bruekner, S.M., Piercey, S.J., Sylvester, P.J., Maloney, S., and Pilgrim, L., 2014, Evidence for syngenetic precious metal enrichment in an Appalachian volcanogenic massive sulfide system: the 1806 zone, Ming Mine, Newfoundland, Canada: Economic Geology, v. 109, p. 1611-1642.

Butterfield, D.A., Massoth, G.J., McDuff, R.E., Lupton, J.E., and Lilley, M.D., 1990, Geochemistry of hydrothermal fluids from Axial Seamount Hydrothermal Emissions Study vent field, Juan de Fuca Ridge: subseafloor boiling and subsequence fluid-rock interaction: Journal of Geophysical Research, v. 95, p. 12,895-12,921.

Caté, A., 2016, Geology of the Paleoproterozoic Zn-Cu-Au Lalor volcanogenic massive sulfide deposit and its gold-rich lenses, Snow Lake, Manitoba. / Géologie du gisement de sulfures massifs volcanogène Paléoprotérozoïque à Zn-Cu-Au de Lalor et de ses lentilles riches en or, Snow Lake, Manitoba : Unpublished Ph.D. thesis, Université du Québec, Institut national de la recherche scientifique, Québec, Québec, 430 p.

Caté, A., Mercier-Langevin, P., Ross, P.-S., Duff, S., Hannington, M.D., Dubé, B., and Gagné, S., 2014a, The Paleoproterozoic Lalor VMS deposit, Snow Lake, Manitoba: preliminary observations on the nature and architecture of the gold- and base metal-rich ore and alteration zones: Geological Survey of Canada, Open File 7483, 19 p.

Caté, A., Mercier-Langevin, P., Ross, P.-S., and Simms, D., 2014b, Structural controls on geometry and ore distribution in the Lalor auriferous VMS deposit, Snow Lake, west-central Manitoba (part of NTS 63K16): preliminary results from underground mapping, in Report of Activities 2014. Manitoba Mineral Resources, Manitoba Geological Survey, p. 104-155.

Caté, A., Mercier-Langevin, P., Ross, P.-S., Duff, S., Hannington, M.D., Dubé, B., and Gagné, S., 2015, Geology and Au enrichment processes at the Paleoproterozoic Lalor auriferous volcanogenic massive sulphide deposit, Snow Lake, Manitoba: Geological Survey of Canada Open File 7853, p. 131-145.

Charlou, J.L., Fouquet, Y., Donval, J.P., and Auzende, J.M., 1996, Mineral and gas chemistry of hydrothermal fluids on an ultrafast spreading ridge: East Pacific Rise, 17° to 19°S (Naudur cruise, 1993) phase separation processes controlled by volcanic and tectonic activity: Journal of Geophysical Research, v. 101, p. 15,899-15,919.

Cook, N.J. and Chryssoulis, S.L., 1990, Concentrations of “invisible gold” in the common sulfides: Canadian Mineralogist, v. 28, p. 1-16.

Corrigan, D., Galley, A.G., and Pehrsson, S., 2007, Tectonic evolution and metallogeny of the southwestern Trans-Hudson Orogen, in Goodfellow, W.D., ed., Mineral Deposits of Canada: A Synthesis of Major Deposit-Types, District Metallogeny, the Evolution of Geological Provinces, and Exploration Methods: Geological Association of Canada, Mineral Deposits Division, Special Publication No. 5, p. 881-902.

Corrigan, D., Pehrsson, S., Wodicka, N., and de Kemp, E., 2009, The Palaeoproterozoic Trans-Hudson Orogen: a prototype of modern accretionary processes: Geological Society, London, Special Publications, v. 327, p. 457-479.

Craig J.R., and Vokes, F.M., 1993, The metamorphism of pyrite and pyritic ores: an overview: Mineralogical Magazine, v. 57, p. 3-18.

Craig, J.R., Vokes, F.M., and Solberg, T.N., 1998, Pyrite: physical and chemical textures: Mineralium Deposita, v. 34, p. 82-101.

David, J., Bailes, A.H., and Machado, N., 1996, Evolution of the Snow Lake portion of the Paleoproterozoic Flin Flon and Kisseynew belts, Trans-Hudson Orogen, Manitoba, Canada: Precambrian Research, v. 80, p. 107-124.

de Ronde, C.E.J., Hannington, M.D., Stoffers, P., Wright, I.C., Ditchnurn, R.G., Reyes, A.G., Baker, E.T., Massoth, G.J., Lupton, J.E., Walker, S.L., Greene, R.R., Soong, C.W.R., Ishibashi, J., Lebon, G.T., Bray, C.J., and Resing, J.A., 2005, Evolution of a submarine magmatic-hydrothermal system: Brothers Volcano, Southern Kermadec Arc, New Zealand: Economic Geology, v. 100, p. 1097-1133.

de Ronde, C.E.J., Massoth, G.J., Butterfield, D.A., Christenson, B.W., Ishibashi, J., Ditchburn, R.G., Hannington, M.D., Brathwaite, R.L., Lupton, J.E., Kamenetsky, V.S., Graham, I.J., Zellmer, G.F., Dziak, R.P., Embley, R.W., Dekov, V.M., Munnik, F., Lahr, J., Evans, L.J., and Takai, K., 2011, Submarine hydrothermal activity and gold-rich mineralization at Brothers Volcano, Kermadec Arc, New Zealand: Mineralium Deposita, v. 46, p. 541-584.

Doyle, M.G. and Allen, R.L., 2003, Subsea-floor replacement in volcanic-hosted massive sulfide deposits: Ore Geology Reviews, v. 23, p. 183-222.

Dubé, B., Mercier-Langevin, P., Hannington, M., Lafrance, B., Gosselin, G., and Gosselin, P., 2007, The LaRonde Penna world-class Au-rich volcanogenic massive sulfide deposit,

Abitibi, Québec: mineralogy and geochemistry of alteration and implications for genesis and exploration: Economic Geology, v. 102, p. 633-666.

Dubé, B., Mercier-Langevin, P., Kjaarsgaard, I., Hannington, M., Bécu, V., Coté, J., Moorhead, J., Legault, M., and Bédard, N., 2014, The Bousquet 2-Dumagami World-Class Archean Au-Rich Volcanogenic Massive Sulfide Deposit, Abitibi, Québec: Metamorphosed Submarine Advanced Argillic Alteration Footprint and Genesis: Economic Geology, v. 109, p. 121-166.

Duff, S. 2016. Ore types of the auriferous Lalor VMS deposit, Snow Lake, Manitoba: implications for genesis and post-depositional processes. Unpublished M.Sc. thesis, Ottawa University, 123 pages.

Duff, S., Hannington, M.D., Caté, A., Mercier-Langevin, P., and Kjarsgaard, I.M., 2015, Major ore types of the Paleoproterozoic Lalor auriferous volcanogenic massive sulphide deposit, Snow Lake, Manitoba: Geological Survey of Canada Open File 7853, p. 147-170.

Eldridge, C.S., Barton, P.B., and Ohmoto, H., 1983, Mineral textures and their bearing on the formation of the Kuroko orebodies: Economic Geology Monograph 5, p. 241-281.

Engelbert, M.S., Friesen, V., Gibson, H.L., and Lafrance, B., 2014a, Volcanic reconstruction of the productive VMS ore interval in the Paleoproterozoic Chisel sequence, Snow Lake, Manitoba [abs.]: Geological Association of Canada – Mineralogical Association of Canada Joint Annual Meeting, Fredericton, 2014, Abstract Volume, p. 83-84.

Engelbert, M.S., Gibson, H.L., and Lafrance, B., 2014b, Geologic setting, mineralogy, and geochemistry of the Paleoproterozoic Photo Lake VMS deposit, Snow Lake, Manitoba

[abs.]: Geological Association of Canada – Mineralogical Association of Canada Joint Annual Meeting, Fredericton, 2014, Abstract Volume, p. 84.

Fisher, R.V., 1961, Proposed classification of volcaniclastic sediments and rocks: Geological Society of America Bulletin, v. 72, p. 1395-1408.

Fisher, R.V., 1966, Rocks composed of volcanic fragments and their classification: Earth Science Reviews, v. 1, p. 287-298.

Franklin, J.M., Gibson, H.L., Jonasson, I.R., and Galley, A.G., 2005, Volcanogenic massive sulfide deposits, in Hedenquist, J.W., Thompson, J.F.H., Goldfarb, R.J., and Richards, J.P., eds., Economic Geology 100th Anniversary Volume, p. 523-560.

Freitag, K., Boyle, A.P., Nelson, E., Hitzman, M., Churchill, J., and Lopez-Pedrosa, M., 2004, The use of electron backscatter diffraction and orientation contrast imaging as tools for sulphide textural studies: example from the Greens Creek deposit (Alaska): Mineralium Deposita, v. 39, p. 103-113.

Friesen, V.C., Engelbert, M., DeWolfe, Y.M., and Gibson, H.L, 2015, Volcanic reconstruction of the Powderhouse dacite in the Paleoproterozoic VMS hosting Chisel sequence, Snow Lake, Manitoba [abs.]: AGU-GAC-MAC-CGU 2015 Joint Assembly Abstracts Listing, p. 276.

Gallant, R.M., and Von Damm, K.L., 2006, Geochemical controls on hydrothermal fluids from the Kairei and Edmond vent fields, 23°-25°S, Central Indian Ridge: Geochemistry, Geophysics, Geosystems, v. 7, Q06018.

Galley, A.G., Bailes, A.H., and Kitzler, G., 1993, Geological setting and hydrothermal evolution of the Chisel Lake and North Chisel Zn-Pb-Cu-Ag-Au massive sulfide deposits, Snow Lake, Manitoba: Exploration and Mining Geology, v. 2 (4), p. 271-295.

Galley, A.G., Hannington, M.D., and Jonasson, I.R., 2007a, Volcanogenic massive sulphide deposits, in Goodfellow, W.D., ed., Mineral Deposits of Canada: A Synthesis of Major Deposit Types, District Metallogeny, the Evolution of Geological Provinces, and Exploration Methods: Geological Association of Canada, Mineral Deposits Division, Special Publication No. 5, p. 141-161.

Galley, A.G., Syme, R., and Bailes, A.H., 2007b, Metallogeny of the Paleoproterozoic Flin Flon Belt, Manitoba and Saskatchewan, in Goodfellow, W.D., ed., Mineral Deposits of Canada: A Synthesis of Major Deposit Types, District Metallogeny, the Evolution of Geological Provinces, and Exploration Methods: Geological Association of Canada, Mineral Deposits Division, Special Publication No. 5, p. 509-531.

Gibson, H.L., Morton, R.L., and Hudak, G.J., 1999, Submarine volcanic processes, deposits, and environments favorable for the location of volcanic-associated massive sulfide deposits: Reviews in Economic Geology, v. 8, p. 13-51.

Gibson, H.L., Allen, R.L., Riverin, G., and Lane, T.E., 2007, The VMS Model: Advances and application to exploration targeting, in Milkereit, B., ed., Proceedings of Exploration 07: Fifth Decennial International Conference on Mineral Exploration, Plenary Session: Ore Deposits and Exploration Technology, p. 713-730.

Gibson, H.L., Engelbert, M., Lafrance, B., Friesen, V., DeWolfe, M., Tinkham, D., and Bailes, A., 2014, Reconstruction of the ore interval and environment for the Paleoproterozoic Lost and Ghost Lake VMS deposits, Snow Lake, Manitoba [abs.]: Geological Association of Canada – Mineralogical Association of Canada Joint Annual Meeting, Fredericton, 2014, Abstract Volume, p. 102.

Hannington, M.D., Peter, J.M., and Scott, J.D., 1986, Gold in sea-floor polymetallic sulfide deposits: Economic Geology, v. 81, p. 1867-1883.

Hannington, M.D., Tivey, M.K., Larocque, A.C.L., Petersen, S., and Rona, P.A., 1995, The occurrence of gold in sulfide deposits of the TAG hydrothermal field, Mid-Atlantic Ridge: The Canadian Mineralogist, v. 33, p. 1285-1310.

Hannington, M.D., Bleeker, W., and Kjarsgaard, I., 1999a, Sulfide mineralogy, geochemistry, and ore genesis of the Kidd Creek deposit: Part II. The Bornite Zone: Economic Geology Monograph 10, p. 225-266.

Hannington, M.D., Poulsen, K.H., Thompson, J.F.H., and Sillitoe, R.H., 1999b, Volcanogenic gold in the massive sulfide environment: Reviews in Economic Geology, v. 8, p. 325-356.

Hannington, M.D., Petersen, S., Monecke, T., and Mercier-Langevin, P., 2017, Divining gold in VMS systems: news from the seafloor: Proceedings of the 14th Biennal SGA Meeting, Quebec City, Canada, p. 43-46.

Hart, T.R., Gibson, H.L., and Lesher, C.M., 2004, Trace element geochemistry and petrogenesis of felsic volcanic rocks associated with volcanogenic massive Cu-Zn-Pb sulfide deposits: Economic Geology, v. 99, p. 1003-1013.

Hedenquist, J.W. and Lowenstern, J.B., 1994, The role of magmas in the formation of hydrothermal ore deposits: Nature, v. 370, p. 519-527.

Herzig, P.M., Hannington, M.D., Fouquet, Y., von Stackelberg, U., and Petersen, S., 1993, Gold-rich polymetallic sulfides from the Lau back arc and implications for the geochemistry of gold in sea-floor hydrothermal systems of the southwest Pacific: Economic Geology, v. 88, p. 2182-2209.

Herzig, P.M., Hannington, M.D., and Arribas Jr., A., 1998, Sulfur isotopic composition of hydrothermal precipitates from the Lau back-arc: implications for magmatic contributions to seafloor hydrothermal systems: Mineralium Deposita, v. 33, p. 226-237.

Heine, T.H. and Prouse, D., 1998, Photo Lake mine archive project (NTS 63K/16SE): Manitoba Energy and Mines, Geological Services, Report of Activities 1998, p. 23-24.

Huston, D.L., 2000, Gold in volcanic-hosted massive sulfide deposits: distribution, genesis, and exploration, in Hagemann, S.G., ed., Gold in 2000: Reviews in Economic Geology, v. 13, p. 401-426.

Huston, D.L., and Large, R.R., 1989, A chemical model for the concentration of gold in volcanogenic massive sulphide deposits: Ore Geology Reviews, v. 4, p. 171-200.

Huston, D.L., Bolger, C., and Cozens, G., 1993, A comparison of mineral deposits at the Gecko and White devil deposits: Implications for ore genesis in the Tennant Creek district Northern Territory, Australia: Economic Geology, v. 88, p. 1198-1225.

Huston, D.L., Sie, S.J., Suter, G.F., Cooke, D.R., and Both, R.A., 1995, Trace elements in sulfide minerals from eastern Australian volcanic-hosted massive sulfide deposits: Part I. Proton microprobe analyses of pyrite, chalcopyrite, and sphalerite, and Part II. Selenium levels in pyrite: comparison with ∂^{34}S values and implications for the source of sulfide in volcanogenic hydrothermal systems: Economic Geology, v. 90, p. 1167-1196.

Huston, D.L., Relvas, J.M.R.S., Gemmell, J.B., and Drieberg, S., 2011, The role of granites in volcanic-hosted massive sulphide ore-forming systems: an assessment of magmatic-hydrothermal contributions: Mineralium Deposita, v. 46, p. 473-507.

Kerr, D.J. and Gibson, H.L., 1993, A comparison between the Horne volcanogenic massive sulfide deposit and intracauldron deposits of the Mine Sequence, Noranda, Quebec: Economic Geology, v. 88, p. 1419-1442.

Kraus, J., and Williams, P.F., 1999, Structural development of the Snow Lake Allochthon and its role in the evolution of the southeastern Trans-Hudson Orogen in Manitoba, central Canada: Canadian Journal of Earth Sciences, v. 36, p. 1881-1899.

Large, R.R., 1992, Australian volcanic-hosted massive sulfide deposits: features, styles, and genetic models: Economic Geology, v. 87, p. 471-510.

Large, R.R., Gemmell, J.B., Paulick, H., and Huston, D.L., 2001, The alteration box plot: a simple approach to understanding the relationship between alteration, mineralization, and lithogeochemistry associated with volcanic-hosted massive sulfide deposits: Economic Geology, v. 96, p. 957-971.

Larocque, A.C.L. and Hodgson, C.J., 1995, Effects of greenschist-facies metamorphism and related deformation on the Mobrun massive sulfide deposit, Quebec, Canada: Mineralium Deposita, v. 30, p. 439-448.

Le Maitre, R.W., Bateman, P., Dudek, A., Keller, J., Lameyre, J., Le Bas, M.J., Sabine, P.A., Schmid, R., Sorensen, H., Streckeisen, A., Woolley, A.R., and Zanettin, B., 1989, A classification of igneous rocks and glossary terms: recommendations of the International Union of Geological Sciences Subcommission on the Systematics of Igneous Rocks: Oxford, Blackwell Scientific, 193 p.

Lentz, D.R., 1998. Petrogenetic evolution of felsic volcanic sequences associated with Phanerozoic volcanic-hosted massive sulphide systems: The role of extensional geodynamics. Ore Geology Reviews, **12**: 289–327.

Lucas, S.B., Stern, R.A., Syme, E.C., Reilly, B.A., and Thomas, D.J., 1996, Intraoceanic tectonics and the development of continental crust: 1.92-1.84 Ga evolution of the Flin Flon Belt, Canada: GSA Bulletin, v. 108 (5), p. 602-629.

Lydon, J.W., 1984, Ore deposit models; 8, Volcanogenic sulphide deposits; Part I, A descriptive model: Geoscience Canada, v. 11, p. 195-202.

Lydon, J.W., 1988, Volcanogenic massive sulfide deposits part 2: genetic models: Geoscience Canada, v. 15, p. 43-65.

MacLean, W.H., 1990, Mass changes in altered rock series: Mineralium Deposita, v. 25, p. 44-49.

Marquis, P., Hubert, C., Brown, A.C., and Rigg, D.M., 1990, Overprinting of early, redistributed Fe and Pb-Zn mineralization by late stage Au-Ag-Cu deposition at the Dumagami mine, Bousquet district, Abitibi, Quebec: Canadian Journal of Earth Sciences, v. 27, p. 1651-1671.

Menard, T., and Gordon, T.M., 1995, Syntectonic alteration of VMS deposits, Snow Lake, Manitoba: Manitoba Energy and Mines, Minerals Division, Report of Activities 1995, p. 164-167.

Menard, T., and Gordon, T.M., 1997, Metamorphic P-T paths from the eastern Flin Flon belt and Kisseynew Domain, Snow Lake, Manitoba: The Canadian Mineralogist, v. 35, p. 1093-1115.

Mercier-Langevin, P., Dubé, B., Hannington, M.D., Davis, D.W., Lafrance, B., and Gosselin, G., 2007a, The LaRonde Penna Au-rich volcanogenic massive sulfide deposit, Abitibi greenstone belt, Quebec: Part I. Geology and geochronology: Economic Geology, v. 102, p. 585-609.

Mercier-Langevin, P., Dubé, B., Hannington, M.D., Richer-Laflèche, M., and Gosselin, G., 2007b, The LaRonde Penna Au-rich volcanogenic massive sulfide deposit, Abitibi greenstone belt, Quebec: Part II. Lithogeochemistry and paleotectonic setting: Economic Geology, v. 102, p. 611-631.

Mercier-Langevin, P., Hannington, M.D., Dubé, B., and Bécu, V., 2011, The gold content of volcanogenic massive sulfide deposits: Mineralium Deposita, v. 46, p. 509-539.

Mercier-Langevin, P., McNicoll, V., Allen, R.L., Blight, J.H.S., and Dubé, B., 2013, The Boliden gold-rich volcanogenic massive sulfide deposit, Skellefte district, Sweden: new U-Pb age constraints and implications at deposit and district scale: Mineralium Deposita, v. 48, p. 485-504.

Mercier-Langevin, P., Caté, A., and Ross, P.-S., 2014a., Whole-rock oxygen-isotope mapping of the footwall alteration zones at the Lalor auriferous VMS deposit, Snow Lake, west-central Manitoba (NTS 63K16): Manitoba Mineral Resources, Manitoba Geological Survey, Report of Activities 2014, p. 94-103.

Mercier-Langevin, P., Lafrance, B., Bécu, V., Dubé, B., Kjarsgaard, I., and Guha, J., 2014b, The Lemoine auriferous volcanogenic massive sulfide deposit, Chibougamau Camp, Abitibi Greenstone Belt, Quebec, Canada: geology and genesis: Economic Geology, v. 109, p. 231-269.

Mercier-Langevin, P., Hannington, M.D., Dubé, B., Piercey, S.J., Peter, J.M., and Pehrsson, S.J., 2015, Precious metal enrichment processes in volcanogenic massive sulphide deposits – a summary of key features, with an emphasis on TGI-4 research contributions: Geological Survey of Canada Open File 7853, p. 117- 130.

Monecke, T., Petersen, S., and Hannginton, M.D., 2014, Constraints on water depth of massive sulfide formation: evidence from modern seafloor hydrothermal systems in arc-related settings: Economic Geology, v. 109, p. 2079-2101.

Moss, R., and Scott, S.D., 2001, The geochemistry and mineralogy of gold-rich hydrothermal precipitates from the eastern Manus Basin, Papua New Guinea: The Canadian Mineralogist, v. 39, p. 957-978.

Moss, R., Scott, S.D., and Binns, R.A., 2001, Gold content of Eastern Manus basin volcanic rocks: implications for enrichment in associated hydrothermal precipitates: Economic Geology, v. 96, p. 91-107.

Ohmoto, H., 1996, Formation of volcanogenic massive sulfide deposits: the Kuroko perspective: Ore Geology Reviews, v. 10, p. 135-177.

Parr, J., 1994, The preservation of pre-metamorphic colloform banding in pyrite from the Broken Hill-type Pinnacles deposit, New South Wales, Australia: Mineralogical Magazine, v. 58, p. 461-471.

Pearce, J.A, 1996, A user's guide to basalt discrimination diagrams, in Trace element geochemistry of volcanic rocks; applications for massive sulphide exploration. Geological Association of Canada, Short Course Notes 12, p. 79-113.

Pearce, J.A. and Peate, D.W., 1995, Tectonic implications of the composition of volcanic arc magmas: Annual Reviews in Earth and Planetary Science, v. 23, p. 251-285.

Pearce, J.A., Harris, N.B.W., and Tindle, A.G., 1984, Trace element discrimination diagrams for the tectonic interpretation of granitic rocks: Journal of Petrology, v. 25, p. 956–983.

Percival, J.A., Whalen, J.B., and Rayner, N., 2005, Pikwitonei-Snow Lake Manitoba transect (parts of NTS 63J, 63O and 63P), Trans-Hudson Orogen-Superior Margin Metallotect

Project: new results and tectonic interpretation: Manitoba Industry, Economic Development and Mines, Manitoba Geological Survey, Report of Activities 2005, p. 69-91.

Pilote, J.-L., Piercey, S., and Mercier-Langevin, P., 2017, Volcanic and structural reconstruction of the deformed and metamorphosed Ming volcanogenic massive sulfide deposit, Canada: implications for ore zone geometry and metal distribution: Economic Geology, v. 112, p. 1305-1332.

Poulsen, K.H., and Hannington, M.D., 1995, Volcanic-associated massive sulfide gold, *in* Eckstrand, R.O., Sinclair, W.D., and Thorpe, R.I., eds., Geology of Canadian mineral deposit types: Geological Society of America, DNAG, v. P-1, Geology of Canada, no. 8, p. 183-196.

Riverin, G. and Hodgson, C.J., 1980, Wall-rock alteration at the Millenbach Cu-Zn mine, Noranda, Quebec: Economic Geology, v. 75, p. 424-444.

Roth, T., Thompson, J., and Barrett, T., 1999, The precious metal-rich Eskay Creek deposit, northwestern British Columbia: Reviews in Economic Geology, v. 8, p. 357-374.

Rubingh, K.E., Lafrance, B., and Gibson, H.L., 2012, Lithostratigraphy and structural geology of the McLeod Road-Birch Lake thrust panel, Snow Lake, west-central Manitoba (parts of NTS 63K16, 63J13): Manitoba Innovation, Energy and Mines, Manitoba Geological Survey, Report of Activities 2012, p. 104-114.

Spitz, G. and Darling, E., 1978, Major and minor element lithogeochemical anomalies surrounding the Louvern copper deposit, Val d'Or, Quebec: Canadian Journal of Earth Sciences, v. 15, p. 1161-1169.

Stern, R.A., Syme, E.C., Bailes, A.H., Galley, A.G., Thomas, D.J., and Lucas, S.B., 1992, Nd-isotopic stratigraphy of Early Proterozoic Amisk group metavolcanic rocks from the Flin Flon Belt, Manitoba and Saskatchewan: Geological Survey of Canada, Radiogenic age and isotopic studies report 6, p. 73-84.

Stern, R.A., Syme, E.C., Bailes, A.H., and Lucas, S.B., 1995, Paleoproterozoic (1.90-1.86 Ga) arc volcanism in the Flin Flon Belt, Trans-Hudson Orogen, Canada: Contributions to Mineralogy and Petrology, v. 119, p. 117-141.

Stewart, M., Lafrance, B., and Gibson, H., 2018, Early thrusting and folding in the Snow Lake camp, Manitoba: implications and effects on volcanogenic massive sulfide deposits: Canadian Journal of Earth Sciences, v. 55, p. 935-957.

Sun, S.-s. and McDonough, W.F., 1989, Chemical and isotope systematics of oceanic basalts: implications for mantle composition and processes, in Saunders, A.D. and Norry, M.J., eds., Magmatism in the Ocean Basins: Geological Society, London, p. 313-345.

Syme, E.C., Lucas, S.B., Bailes, A.H., and Stern, R.A., 1999, Contrasting arc and MORB-like assemblages in the Paleoproterozoic Flin Flon Belt, Manitoba, and the role of intra-arc extension in localizing volcanic-hosted massive sulphide deposits: Canadian Journal of Earth Sciences, v. 36, p. 1767-1788.

Taylor, C.D., Sutley, S.J., and Lichte, F.E., 2010, Chapter 9: Mineralogical, textural, and metal residence studies of primary, recrystallized, and remobilized ores of the Greens Creek deposit: U.S. Geological Survey Professional Paper 1763, p. 183-236.

Tessier, A.C., 1996, Secondary structural controls of the mineralization at the Photo Lake mine; Snow Lake, Manitoba: Hudson Bay Mining and Smelting Co., Ltd. Internal report, 42 p. with additional figures.

Tinkham, D.K., 2013, A model for metamorphic devolatilization in the Lalor deposit alteration system, Snow Lake, MB [abs.]: Geological Association of Canada – Mineralogical Association of Canada Joint Annual Meeting, Winnipeg, 2013, Abstract Volume, P. 187.

Tomkins, A.G., 2007, Three mechanisms of ore re-mobilisation during amphibolite facies metamorphism at the Montauban Zn-Pb-Au-Ag deposit: Mineralium Deposita, v. 42, p. 627-637.

Tomkins, A.G., Pattison, D.R., Zaleski, E., 2004, The Hemlo gold deposit, Ontario: an example of melting and mobilization of a precious metal-sulfosalt assemblage during amphibolite facies metamorphism and deformation: Economic Geology, v. 99, p. 1063-1084.

Tourigny, G., Brown, A.C., Hubert, C., and Crépeau, R., 1989, Synvolcanic and syntectonic gold mineralization at the Bousquet mine, Abitibi greenstone belt, Quebec: Economic Geology, v. 84, p. 1875-1890.

Welch, M.J., 1995, Metal zoning, geochemistry and alteration of the Archean, Estrades Zn-Au massive sulfide deposit, Northwestern Quebec, Canada: Unpublished M.Sc. thesis, Sudbury, Ontario, Laurentian University, 200 p.

White, J.D.L., and Houghton, B.F., 2006, Primary volcaniclastic rocks: Geology, v. 34 (8), p. 677-680.

Williams, N.C., and Davidson, G.J., 2004, Possible submarine advanced argillic alteration at the Basin Lake prospect, Western Tasmania, Australia: Economic Geology, v. 99, p. 987-1002.

Williams-Jones, A.E. and Heinrich, C.A., 2005, Vapor transport of metals and the formation of magmatic-hydrothermal ore deposits, in Hedenquist, J.W., Thompson, J.F.H., Goldfarb,

R.J., and Richards, J.P., eds., Economic Geology 100th Anniversary Volume, p. 1287-1312.

Yergeau, D., Mercier-Langevin, P., Dubé, B., Malo, M., McNicoll, V.J., Jackson, S.E., Savoie, A., and La Rochelle, F., 2015, The Archean Westwood Au deposit, southern Abitibi: telescoped Au-rich VMS and intrusion-related Au systems: Geological Survey of Canada Open File 7852, p. 177-191.

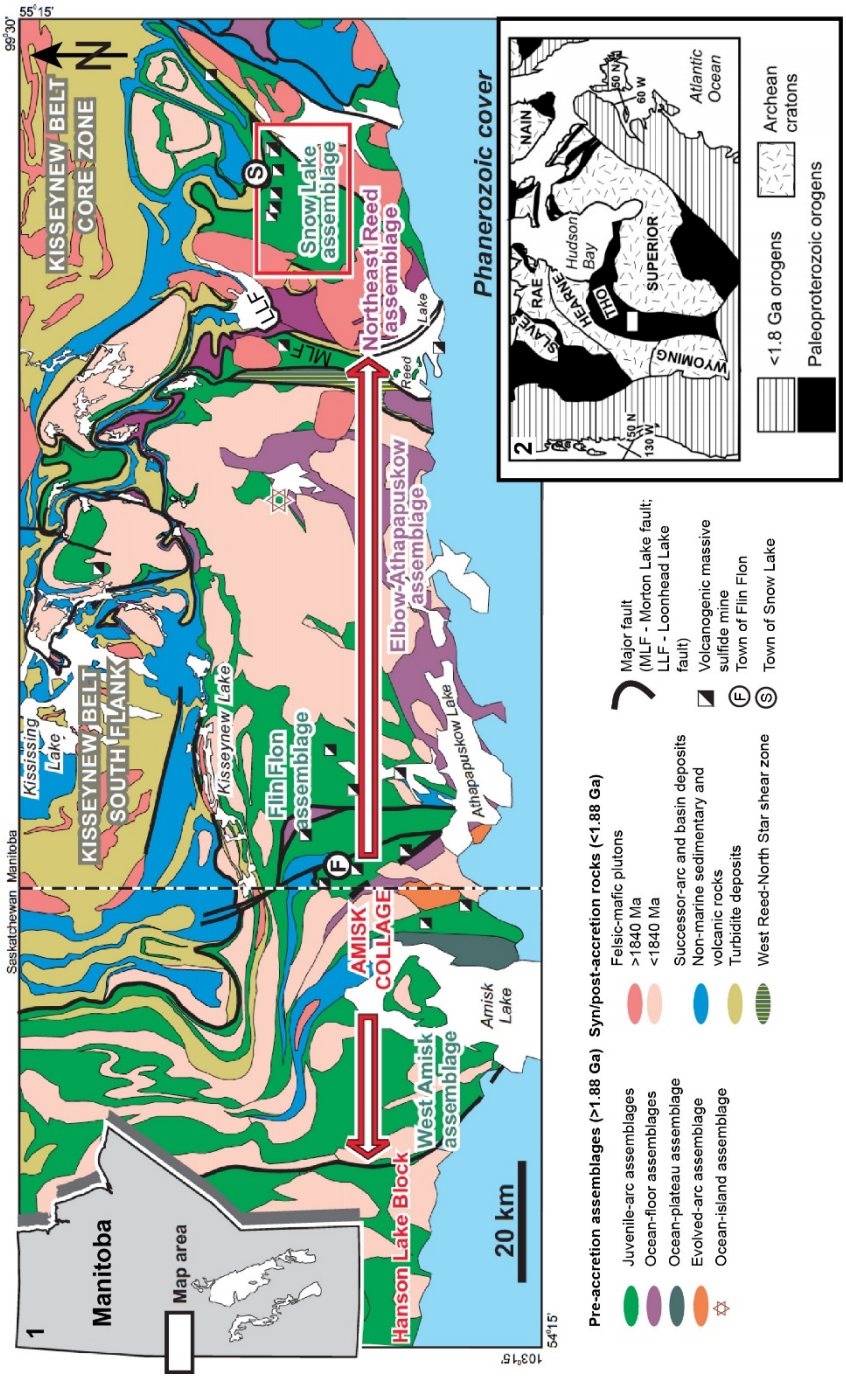

Figure 3-1. Location of the Snow Lake arc assemblage within the Flin Flon Belt and the Trans-Hudson Orogen, Manitoba, Canada (modified after Syme et al. 1999). Inset maps showing location of Flin Flon belt within the Trans-Hudson Orogen (modified after Syme et al. 1999) and within Manitoba.

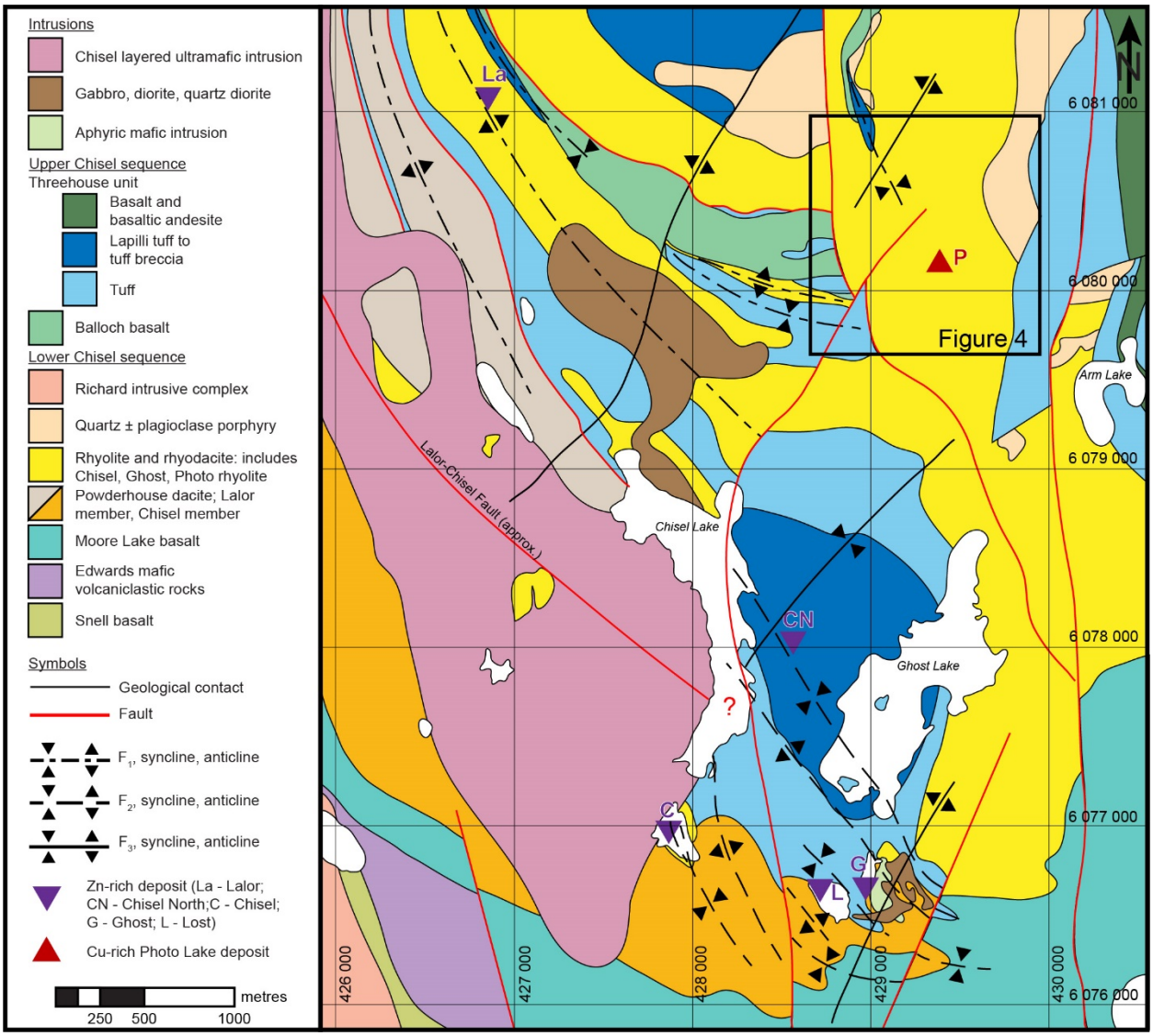

Figure 3-2. Geology of the Chisel sequence (modified from Bailes and Galley, 2007). Folds, structural fabrics, and minor intrusions not shown. Up-plunge locations of the Photo, Chisel, Ghost, and Lost ore bodies and vertical projections of Lalor and Chisel North ore bodies shown. Box outlines map area in Figure 4.

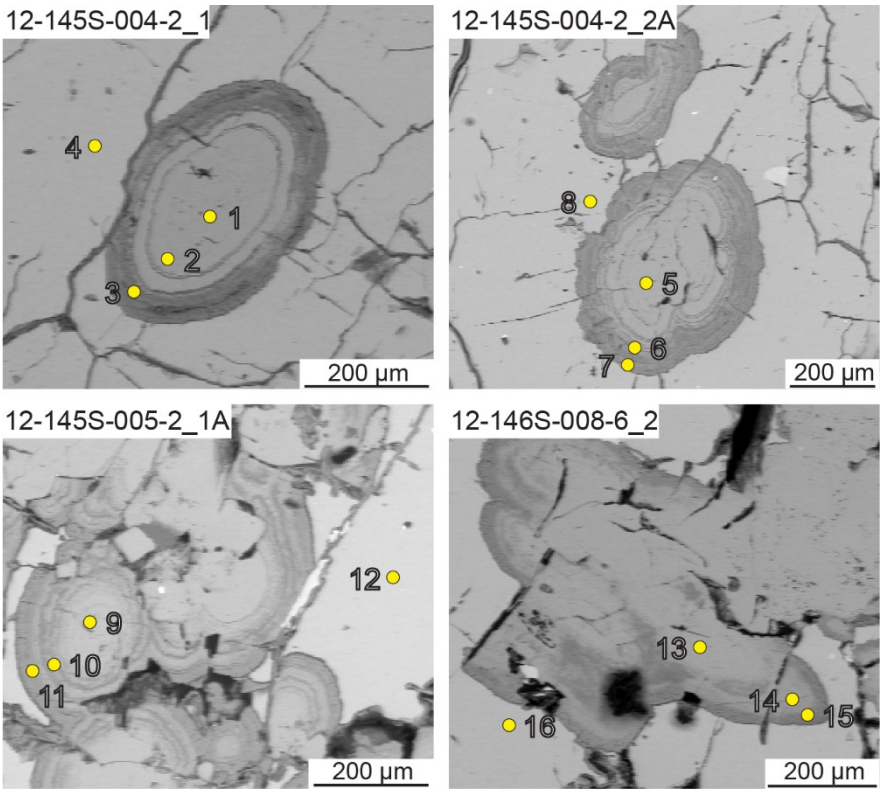

Figure 3-3. Backscattered electron images of concentric pyrite (Py1) in pyrrhotite showing locations of microprobe analyses in Table 2.

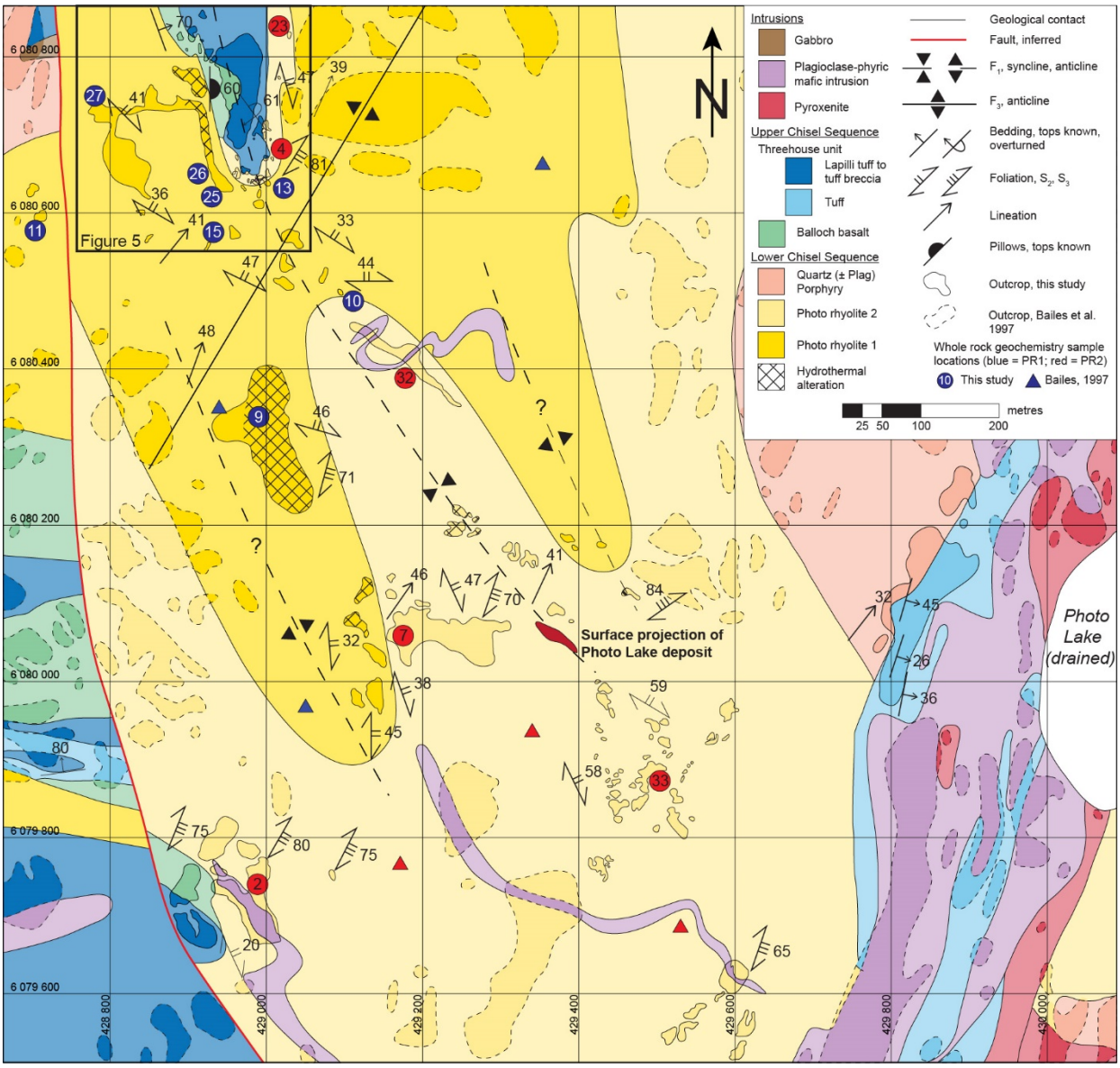

Figure 3-4. Geology of the Photo Lake area (see Fig. 2 for location). Box outlines map area in Figure 5. Sample locations refer to samples listed in Table 5.

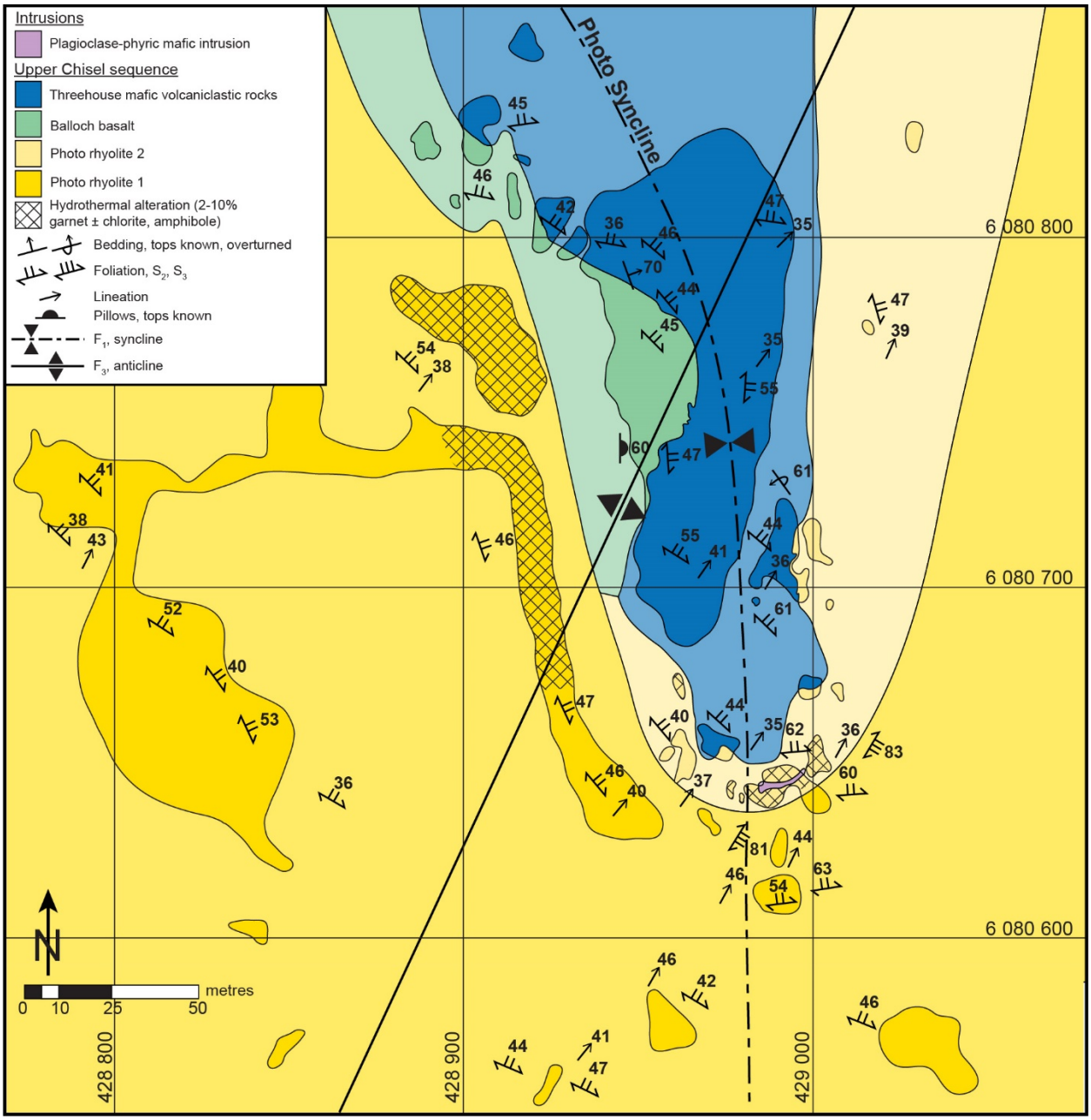

Figure 3-5. Geology of the Photo Lake quarry (see Fig. 4 for location).

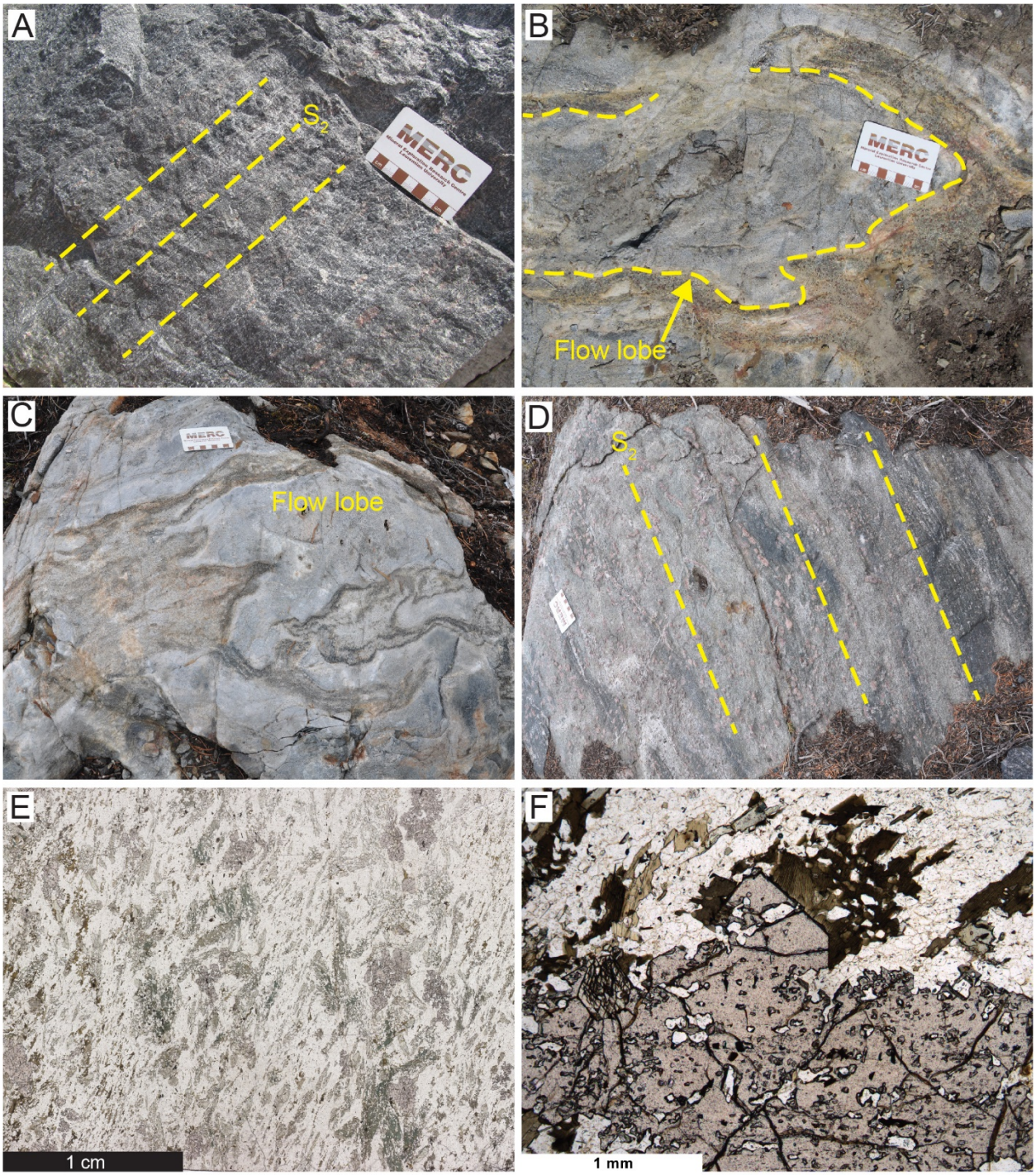

Figure 3-6. Geological characteristics of Photo rhyolite 1 (PR1). Scale card in field photographs is 9 cm in length. (A) Field photograph showing massive flow facies with strong S_2 spaced cleavage. (B) Field photograph showing lobe facies proximal to the contact with PR2. (C) Field

photograph showing lobes grading out into a fluidal flow top breccia marking the margins of the flow. (D) Field photograph showing flow banding overprinted by the strong S_2 cleavage. (E) Representative natural light photomicrograph of PR1. Large porphyroblasts of garnet, biotite, and amphibole are visible and define the S_2 fabric. (F) Natural light photomicrograph showing garnet porphyroblasts overgrowing biotite due to peak metamorphic reactions.

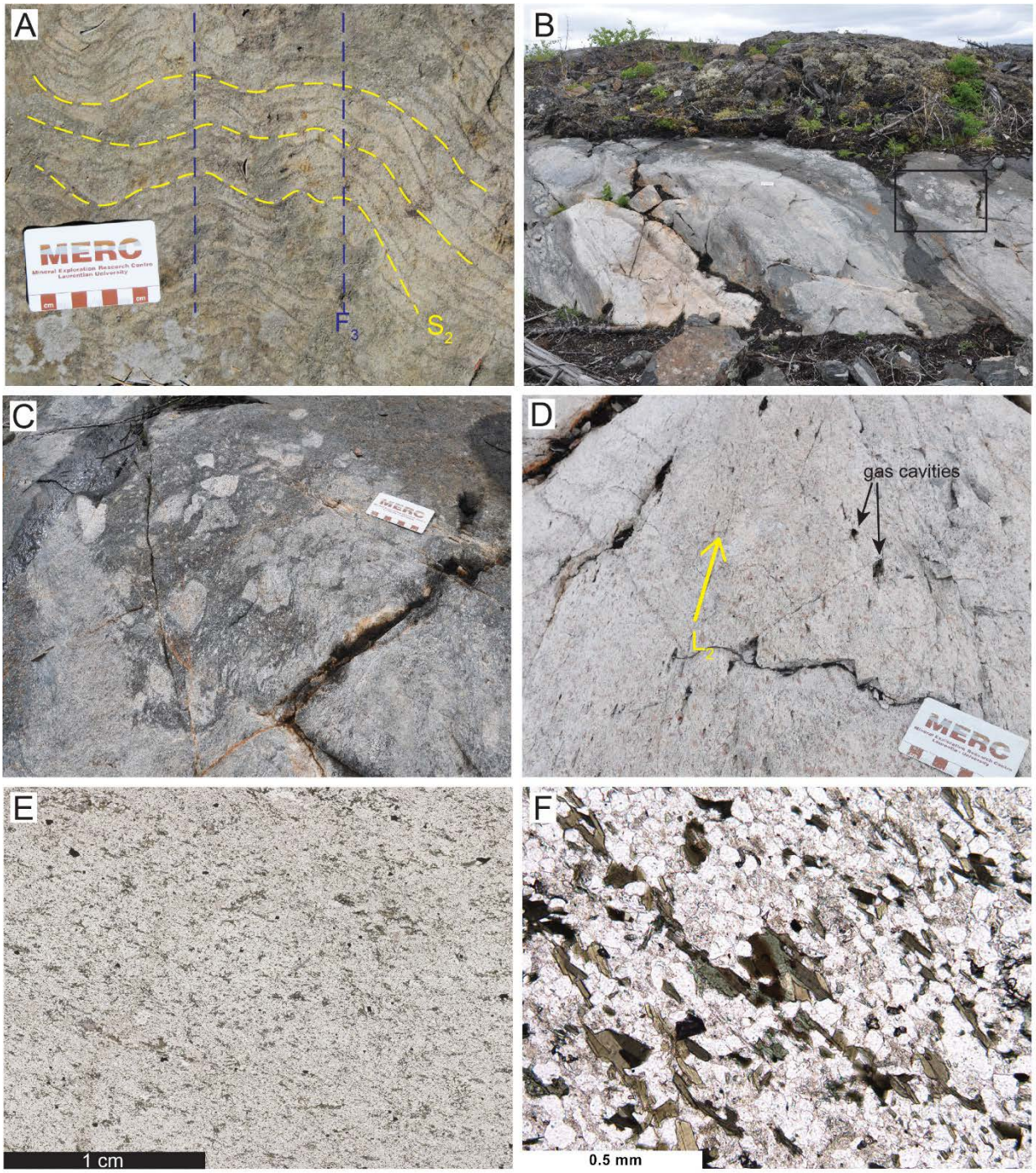

Figure 3-7. Geological characteristics of Photo rhyolite 2 (PR2). Scale card in field photographs is 9 cm in length. (A) Field photograph showing massive flow facies. Strong S_2 spaced cleavage is visible and refolded by open F_3 folds. (B) Field photograph showing breccia development along the margin of a lobe at the contact with the overlying Threehouse mafic volcaniclastic

rocks. Box outlines area shown in (C). (C) Field photograph showing brecciation along the margin of a rhyolite lobe. (D) Field photograph showing weakly altered massive flow facies proximal to the contact with the overlying Threehouse unit. Elongated gas cavities define L_2. (E) Representative natural light photomicrograph of PR2. (F) Natural light photomicrograph showing chloritization of biotite.

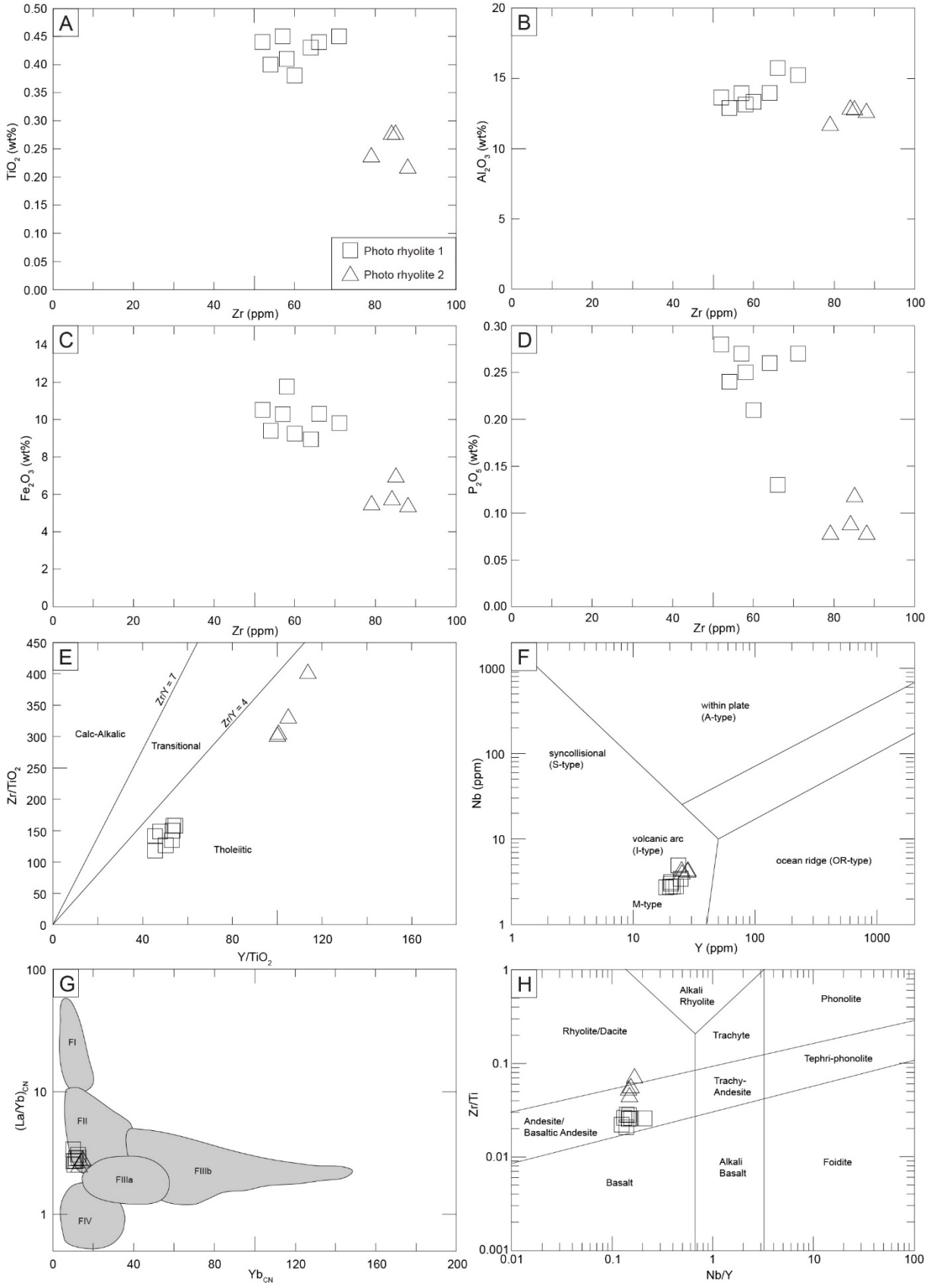
A
TiO2 (wt%)
Zr (ppm)
Photo rhyolite 1
Photo rhyolite 2
B
Al2O3 (wt%)
Zr (ppm)
C
Fe2O3 (wt%)
Zr (ppm)
D
P2O5 (wt%)
Zr (ppm)
E
Zr/TiO2
Y/TiO2
Zr/Y = 7
Zr/Y = 4
Calc-Alkalic
Transitional
Tholeiitic
F
Nb (ppm)
Y (ppm)
within plate
(A-type)
syncollisional
(S-type)
volcanic arc
(I-type)
ocean ridge (OR-type)
M-type
G
(La/Yb)CN
YbCN
FI
FII
FIIIa
FIIIb
FIV
H
Zr/Ti
Nb/Y
Alkali
Rhyolite
Phonolite
Rhyolite/Dacite
Trachyte
Tephri-phonolite
Trachy-
Andesite
Andesite/
Basaltic Andesite
Alkali
Basalt
Foidite
Basalt

Figure 3-8. Geochemical plots of least altered rhyolite in the Photo Lake area. (A-D) Binary plots of Zr vs. selected elements illustrating two distinct geochemical populations. (E) Y/TiO_2 vs. Zr/TiO_2 diagram (Lentz, 1998) showing a tholeiitic affinity for the two Photo rhyolite units. (F) Yb vs. Ta diagram (Pearce et al., 1984) showing the volcanic arc classification for the two Photo rhyolite units. (G) Yb_{CH} vs. $(La/Yb)_{CH}$ (Hart et al., 2004) showing that the two Photo rhyolite units plot in or near the FII field. (H) Discrimination diagram (Pearce, 1996) for the two Photo rhyolite units.

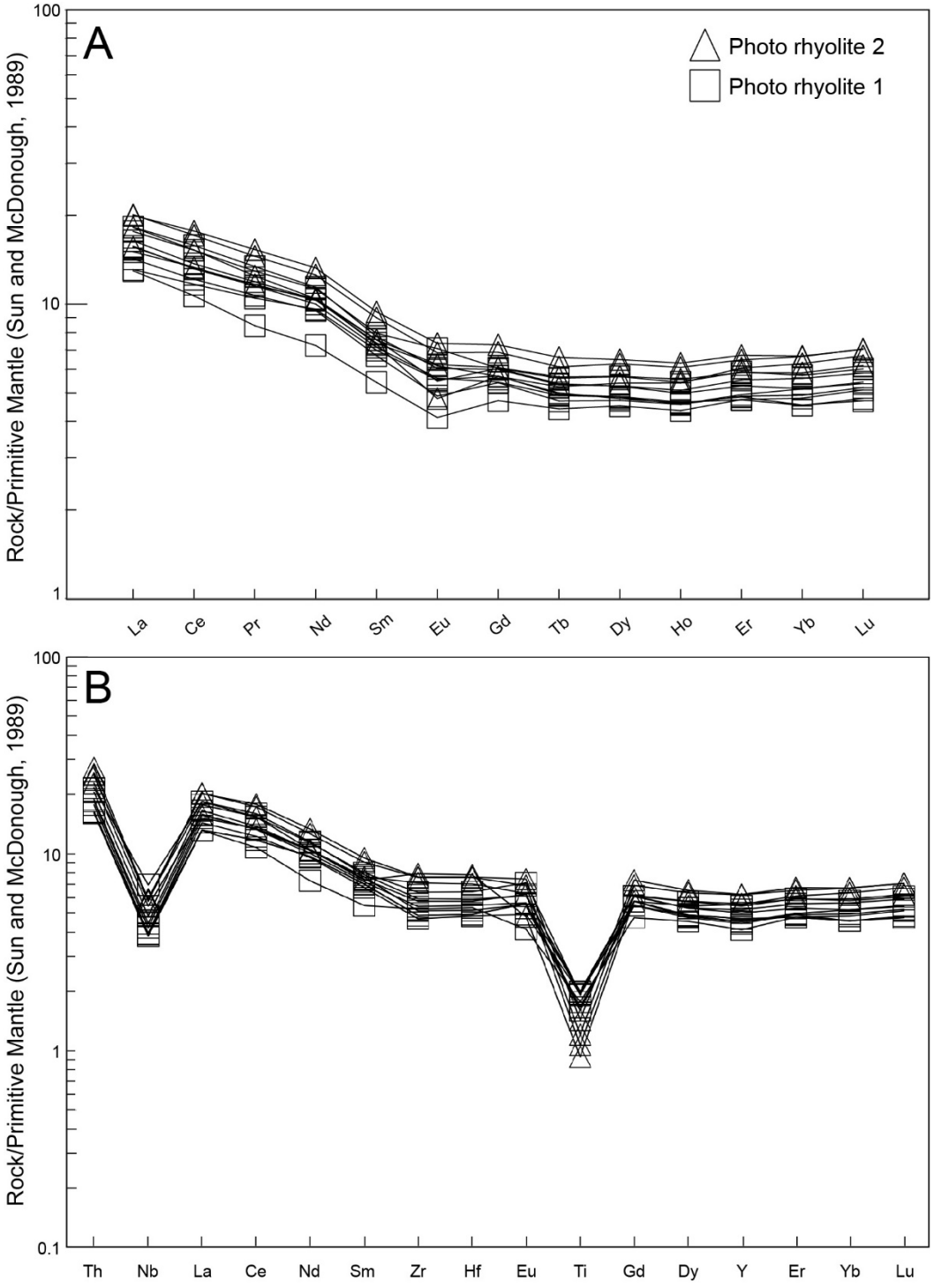

Figure 3-9. Primitive mantle-normalized trace element plots for the two Photo rhyolite units. Primitive mantle values from Sun and McDonough (1989). (A) REE; and (B) select trace elements.

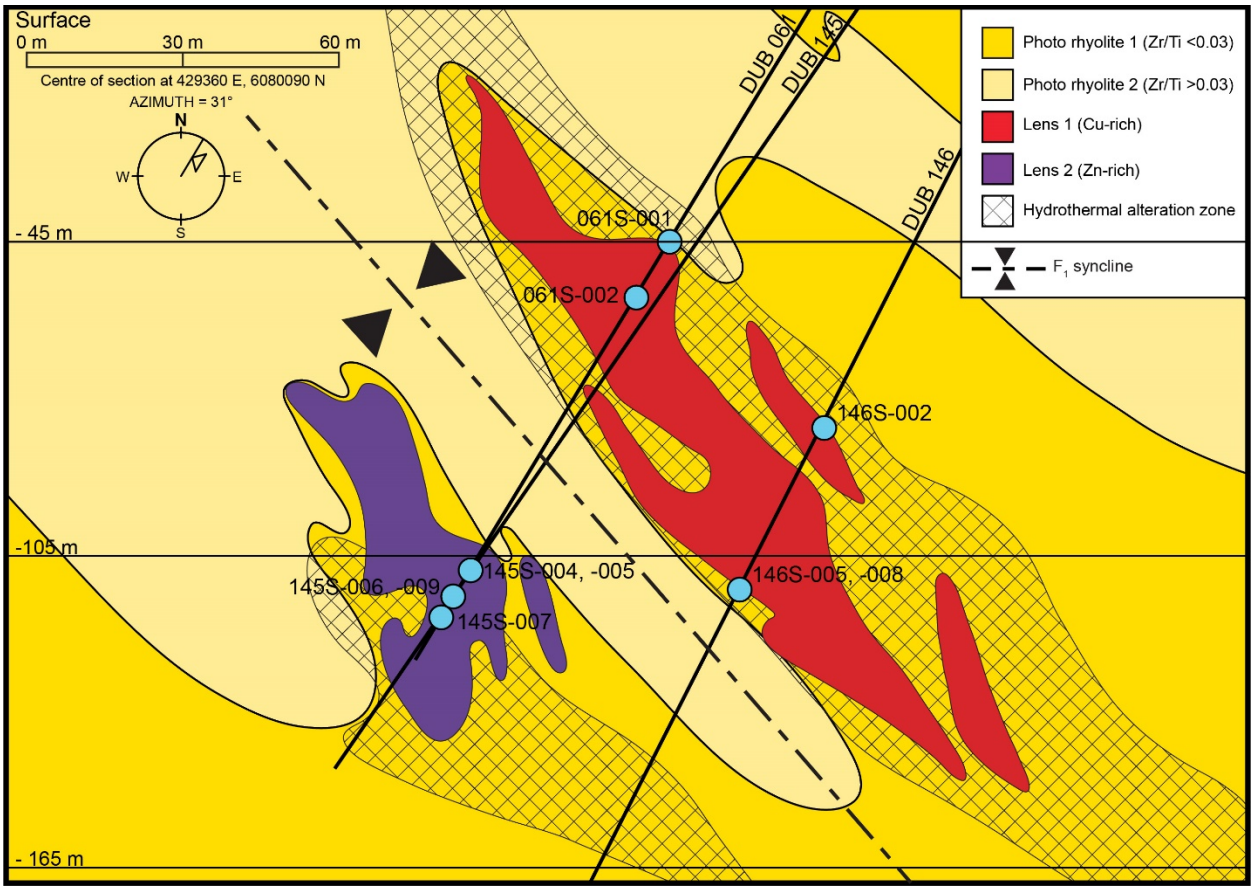

Figure 3-10. Geological cross-section through the Photo Lake deposit showing the distribution of the two Photo rhyolite units, the two ore lenses, and the alteration zone. The section is oriented along 031° looking towards 301°.

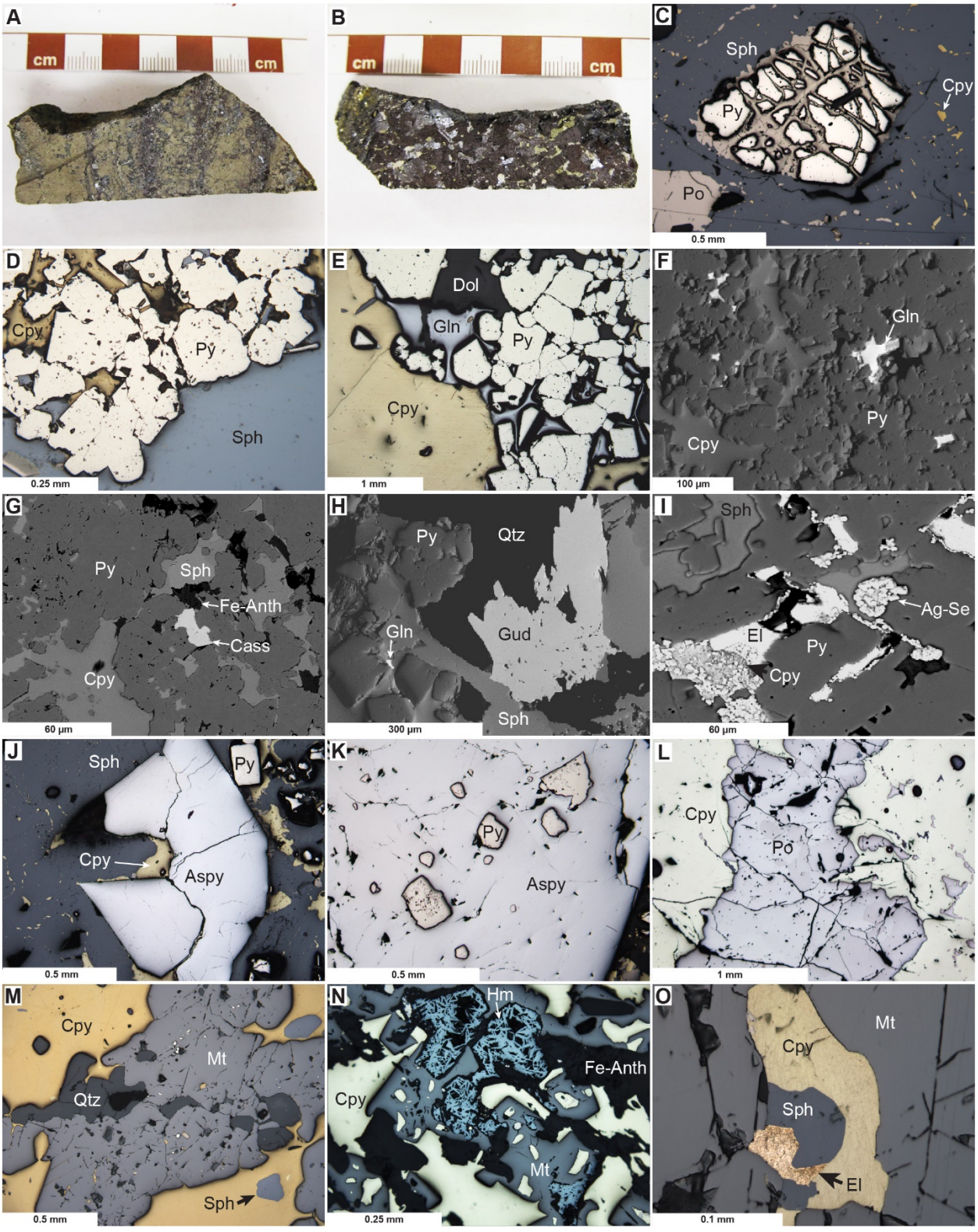
A
cm
cm
B
cm
cm
C
Sph
Cpy
Py
Po
0.5 mm
D
Cpy
Py
Sph
0.25 mm
E
Dol
Gln
Py
Cpy
1 mm
F
Gln
Py
Cpy
100 µm
G
Py
Sph
Fe-Anth
Cass
Cpy
60 µm
H
Py
Qtz
Gln
Gud
Sph
300 µm
I
Sph
Ag-Se
El
Py
Cpy
60 µm
J
Sph
Py
Cpy
Aspy
0.5 mm
K
Py
Aspy
0.5 mm
L
Cpy
Po
1 mm
M
Cpy
Mt
Qtz
Sph
0.5 mm
N
Hm
Fe-Anth
Cpy
Mt
0.25 mm
O
Mt
Cpy
Sph
El
0.1 mm

Figure 3-11. Core photographs, reflected light photomicrographs, and backscattered electron images of typical sulfide textures in the Photo Lake deposit. Ag-Se – Unidentified Ag-Se mineral phase, Aspy - Arsenopyrite, Cass – Cassiterite, Cpy - Chalcopyrite, Dol - Dolomite, El – Electrum, Fe-Anth – Ferro-anthophyllite, Gln - Galena, Gud – Gudmundite, Hm – Hematite, Mt – Magnetite, Po - Pyrrhotite, Py - Pyrite, Qtz – Quartz, Sph - Sphalerite. (A) Natural light photograph of banded massive chalcopyrite, pyrite, and sphalerite. (B) Natural light photograph of coarse recrystallized sphalerite with some chalcopyrite and carbonate. (C) Reflected light photomicrograph of brittle-deformed pyrite surrounded by sphalerite. Pyrrhotite fills the fractures surrounding the pyrite fragments. (D) Reflected light photomicrograph of recrystallized subhedral pyrite in a matrix of chalcopyrite and sphalerite. (E) Reflected light photomicrograph of recrystallized subhedral pyrite in a matrix of chalcopyrite, galena, and dolomite. (F) Scanning electron image of a large mass of recrystallized pyrite crystals in a matrix of chalcopyrite. Selenium-bearing galena occurs throughout matrix to the pyrite crystals and in areas is classified as clausthalite. (G) Scanning electron image of cassiterite cutting subhedral recrystallized pyrite crystals in a matrix of chalcopyrite and sphalerite. (H) Scanning electron image of a large crystal of gudmundite surrounded by quartz, sphalerite and pyrite. (I) Scanning electron image of ecrystallized pyrite crystals surrounded by electrum and an unidentified Ag-Se mineral phase. This mineral phase forms framboids as observed right of the centre of the image. (J) Reflected light photomicrograph of subhedral metamorphic arsenopyrite in a matrix of sphalerite and chalcopyrite. (K) Reflected light photomicrograph of inclusions of subhedral pyrite within a large crystal of arsenopyrite. (L) Reflected light photomicrograph of a pod of pyrrhotite within a matrix of chalcopyrite. (M) Reflected light photomicrograph of subhedral magnetite cut by quartz in a matrix of chalcopyrite. Inclusions in magnetite are electrum, galena, chalcopyrite, and

pyrrhotite. (N) Reflected light photomicrograph of acicular polycrystalline aggregates of hematite cut by ferro-anthophyllite and rimmed by magnetite in a matrix of chalcopyrite. (O) Reflected light photomicrograph of an inclusion of electrum with chalcopyrite and sphalerite in a subhedral crystal of magnetite.

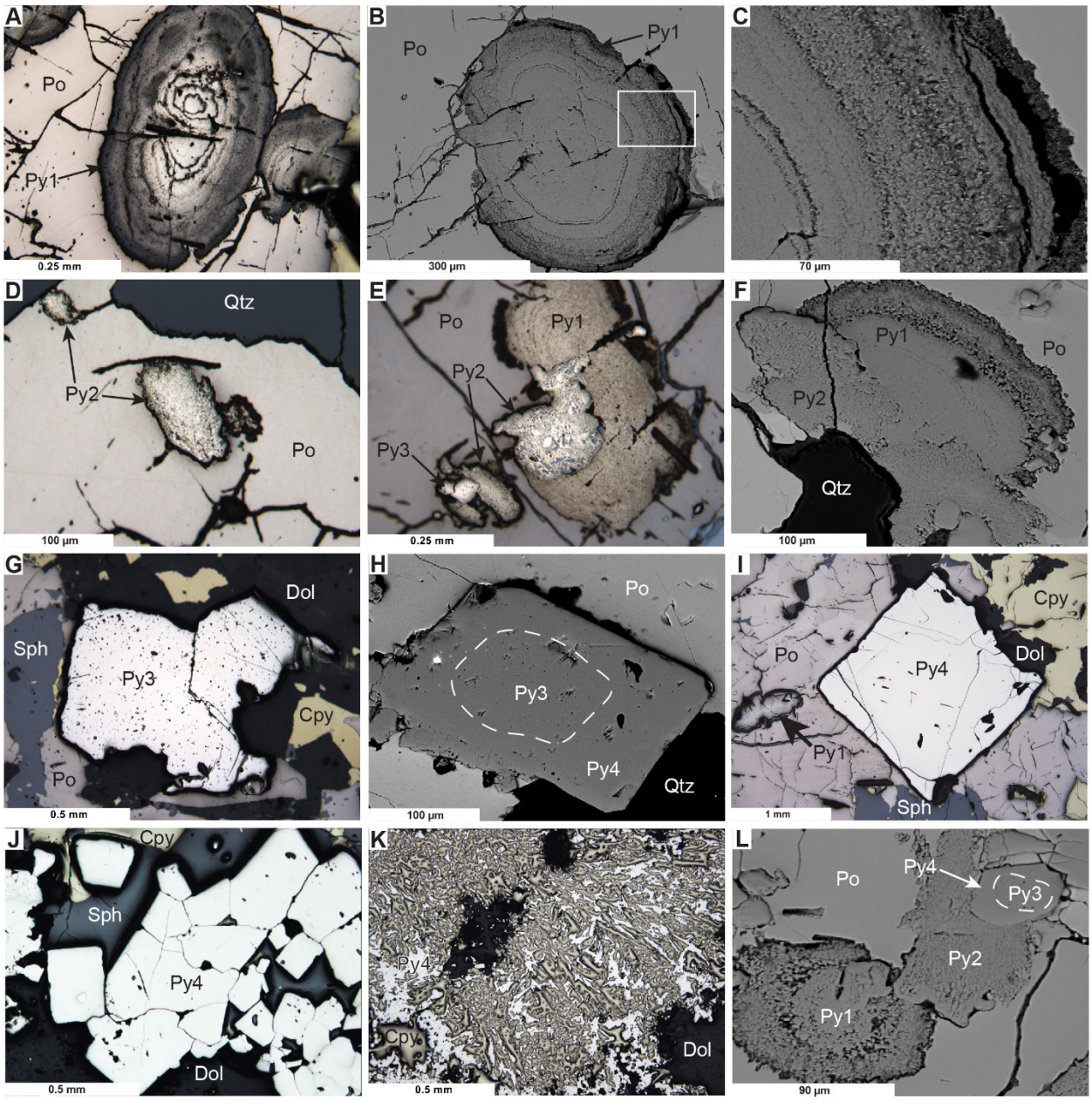

Figure 3-12. Reflected light photomicrographs and backscattered electron images illustrating the main pyrite textural varieties in the two ore lenses of the Photo Lake deposit. Cpy - Chalcopyrite, Dol - Dolomite, Po - Pyrrhotite, Py1 – Concentric pyrite, Py2 – Spongy pyrite, Py3 – Pitted pyrite, Py4 – Crystalline pyrite, Qtz – Quartz, Sph - Sphalerite. (A) Reflected light photomicrograph of concentric pyrite in a matrix of pyrrhotite. (B) Scanning electron image of

concentric pyrite in a matrix of pyrrhotite where the concentric bands are clearly cut by pyrrhotite. White box indicates area shown in (C). (C) Scanning electron image of pyrite bands in (B). Crystal growth is perpendicular to banding and indicates growth by void space filling. (D) Reflected light photomicrograph of anhedral spongy pyrite in a matrix of pyrrhotite. (E) Reflected light photomicrograph of spongy pyrite with inclusions of hematite cutting concentric pyrite. (F) Scanning electron image of spongy pyrite cutting concentric pyrite. (G) Representative reflected light photomicrograph of pitted pyrite with annealed grain boundaries. (H) Scanning electron image of pitted pyrite (white dashed line) with a rim of crystalline pyrite. (I) Reflected light photomicrograph of crystalline pyrite. (J) Reflected light photomicrograph of annealed crystalline pyrite with 120° dihedral grain boundaries. (K) Reflected light photomicrograph of skeletal crystalline pyrite with chalcopyrite. (L) Scanning electron image showing the full paragenesis of the four textural varieties of pyrite. Concentric pyrite is the earliest phase and is cut by spongy pyrite, which is in turn cut by pitted pyrite that is rimmed by crystalline pyrite.

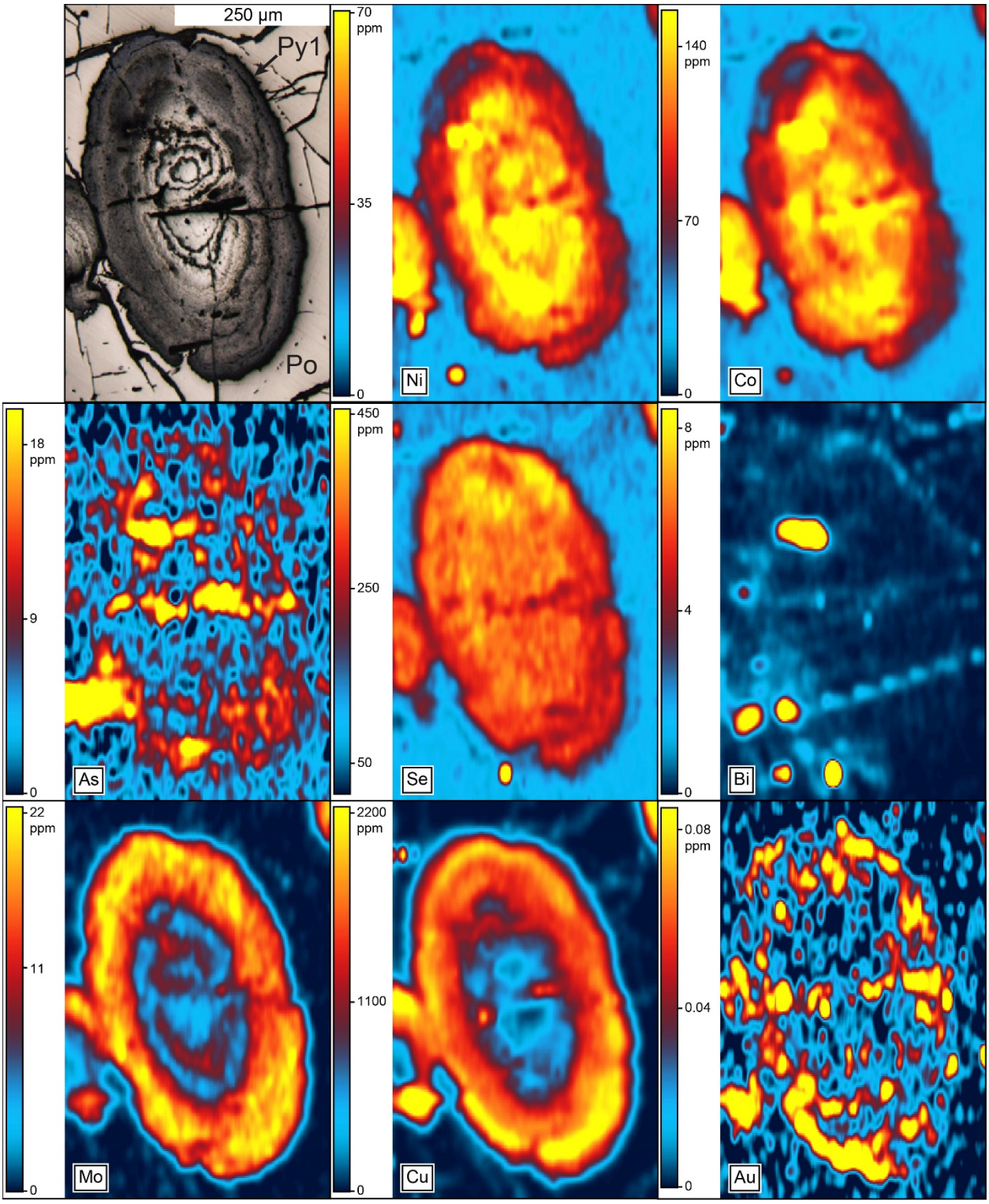

Figure 3-13. LA-ICP-MS trace element maps of concentric pyrite. Concentrations are semi-quantitative.

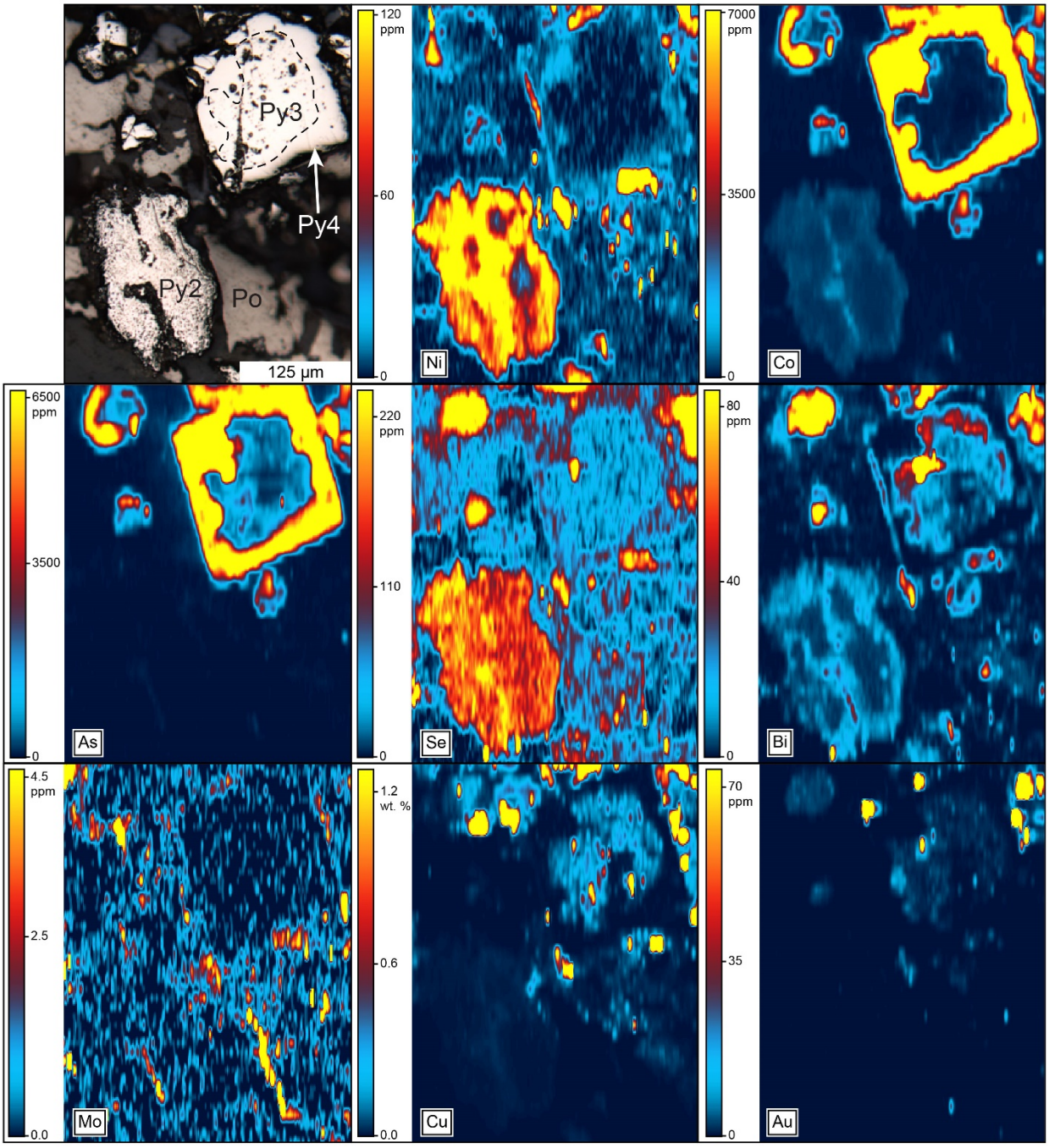

Figure 3-14. LA-ICP-MS trace element maps of spongy (Py2), pitted (Py3), and crystalline pyrite (Py4). Dashed line indicates boundary of Py3. Po – Pyrrhotite. Concentrations are semi-quantitative.

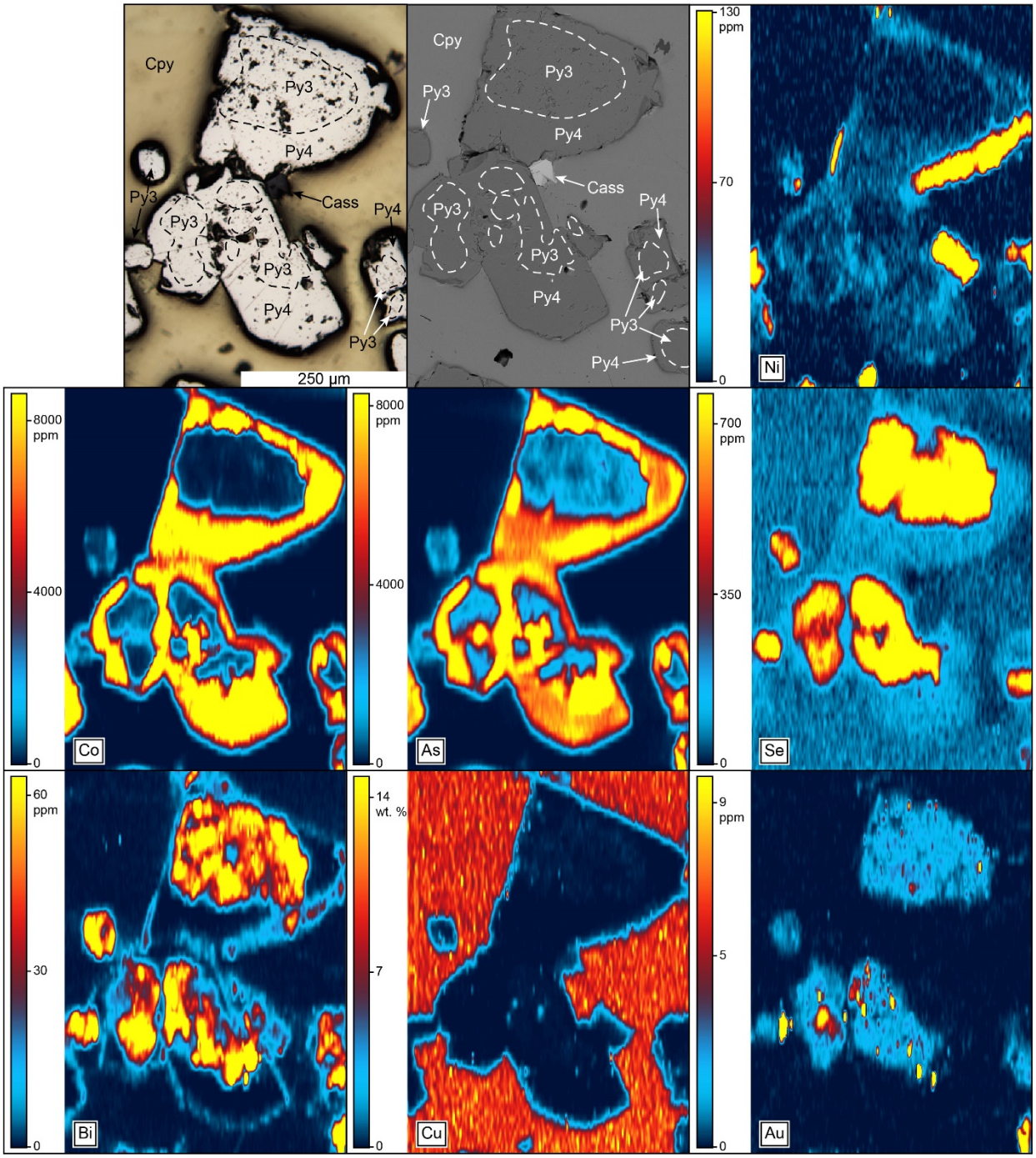

Figure 3-15. LA-ICP-MS trace element maps of crystalline pyrite (Py4) forming a rim around pitted pyrite (Py3). Dashed lines indicate boundaries of Py3. Cass – Cassiterite, Cpy – Chalcopyrite. Concentrations are semi-quantitative.

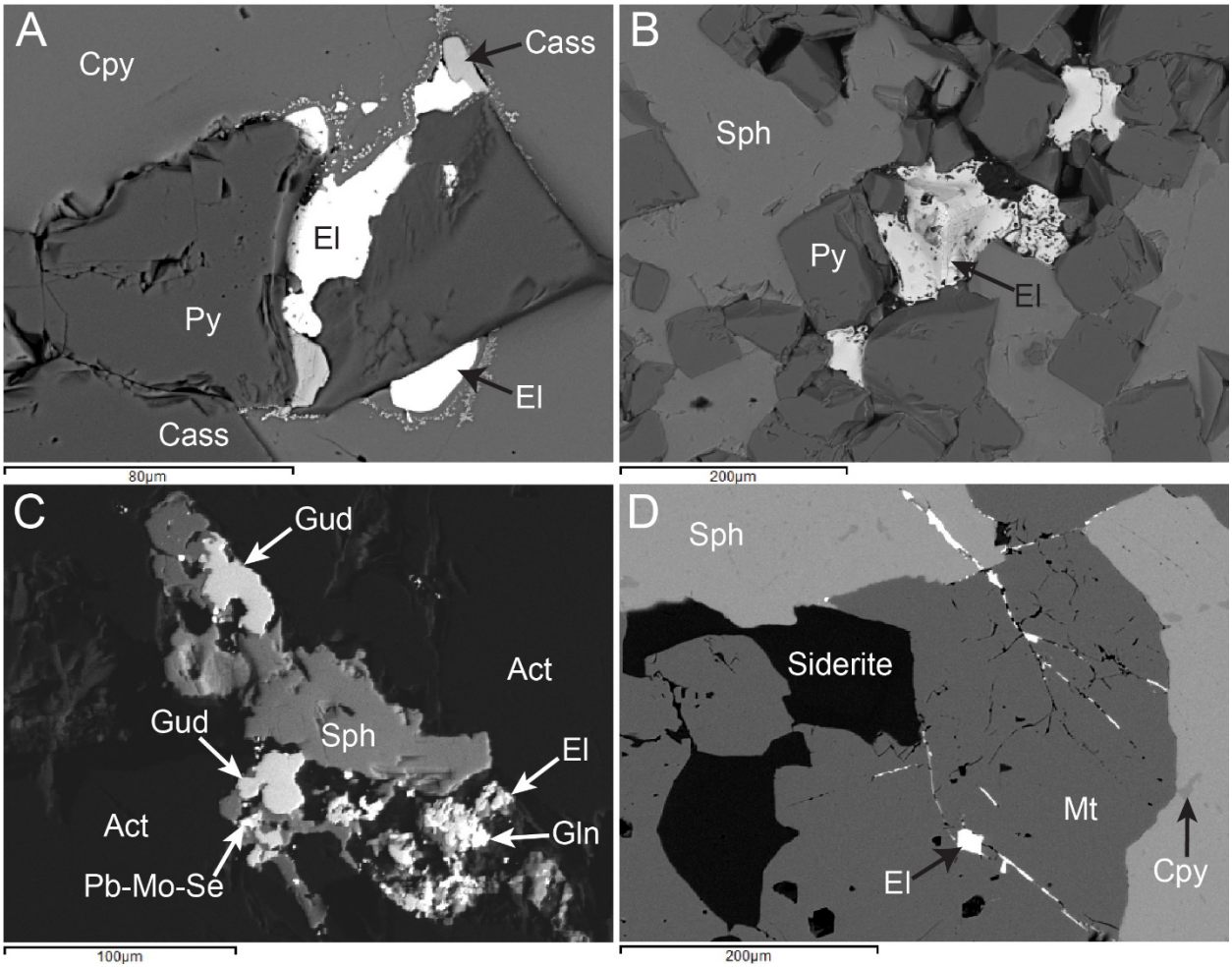

Figure 3-16. Backscattered electron images of Au-rich ores illustrating the mineral associations with electrum in the Photo Lake deposit. A, B, and C are taken from the #2 lens and D is taken from the #1 lens. Act - Actinolite, Cass - Cassiterite, Cpy - Chalcopyrite, El - Electrum, Gln - Galena, Gud - Gudmundite, Mt - Magnetite, Py - Pyrite, Sid – Siderite, Sph - Sphalerite. (A) Electrum and cassiterite cut pyrite. The exsolution around the electrum contains Ag and Cu. (B) Electrum occurs around pyrite grain boundaries. (C) Electrum is associated with gudmundite and galena and cuts actinolite. (D) Electrum crosscuts magnetite along fractures.

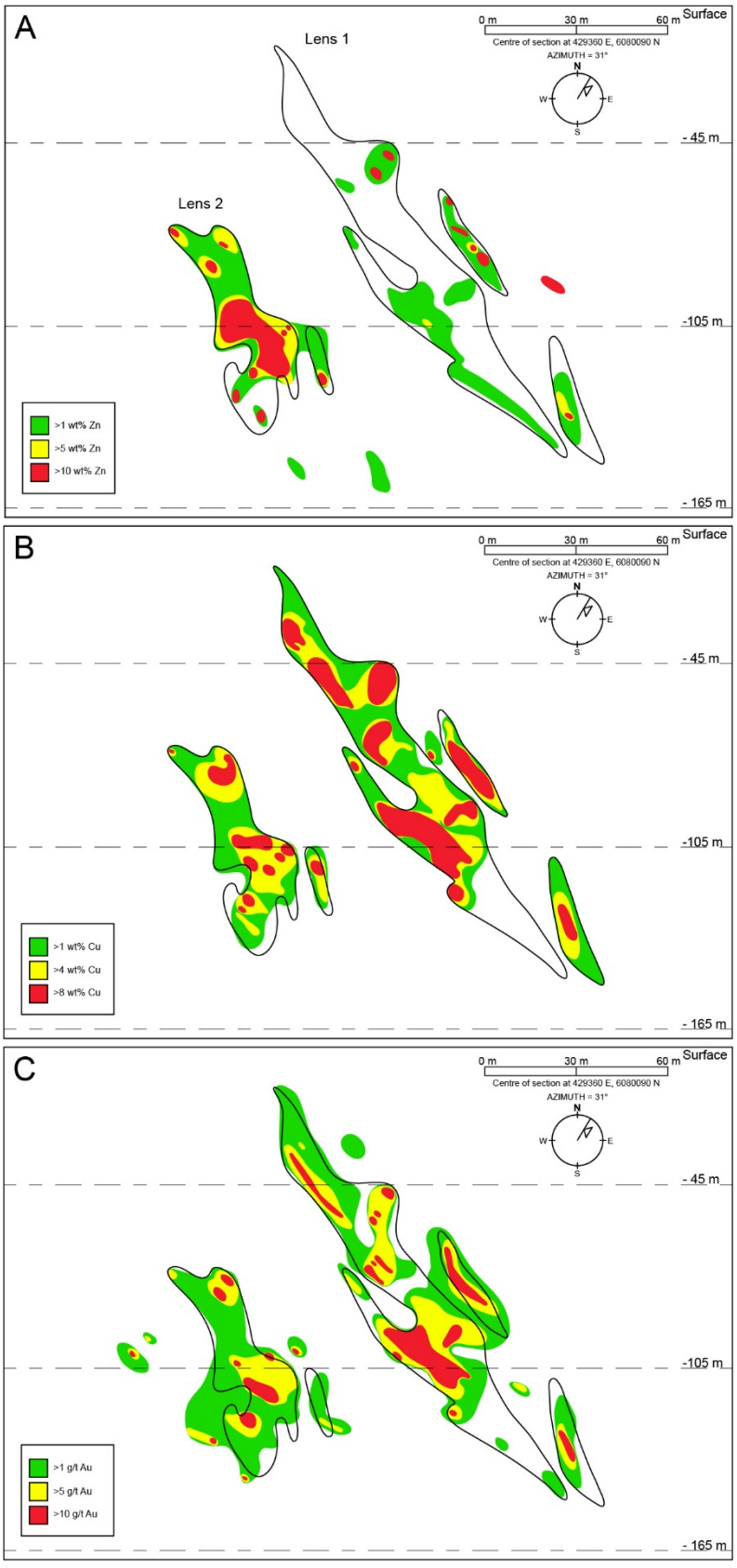
A
Lens 1
Lens 2
0 m
30 m
60 m
Surface
Centre of section at 429360 E, 6080090 N
AZIMUTH = 31°
N
W
E
S
- 45 m
-105 m
- 165 m
>1 wt% Zn
>5 wt% Zn
>10 wt% Zn
B
>1 wt% Cu
>4 wt% Cu
>8 wt% Cu
C
>1 g/t Au
>5 g/t Au
>10 g/t Au

Figure 3-17. Metal zoning contours showing the distribution of (A) Zn, (B) Cu, and (C) Au in the Photo Lake deposit, based on continuous assays along all drill holes. Drill holes shown in Figure 9A. Assays every 60 cm outside of the ore zones and every 30 cm within the ore zones. The highest Au grades are associated with Cu in the #1 lens. Metal concentrations from Hudson Bay Mining and Smelting Co. Ltd.

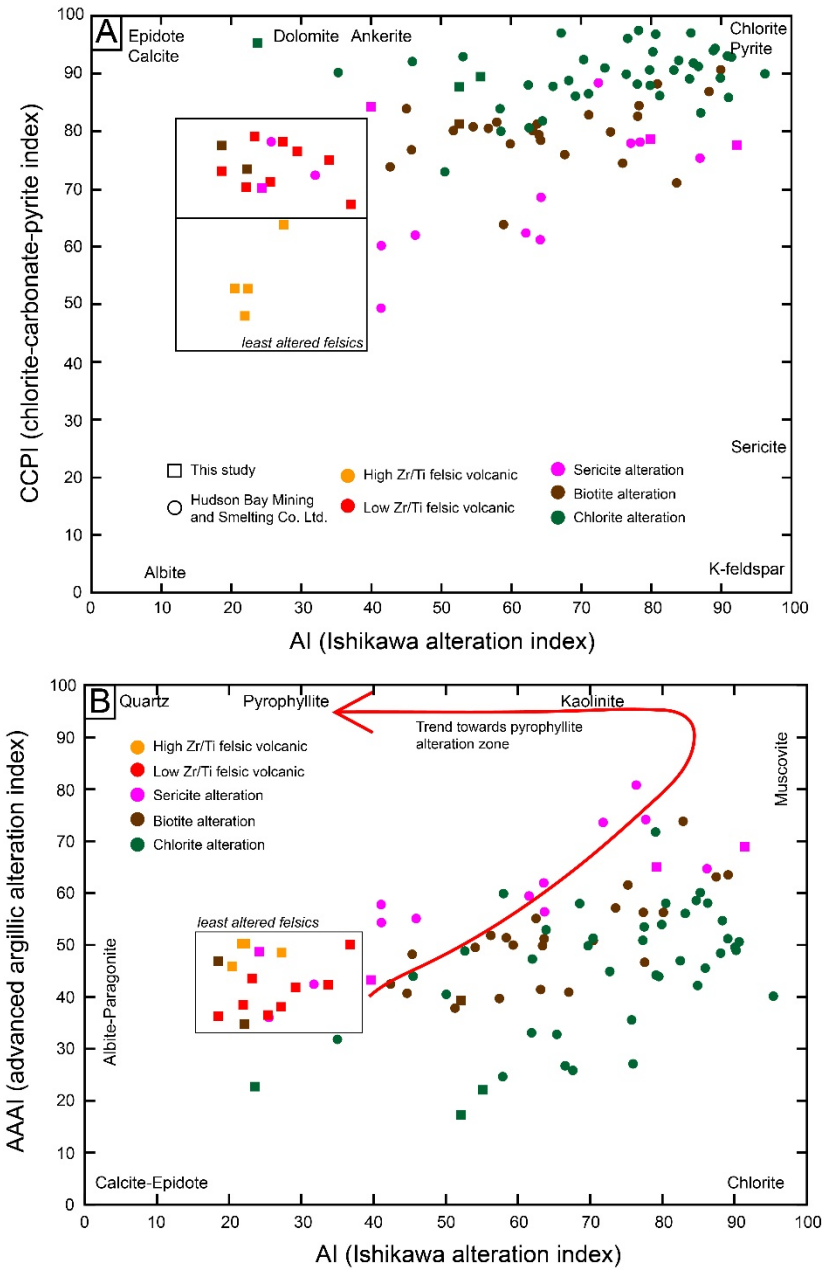

Figure 3-18. (A) Alteration box plot (Large et al., 2001) showing a distribution of the altered rocks in the Photo Lake deposit towards chlorite. (B) Plot of the Ishikawa alteration index (AI) versus the advanced argillic alteration index (AAAI; Williams and Davidson, 2004) showing a distribution of the altered rocks towards muscovite with no indication of a trend towards pyrophyllite as would be expected for advanced argillic alteration.

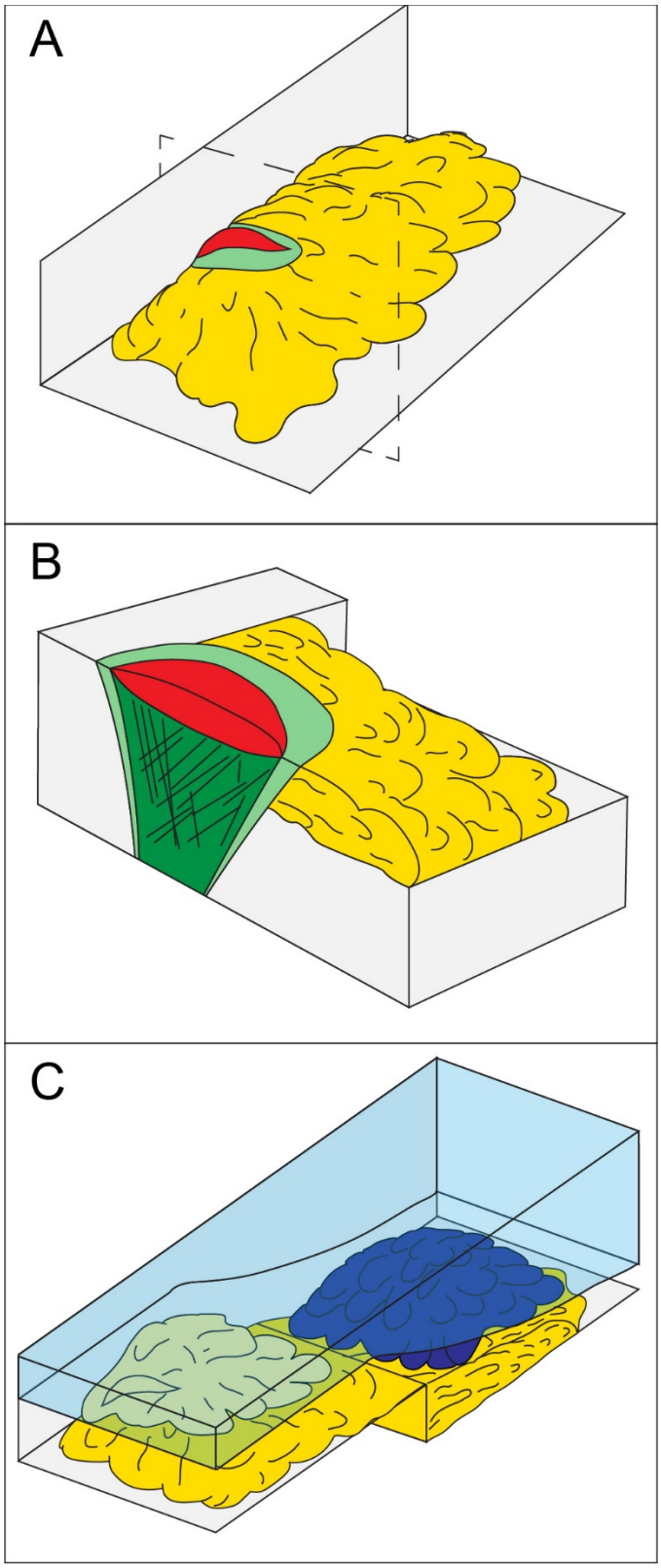
A
B
C

Figure 3-19. Schematic block diagram showing the evolution of the Photo Lake deposit and its host rocks. Diagram not to scale and only upper lobe facies of the Photo rhyolite complex shown. (A) Extrusion of Photo rhyolite 1 (yellow) along major crustal-scale fault and development of the Photo Lake deposit. Dotted line shows plane of cross-section in (B). (B) Cross-section through the Photo Lake deposit showing the discordant alteration and stringer sulfide zone beneath the massive sulfide lens. (C) Volcanic environment following eruption of Photo rhyolite 2, Balloch basalt, and Threehouse mafic volcaniclastic rocks. Photo rhyolite 2 has covered the massive sulfide lens, which is shown as an outline. Colours: dark yellow – Photo rhyolite; light yellow – Photo rhyolite 2; light green – discordant alteration zone; dark green – stringer mineralization (#1 lens) and discordant alteration zone; red – massive sulfide (#2 lens); dark blue – Balloch basalt; light blue – Threehouse mafic volcaniclastic rocks.

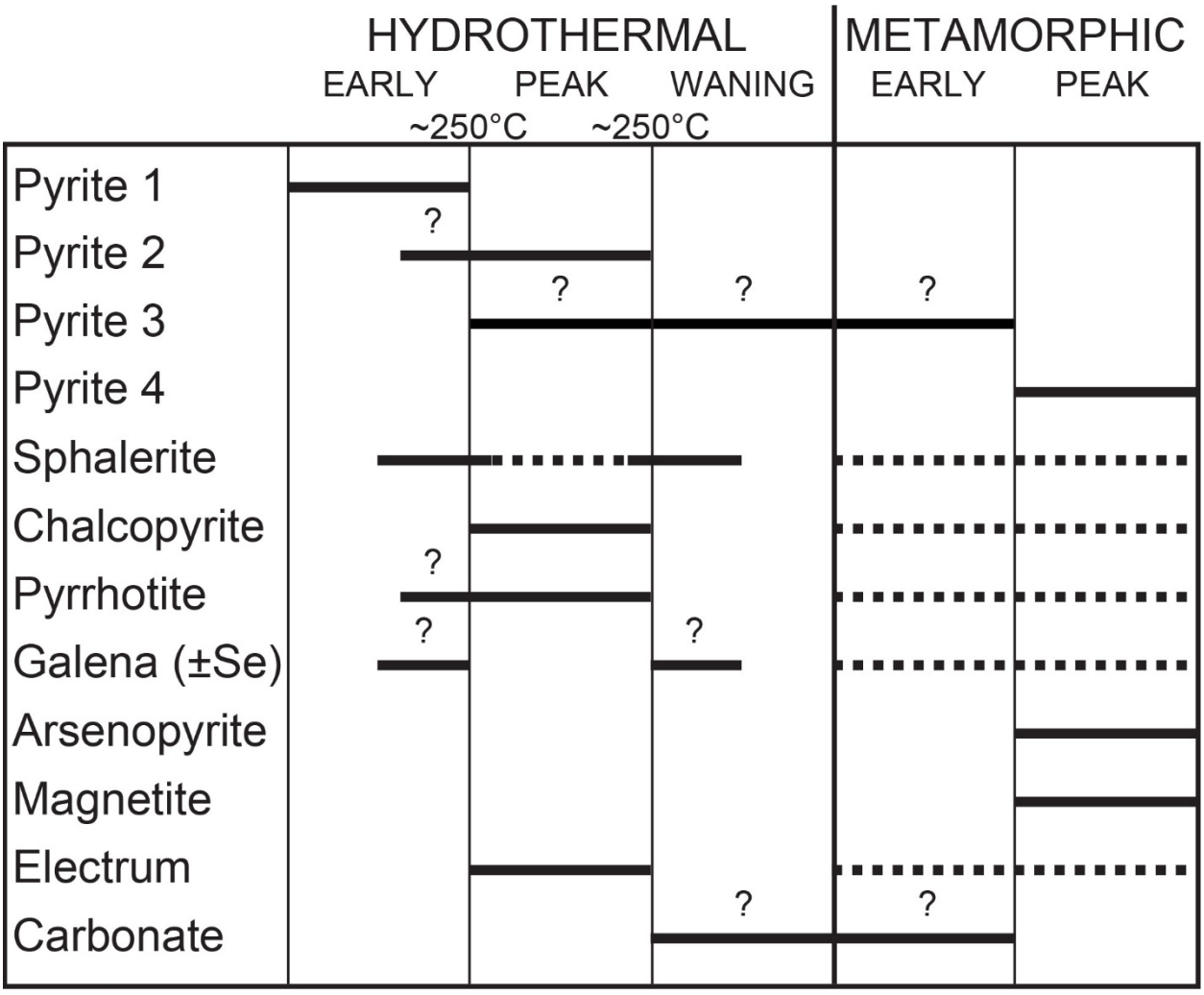

Figure 3-20. Post-metamorphic paragenetic sequence for the sulfides in the two ore lenses. Magnetite is only present in the #1 lens and arsenopyrite and galena are only present in the #2 lens. Non-sulfides are dolomite, calcic clinoamphibole and chlorite. The primary paragenesis is overprinted by metamorphism and deformation and is therefore assumed to approximate that of a typical VMS deposit. The dashed lines represent a mineral phase that was present at the time but dominantly mobile.

TABLE 1. Metal grades of the Anderson and Chisel sequence VMS deposits (modified from Galley et al., 2007b)

Deposit	**Au (g/t)**	**Ag (g/t)**	**Cu (%)**	**Zn (%)**	**Tonnes***
Chisel Sequence					
Photo Lake	4.87	29.49	4.58	6.35	689,885
Lalor**	2.90	34.1	0.70	8.19	13,200,000
Chisel Lake	1.77	44.77	0.54	10.60	7,153,536
Lost & Ghost	1.20	39.09	1.34	8.60	581,437
Chisel North	0.40	21.54	0.15	9.36	2,847,194
Anderson Sequence					
Rod	1.71	16.11	6.63	2.90	735,219
Stall Lake	1.41	12.34	4.41	0.50	6,381,129
Anderson	0.62	7.54	3.40	0.10	2,513,290

* Tonnages and grades are not NI 43-101 compliant.

** Lalor data from NI 43-101 inferred resources.

TABLE 2. EMPA data for concentric pyrite (Py1) and pyrrhotite in the sulfide lenses of the Photo Lake deposit

Sample	**12-145S-004-2_1**				**12-145S-004-2_2A**				**12-145S-005-2_1A**				**12-146S-008-6_2**			
Mineral	Pyrite			Pyrrhotite	Pyrite			Pyrrhotite	Pyrite			Pyrrhotite	Pyrite			Pyrrhotite
	core	inner rim	outer rim		core	inner rim	outer rim		core	inner rim	outer rim		core	inner rim	outer rim	
Site	1	2	3	4	5	6	7	8	9	10	11	12	13	14	15	16
S	52.38	52.45	4.53	39.46	51.71	30.91	13.88	39.45	52.02	35.69	20.96	39.80	52.37	40.39	2.39	39.63
Fe	45.96	45.85	53.77	60.92	46.56	48.87	53.12	60.82	46.09	47.03	51.66	61.26	45.54	46.24	53.55	60.74
Cu	-	-	-	-	0.01	-	0.02	-	0.01	0.01	-	0.01	-	-	-	-
As	0.01	0.02	0.03	0.02	0.01	0.01	0.02	0.02	-	0.02	0.03	0.03	-	0.01	0.05	0.01
Se	0.04	0.05	0.05	0.04	0.05	0.03	0.05	0.03	0.03	0.05	0.05	0.03	0.09	0.11	0.03	0.08
Co	-	0.01	-	-	-	-	-	-	0.01	-	-	0.01	0.03	0.03	0.01	-
Zn	-	-	0.16	-	0.01	0.02	0.08	-	0.01	0.11	0.14	-	0.01	0.02	0.03	-
Ni	-	-	-	-	-	-	-	-	-	-	0.01	-	-	-	0.01	-
Si	-	-	-	-	-	-	-	-	-	-	-	-	-	-	-	-
Ti	-	-	-	-	-	-	-	-	-	-	-	-	-	-	-	-
Total	98.38	98.39	58.54	100.44	98.35	79.86	67.16	100.33	98.16	82.91	72.85	101.15	98.04	86.80	56.07	100.47

TABLE 3. Ranges, Mean and 2σ Error Values for Geochemical Data for the Photo rhyolite units

	Range Photo Rhyolite 1 (n = 8)	Average Photo Rhyolite 1 (n = 8)	2σ	Range Photo Rhyolite 2 (n = 4)	Average Photo Rhyolite 2 (n = 4)	2σ
SiO_2 (wt%)	61.82 – 66.72	64.13	3.85	69.49 – 73.63	71.28	3.69
Al_2O_3	12.90 – 15.75	13.99	2.02	11.82 – 12.99	12.63	1.10
Fe_2O_3(T)	8.94 – 11.76	10.03	1.79	5.47 – 7.05	5.98	1.46
FeO^o	4.92 – 10.58	7.43	4.58	8.04 – 9.47	8.57	1.24
MnO	0.094 – 0.185	0.154	0.073	0.082 – 0.185	0.140	0.091
MgO	1.20 – 2.38	1.83	0.95	0.66 – 1.21	0.88	0.53
CaO	3.17 – 5.71	4.78	2.07	1.73 – 3.62	2.65	1.89
Na_2O	1.72 – 3.9	2.87	1.71	3.09 – 4.86	4.12	1.53
K_2O	0.21 – 2.08	0.98	1.19	0.88 – 1.29	1.14	0.36
TiO_2	0.38 – 0.45	0.43	0.05	0.22 – 0.28	0.26	0.06
P_2O_5	0.13 – 0.28	0.24	0.10	0.08 – 0.12	0.09	0.04
LOI	-0.2 – 1.86	0.59	1.37	0.60 – 1.51	1.11	0.79
Total	99.61 – 100.6	100.08	0.70	99.89 – 100.40	100.17	0.53
Cr (ppm)	14 – 20	16	4	23 – 29	25	6
Ni	1.70 – 3.10	2.46	1.04	1.70 – 3.50	2.48	1.67
Co	11.69 – 17.12	14.29	4.29	2.42 – 6.86	4.49	4.39
Sc	26.0 – 32.8	30.1	4.6	15.1 – 26.9	21.9	10.1
V	25.3 – 68.0	41.6	29.7	2.8 – 20.5	10.0	16.0
Cu	<1.4 – 39.1	17.3	35.8	3.1 – 33.6	18.7	25.2
Pb	1.3 – 5.2	2.7	3.0	1.1 – 4.1	2.9	2.6
Zn	64 – 133	99	48	65 – 116	87	47
In	0.0520 – 0.0832	0.0643	0.0196	0.0420 – 0.0790	0.0681	0.0353
Sn	0.40 – 0.97	0.69	0.45	0.92 – 1.16	1.04	0.20
Mo	0.63 – 1.71	1.10	0.67	1.39 – 2.59	1.94	0.99
Sb	0.05 – 0.20	0.10	0.09	0.07 – 0.16	0.11	0.08
Rb	0.76 – 28.23	12.62	17.56	10.10 – 19.07	15.35	8.35
Cs	<0.013 – 1.585	0.641	0.922	0.413 – 0.811	0.575	0.350
Ba	67.4 – 416.9	234.6	230.9	291.9 – 391.4	336.2	97.5
Sr	102.4 – 230.8	165.8	103.4	98.0 – 269.1	162.8	154.3
Tl	0.005 – 0.152	0.055	0.088	0.026 – 0.064	0.047	0.038
Ga	12.38 – 16.45	14.67	2.65	12.22 – 14.66	13.35	2.22
Ta	0.130 – 0.317	0.171	0.122	0.198 – 0.215	0.210	0.016
Nb	2.708 – 4.913	3.184	1.478	3.852 – 4.159	4.054	0.283
Hf	1.48 – 1.97	1.68	0.33	2.16 – 2.40	2.31	0.20
Zr	52 – 71	60	13	79 – 88	84	7
Y	18.63 – 24.56	21.41	3.93	24.98 – 28.12	26.57	3.45
Ti	2066 – 2578	2390	400	1201 – 1847	1495	552
Th	1.360 – 1.827	1.540	0.349	1.926 – 2.312	2.122	0.317
U	0.543 – 0.850	0.613	0.203	0.677 – 0.908	0.826	0.205
La	8.92 – 12.56	10.61	2.70	10.73 – 13.84	12.72	2.91
Ce	18.95 – 28.08	23.48	6.17	23.60 – 31.46	28.15	7.11
Pr	2.331 – 3.704	3.139	0.855	3.219 – 4.232	3.727	0.951
Nd	9.80 – 15.45	13.52	3.54	13.97 – 17.98	15.77	4.06
Sm	2.408 – 3.536	3.156	0.710	3.241 – 4.184	3.695	0.928
Eu	0.6919 – 1.1866	0.9430	0.2956	0.8025 – 1.2368	1.0588	0.3752
Gd	2.80 – 3.61	3.36	0.54	3.39 – 4.34	3.86	0.86
Tb	0.4760 – 0.6046	0.5428	0.0836	0.5656 – 0.7120	0.6374	0.1263
Dy	3.326 – 4.179	3.674	0.561	3.974 – 4.777	4.392	0.746
Ho	0.7131 – 0.8907	0.7839	0.1165	0.8859 – 1.0340	0.9579	0.1408
Er	2.271 – 2.826	2.447	0.405	2.810 – 3.217	3.011	0.368
Tm	0.3356 – 0.4149	0.3646	0.0597	0.4304 – 0.4902	0.4646	0.0555
Yb	2.233 – 2.824	2.490	0.440	2.881 – 3.286	3.133	0.378
Lu	0.3474 – 0.4461	0.3928	0.0690	0.4579 – 0.5213	0.4982	0.0592

TABLE 4. Ranges, Mean and 2σ Error Values for Geochemical Data for Mineralized Samples from the Photo Lake Deposit

	Range #1 Lens (n = 6)	Average #1 Lens (n = 6)	2σ	Range #2 Lens (n = 14)	Average #2 Lens (n = 14)	2σ
Cu (wt%)	1.1 – 20.3	6.7	10.5	8.2 – 18.5	14.3	6.9
Fe	12.9 – 47.7	28.3	20.5	36.2 – 47.7	40.9	10.8
Zn	3.75 – 37.15	21.31	24.98	1.13 – 3.91	2.83	2.30
S	27.3 – 42.8	35.4	8.0	24.5 – 37.7	28.9	9.1
CO_2	0.26 – 4.11	1.59	2.33	0.08 – 10.90	6.53	7.10
Ag (ppm)	43.06 – 175.86	99.35	88.79	45.70 – 107.02	75.74	40.76
As	509.0 – 977.5	773.0	238.7	55.5 – 388.0	159.8	237.3
Au	0.257 – 51.691	10.760	29.478	6.286 – 44.863	17.038	28.133
Bi	0.33 – 87.93	16.29	48.97	14.15 – 62.45	25.04	37.25
Co	13 – 784	413	630	155 – 835	405	529
Hg	31.93 – 180.56	82.72	95.71	13.43 – 36.06	27.24	15.12
In	3.946 – 66.350	29.978	39.153	13.773 – 19.273	17.228	4.252
Mo	0.58 – 4.22	1.87	1.98	0.56 – 1.17	0.84	0.50
Ni	1.2 – 19.8	8.3	8.9	5.4 – 8.6	6.4	2.3
Pb	51 – 25296	2396	13282	76 – 136	101	45
Sb	15.28 – 78.44	51.62	49.49	7.50 – 19.50	11.28	8.39
Se	93.7 – 360.3	207.1	147.7	389.1 – 561.8	491.9	127.3
Sn	6.69 – 219.64	85.20	139.05	25.15 – 40.09	32.31	10.20
Te	0.09 – 3.42	0.65	1.70	2.28 – 3.40	2.82	0.82

Note: Cu analyzed by AAS-Flame; Fe, Zn, Co, Pb analyzed by ICP-AES; S, CO_2 analyzed by infrared absorption; all other elements analyzed by ICP-MS.

TABLE 5. Mineralogical and geochemical characteristics of the two Photo rhyolite units.

Samples	Mineralogy	Chemistry	Element Ratios and Abundances
Photo Rhyolite 1 12-ME-009 12-ME-010 12-ME-011 12-ME-013 12-ME-015 12-ME-025 12-ME-026 12-ME-027	• ~50-60% matrix of recrystallized quartz and feldspar (oligoclase to albite, trace orthoclase) with consistently more quartz than feldspar; annealed grain boundaries • Up to 40% amphibole porphyroblasts (cummingtonitegrunerite and actinolite moving towards hornblende); calcic amphiboles form rims on ferromagnesian amphiboles (Fig. 5e) • Up to 10% biotite porphyroblasts (Fig. 5e) • Up to 10% inclusion-rich almandine garnet porphyroblasts (Fig. 5f) • Up to 5% epidote-clinozoisite • Trace subhedral to euhedral magnetite porphyroblasts • Trace calcite throughout matrix; spatial association with garnet • Trace sericitization of feldspar	• Tholeiitic affinity according to Lentz, 1998 diagram (Fig. 7e) • HFSE content characteristic of volcanic arc rocks with I-type affinity (Fig. 7f) • FII rhyolite according to Hart et al., 2004 diagram (7g) • Elevated LREE pattern with a negative slope to Eu, slight negative Eu anomaly to no anomaly, and flat HREE pattern on PM-normalized REE diagram (Fig. 8a) • Negative Nb and Ti anomalies on PM-normalized multi-element diagram (Fig. 8b)	Zr/TiO_2 = 0.012 – 0.016 Zr/Al_2O_3 = 0.00038 – 0.00047 Zr/P_2O_5 = 0.0057 – 0.017 $Zr/Fe_2O_{3(total)}$ = 2.0 x 10^{-7} – 3.0 x 10^{-7} Zr/Co = 3.2 – 5.8 Zr/Sc = 0.00066 – 0.0010 Zr/V = 0.72 – 1.5 $(La/Sm)_{PM}$ = 1.88 – 2.39 $(La/Yb)_{PM}$ = 2.71 – 3.62 Eu/Eu* = 0.804 – 1.01
Photo Rhyolite 2 12-ME-002 12-ME-004 12-ME-023 12-ME-032	• ~80-85% matrix of recrystallized quartz and feldspar (oligoclase to albite, trace orthoclase) with approximately 70-75% quartz and 10-15% feldspar; annealed grain boundaries (Fig. 6e) • 0-12% amphibole (actinolite moving towards hornblende) • 0-10% biotite and chloritized biotite; biotite is dominant in samples absent of amphibole; much more fine-grained than amphibole when amphibole is present (Fig. 6f) • Trace to 3% inclusion-rich almandine garnet porphyroblasts • ~2-3% muscovite • Trace to 1% subhedral to euhedral magnetite porphyroblasts • Trace calcite throughout matrix; very little to no calcite when calcic amphibole is present • Trace epidote in samples absent of calcite • Trace sericitization of feldspar	• Tholeiitic affinity according to Lentz, 1998 diagram (Fig. 7e) • HFSE content characteristic of volcanic arc rocks with I-type affinity (Fig. 7f) • FII rhyolite according to Hart et al., 2004 diagram (7g) • Elevated LREE pattern with a negative slope to Eu, slight negative Eu anomaly, and flat HREE pattern on PM-normalized REE diagram (Fig. 8a) • Negative Nb and Ti anomalies on PM-normalized multi-element diagram (Fig. 8b)	Zr/TiO_2 = 0.030 – 0.040 Zr/Al_2O_3 = 0.00065 – 0.00069 Zr/P_2O_5 = 0.021 – 0.034 $Zr/Fe_2O_{3(total)}$ = 6.5 x 10^{-7} – 1.3 x 10^{-6} Zr/Co = 13 – 33 Zr/Sc = 0.0017 – 0.0049 Zr/V = 2.6 – 16 $(La/Sm)_{PM}$ = 2.06 – 2.50 $(La/Yb)_{PM}$ = 2.67 – 3.04 Eu/Eu* = 0.736 – 0.913

TABLE 6. Pearson's correlation coefficients of selected elements for the sulfides in the Photo lake deposit (data are based on sulfides normalized to 100 wt%).

	Ag	As	Au	Bi	Co	Cu	Fe	Hg	In	Mo	Ni	Pb	Sb	Se	Sn	Te	Zn	CO2	S
Ag		0.26	0.33	0.23	0.17	0.14	0.25	-0.20	-0.13	-0.01	0.69	0.48	0.35	-0.04	0.40	0.05	-0.29	-0.15	0.24
As	0.26		-0.21	-0.08	0.03	-0.72	-0.62	0.63	0.25	0.32	0.16	0.27	0.60	-0.87	0.27	-0.71	0.66	-0.65	0.53
Au	0.33	-0.21		-0.08	-0.19	0.48	0.28	-0.07	-0.11	-0.25	0.00	-0.21	-0.05	0.32	0.11	0.15	-0.36	0.20	-0.14
Bi	0.23	-0.08	-0.08		0.16	-0.15	0.42	-0.34	-0.52	-0.24	0.44	0.75	-0.08	0.34	-0.40	0.67	-0.34	-0.14	0.29
Co	0.17	0.03	-0.19	0.16		-0.10	0.51	-0.53	-0.28	-0.18	0.31	-0.06	0.45	-0.10	-0.02	0.06	-0.40	-0.01	0.49
Cu	0.14	-0.72	0.48	-0.15	-0.10		0.57	-0.55	-0.27	-0.34	-0.01	-0.36	-0.20	0.63	0.34	0.38	-0.69	0.43	-0.39
Fe	0.25	-0.62	0.28	0.42	0.51	0.57		-0.90	-0.60	-0.42	0.36	0.03	-0.02	0.60	-0.14	0.64	-0.93	0.31	0.16
Hg	-0.20	0.63	-0.07	-0.34	-0.53	-0.55	-0.90		0.61	0.33	-0.48	-0.10	0.11	-0.55	0.07	-0.62	0.87	-0.41	-0.03
In	-0.13	0.25	-0.11	-0.52	-0.28	-0.27	-0.60	0.61		0.55	-0.36	-0.33	-0.03	-0.29	0.19	-0.53	0.68	-0.33	-0.12
Mo	-0.01	0.32	-0.25	-0.24	-0.18	-0.34	-0.42	0.33	0.55		0.07	0.05	0.01	-0.51	0.34	-0.49	0.51	-0.44	0.15
Ni	0.69	0.16	0.00	0.44	0.31	-0.01	0.36	-0.48	-0.36	0.07		0.71	0.29	-0.09	0.12	0.22	-0.32	-0.16	0.38
Pb	0.48	0.27	-0.21	0.75	-0.06	-0.36	0.03	-0.10	-0.33	0.05	0.71		0.00	-0.04	-0.20	0.37	-0.01	-0.20	0.20
Sb	0.35	0.60	-0.05	-0.08	0.45	-0.20	-0.02	0.11	-0.03	0.01	0.29	0.00		-0.60	0.41	-0.55	0.08	-0.54	0.67
Se	-0.04	-0.87	0.32	0.34	-0.10	0.63	0.60	-0.55	-0.29	-0.51	-0.09	-0.04	-0.60		-0.36	0.83	-0.65	0.55	-0.45
Sn	0.40	0.27	0.11	-0.40	-0.02	0.34	-0.14	0.07	0.19	0.34	0.12	-0.20	0.41	-0.36		-0.46	0.08	-0.30	0.00
Te	0.05	-0.71	0.15	0.67	0.06	0.38	0.64	-0.62	-0.53	-0.49	0.22	0.37	-0.55	0.83	-0.46		-0.67	0.51	-0.35
Zn	-0.29	0.66	-0.36	-0.34	-0.40	-0.69	-0.93	0.87	0.68	0.51	-0.32	-0.01	0.08	-0.65	0.08	-0.67		-0.53	0.04
CO2	-0.15	-0.65	0.20	-0.14	-0.01	0.43	0.31	-0.41	-0.33	-0.44	-0.16	-0.20	-0.54	0.55	-0.30	0.51	-0.53		-0.69
S	0.24	0.53	-0.14	0.29	0.49	-0.39	0.16	-0.03	-0.12	0.15	0.38	0.20	0.67	-0.45	0.00	-0.35	0.04	-0.69	

Chapter 4

Petrogenesis and volcanic reconstruction of a VMS-hosting subsidence structure: the Chisel sequence, Snow Lake, Manitoba

4.1 Abstract

The Snow Lake arc assemblage of the Paleoproterozoic Trans-Hudson Orogen records a complete arc cycle, from primitive arc formation, to arc rifting, to seafloor spreading. Volcanogenic massive sulfide (VMS) deposit formation is associated with a protracted arc rifting event, which is recorded by the Chisel sequence. Two distinct VMS deposit types formed during arc rifting: 1) the Anderson deposits, which are Cu rich and associated with felsic domes at the base of the Chisel sequence; and 2) the Chisel deposits, which are typically Zn rich and associated with a localized volcanic subsidence structure. Two of the Chisel deposits are anomalously enriched in Cu and Au relative to the other deposits (Photo Lake and Lalor deposits). Light rare earth element (LREE) enrichment of volcanic strata is restricted to the Chisel sequence ore interval and is interpreted to be related to arc rifting and preferential melting of an enriched component in the heterogeneous sub-arc mantle through one of two processes: 1) decreased fluid addition to the mantle during arc rifting, causing smaller degrees of partial melting; or 2) upwelling of deep enriched mantle due to crustal thinning. Selective Cu and Au enrichment in the Photo Lake and Lalor deposits results from greater water depth and boiling of hydrothermal fluids proximal to the seafloor and the occurrence of these deposits at deep-penetrating structures associated with significant subsidence. Therefore, identification of LREE enrichment and major synvolcanic structures are additional tools for VMS exploration in the Snow Lake arc assemblage.

4.2 Introduction

Volcanogenic massive sulfide (VMS) deposits form during extension and active rifting in divergent tectonic settings, such as back-arc spreading centers, and in collisional tectonic settings, such as oceanic and continental rifted arcs and back-arcs (Franklin et al. 2005; Galley et al. 2007). Due to poor preservation of oceanic crust in the ancient rock record, most VMS deposits preserved in ancient successions formed in collisional environments (Franklin et al. 2005; Huston et al., 2010).

The Flin-Flon Glennie Domain, of the Trans-Hudson Orogen, hosts the largest Paleoproterozoic VMS district in the world (Syme et al. 1999), with most of the VMS deposits occurring within the Flin Flon and Snow Lake arc assemblages. The Flin Flon arc assemblage developed as an oceanic arc, whereas the Snow Lake arc assemblage is interpreted to have evolved as a pericratonic arc outboard of the Superior craton (Stern et al. 1992, 1995; David et al. 1996; Percival et al. 2004; Corrigan et al. 2007, 2009). This resulted in different volcanic and petrogenetic histories, which may have influenced the size and base and precious metal tenor of their VMS deposits.

The Snow Lake arc assemblage is divided into primitive arc (Anderson), mature arc (Chisel), and arc rift (Snow Creek) sequences based on the geochemistry of mafic volcanic rocks within these sequences (Bailes and Galley 1999; Stern et al. 1992, 1995). The Chisel sequence is host to six VMS deposits along a single ore interval that represents a hiatus in explosive volcanism at the transition between the Lower and Upper Chisel sequences (Bailes and Galley 1996, 1999, 2007;

Engelbert et al. 2014). In a recent detailed structural study on the Chisel sequence, Stewart et al. (2018a) established the stratigraphy of previously undivided rocks, providing, for the first time, a foundation to re-evaluate the volcanic environment of the entire Chisel sequence and associated VMS deposits.

In this manuscript we present a volcanic and magmatic reconstruction of the Chisel sequence prior to, during, and after ore formation, which will provide constraints on the metallogeny and evolution of arc sequences in the Trans-Hudson Orogen. Specifically we: (1) reconstruct the volcanic environment of the Chisel sequence and determine the petrogenesis of its volcanic rocks; (2) establish the internal stratigraphy and emplacement of the Threehouse unit to characterize the volcanic environment immediately following ore formation and identify water depth constraints; (3) explore the effects of water depth on the base and precious metal tenor of VMS deposits located at the same stratigraphic interval; and (4) compare the volcanic setting and petrogenesis of the Snow Lake and Flin Flon arc assemblages.

4.3 Terminology

Volcaniclastic rocks are fragmental deposits produced either by direct deposition from explosive or effusive eruptions or by resedimentation from non-lithified volcanic deposits (Fisher, 1966; Gibson et al., 1999; White and Houghton, 2006). Volcaniclastic rocks are classified herein using the granulometric terms and classifications proposed by Fisher (1961, 1966) and White and Houghton (2006) but in a non-genetic sense (Gibson et al., 1999; Busby-Spera et al., 2003). In this classification, particles <2 mm, 2-64mm and >64mm are referred to as ash, lapilli, and

blocks and bombs, respectively. The term ‘vitric’ is used to define aphanitic material interpreted to have been glassy when formed due to rapid cooling or quenching by seawater.

Peak, middle almandine-amphibolite facies metamorphism (5 kbar, 570°C; Menard and Gordon 1997) has overprinted rocks of the Snow Lake arc assemblage, and the term “meta” is implicit and not used as a prefix in the text. Textures indicative of deformation and metamorphism are observed in all of the rocks in the Snow Lake arc assemblage, including subgrain boundaries, undulatory extinction, and granoblastic polygonal textures. Outcrop- and hand specimen-scale primary volcanic and sedimentary features are preserved (e.g., flow banding, cross bedding), but overprinting alteration, deformation, and metamorphism have destroyed microscopic primary textures. Where primary phenocrysts have been replaced by a pseudomorph (e.g., pyroxene replacement by amphibole in a porphyritic basalt), the primary igneous mineral name is used. The volcanic rocks of the Snow Lake arc assemblage have anomalously low HFSE and REE contents, which result in felsic rocks plotting as andesites and basaltic andesites on the Nb/Y vs. Zr/Ti classification diagram of Pearce (1996). Classification diagrams using major element criteria (e.g., SiO_2 versus $Na_2O + K_2O$ diagram of Le Maitre et al. 1989) cannot be reliably used in these rocks because of major element mobility during alteration and metamorphism. Therefore, rocks are classified as felsic where possible and terms such as ‘rhyolite,’ ‘rhyodacite,’ and ‘dacite’ are only retained where they refer to existing informal stratigraphic units.

4.4 Regional geology, structure, and metamorphism

The Flin Flon belt, located in the southern portion of the Reindeer Zone of the Paleoproterozoic Trans-Hudson Orogen (Fig. 1), comprises primitive and mature arc, ocean floor, and ocean

plateau tectono-stratigraphic assemblages that formed at 1.92 to 1.88 Ga (Lucas et al. 1996). The Snow Lake arc assemblage occurs at the eastern extent of the Flin Flon belt and was interpreted to have evolved independently of the rest of the belt until accretion at ca. 1.86 to 1.84 Ga (Stern et al. 1992, 1995b; David et al. 1996; Lucas et al. 1996; Corrigan et al. 2007, 2009). However, Stewart et al. (2018a) documented a pre-1.86 Ga deformation event, which suggests that the Snow Lake arc assemblage underwent early intraoceanic accretion or was accreted to the Flin Flon belt earlier than previously thought. Most of the previous work in the volcanic rocks of the Snow Lake arc assemblage has focused on the primitive arc Anderson sequence and mature arc Chisel sequence (e.g., Bailes and Galley 1991, 1996, 1999, 2007; Zaleski et al. 1991; Galley et al. 1993; Menard and Gordon 1997; Bailes 1996, 1997; Gagné et al. 2007; Caté et al. 2014; Caté 2016) due to the occurrence of VMS deposits in these sequences. The youngest supracrustal rocks in the Snow Lake district are ca. 1.86-1.84 Ga sedimentary rocks of the Kisseynew Basin, which is located north of the Flin Flon belt and is interpreted to have developed as a back-arc basin behind the arc assemblages of the Flin Flon belt (Ansdell et al. 1995; David et al. 1996; Machado et al. 1999). In the Snow Lake area these rocks comprise alluvial-fluvial rocks of the Missi Group and turbidities of the Burntwood Group (Bailes 1980a, 1980b; Zwanzig 1990), which were structurally interleaved with the Snow Lake volcanic rocks at ca. 1.84-1.81 Ga (Ansdell et al. 1995; Connors 1996; Kraus and Williams 1999).

The primitive arc Anderson sequence comprises mafic and felsic coherent flows with minor heterolithic volcaniclastic rocks (Fig. 2; Bailes and Galley 1996, 1999, 2007). The mafic flows are grouped into a single unit referred to as the Welch basalt, which consists of aphyric and plagioclase and/or pyroxene porphyritic pillowed and massive low-Ti tholeiitic basalt, basaltic

andesite and andesite (Bailes and Galley 1991, 1996, 1999, 2007; Stern et al. 1995). Boninitic andesite and basaltic andesite flows occur near the top of the Welch basalt and the uppermost basalt flows are silicified along their entire 20 km strike length (Bailes and Galley 1991, 1996, 1999, 2007; Stern et al. 1995). Aphyric and quartz- or quartz-plagioclase-porphyritic massive and lobe-hyaloclastite facies felsic flows comprise four flow-dome complexes that are interpreted to have been emplaced during ongoing Welch basalt volcanism (Daly, Sneath, Konzie, and Anderson-Stall rhyolite complexes; Bailes and Galley 1996, 1999, 2007).

The mature arc Chisel sequence has been divided into lower and upper sequences (Bailes and Galley 2007). The Lower Chisel sequence comprises mafic and felsic flows and abundant volcaniclastic rocks, which have been divided into six informal stratigraphic units (Figs. 2, 3; Bailes and Galley 1996, 1999, 2007; Bailes et al. 1996, 1997). The Stroud Breccia marks the base of the Lower Chisel sequence, and the laminated tuffs at the top of this unit are conformably overlain by the Snell basalt (DeWolfe and Gibson 2016). The Snell basalt is overlain by mafic volcaniclastic rocks of the Edwards unit, which in turn are overlain by the Caboose andesite and volcaniclastic rocks and lesser coherent flows of the Moore Lake basalt (Bailes and Galley 1996, 2007; Bailes et al. 1996). The Powderhouse dacite unit, which consists of heterolithic volcaniclastic rocks and lesser flows, overlies the Moore Lake basalt (Bailes and Galley 1996, 1999, 2007; Bailes et al. 1996, 1997). Volcaniclastic lithofacies of the Powderhouse dacite unit were interpreted to be a product of subsidence and voluminous pyroclastic eruptions (Galley et al. 1993; Friesen, et al., 2015; Friesen, 2018) at inferred water depths of <1,000 m (Galley et al. 1993).

The Upper Chisel sequence has been interpreted as comprising a younger, homoclinal succession consisting of, in ascending order, the North Balloch rhyolite, the Balloch basalt, the Ghost and Photo rhyolites, the Threehouse mafic volcaniclastic rocks and flows (Threehouse unit), and the North Chisel dacite and unsubdivided rocks (Bailes and Galley 2007; Bailes 2014; Bailes et al. 2016). However, recent work suggests that, with the exception of the Threehouse unit, the entire Upper Chisel sequence represents folded and thrust-repeated Lower Chisel sequence strata (Fig. 2; Stewart et al. 2018a; Friesen, 2018). The Threehouse unit forms the hanging wall to the Chisel sequence VMS deposits and constitutes the entire Upper Chisel sequence within the new stratigraphic framework (Figs. 2, 3; Engelbert et al., 2014; Stewart et al. 2018a).

The Snow Lake arc assemblage has undergone four main deformation events related to closure of the Manikewan Ocean and development of the Trans-Hudson Orogen as summarized in Table 1 (Froese and Moore 1980; Galley et al. 1988; Kraus and Williams 1993, 1994, 1998, 1999; Rubingh et al., 2012; Stewart et al. 2018a). Peak metamorphic conditions reached middle almandine-amphibolite facies (~5 kbar, 550-570°C; Menard and Gordon 1997) syn- to post-D_2 but prior to D_3 at ca. 1.81 Ga (David et al. 1996; Menard and Gordon 1997).

4.5 Analytical techniques

4.5.1 Field techniques

Detailed field mapping and sampling targeted three areas representative of variations in the Chisel sequence volcanic rocks (Fig. 3): 1) the Lalor section, including the Lalor deposit, referred to as the Lalor area; 2) the Photo Lake section, including the Photo Lake VMS deposit, referred to as the Photo Lake area; and 3) the Chisel, Chisel North, Lost, and Ghost deposits

section, referred to as the South Chisel area. Lithofacies mapping complemented structural mapping completed by Stewart et al. (2018a) at the 1:2,000 scale, with local detailed areas at 1:100 or 1:200 scale. Core from 20 Hudson Bay Exploration and Development (HBED) drill holes were re-logged; 10 in the Lalor section and 10 in the Photo Lake area. An additional 39 drill holes were examined using whole-rock geochemistry and drill logs provided by HBED to trace the extent of units. Nine holes logged in the Lalor section and 18 of the additional holes were used to interpret the 3D geology of the Lalor deposit with Leapfrog Geo™ software.

4.5.2 Geochemistry

Eighty-two samples collected for whole rock geochemistry were crushed in a steel jaw-crusher and pulverized in an agate mill at the Ontario Geoscience Laboratories (OGL; Sudbury, Ontario). Total abundances of trace elements were analyzed by inductively coupled plasma – mass spectrometry (ICP-MS) at OGL following closed vessel multi-acid (hydrofluoric, hydrochloric, nitric, and perchloric) digestion. Splits of the pulverized samples were analyzed by X-ray fluorescence (XRF) fusion for total abundances of major oxides following a lithium metaborate-tetraborate fusion and weak nitric acid digestion at Activation Laboratories (ActLabs; Ancaster, Ontario). Relative standard deviations (%RSD) calculated for replicate analyses and standards are <10% for ICP-MS determinations for all samples.

The geochemical analyses were supplemented with data from the HBED geochemistry and assay database compiled from drill core samples. HBED data for the Photo Lake deposit (1994 to 1996) was analyzed at X-Ray Assay Laboratories (XRAL; now SGS Minerals Services) by X-ray fluorescence (XRF) for total abundances of major oxides. Samples from the Lalor deposit

(2007-11) were analyzed at AcmeLabs (now Bureau Veritas Minerals) by inductively coupled plasma – emission spectrometry (ICP-ES) for total abundances of major oxides, carbon, and sulfur following lithium borate fusion and for total abundances of trace elements by ICP-MS following a modified aqua regia digestion (1:1:1 HNO_3:HCl:H_2O).

4.5.3 Radiogenic isotope analysis

Eight representative samples were analyzed for whole rock Nd, Hf, and Pb isotopes at the Pacific Centre for Isotopic and Geochemical Research (PCIGR) following the methods of Weis et al. (2005, 2006, 2007). Isotopic analyses were performed using a Finnigan Triton thermo-ionization mass spectrometer (TIMS; Nd) and a Nu Instruments multiple collector inductively coupled plasma mass spectrometer (MC-ICP-MS; Hf, Pb). Samples were also analyzed for total abundances of Pb, Th, U, Nd, Sm, Lu, and Hf on a Thermo Finnigan Element2 high resolution ICP-MS (HR-ICP-MS). Samples were dissolved in high-pressure Teflon® polytetrafluoroethylene (PTFE) bombs prior to isotopic and trace element analysis. Reference material measurements used for data normalization are outlined in Appendix A. Relative standard deviations (%RSD) calculated for replicate analyses and reference materials are <6% for ICP-MS determinations for all samples.

Initial $^{143}Nd/^{144}Nd$ and $^{176}Hf/^{177}Hf$ ratios and εNd and εHf were calculated at 1890 Ma in order to maintain consistency with previous Nd isotopic analyses by Stern et al. (1992) and because this is considered to be the minimum age for the volcanic rocks at Snow Lake (Machado and David 1992; David et al. 1996). Present day values for CHUR used for these calculations are $^{143}Nd/^{144}Nd = 0.512638$ (Goldstein et al., 1984), $^{147}Sm/^{144}Nd = 0.1967$ (Jacobsen and

Wasserburg 1980), $^{176}Hf/^{177}Hf = 0.282785$, and $^{176}Lu/^{177}Hf = 0.0336$ (Bouvier et al. 2008). Depleted mantle model ages (T_{DM}) were calculated from measured Nd isotopic ratios using the values of $^{143}Nd/^{144}Nd = 0.513163$ and $^{147}Sm/^{144}Nd = 0.2137$ for depleted mantle (Goldstein et al. 1984).

4.6 Stratigraphy and lithofacies of the Chisel sequence

The lithofacies descriptions focus on the informal stratigraphic units within the Chisel sequence ore interval and on units immediately below and above the ore interval. The descriptions build on previous work (Froese and Moore 1980; Galley et al. 1988; Bailes and Galley 1991, 1996, 2007; Bailes et al. 1996, 1997, 2011; Bailes and Schledewitz 1999; Rubingh et al. 2017; Friesen 2018) and add detail to better establish the volcanic history of the Chisel sequence. Brief descriptions summarizing the findings of previous workers are provided for the lowermost units of the Chisel sequence.

4.6.1 Stroud breccia

The Stroud breccia is the lowermost unit of the Chisel sequence and is a predominantly felsic package of volcaniclastic rocks up to ~300 m thick (Figs. 2, 3; Bailes and Galley 1996, 2007; Bailes et al. 1996; DeWolfe and Gibson 2016). It consists of heterolithic to monolithic felsic tuff breccia, lapilli tuff, and tuff and mafic tuff and lapilli tuff. The felsic fragments in the Stroud breccia are geochemically and texturally identical to the felsic flow-dome complexes of the Anderson sequence and the Sneath intrusive complex, which is a synvolcanic intrusion in the Anderson sequence (Bailes and Galley 2007). The Anderson sequence felsic flow-dome complexes were previously interpreted to be older than the Stroud breccia (Bailes and Galley

1991, 1996, 1999, 2007); however, recent work indicates that the felsic flow-dome complexes occur within the same stratigraphic interval as the Stroud breccia (DeWolfe and Gibson 2016). Because the Stroud breccia is interpreted to mark the base of the Chisel Sequence (DeWolfe and Gibson 2016), this new interpretation places the Cu-rich Anderson, Stall, and Rod VMS deposits at the base of the Chisel sequence rather than the top of the Anderson sequence.

4.6.2 Snell basalt, Edwards mafic volcaniclastic rocks, and Caboose andesite

Overlying the Stroud breccia is a succession of basaltic and andesitic flows and volcaniclastic rocks, which, in ascending stratigraphic order, include the Snell basalt, Edwards mafic volcaniclastic rocks, and Caboose andesite (Figs. 2, 3). The Snell basalt is up to 500 m thick and consists of pillowed and massive plagioclase- and plagioclase-pyroxene-porphyritic flows (Bailes and Galley 1996, 2007). The Edwards mafic volcaniclastic rocks are 500 m thick and consist of thin-bedded tuff that coarsens upwards into thick-bedded heterolithic mafic breccia dominated by plagioclase-porphyritic clasts (Bailes and Galley 1996, 2007; Bailes et al. 2013). The Caboose andesite consists of amphibole-porphyritic, massive and pillowed flows with a very limited lateral extent (Bailes and Galley 2007). These flows are intercalated within flows and pillow breccia of the overlying Moore Lake unit (Bailes et al. 1996; Bailes and Galley 2007).

4.6.3 Moore Lake basalt and mafic volcaniclastic rocks (Moore Lake unit)

The Moore Lake unit consists of pillow-fragment and heterolithic mafic breccia where it underlies the Powderhouse dacite and of pillowed aphyric basalt east of the South Chisel area (Bailes et al. 1996; Bailes and Galley 2007; Figs. 2, 3). At depth, clasts of the Moore Lake unit

occur in a sequence of volcaniclastic rocks immediately below the Lalor-Chisel fault, which separates the shallowly dipping host rocks to the Lalor deposit from the steeply dipping strata observed at surface in the Lalor area (Bailes 2009, 2014; Bailes et al. 2013; Caté 2016; Stewart et al. 2018a; Fig. 4). These volcaniclastic rocks are host to the uppermost ore lenses of the Lalor deposit (Fig. 4). Where altered and primary volcanic textures are identified, the clasts of the Moore Lake unit are predominantly aphyric. Intervals of coherent basalt up to several metres thick may represent flows or large blocks. The Lalor and Chisel members of the Powderhouse dacite host the remaining ore lenses of the Lalor deposit (Fig. 4) and clasts with Moore Lake basalt chemistry occur throughout these units.

4.6.4 Powderhouse dacite

Friesen (2018) divided the Powderhouse dacite formation into three members: the Chisel, Lalor, and Lost members. The basal lithofacies of the Chisel and Lalor members is a massive crystal-vitric lapilli tuff. In the Chisel member this lithofacies is overlain by heterolithic mafic and felsic breccias intercalated with mafic and felsic tuff and lapilli tuff, and in the Lalor member it is overlain by bedded crystal tuff (Bailes and Galley 2007; Friesen et al. 2015; Friesen 2018). The Lost member occurs at the top of the Powderhouse dacite and consists of stratified heterolithic tuff, lapilli tuff, and tuff breccia (Friesen et al. 2015; Friesen 2018). The Lalor member occurs in the structural hanging wall to the Lalor VMS deposit (Figs. 3, 4). These exposures were mapped in order to better constrain the depositional environment and host rocks to the Lalor deposit. The Lost member of the Powderhouse dacite is also a significant unit in the South Chisel basin area (Fig. 3).

Heterolithic felsic to intermediate volcaniclastic rocks of the Lalor member of the Powderhouse dacite are located at the southwestern margin of the Lalor section (Fig. 3). Outcrop exposure is poor in this area and the unit is interpreted to be cut by faulting (Stewart et al. 2018a), making it impossible to estimate its true thickness and lateral extent. Mapping by Bailes and Galley (2007) and Bailes et al. (2011) indicates that this unit presently has an approximate thickness of 400 m and extends laterally for approximately 3.5 km. Where exposed along the Lalor section, these rocks are classified as coarse tuff to lapilli tuff. The rocks are characterized by plagioclase crystals and rhyolitic and dacitic lapilli in a mafic matrix of medium to coarse tuff dominated by amphibole, plagioclase, and garnet (Fig. 5a). Juvenile mafic lapilli similar to those identified by Friesen (2018) in the Lalor and Chisel members are also present. Felsic and mafic lapilli range in size from 2 to 30 mm. This unit is poorly bedded with beds defined by variation in clast content. Normal grading of clast size and content indicates facing towards the west, and beds typically grade from lapilli tuff at the base to tuff at the top. Poor outcrop exposure did not allow for subdivision of this unit into more detailed lithofacies or into depositional units.

The Lost member of the Powderhouse dacite was mapped in the vicinity of the Ghost and Lost deposits (Figs. 3; 6). It consists of well-bedded tuff to lapilli tuff that is felsic at its base, becomes increasingly mafic upwards, and eventually grades into the overlying mafic tuffs of the Threehouse unit. Beds range in thickness from laminae to several centimetres thick (Fig. 5b). Facing reversals defined by scours and slumping indicate this unit has been folded by an F_2 anticline and consistently occurs stratigraphically below the Threehouse unit (Stewart et al., 2018a; Figs. 2-4). Trace sulfides occur throughout this unit but are more concentrated in the felsic beds towards the base. A coarse bed of monolithic felsic blocks and lapilli is also present

towards the centre of this unit, and the clasts are identical in composition and phenocryst content to the Chisel rhyolite (Fig. 5c). The clasts in this bed are angular, scour the underlying tuffs, and display weak normal grading with respect to clast size.

4.6.5 Powderhouse rhyolite

The Powderhouse rhyolite is a localized aphyric felsic flow in the South Chisel area (Figs. 2, 3, 6) that has not previously been recognized. It consists of massive and lobe lithofacies (Fig. 5d). The lower contact of the Powderhouse rhyolite is not observed and at its upper contact it transitions from a massive flow into a monolithic lapilli tuff interpreted to be a flow top breccia. It is overlain by bedded felsic lapilli tuff of the Lost member. The thickest section of Powderhouse rhyolite occupies the core of an F_2 anticline (Fig. 6); it is also observed southeast of Lost Lake.

4.6.6 Felsic coherent lithofacies

Aphyric to sparsely porphyritic felsic coherent lithofacies of the Chisel, Photo, Ghost, and North Balloch rhyolite units are interpreted to occur at the same stratigraphic interval by Stewart et al. (2018). These units are described separately.

4.6.6.1 Chisel rhyolite

The Chisel rhyolite is exposed in the Chisel open pit and hosts the Chisel VMS deposit (Fig. 3; Galley et al. 1993; Bailes and Galley 1996); a small lens occurs in the South Chisel area. The Chisel rhyolite contains approximately 2% 1-3 mm quartz and 1-2% ≤1 mm feldspar phenocrysts and consists of massive, lobe, and breccia lithofacies. The Chisel rhyolite is divisible into two

phases. The lowermost phase is volcaniclastic and consists entirely of lapilli tuff that is strongly altered and metamorphosed to an assemblage dominated by chlorite-biotite-actinolite-sericite-garnet ± staurolite ± kyanite (Galley et al. 1993). The matrix of this unit is strongly altered but relict monolithic felsic clasts can be identified (Fig. 5e). The clasts are typically 1-5 cm but can be up to 16 cm. Bedding was not observed where alteration is strongest, but normal-graded bedding is observed towards the margins of this unit where the alteration is weaker (Fig. 5f).

The second phase consists of felsic flows that are massive and coherent at their centre. Lobes and breccia are well developed along the margins of these flows, and lobes are best developed towards the top (Fig. 5g). This phase of the Chisel rhyolite does not exhibit VMS-related alteration (Fig 5g). It overlies the altered volcaniclastic phase and is brecciated along this contact (Fig. 5e). Galley et al (1993) described rhyolite breccia that forms aprons surrounding massive and lobe portions of the felsic flows (Galley et al. 1993). The thickest zones of massive sulfide are located along the flanks of the Chisel rhyolite (Galley et al., 1993).

4.6.6.2 Ghost and Photo rhyolites

The Photo rhyolite is host to the Photo Lake deposit (Fig. 3) and consists of two distinct felsic units, a lower PR1 and an upper PR2, that are distinguished based on amphibole content and composition (Stewart et al. 2018b). The Photo deposit occurs at the contact between the two units (Stewart et al. 2018b). Both felsic units are aphyric to sparsely quartz- or plagioclase-porphyritic and consist of massive to lobe lithofacies with lobes best developed along the margins of the flows (Fig. 5h). Amygdules and flow banding are also observed in the unit and are more prominent at the top and the margins. Minor rhyolite breccia is developed mantling

lobe margins towards the top of PR2. The lobes are in contact with variably altered zones (5 to 30 cm thick) consisting of an assemblage metamorphosed to chlorite + calcic amphibole ± garnet. These zones are similar in appearance and distribution to microbreccia surrounding lobes in the Daly rhyolite of the Anderson sequence (Bailes and Galley 2007; Bailes et al. 2016). Incipient columnar jointing is observed in PR2.

In the Lalor and South Chisel areas, the Photo rhyolite is referred to as the Ghost rhyolite (Bailes et al. 2016). It contains <10% amphibole and typically more biotite than amphibole, which is consistent with the mineralogy of PR2. Lobes, flow banding, and quartz-filled amygdules are observed throughout the unit but are best developed towards the margins.

4.6.6.3 North Balloch rhyolite

The North Balloch rhyolite occurs in the Lalor section (Figs. 3, 4) and is divisible into aphyric, quartz-porphyritic, and quartz-feldspar-porphyritic phases that are spatially distinct and consist of coherent flows and associated volcaniclastic rocks. The aphyric phase is a massive coherent flow that transitions into lobes with minor localized brecciation and is similar to the Photo and Ghost rhyolites. Monolithic, felsic lapilli tuff to tuff breccia developed at its northeast contact with the quartz-feldspar-porphyritic phase is interpreted to be flow top breccia. At its southwestern margin it is hydrothermally altered and metamorphosed to an assemblage dominated by chlorite + garnet that has completely overprinted all primary volcanic textures.

The quartz-feldspar-porphyritic phase contains 2%, 1-4 mm quartz and trace to 1%, ≤1 mm feldspar phenocrysts. It is similar to quartz-feldspar-porphyritic felsic flows east of the Photo

Lake deposit (Fig. 5i). This felsic unit transitions from massive to breccia lithofacies towards the southeast, consistent with a southeast facing direction. However, the 30 m-thick breccia is overprinted by hydrothermal alteration and disseminated sulfide (Fig. 5j), obscuring the contact and facing indicators.

The quartz-porphyritic unit contains 1-3%, ≤1 mm quartz phenocrysts and is similar to the Chisel rhyolite. It consists dominantly of massive and lobe lithofacies, and a transition from massive, to lobe, to breccia lithofacies suggests that younging is towards the northeast. Lobes are best developed towards the top of the unit. There is no exposed contact between this felsic unit and either the aphyric or quartz-feldspar-porphyritic felsic units.

4.6.6.4 Quartz-feldspar-porphyritic flows

In this study, quartz-feldspar-porphyritic (QFP) felsic rocks were mapped in the area east of the Photo Lake deposit (Fig. 3), where they contain 5-8%, 1-5 mm quartz and trace to 1%, ≤1 mm feldspar phenocrysts. The QFP unit transitions from massive coherent facies into a volcaniclastic facies classified as monolithic lapilli tuff to tuff breccia and consisting of clasts identical to the massive component (Fig. 5k). Disseminated sulfide occurs in the matrix to volcaniclastic rocks, and the sulfide content increases moving towards the upper contact with the Threehouse unit. The contact between the QFP unit and the overlying bedded mafic tuffs of the Threehouse unit is not exposed in this area; however, the matrix to the QFP volcaniclastic rocks becomes increasingly mafic moving towards this contact and the concentration of felsic clasts decreases, suggesting that this may be a transitional contact as seen elsewhere for the lower contact of the Threehouse unit (e.g., Chisel rhyolite – Threehouse contact; Lost member – Threehouse contact).

Several plugs and sills of quartz and quartz-feldspar porphyritic felsic rocks were identified by previous workers at the northeastern extent of the Lalor section (Bailes et al. 1997; Bailes and Galley 2007). Some of these areas correspond to flows of the North Balloch rhyolite; however, where contacts were not exposed it was not possible to determine whether the areas mapped were intrusive or extrusive.

4.6.7 Threehouse Unit

The Threehouse unit is divided into two broad subunits characterized by different lithofacies (Fig. 7). The first subunit is dominantly volcaniclastic and characterized by 40 to 100 m of well-bedded fine to medium tuff with minor lapilli tuff, overlain by 60 to 200 m of more coarsely bedded crystal tuff to crystal lapilli tuff and tuff breccia interbedded with well-bedded fine to medium tuff, and a minimum of 20 to 40 m of coarsely bedded lapilli tuff to tuff breccia (Fig. 7). Plagioclase crystals are absent until approximately 3 to 8 m, at which point the subunit becomes more plagioclase crystal-rich moving up sequence and can contain up to 30%, 2 to 6 mm crystals but has an average of 10 to 15%. Disseminated carbonate occurs throughout, but is concentrated in coarsely bedded lapilli tuff. The well-bedded fine to medium tuff at the base of this sequence exhibits symmetrical ripple marks with mud drapes (Fig. 8a), hummocky and trough cross-bedding (Fig. 8b), scour channels (Fig. 8a), convolute bedding, volcanic bombs, and possible accretionary lapilli (Bailes and Galley 2007; Gibson et al. 2014). The crystal tuff to crystal lapilli tuff beds contain up to 30% mafic lapilli that increase in size and abundance up stratigraphy. All clasts throughout this sequence are mafic and often have fine-grained chilled rims (Fig. 8c). The dominant clast types present are: 1) amygdaloidal plagioclase-porphyritic clasts; 2) plagioclase-

porphyritic clasts with an aphanitic, glassy groundmass; and 3) vitric clasts. Columnar jointing is developed in a restricted area of massive crystal-lapilli tuff approximately 5 m thick (Fig. 8d). Locally, the uppermost 10 to 20 m of this sequence is a crystal-lapilli tuff defined by large (up to 40 cm), highly vesicular to scoria blocks with chilled rims and juvenile, vitric lapilli (Fig. 8e). This subunit is best developed in the South Chisel area (Fig. 3); however, the lowermost section of bedded tuffs overlies rhyolite flows east of the Photo Lake deposit (Fig. 3). In the Lalor section, the lowermost bedded tuffs are present at surface and a more complete section is observed at depth in drill core, where the uppermost 70 to 80 m is a mafic flow. This may be similar to what is observed east of the Photo Lake deposit, where Threehouse flows overlie bedded tuff and occur along strike of mafic breccia (Bailes and Galley 2007; Fig. 3).

The second subunit comprises volcaniclastic rocks and flows (Fig. 7). The lower 5 to 10 m consists of medium to coarse massive mafic tuff interbedded with normal-graded, well-bedded heterolithic mafic lapilli tuff to tuff breccia (Fig. 8f). These beds are approximately 20 to 60 cm thick and include angular felsic clasts. Coherent mafic massive and pillowed flows with associated flow top breccia (Fig. 8g), referred to by previous workers as the Balloch basalt (Bailes et al. 1997; Bailes and Galley 2007), occur along strike of the volcaniclastic rocks. The basalt flows transition from aphyric flows at the base of the subunit to plagioclase- and pyroxene-porphyritic flows at the top. The flows contain up to 20% plagioclase phenocrysts and up to 8% amphibole after pyroxene phenocrysts. The lower contact of the flows is not exposed and the upper contact is marked by approximately 3 to 5 cm of fine-grained hyaloclastite. This contact contains irregular lenses of fine, bedded tuff. Overlying both the flows and tuff is a massive package of lapilli tuff to tuff breccia characterized by four dominant clast types: 1)

mafic amygdaloidal clasts with <20 volume percent quartz amygdules; 2) mafic amygdaloidal clasts with >35 volume percent quartz amygdules; 3) mafic clasts with phenocrysts of plagioclase and amphibole after pyroxene; and 4) mafic aphanitic, aphyric clasts. Clast types 1 and 2 are the most common and clast type 2 can contain >50 volume percent amygdules, at which point it is classified as scoria. The clasts are subangular to subround and most of the clasts have chilled margins that are either intact or partially broken. Some of the group 4 clasts are glassy rims of other clasts. Many of the clasts also have delicate, intact tails. Clasts from the flow top breccia to the basalt are observed at the base of this volcaniclastic package where it is in contact with the basalt. The upper contact of the volcaniclastic rocks is not exposed. It is not possible to discern the true thickness of the lapilli tuff to tuff breccia due to late folding and/or faulting; however, in the Photo Lake area it has a minimum thickness of 45 m. Mapping by Bailes and Galley (2007) and Bailes et al. (2011) indicates that the lapilli tuff to tuff breccia may be up to 300 m thick and extend laterally for up to 1 km. This subunit is exposed in the structural hanging wall to the Lalor deposit (Fig. 4) and overlying the Photo rhyolite complex in the Photo Lake map area (Fig. 3).

The lower contact of the Threehouse unit is exposed at surface and in drill core in the Lalor, Photo Lake, and South Chisel areas (Figs. 3, 4, 6). This contact was previously interpreted to be a thrust fault (Bailes 2009, 2014; Bailes et al. 2016). However, in all exposures examined the contact is conformable and transitional, with no evidence of increased deformation that could be attributed to a structural contact. Where the Threehouse unit is in direct contact with the Chisel rhyolite, Lost member, QFP rhyolite, and the western margin of the Ghost rhyolite, there is a transition from felsic to mafic tuff that is also reflected by a change from felsic to mafic

geochemistry. This contact is also associated with a disseminated, pyrrhotite-rich sulfide zone (Fig. 8h). Where the Threehouse unit is in contact with the Photo rhyolite and the eastern margin of the Ghost rhyolite, the Threehouse mafic volcaniclastic rocks contain felsic clasts, presumably sourced from the underlying rhyolite flows, which decrease in abundance away from the contact (Fig. 8i). The upper contact of the Threehouse unit is not exposed.

4.6.8 Threehouse intrusions

Aphyric and plagioclase porphyritic intrusions have been interpreted as feeders for Threehouse volcanism (Bailes et al. 1996, 1997; Bailes and Galley 2007). The aphyric and aphanitic basaltic intrusions, previously referred to as the Balloch or Vent raise basalt (Bailes and Galley, 2007), are restricted to the South Chisel area (Figs. 6, 9). At their lower and upper margins, the aphyric intrusions are in contact with bedded tuffs that are transitional between the Lost member of the Powderhouse dacite and the Threehouse unit. Both contacts are defined by well-developed peperite that transitions into in situ breccia and fractured zones moving towards the coherent centre of the intrusions (Fig. 10a, b), indicating that the aphyric intrusions were emplaced into the surrounding bedded tuffs when the tuffs were wet and unconsolidated.

Plagioclase porphyritic intrusions occur throughout the map area. They consist of 10-20%, 1-5 mm plagioclase phenocrysts in an aphanitic groundmass. Contacts with Threehouse volcaniclastic rocks and supracrustal strata are typically sharp and chilled. However, where plagioclase porphyritic intrusions intrude peperite associated with the aphyric intrusions, they are fractured and in situ brecciated, and fragments of the porphyritic intrusion occur in the peperite, resulting in a mixture of both aphyric and plagioclase-porphyritic peperite (Figs. 9, 10c). These

contact relationships indicate synvolcanic emplacement for the plagioclase porphyritic intrusions.

4.7 Geochemistry of the ore interval and Upper Chisel sequence

All major element oxide geochemical data were normalized to 100 wt.%. In order to identify samples least affected by hydrothermal alteration, visibly altered samples were rejected, and the remaining samples were screened according to geochemical criteria such that samples with loss on ignition (LOI) > 4.5 wt.%, Na_2O < 1 wt.%, and Al_2O_3/Na_2O > 10 (Spitz and Darling, 1978) were rejected. Three samples from the Threehouse unit (13-ME-025, 13-ME-026, 13-ME-028) and one sample from a plagioclase-porphyritic mafic dike (13-ME-009) were not rejected in spite of slightly high Al_2O_3/Na_2O values (10.3-19.2) because they met the other geochemical criteria and provided complete coverage of these units. Of the 82 samples analyzed for whole rock geochemistry, 22 were rejected due to alteration, and 6 were rejected due to mixed geochemical signatures in volcaniclastic units. Trace element mobility was assessed using X-Y plots with Zr as the immobile element monitor (Figure 11; MacLean 1990; Barrett and McLean 1994). Elements that exhibit little to no scatter are assumed to be immobile during alteration and metamorphism and have correlation coefficients >0.8. These elements include the REE, Be, Hf, Nb, Sn, Ta, Th, Tm, and Y. Geochemical data is summarized in Table 2 and in Figures 11 – 16. Important element ratios are summarized in Table 3. Additional geochemical data from Stern et al. (1995), Bailes (1997), Bailes and Galley (1999), and Friesen (2018) are used for comparison and to provide completed stratigraphic coverage of the Chisel sequence stratigraphy. Whole rock Nd, Hf, and Pb isotopic data is summarized in Table 4. The epsilon Nd and Hf should display a positive correlation; however, there is an inconsistent relationship between these values. This

may be a product of element mobility in the Lu-Hf system due to alteration and metamorphism as Lu displays more scatter on a binary plot versus Zr than Sm, Nd, or Hf (Figs. 11b, c, d). There is also no relationship between $\varepsilon Nd_{(1.9Ga)}$ values and Pb isotopes.

4.7.1 Geochemistry of felsic rocks

Chisel sequence felsic rocks have high field strength element (HFSE; Nb, Ta, Zr, Hf, Y, Th) concentrations characteristic of volcanic arc rocks with I-type affinity (Fig. 12a). Establishing the magmatic affinity for the Chisel sequence volcanic rocks is a challenge. Major element oxide ratios involving some combination of FeO, Na_2O, K_2O, MgO and SiO_2 (e.g., Gill 1981) cannot be used because these elements are typically mobile during VMS-related hydrothermal alteration. Trace element ratios involving Zr (e.g., Zr/Y; Lesher et al. 1986; Lentz 1998) cannot be used because of unusually low Zr concentrations in the felsic rocks, which is interpreted to be the result of their derivation from a Zr-depleted, refractory mantle (Stern et al. 1995). This is indicated by several of the felsic rocks plotting as basaltic andesites on the Zr/Ti versus Nb/Y discrimination diagram of Pearce (1996; Figure 12b).

All of the felsic rocks are classified as subalkaline based on Nb/Y ratios (Figure 12b). Ratios of Th/Co indicate that all of the felsic rocks have calc-alkaline affinities with the exception of the QFP rhyolite, which has a tholeiitic affinity (Fig. 12c). However, Th/Yb and La/Yb ratios suggest that the QFP, Photo, Ghost, and North Balloch rhyolites have transitional affinities and the Chisel and Powderhouse rhyolites have calc-alkaline affinities (Fig. 12d). Two samples of the North Balloch rhyolite (13-ME-049, 14-ME-079) have trace element ratios that are consistently similar to the Chisel rhyolite (Fig. 12). The majority of the felsic samples fall within

the FII rhyolite field of the Hart et al. (2004) rhyolite classification diagram, with the Powderhouse rhyolite samples plotting at the boundary between the FI and FII fields (Fig. 12e).

Three geochemical patterns corresponding to specific units can be identified on chondrite-normalized plots (Fig. 13): 1) Chisel and Powderhouse rhyolites and the uppermost quartz-porphyritic flows of the North Balloch rhyolite; 2) Photo and Ghost rhyolites and the aphyric and sparsely quartz-feldspar-porphyritic flows of the North Balloch rhyolite ("Photo-type" chemistry; Figs. 13b, c); and 3) QFP rhyolite (Fig. 13c). All of the felsic units are LREE enriched, but the Chisel-type rhyolites have the most pronounced LREE enrichment (La/Yb_{CN} = 5.5-12.7), followed by the Photo-type rhyolites (La/Yb_{CN} = 2.5-5.4) and the QFP rhyolite, which has the lowest LREE enrichment (La/Yb_{CN} =1.6; Fig. 13). All of the felsic units display flat HREE patterns with the exception of the QFP rhyolite, which has a positive HREE slope (Fig. 13). The Powderhouse rhyolite has higher total REE and HFSE than all other felsic units and the QFP rhyolite has the lowest REE and HFSE. The Chisel rhyolite and two anomalous North Balloch rhyolite samples have higher HFSE and REE concentrations than the Photo-type rhyolites but similar HREE concentrations (Fig. 13). The Photo-type rhyolites PR1 and PR2 have slightly different total REE and HFSE concentrations (Stewart et al 2018 b; Figs. 13, 14). Primitive-mantle normalized patterns for all of the felsic units have flat to slightly negative Eu anomalies and pronounced negative Nb, Ti, and V anomalies (Fig. 14; Table 3). The three geochemical groups outlined above can also be distinguished using immobile incompatible element ratios and these are summarized in Table 3.

The felsic units are isotopically distinct and isotopic characteristics vary within and between the geochemical groups outlined above. Photo rhyolite 1 and the QFP rhyolite are the most isotopically primitive, with $\varepsilon Nd_{(1.9Ga)}$ values of +5.4 and +5.7 and $\varepsilon Hf_{(1.9Ga)}$ values of +8.7 and +6.4, respectively (Table 4). The Chisel rhyolite has an $\varepsilon Nd_{(1.9Ga)}$ value of +4.0, which is similar to the Powderhouse rhyolite $\varepsilon Nd_{(1.9Ga)}$ value of +3.2; however, the $\varepsilon Hf_{(1.9Ga)}$ values for these units differ, with the Chisel rhyolite having $\varepsilon Hf_{(1.9Ga)}$ = +10.7 and the Powderhouse rhyolite having $\varepsilon Hf_{(1.9Ga)}$ = 5.8 (Table 4). Photo rhyolite 2 is the most isotopically evolved felsic unit, with $\varepsilon Nd_{(1.9Ga)}$ = +1.6 and $\varepsilon Hf_{(1.9Ga)}$ = +4.6. Photo rhyolite 1 and PR2 share very similar Pb isotopic ratios (Table 4). The Chisel and QFP rhyolites also share similar Pb isotopic ratios, and these values are lower than those for PR1 and PR2 (Table 4). The Powderhouse rhyolite has unique Pb isotopic values that are significantly higher than all of the other felsic units analyzed (Table 4).

4.7.2 Geochemistry of mafic rocks

As with the felsic rocks, classification schemes for mafic volcanic rocks that rely on the major elements and Zr should not be used. All of the mafic rocks are subalkaline basalts (Fig. 12b), with the Threehouse unit, Balloch basalt, and mafic intrusions having tholeiitic to transitional affinities and the Moore Lake unit having a calc-alkaline affinity (Fig. 12d,f). The majority of the mafic rocks plot as low-Ti island arc basalts to island arc basalts and one sample from the Moore Lake unit plots as MORB (Fig. 12f).

All of the mafic rocks are LREE enriched, but the Moore Lake unit is significantly more LREE enriched than the other mafic units. The Moore Lake unit has La/Yb_{CN} >5 and typically >10, whereas the Threehouse unit, Balloch basalt, and mafic intrusions have La/Yb<5, and the Threehouse unit is typically <2 (Table 3). All of the mafic units display flat HREE chondrite-

normalized patterns with the exception of the Moore Lake unit, which has a negative HREE slope (Fig. 15). The Moore Lake unit also has higher total REE and HFSE and a different primitive mantle-normalized trace element pattern than the other mafic units (Figs. 15, 16). All of the mafic units have positive Eu anomalies, moderate negative Zr anomalies, pronounced negative Nb anomalies, and positive Sr anomalies, but the latter is much less pronounced for the Moore Lake unit than for the other mafic units (Figs. 15, 16; Table 3). The Moore Lake unit has a strong negative Ti anomaly, whereas the other mafic units have flat to positive Ti patterns (Fig. 16; Table 3). Other important geochemical ratios for the mafic units are summarized in Table 3.

Three mafic samples were analyzed for whole rock Nd, Hf, and Pb isotopes: one sample of a plagioclase porphyritic mafic intrusion, one sample of crystal-poor mafic bedded tuff from the Threehouse unit, and one aphyric sample from the Balloch basalt. The bedded tuff and basalt samples are isotopically evolved, having $\varepsilon Nd_{(1.9Ga)}$ values of +1.1 and 1.8, respectively (Table 4). The mafic intrusion has $\varepsilon Nd_{(1.9Ga)} = 4.2$, which is similar to the Chisel rhyolite. The $\varepsilon Hf_{(1.9Ga)}$ results for the mafic samples are $\varepsilon Hf_{(1.9Ga)} = 13.0$ for the bedded tuff, $\varepsilon Hf_{(1.9Ga)} = 15.4$ for the basalt, and $\varepsilon Hf_{(1.9Ga)} = 18.4$ for the intrusion. Whole rock Pb isotopic data is similar for all three mafic samples, with $^{208/}Pb/^{204}Pb = 35.24 – 35.40$, $^{207/}Pb/^{204}Pb = 15.22 – 15.27$, and $^{206/}Pb/^{204}Pb = 15.82 – 16.32$ (Table 4).

4.8 Discussion

4.8.1 Interpretation of Lower Chisel sequence volcanic lithofacies

The Lower Chisel sequence rocks are interpreted to have been emplaced in a subaqueous volcanic environment during active rifting (Bailes and Galley 1999, 2007). Evidence for a subaqueous setting includes ubiquitous pillows and hyaloclastite in the mafic flows, and lobe

facies and hyaloclastite in the felsic flows (Bailes and Galley 2007). There are no water depth constraints on the Lower Chisel sequence except those provided by lithofacies of the Powderhouse dacite, which are discussed below. Evidence cited for intra-arc rifting in the Lower Chisel sequence rocks includes voluminous volcaniclastic detritus and synvolcanic dike sets (Bailes and Galley 1999); evidence for synvolcanic subsidence has not been provided in previous work.

4.8.1.1 Stroud Breccia

The Stroud breccia is interpreted to have formed during incipient rifting of the primitive arc Anderson sequence and was emplaced by subaqueous mass flows and suspension sedimentation (DeWolfe and Gibson 2016). The aphyric rhyolite blocks in the felsic tuff breccia at the base of this unit are interpreted to be sourced from over-steepening and collapse of a localized rhyolite dome along strike of the unit (DeWolfe and Gibson 2016). Coarsely quartz and quartz-feldspar-porphyritic lapilli and blocks share pronounced textural, mineralogical, and geochemical similarities with the Sneath Lake tonalitic pluton with the exception of an aphanitic groundmass in the clasts (Bailes and Galley 1999, 2007). These clasts have been interpreted to result from uplift and erosion of volcanic strata of the Anderson sequence and unroofing of the synvolcanic Sneath Lake pluton (Bailes and Galley 1999, 2007). However, the lack of an angular discordance between strata of the Anderson and Chisel sequences does not support large-scale regional uplift. Alternatively, the coarsely porphyritic lapilli may be a product of explosive felsic volcanism, rhyolite dome collapse, or collapse of fault scarps. Some of the clasts have delicate tails reminiscent of deformed pumice, which may support a pyroclastic origin (DeWolfe and Gibson

2016). Mafic tuff intercalated with the felsic volcaniclastic rocks suggests that limited mafic volcanism was ongoing during emplacement of the Stroud breccia (DeWolfe and Gibson 2016).

Quartz and quartz-feldspar porphyritic rhyolite blocks are interpreted to result from the uplift and erosion of felsic units in the underlying Anderson sequence, given the textural and geochemical similarities between the blocks, the rhyolite domes, and the synvolcanic Sneath Lake pluton (Bailes and Galley 1999, 2007); however, the blocks may also be the products of rhyolite dome collapse. Alternatively, the felsic blocks may be resedimented from fault scarps (DeWolfe and Gibson 2016).

4.8.1.2 Snell basalt, Edwards mafic volcaniclastic rocks, and Caboose andesite

Massive and pillowed flows and hyaloclastite (Bailes and Galley 2007) indicate subaqueous emplacement for the Snell basalt. Bailes and Galley (1997, 2007) interpreted thin lenses of Stroud breccia intercalated with the Snell basalt (Bailes and Galley 1996, 2007), to indicate a paleoenvironment that had topographic relief, and that subsidence was ongoing during extrusion of the Snell basalt lavas.

The fine-grained, thin-bedded mafic tuffs at the base of the Edwards mafic volcaniclastic succession are interpreted to have been deposited by turbidity currents, and the thick-bedded heterolithic mafic breccias forming the upper sequence are interpreted to be the product of subaqueous debris flows (Bailes 1987; Bailes and Galley 2007; Bailes et al. 2013). These debris flow deposits suggest topographic relief. The debris flow deposits contain boulder-sized clasts and the beds range in thickness from 1 to 20 m, with one 60 m-thick bed reported (Skirrow 1987;

Bailes et al. 2013). These features suggest that the mafic breccias are locally sourced (Bailes and Galley 1996, 2007; Bailes et al. 2013). Due to their low viscosity, mafic flows do not oversteepen and collapse to produce extensive flank breccias, and the breccias that form by autobrecciation along flow margins are monolithic and have a limited lateral extent (Gibson et al. 1999). Given their thickness, large lateral extent, heterogeneity, and inferred local source, the unit is interpreted to have formed duing synvolcanic tectonic activity and the collapse of fault scarps within coherent mafic flows to produce both the pillow debris and basin, indicating that rifting and subsidence were ongoing during emplacement of the unit.

The presence of the Caboose andesite flows within the Edwards basalt flows suggests that multiple magma sources were present during Lower Chisel sequence volcanism. This is further supported by synvolcanic dacite dikes intruding the Snell basalt and Edwards mafic volcaniclastic rocks (Bailes and Galley 1996, 2007; Bailes et al. 2013).

4.8.1.3 Moore Lake basalt and mafic volcaniclastic rocks (Moore Lake unit)

The Moore Lake basalt and mafic volcaniclastic rocks reflect a lateral facies change from massive and pillowed flows east and southeast of Ghost Lake into amoeboid pillow breccia and pillow fragment breccia to the west (Bailes and Galley 1996, 2007; Bailes et al. 2013). The pillow and pillow fragment breccias were interpreted to be the western and distal downslope equivalents of coherent Moore Lake basalt flows (Bailes and Galley 2007; 2013). Clasts in the pillow fragment breccias include partial and intact pillows, blocks containing multiple pillows, and fragments of laminated mafic tuff that must have been consolidated prior to brecciation (Bailes et al. 2013). These clast types suggest derivation by mass wasting from fault scarps

within coherent Moore basalt to the east and deposition within an adjacent western basin produced during concomitant subsidence. The termination of the overlying Powderhouse dacite unit at the same location as the abrupt east-west transition from flows to volcaniclastic rocks in the Moore basalt suggests a synvolcanic structure is located here (Friesen 2018) and that subsidence was ongoing during emplacement of the Moore Lake and Powderhouse units.

4.8.1.4 Powderhouse dacite

The basal, voluminous, crystal-vitric lapilli tuff of the Lalor and Chisel members of the Powderhouse dacite is interpreted to have been emplaced by subaqueous pyroclastic mass flows (Friesen et al. 2015; Friesen 2018). The fining upwards sequence of lapilli tuff to tuff is also characteristic of the internal organization of submarine pyroclastic flow deposits as described by several workers (e.g., Fiske 1963; Fiske and Matsuda 1964; Bond 1973; Yamada 1973; Niem 1977; Morton and Nebel 1984; Kano 1996; Gibson et al. 1999; Kessel and Busby 2003). This interpretation is consistent with a recent study conducted on the thrust-bounded McLeod Road-Birch Lake (MB) sequence, located northeast of the current study area (Rubingh et al. 2017). This study correlated felsic volcaniclastic rocks of the MB sequence with the Powderhouse dacite of the Chisel sequence and interpreted their formation to be the product of voluminous pyroclastic eruptions and associated subsidence (Rubingh et al. 2017). Water depths during emplacement of the Powderhouse dacite are estimated to have ranged from 200 to 2000 m based on the absence of bedforms indicative of depths above storm wave base, the limiting effects of hydrostatic pressure on the critical pressure of water, and modern seafloor examples (Rubingh et al. 2017; Friesen 2018).

Coarse heterolithic breccia at the top of the Chisel member and stratified tuff, lapilli tuff, and tuff breccia of the Lost member are interpreted to be debris flow deposits derived through mass wasting off fault scarps developed during rifting and subsidence (Bailes and Galley 2007; Engelbert et al. 2014; Friesen et al. 2015; Friesen 2018). The coarse, monolithic, normal-graded beds of felsic blocks and lapilli within the Lost member of the South Chisel area (Fig. 5c) suggest emplacement by mass flow from the nearby Chisel rhyolite. This suggests that effusive felsic volcanism was ongoing during the hiatus in explosive volcanism that coincides with the Chisel sequence ore interval.

4.8.1.5 Aphyric to sparsely porphyritic felsic coherent lithofacies

The Chisel, Photo, Ghost, and North Balloch coherent rhyolitic units are interpreted to occur at the same stratigraphic interval (Figs. 2, 3: Bailes and Galley 2007; Stewart et al. 2018a, 2018b). The Powderhouse rhyolite occurs along strike of the Chisel member of the Powderhouse dacite (Figs. 3, 6). These two units are indistinguishable in terms of whole rock major and trace element concentrations and ratios (Figs. 11-14), share similar isotopic compositions (Table 4), and the Powderhouse rhyolite is interpreted to be the effusive equivalent to the explosive Chisel member of the Powderhouse dacite.

Based on flow morphology and extent, mineralogy, and geochemistry, the coherent felsic units are subdivided into the Chisel-type flows and the Photo-type flows. The QFP rhyolite is a distinct unit that will be described separately below. The Chisel-type felsic flows are small volume and localized with lobes and associated well-developed autoclastic breccia at the flow

margins. These features are consistent with the blocky dome classification of Gibson et al. (1999).

Photo-type flows are voluminous and consist of massive coherent and lobe facies, with lobes best developed towards the top of the flows, where they are brecciated along their margins and are commonly in contact with highly altered zones consisting of chlorite + calcic amphibole ± garnet. These zones are interpreted to have formed as glassy selvages by rapid quenching with seawater (cf. Gibson et al. 1999). Alteration by protracted seawater interaction, possible overprinting by hydrothermal fluids, and later metamorphism at middle almandine-amphibolite facies produced the current mineral assemblage. Lobes developed in flow interiors are not associated with autoclastic breccia or chlorite-rich selvages, suggesting they represent endogenous growth of the rhyolite flows. These characteristics indicate that these Photo-type flows can be classified as lobe-hyaloclastite flows based on the criteria of Gibson et al. (1999). This is consistent with the interpretation of Stewart et al. (2018b) for the Photo Rhyolite complex. The only area where Chisel-type and Photo-type rhyolites are juxtaposed is in the North Balloch rhyolite of the Lalor area (Fig. 3); however, the contact is not exposed.

Photo-type rhyolite flows constitute a significant proportion of the Chisel sequence volcanic rocks (Fig. 3). Voluminous submarine silicic lava flows have recently been identified in the northeast Lau basin, where their large volume and lateral extent have been attributed to high eruption temperatures and high dissolved volatile contents produced by high confining pressures, resulting in lower viscosities than their subaerial counterparts (Embley and Rubin 2018). Large gas cavities (up to 2 cm diameter; Stewart et al. 2018b) are observed in the Photo-type flows,

suggesting that they may have been volatile-rich; however, the Lau basin silicic lavas are only sparsely vesicular (Embley and Rubin 2018), and the vesicle content may therefore not be a direct measure of the volatile content. Compositionally, the Lau basin flows are dacitic, which may also contribute to low viscosities because dacitic melts are only marginally more viscous than andesitic melts (Whittington et al. 2009; Embley and Rubin 2018). The flows occur at water depths of 2,000 to 2,800 m and lava flow lengths range from a few km to >10 km (Embley and Rubin 2018), which is consistent with the lateral extent of the Photo-type flows. Furthermore, the apparent volume of the Photo-type flows may be misleading given that they are repeated by folding and faulting and terminate against a major fault at depth (Stewart et al. 2018a). In the ancient rock record, lobe-hyaloclastite flows are typically fissure-fed (Gibson et al. 1999), which also contributes to greater lateral extents (e.g., Waite Rhyolite: Gibson et al. 1999; V10b unit of the Tisdale assemblage: Dinel et al. 2008). Therefore, the volume and extent of the Photo-type flows, as observed in felsic effusive volcanic rocks in modern and ancient submarine settings, suggests that the viscosity of these flows was lower than that of the Chisel-type flows. This may indicate that the Photo-type flows are dacitic, whereas the Chisel-type flows are rhyolitic. It is not possible to confirm this classification due to overall low Zr concentrations in the rocks of the Snow Lake arc assemblage (Fig. 12b; Syme and Bailes 1993; Bailes 1997); however, the Photo-type flows have lower Zr/Ti and SiO_2 concentrations than the Chisel-type flows (Fig. 12; Tables 2, 3), which is consistent with this interpretation.

4.8.1.6 Quartz-feldspar-porphyritic (QFP) felsic coherent lithofacies

The QFP felsic unit was encountered east of the Photo Lake deposit (Fig. 3), where the coherent facies grades into a monolithic breccia interpreted to be autoclastic flow-top breccia (Fig. 5k).

This facies transition is consistent with an established younging direction towards the east. Its unique geochemical composition and higher phenocryst content distinguish it from the quartz-porphyritic phase of the Balloch rhyolite. East of the Photo Lake deposit the QFP unit overlies the Photo rhyolite, making it the youngest felsic unit of the Chisel sequence; however, its stratigraphic position below the Threehouse unit indicates that it occurs within the ore interval. Feeder intrusions for the QFP unit are documented in the Anderson sequence and lowermost units of the Chisel sequence (Bailes and Galley 2007).

4.8.2 Volcanic setting and implications of the Threehouse unit

The Threehouse unit is critical to understanding the Chisel sequence ore-forming environment. Mapping indicates that its contact with lower Chisel strata is conformable, and, where both are volcaniclastic, the contact is transitional. Volcaniclastic rocks are predominant in the Threehouse unit and provide constraints on magma chamber dynamics. The facies architecture, bedforms, and structures of the unit reflect the volcanic environment and water depth immediately following VMS ore formation. This work complements recent work by Friesen (2018) on the Powderhouse dacite, which proposes an origin through voluminous pyroclastic eruptions that resulted in synvolcanic faulting, subsidence, and VMS mineralization. The water depth during emplacement of the Powderhouse dacite is poorly constrained; however, rapid lateral facies variations suggest that the unit was emplaced in an environment with topographic relief and variations in water depth (Friesen 2018). This is consistent with previous work by Bailes and Galley (2007), who suggested that the relatively high proportion of volcaniclastic rocks in the Chisel sequence was a reflection of topographic relief during extension.

Lateral water depth variations are recorded by lithofacies of the Threehouse unit, which are grouped into two main subunits. The first subunit consists entirely of volcaniclastic material and includes the well bedded, laminated to thick-bedded tuffs and lesser lapilli tuffs at the base of the Threehouse unit. These include laminated to thin-bedded tuffs that exhibit symmetrical ripples with mud drapes, hummocky and trough cross-bedding, and accretionary lapilli, indicating water depths above storm wave base (<200 m) to locally tidal and emergent. Coarser, thin- to thick-bedded tuff to lapilli tuff suggests deposition via mass flow and deeper water conditions (Gibson et al. 2014). Scour channels, load structures, Bouma zonation, and pebble lags suggest deposition by subaqueous density currents (Galley and Bailes 2002; Bailes and Galley 2007). The significant ash-sized component in the lower 40 to 100 m of this subunit and crystal-rich nature of the overlying 60 to 200 m are suggestive of violent explosive eruptions, which are interpreted to indicate <700 m water depth for hydrovolcanic eruptions (Pecover et al. 1973; Gibson et al. 1999) or <500 to 1,000 m for magmatic eruptions (McBirney 1963; Kokelaar 1986; Gibson et al. 1999). Gibson et al. (2014) interpreted the tuffs and lapilli tuffs in this portion of the Threehouse unit to have a phreatomagmatic and lesser magmatic pyroclastic origin based on the dominance of lapilli with a cuspate, equant shard morphology, abundance of ash-sized material, and sparse scoria to pumice lapilli. Furthermore, local columnar jointing in massive tuff suggests a hot state of emplacement, supporting a pyroclastic origin and emergent environment for this lithofacies (e.g., Cas and Wright 1991; Gibson et al. 1999). The second subunit consists of volcaniclastic material and mafic massive and pillowed flows. This sequence lacks water depth constraints; however, the poorly sorted coarse breccia suggests deposition via mass flows within topographic basins. The absence of abundant pyroclastic material in this subunit may indicate that water depths were too great for explosive eruptions; however, evidence to support this interpretation is

lacking. The first subunit shows evidence for reworking by bottom currents (e.g., ripple marks, cross bedding), and both subunits show evidence for possible re-sedimentation. Variation in water depth indicated by lithofacies and their bedforms suggest variations in basement topography as a result of subsidence.

Threehouse flows and volcaniclastic rocks share a similar and consistent composition throughout the unit (Figs. 12, 15, 16), suggesting that they are derived from a common parental magma. The abrupt vertical change from crystal-poor to crystal-rich tuff in the Threehouse unit suggests derivation from a shallow, zoned magma chamber. Studies of magma chamber dynamics (Smith 1979; Hildreth 1981) have found aphyric boundary layers to occur on top of more crystal-rich zoned magma columns. The crystal-poor tuff exhibits a positive Eu anomaly (Fig. 15c), suggesting that it formed in the presence of plagioclase in the magma chamber.

The abrupt vertical change in plagioclase crystal content is also reflected in the timing of aphyric and plagioclase-porphyritic intrusions. Earlier aphyric intrusions have peperitic contacts with volcaniclastic rocks of the Lost member, whereas plagioclase-porphyritic intrusions have sharp contacts with these volcaniclastic rocks and peperitic contacts with peperite associated with aphyric intrusions (Figs. 9, 10d). This indicates that the aphyric intrusions were emplaced first, presumably when the volcaniclastic rocks of the Lost member contained more entrapped water and were unconsolidated, and the plagioclase-porphyritic intrusions were emplaced later; however, both intrusion types are synvolcanic.

Bailes and Galley (2007) suggested that the upward coarsening and increasing clast heterogeneity may indicate an increase in topographic relief and complexity of the source terrane or provenance. However, intact chilled margins around clasts (Fig. 8c, e) and the presence of juvenile clasts (Fig. 8c) in the uppermost portions of the Threehouse unit indicate that the unit is primary and does not represent derivation from a more diverse source. Furthermore, highly vesicular amoeboid clasts with chilled margins (Fig. 8j) in a massive monolithic lapilli tuff to tuff breccia near the top of the Threehouse unit are interpreted as spatter that may be a product of mild fire-fountain eruptions (e.g., Mueller and White 1992; Gibson et al. 1993), which form proximal to their vent. The systematic increase in clast size and decrease in ash-sized component may reflect decreasing volatile content of the magma with depth in the magma chamber, which would be associated with decreasing eruption energy and increasing size of ejecta released from the vent site(s). Alternatively, the upward coarsening and decreasing eruption energy in the Threehouse unit may be the product of a progressive increase in water depth due to ongoing subsidence because explosive hydrovolcanic eruptions become suppressed with increasing water depth (Kokelaar 1986; Gibson et al. 1999).

4.8.3 Petrogenesis of the Chisel sequence volcanic rocks

Previous workers have identified several important geochemical characteristics for the volcanic rocks of the Snow Lake assemblage, which provide a foundation upon which a petrogenetic interpretation can be developed (Stern et al. 1992, 1995; Bailes 1997; Bailes and Galley 1999). Most importantly, the mature arc Chisel sequence is interpreted to have distinctly different geochemistry than the primitive arc Anderson sequence due to the presence of thicker crust and arc magma genesis in a more complex environment that likely included older crustal fragments

and previously formed arc segments in the Chisel sequence (Bailes and Galley 1999). Negative $\varepsilon Nd_{(1.9Ga)}$ values (-0.4 to -0.1) in the Snell basalt (Stern et al. 1992), combined with an inherited Archean zircon population (2650 to 2824 Ma; David et al. 1996) in the underlying Stroud felsic breccia, suggest that some of the arc magmas in the Chisel sequence have been contaminated by Archean crust and that the Snow Lake arc may have been built upon an Archean micro-continental fragment (Stern et al. 1992, 1995; Bailes and Galley 1999). Felsic volcanic units in the Snow Lake arc assemblage display higher $\varepsilon Nd_{(1.9Ga)}$ values than the mafic units, which indicates that the felsic units were not derived by fractionation of the same parental magmas that produced the mafic flows (Stern et al. 1992, 1995; Bailes and Galley 1999). Rather, the felsic magmas are interpreted to be the product of high-temperature partial melting of the base of primitive oceanic lithosphere (Bailes and Galley 1999). The association of isotopically primitive felsic units with VMS mineralization has been attributed to high heat flow, fracturing, and increased fluid circulation associated with arc rifting (Bailes and Galley 1999). This is supported by evidence for intra-arc extension in both the Anderson and Chisel sequences (Bailes and Galley 1999).

The units of the Chisel sequence are divided into two distinct geochemical groups based on LREE enrichment. The Moore Lake basalt, Chisel member of the Powderhouse dacite, and Powderhouse and Chisel rhyolites are all LREE enriched with $(La/Yb)_{CN} > 5$, whereas the Snell basalt, Lalor member of the Powderhouse dacite, Photo rhyolite, and Threehouse unit exhibit less LREE enrichment with $(La/Yb)_{CN} < 5$ (Fig. 12e; Table 3). Variable intracrustal contamination by older, LREE-enriched lithosphere has been interpreted as a possible source for the low $\varepsilon Nd_{(1.9Ga)}$ values in the Snell basalt (Stern et al. 1992) and may explain the variations in LREE enrichment.

However, there is no correlation between LREE enrichment and $\varepsilon Nd_{(1.9Ga)}$ values (Fig. 17a), indicating that variable LREE enrichment is not the product of crustal contamination. Previous workers have suggested that the Moore Lake basalt may be more strongly LREE enriched due to one or a combination of a more fertile mantle source, lower average extent of melting, or greater depths of melting (Stern et al. 1995; Bailes and Galley 1999). These processes and processes that may be responsible for variations in the geochemistry of the felsic volcanic rocks are considered below.

4.8.3.1 Petrogenesis of mafic rocks

In addition to greater LREE enrichment, the Moore Lake basalt exhibits several unique geochemical characteristics when compared to the other mafic units of the Chisel sequence (Snell basalt and Threehouse unit; Stern et al. 1995). It has higher HFSE concentrations, is classified as calc-alkaline rather than tholeiitic based on the trace element classification schemes of Ross and Bédard (2009), and exhibits a strong negative Ti anomaly on primitive mantle-normalized trace element diagrams, whereas the Snell basalt and Threehouse unit display flat Ti patterns (Fig. 16). When LREE enrichment is attributed to greater depths of melting, it is due to HREE retention by garnet, which results in depletion and fractionation of the HREE (Shen and Forsyth 1995 and references therein). The Moore Lake basalt exhibits minimal HREE fractionation, with $(Gd/Yb)_{CN}$ = 1.3-2.6 versus $(Gd/Yb)_{CN}$ = 0.9-1.4 for the Snell basalt and Threehouse unit, which suggests depth of melting is not a viable explanation for the chemical variations between the mafic rocks of the Chisel sequence. The Th/Yb, Nb/Yb, and Zr-Nb-Y ratios for the Moore Lake basalt suggest that it has E-MORB affinity (Fig. 18). Furthermore, the negative Ti anomaly is not a depletion in Ti relative to the other mafic units of the Chisel

sequence, but rather an enrichment of Sm and Gd (Fig. 16), suggesting that the mantle source of the Moore Lake unit was enriched. The $\varepsilon Nd_{(1.9Ga)}$ values for two samples of the Moore Lake unit are +2.5 and +2.7 (Stern et al. 1992, 1995), which are similar to the +2.2 value interpreted for the enriched mantle endmember beneath the Flin Flon arc (Stern et al. 1995; Figs. 17b, 19). This suggests that the mantle beneath the Snow Lake arc was heterogeneous and contained an enriched component, which is consistent with the interpretation of Stern et al. (1995). There are several models for variable mantle enrichment and heterogeneity: 1) the "plum pudding" model of Zindler et al. (1984), in which blobs of enriched mantle material are surrounded by a depleted matrix; 2) the "marble cake" model of Allègre and Turcotte (1986), in which layers of enriched mantle are intercalated with depleted mantle due to the incorporation of subducted oceanic lithosphere; or 3) mantle stratification, with enriched mantle occurring at greater depths than depleted mantle, and mantle flow induced by the subducting slab results in upwelling of enriched mantle material (e.g., Taylor et al. 1992; Tatsumi and Eggins 1995; Schellart 2004). However, an enriched mantle source does not eliminate the possibility that the Moore Lake basalt was also generated by smaller degrees of partial melting, and we propose that both of these processes contributed to its petrogenesis. These processes are described in further detail and related to the tectonic environment below.

Of particular interest is a possible relationship between the unique chemistry of the Moore Lake basalt and VMS formation, as it is the last mafic unit to be emplaced before VMS formation. In the South Chisel area the Moore Lake Basalt is overprinted by VMS-style alteration, and a wedge of volcaniclastic rocks containing clasts with Moore Lake basalt chemistry occurs in the immediate hanging wall to the Lalor deposit (Bailes and Galley 2007; Bailes et al. 2013; Caté

2016, Stewart et al. 2018a; Fig. 4). Although the Threehouse unit forms the hanging wall to the Chisel sequence VMS deposits, it contains no VMS-related alteration, suggesting that the hydrothermal system ceased prior to its eruption and emplacement.

We propose that the unique chemistry of the Moore Lake basalt provides a window on the tectonic environment immediately prior to VMS formation. It is well established that VMS deposits in the Snow Lake arc assemblage, as well as in the Flin Flon arc assemblage, formed during periods of arc rifting (Bailes and Galley 1999; Syme et al. 1999). Rifting of suprasubduction zones is typically attributed to slab roll back, which is accompanied by a slowed rate of subduction (e.g., Yoshida 2017). The chemistry of arc magmas is widely recognized to be influenced by fluid additions to the mantle wedge from the subducting slab (e.g., Hawkesworth et al. 1993), and slowed rates of convergence result in a decreased contribution of fluids to the mantle wedge (Stolper and Newman 1984; Woodhead et al. 1998). Less fluid addition to the mantle results in lower degrees of partial melting (e.g., Stolper and Newman 1984; Woodhead et al. 1998; Tian et al. 2011), which would preferentially melt the enriched component in a heterogeneous mantle ("plum pudding" or "marble cake" models). Preferential melting of enriched mantle has also been suggested to explain variable LREE enrichment in the hanging wall to the VMS deposits in the Flin Flon arc assemblage (DeWolfe et al. 2009). This process is further supported by the LILE/HFSE ratios of the Chisel mafic rocks, as they are higher in least altered samples of the Snell basalt and Threehouse unit than in least altered samples of the Moore Lake basalt. High LILE/HFSE ratios have been interpreted to result from fluid additions to the mantle from the subducting slab (Fig. 20; Woodhead et al. 1998). The more pronounced negative Ti anomaly in the Moore Lake basalt than in the other mafic units also supports

decreased H_2O during Moore Lake magma generation because H_2O and TiO_2 have a negative correlation in arc magmas (Kelley et al. 2006). Bailes and Galley (2007) suggested that a shorter adiabatic column beneath thicker crust in the mature arc Chisel sequence may have resulted in smaller degrees of partial melting; however, this does not account for the chemistry of the other mafic units in the Chisel sequence that do not have enriched signatures but would also have been erupted through a shorter adiabatic column. Alternatively, mantle upwelling during arc rifting may have resulted in melting of deeper, more enriched mantle. This process has been suggested for the Trout Lake VMS deposit, 8 km northeast of the VMS deposits in the Flin Flon arc assemblage (Ordonez-Calderon et al. 2016) and may reflect a stage of arc rifting in which extension, subsidence, and mantle upwelling were at a maximum. Regardless of the mechanism responsible for melting of enriched mantle, it is likely that the tectonic environment associated with VMS formation resulted in the unique chemistry of the Moore Lake basalt, and identification of LREE-enriched basaltic units may be a useful exploration tool.

4.8.3.2 Petrogenesis of felsic rocks

The Chisel, Powderhouse, and Photo rhyolites have markedly different geochemical characteristics (Fig. 12-14; Tables 2, 3). The Lalor member of the Powderhouse dacite is similar to the Photo rhyolite, whereas the Chisel member is similar to the Chisel and Powderhouse rhyolites (Figs. 12-14). Two possible explanations may explain the elevated LREE and HFSE of the Chisel and Powderhouse rhyolites and Chisel member. The first possibility is that all of the rhyolites in the Chisel sequence are petrogenetically related and represent fractionation of a single parental magma, with the Photo rhyolite flows representing the smallest amount of fractionation and the Chisel and Powderhouse rhyolite flows representing the greatest amount of

fractionation. Alternatively, the different rhyolite complexes represent distinct magma sources. The latter explanation is favoured due to the differences in the isotopic characteristics for the rhyolites (Fig. 19; Table 4) and more pronounced HREE fractionation for the Chisel and Powderhouse rhyolites ($(Gd/Yb)_{CN}$ = 1.3-1.9) as compared to the Photo rhyolite ($(Gd/Yb)_{CN}$ = 0.9-1.3).

Based on their distinct chemical similarities, the Chisel member of the Powderhouse dacite was interpreted by Bailes and Galley (1999, 2007) to be comagmatic with the Moore Lake basalt. An average $\varepsilon Nd_{(1.9Ga)}$ value of +2.4 for the Chisel member, which is similar to that of the Moore Lake basalt (~ +2.5; Stern et al. 1992), supports this interpretation.

Photo rhyolite 1 is the most isotopically primitive felsic unit in the Chisel sequence ($\varepsilon Nd_{(1.9Ga)}$ = +5.4; Fig. 19), whereas PR2 is the most isotopically evolved felsic unit ($\varepsilon Nd_{(1.9Ga)}$ = +1.6; Fig. 19). The Nd isotopic value for PR1 is the same as the most depleted mantle beneath the Flin Flon arc ($\varepsilon Nd_{(1.9Ga)}$ = +5.4; Stern et al. 1995) and is more primitive than any of the mafic rocks in the Chisel sequence (Fig. 19). This suggests that the PR1 melt was derived through partial melting of primitive mafic crust (Bailes and Galley 1999) or fractionation of a mafic magma produced by partial melting of a depleted mantle source. The similar trace element signatures for PR1 and PR2 (Figs. 12-14) suggest that they may be comagmatic; however, the Nd isotopic data suggests that PR2 has undergone crustal contamination and PR1 has not. In order to produce an $\varepsilon Nd_{(1.9Ga)}$ value of +1.6 for PR2 from an initial value of +5.4, approximately 3-4% contamination by older crust is required (Fig. 17b; Stern et al. 1995). Therefore, PR1 and PR2 may represent variable crustal contamination of the same melt or separate melts of similar basaltic crust, with the PR2

melt having undergone crustal contamination. A similar explanation may be inferred for the Lalor member of the Powderhouse dacite, which shares similar whole rock chemistry with PR1 and PR2 (Figs. 12-14) but has different Nd isotopic characteristics (average $\varepsilon Nd_{(1.9Ga)}$ = +3.5: Friesen 2018). It may have formed by melting of similar basaltic crust as that which produced PR1 and PR2 but underwent different amounts of crustal contamination and was erupted explosively rather than effusively.

The Chisel rhyolite has similar LREE and HFSE enrichment as the Powderhouse rhyolite but a more primitive $\varepsilon Nd_{(1.9Ga)}$ value ($\varepsilon Nd_{(1.9Ga)}$ =+4.0 for Chisel rhyolite; $\varepsilon Nd_{(1.9Ga)}$ = +3.2 for Powderhouse rhyolite; Fig. 19) and slightly less HREE fractionation ($(Gd/Yb)_{CN}$ = 1.3-1.6 for Chisel rhyolite; $(Gd/Yb)_{CN}$ = 1.6-1.9 for Powderhouse rhyolite; Fig. 13; Table 3). It plots along the same trend as the Photo rhyolite on binary incompatible element diagrams (Fig. 11). Therefore, it does not appear to be comagmatic with the Moore Lake basalt and is distinct from the Powderhouse rhyolite. There are four equally plausible scenarios for the petrogenesis of the Chisel rhyolite: 1) partial melting of LREE-enriched mafic crust; 2) small degrees of partial melting at greater depths than the Photo rhyolite melt (e.g., Lesher et al. 1986; Hart et al. 2004); 3) fractionation of a primitive mafic melt to produce LREE enrichment combined with crustal contamination to decrease the $\varepsilon Nd_{(1.9Ga)}$ signature; or 4) higher temperature melting of a similar source region to produce an HFSE- and REE-enriched melt (e.g., Creaser and White 1991; Bea 1996; Lentz 1998; Hanchar and Watson 2003; Piercey et al. 2008). The Powderhouse rhyolite shares similar geochemical characteristics with the Chisel member of the Powderhouse dacite and the Moore Lake basalt (Figs. 12-16) and plots along similar trends on binary incompatible element diagrams (Fig. 11) but has a more primitive $\varepsilon Nd_{(1.9Ga)}$ value (Fig. 19; Table 4). It may

therefore be comagmatic with the Chisel member and Moore Lake basalt but with less crustal contamination. It also shares similar geochemical characteristics with the Chisel rhyolite (Figs. 12-14), and it may represent a similar melt to the Chisel rhyolite that has undergone more crustal contamination.

The QFP rhyolite is interpreted to have a separate petrogenesis from the Chisel, Powderhouse, and Photo-type rhyolites. It has similar Zr/Ti and Nb/Y ratios as PR2 but lower REE and HFSE concentrations and a positive HREE slope (Figs. 12-14). It also has the most primitive $\varepsilon Nd_{(1.9Ga)}$ measured to date for the Chisel sequence rocks ($\varepsilon Nd_{(1.9Ga)} = +5.7$). The chondrite-normalized REE pattern of the QFP rhyolite is similar to the U-shaped pattern characteristic of low-Ca boninites (Taylor et al. 1994). Boninites are present in the Welch basalt of the Anderson sequence (Stern et al. 1995), but are high-Ca and do not have U-shaped REE patterns (Stern et al. 1995), which is common for high-Ca boninites (e.g., North Tonga: Falloon et al. 2007; Tonga arc: Cooper et al. 2010). Rather, the positive HREE slope of the QFP rhyolite may be the product of shallow melting above the garnet zone. The low REE and HFSE concentrations and primitive $\varepsilon Nd_{(1.9Ga)}$ value suggest that the melt source was depleted. We therefore suggest that the QFP rhyolite was produced by partial melting of a hydrated depleted source at shallow depths.

4.8.3.3 Implications of Nd isotopes

In considering the Nd isotopic values for the felsic and mafic rocks of the Anderson and Chisel sequences as a whole, a clear pattern emerges that may reflect the changing tectonic environment as it relates to VMS formation (Fig. 19). The most primitive $\varepsilon Nd_{(1.9Ga)}$ values coincide with the felsic units at the ore interval of each sequence, whereas the most evolved $\varepsilon Nd_{(1.9Ga)}$ values are

recorded by the basalt flows and volcaniclastic units immediately overlying the ore intervals (Snell basalt and Threehouse unit; Fig. 19). This pattern is interpreted to result from crustal thinning due to arc rifting during VMS formation followed by crustal thickening due to magmatic underplating. This is consistent with Bailes and Galley (1999), who concluded that the isotopically primitive rhyolites were produced through high-temperature melting of oceanic lithosphere in zones of arc rifting. The low $\varepsilon Nd_{(1.9Ga)}$ values for the Snell basalt are interpreted to be the result of intracrustal contamination (Stern et al. 1992, 1995), and this process is inferred to also be the source of the low $\varepsilon Nd_{(1.9Ga)}$ values for the Threehouse (Balloch) basalt. This is further supported by the lack of correlation between $\varepsilon Nd_{(1.9Ga)}$ values and LREE enrichment (Fig. 17a), which indicates that low $\varepsilon Nd_{(1.9Ga)}$ values do not reflect an enriched mantle component. The effects of intracrustal contamination persist in the tuffs of the Threehouse unit (Fig. 19). The occurrence of these low $\varepsilon Nd_{(1.9Ga)}$ values immediately above the ore intervals suggests that the mantle-derived melts stagnated in the crust and assimilated crustal material prior to eruption. This may have occurred due to crustal thickening associated with magmatic underplating following arc rifting, which has been documented in modern arc settings in the Lau Basin (Clift and Dixon 1994). The Snell basalt and Threehouse unit have flat to slightly LREE-enriched N-MORB-normalized REE patterns, suggesting that these units were derived from more depleted mantle melts. This may suggest that the melts initially formed during arc rifting when the thinned crust would have promoted shallower depths of melting where the mantle is more depleted.

4.8.4 Reconstruction of the Chisel sequence ore-forming environment

The volcanic units and lithofacies associated with the Chisel sequence ore interval suggest that VMS deposit formation was associated with a major synvolcanic subsidence structure formed

during rifting of the Snow Lake arc assemblage (Fig. 21; Bailes and Galley 2007). Subsidence followed large-volume Powderhouse dacite eruptions to produce the Lalor-Chisel basin (Friesen 2018), which is divided into at least two smaller nested basins; one basin contains the Lalor member and the other contains the Chisel member (Fig 21; Friesen 2018). The abrupt termination of the Powderhouse dacite against the underlying Moore unit (Fig. 3; Bailes and Galley 2007), defines one wall of the basin in which the VMS deposits formed. The geometry of the subsidence structure is unknown. Previous workers have suggested a caldera (Bailes and Galley 2007); however, we prefer the term cauldron as per the definition by Smith and Bailey (1968), which does not specify shape, size, or a connection with surface volcanism. The exact size of the subsidence structure is not determinable due to deformation. An approximate minimum size estimate based on the strike length of the Powderhouse dacite is 4.5 km.

Lateral variations in the lithofacies architecture of the Powderhouse dacite (Friesen 2018) and Threehouse units, which form the footwall and hanging wall to the Chisel sequence VMS deposits, indicate that there were variations in water depth along the Chisel sequence ore interval during VMS formation. These variations occurred over 100s of metres to kilometres and resulted from variable amounts of subsidence throughout the cauldron. The lateral changes in water depth may have important consequences for the metal endowment of Chisel sequence VMS deposits. For example, Monecke et al. (2014) have shown that, of the 130 seafloor massive sulfide occurrences in suprasubduction settings, Cu-rich deposits are generally restricted to water depths >1,000 m, Zn- and Pb-rich deposits may form at any water depth, and deposits containing >5% Zn commonly form at water depths <1,000 m. This water depth control on base metal content is attributed, in part, to boiling, because Cu solubility in typical black smoker fluids is temperature

dependent (>300°C), and cooling associated with boiling may result in Cu precipitation at depth within the subseafloor hydrothermal system (Monecke, et al., 2014). Using this analogy, Stewart et al. (2018b) proposed that the Photo Lake deposit may be enriched in Cu because it formed at greater water depths greater than the other, more Zn-rich, Chisel sequence VMS deposits.

The Photo Lake deposit is interpreted to have formed at a major structure along the periphery of the Lalor-Chisel cauldron that acted as a magma conduit for the fissure-fed Photo rhyolite flows and, subsequently, for ascending hydrothermal fluids (Fig. 21; Stewart et al. 2018b). This major structure may have resulted in higher Cu concentrations at Photo Lake by allowing ascending high-temperature fluids to rapidly reach the seafloor. The Au enrichment at Photo Lake has been interpreted to be the product of a magmatic input (Stewart et al. 2018b), and the proximity of the deposit to a deep-penetrating, crustal-scale fault may have been critical for magmatic volatiles to be incorporated into the hydrothermal system.

The Lalor VMS deposit is also enriched in Au relative to the other Chisel sequence deposits (3.08 g/t: Hudbay 2016). The Au is concentrated within a Cu-rich stringer zone that formed below Zn-rich massive sulfide lenses but is now transposed parallel to the Zn-rich lenses due to later deformation (Bailes 2014; Caté et al. 2014; Caté 2016; Stewart et al. 2018a). Reconstruction of the lithofacies architecture at Lalor indicates the deposit occurs in proximity to a major synvolcanic fault as evidenced by: 1) the location of the deposit at the contact between the Lalor and Chisel members of the Powderhouse dacite, suggesting proximity to a structure separating the Lalor member basin from the Chisel member basin (Fig. 21; Friesen, 2018; Stewart et al., 2018a; Figs. 4, 21); and 2) the uppermost massive sulfide lens occurs within a

package of volcaniclastic rocks dominated by clasts of Moore Lake basalt chemistry but containing clasts of the Lalor and Chisel members (Fig. 4), indicating that the Moore Lake unit is resedimented. The inclusion of Moore Lake basalt clasts in the volcaniclastic host rocks requires that the older basalt unit was exposed to the seafloor, presumably through faulting and subsidence. Clasts with Moore Lake basalt chemistry also occur in tuff breccia to breccia lithofacies of the Lost and Chisel members of the Powderhouse dacite in the South Chisel basin area (Friesen 2018), suggesting that resedimentation of the Moore Lake unit coincided with the ore interval. This indicates that the Lalor deposit did not form at the base of the Moore Lake basalt as has been suggested by previous workers (Caté 2016), but formed on and within localized deposits of resedimented volcaniclastic rocks dominated by clasts of older basaltic strata and adjacent to a synvolcanic fault (Fig. 21). Furthermore, the deposit must have formed after emplacement of both the Chisel and Lalor members of the Powderhouse dacite because the Cu-Au-rich stringer zone and VMS-related alteration occur in both of these units (Fig. 4), suggesting that the Lalor deposit formed at the same ore interval as all of the other Chisel sequence VMS deposits. The stratigraphic hanging wall to the Lalor deposit is cut by the large-scale Lalor-Chisel fault and it is therefore unclear if the deposit occurs immediately below the Threehouse unit; however, structural slivers of Threehouse volcaniclastic rocks and flows were identified in the structural hanging wall (Fig. 4). A magmatic input has been proposed as the source of Au in the Lalor deposit (Caté 2016), and the major, deep-penetrating structure interpreted to be associated with deposit formation may have facilitated this input. Therefore, Au enrichment in the Lalor and Photo Lake deposits of the Chisel sequence may be attributed to proximity to large, deep-penetrating structures that allowed magmatic volatiles to reach the seafloor.

4.8.5 Volcanic setting of the Snow Lake arc assemblage

In order to better understand the VMS metallogeny of the Snow Lake arc assemblage within the context of the larger Trans-Hudson Orogen, it is important to identify controls on mineralization at a variety of scales, from the deposit to the regional scale. The main controls on mineralization at a deposit scale are major faults associated with a synvolcanic subsidence structure. These faults focused high-temperature hydrothermal fluid flow and facilitated metal deposition during a period of quiescence in volcanism. At the district scale, mineralization is associated with intra-arc extension and rifting (Bailes and Galley 1999, 2007; Fig. 22). At the regional scale, the Snow Lake arc assemblage is one VMS-hosting volcanic centre and can be compared with the Flin Flon arc assemblage, which is located approximately 120 km west of Snow Lake and contains 13 of the 28 deposits in the Flin Flon belt (Galley et al. 2007).

Evidence for intra-arc extension and rifting in the Snow Lake arc assemblage includes: a) voluminous and areally restricted volcaniclastic rocks (>40% of Chisel sequence; Bailes and Galley 1999), a significant proportion of which are resedimented; b) rapid lateral facies changes indicative of synvolcanic faulting; and 3) isotopically juvenile felsic magmas in a bimodal volcanic suite, interpreted to be the product of partial melting of primitive oceanic lithosphere in a zone of high heat flow (Bailes and Galley 1999). Evidence for intra-arc extension and rifting begins with the Stroud breccia and continues throughout the Chisel sequence until the Snow Creek sequence, indicating a protracted rifting event (Fig. 22). The Snow Creek sequence, which comprises mafic flows with MORB chemistry (Fig. 2; Bailes and Galley 1996, 1999), represents the transition from arc rifting to seafloor spreading (Fig. 22e). A similar transition is reported for

modern back-arc basins, which form by initial arc rifting followed by seafloor spreading and extrusion of back-arc basin basalts (e.g., Lau Basin: Clift et al. 1994, Parson and Wright 1996; Mariana Trough: Hagen et al. 1992).

The timing of VMS deposit formation during arc rifting is critical for understanding the evolution of ore-forming hydrothermal systems. The recent interpretation that the rhyolite flow-domes in the Anderson sequence occur at the same stratigraphic interval as the Stroud breccia (DeWolfe and Gibson 2016) implies that the Anderson VMS deposits formed at the base of the Chisel sequence rather than the top of the Anderson sequence. This is consistent with previous interpretations that the Anderson deposits formed during intra-arc rifting (Bailes and Galley 1996, 1999). Therefore, the entire Chisel sequence is interpreted to represent a period of continuous arc rifting, associated magmatism and volcanism, and VMS formation. In order to maintain consistency with historical naming and account for the new stratigraphic interpretation, the Anderson sequence deposits are herein referred to simply as the Anderson deposits.

The Anderson and Chisel VMS deposits are distinct in terms of their stratigraphic positions and metal contents, with the Anderson deposits being Cu rich and the Chisel deposits being dominantly Zn rich (Bailes and Galley 1996; Galley et al. 2007). Previous workers have suggested that the Zn-rich nature of the Chisel deposits may be due to their permeable volcaniclastic host rocks, which would have introduced more seawater into the hydrothermal system and lowered fluid temperatures (Bailes and Galley 1999). The contrast in base metal concentrations between the two deposit groups may also be due, in part, to variations in water

depth (e.g., Monecke et al. 2014), with the Cu-rich Anderson deposits having formed at greater water depths than the Zn-rich Chisel deposits.

The Threehouse unit occurs in the stratigraphic hanging wall to the Anderson and Chisel deposits (Bailes and Galley 1996 and references therein); however, the only Lower Chisel sequence unit recognized in the hanging wall of the Anderson deposits is the Moore Lake unit, which overlies the Anderson Lake deposit (Walford and Franklin 1982; Bailes and Galley 1996). This indicates that the majority of the units in the Chisel sequence are restricted to the Lalor-Chisel subsidence structure. Above the Anderson deposits, the Threehouse unit consists of heterolithic mafic breccia, which indicates a more complicated provenance for, or resedimentation of, the Threehouse formation as compared to Threehouse flows (Balloch basalt) and vent-proximal fire-fountain deposits associated with the Chisel deposits (Fig. 8j). Furthermore, as the Chisel deposits do not occur directly above the Anderson deposits, but rather approximately 7 to 10 km along strike (Bailes and Galley 2007), they are spatially distinct and their timing relative to the Anderson deposits is difficult to constrain. Typically, deposits in a single VMS district formed during a time-limited (<2 million years) volcanic episode or stratigraphic interval (Franklin 1995; Franklin et al. 2005), which suggests that formation of the Anderson and Chisel VMS deposits occurred over a relatively short period of time. This is further supported by the overlapping ages of the Sneath Lake (1886 +17/-9 Ma: Bailes et al. 1988, 1991) and Richard Lake (1889 +5/-6 Ma: Bailes et al. 1988, 1991) plutons, which have been interpreted as part of the magmatic heat source driving the hydrothermal convective systems responsible for the Anderson and Chisel deposits, respectively (Bailes and Galley 1996, 1999, 2007; Bailes et al. 2007). The Chisel deposits are associated with a localized volcanic subsidence structure, and the

Anderson deposits occur over a more laterally extensive interval associated with rhyolite flow-dome volcanism, but both are related to arc rifting. Given their close association with the primitive Welch basalt, the Anderson deposits may have formed during initial arc rifting, and the Chisel deposits formed during localized extension driven by subsidence related to volcanism and magma chamber collapse (Figs. 22b, c).

The Snow Lake and Flin Flon arc assemblages are interpreted to have formed during arc rifting (Syme et al. 1999; DeWolfe et al. 2009), and at Flin Flon, several of the deposits (Flin Flon, 777, Callinan) are interpreted to have formed in a subsidence structure (Syme and Bailes 1993; Gibson et al. 2006, 2007, 2009; MacLachlan and Devine 2007). However, there are distinct differences between the two arc assemblages that may have influenced their metallogeny. The volcanic rocks in the Snow Lake arc assemblage are interpreted to have interacted with older arc crust to a greater extent than the volcanic rocks of the Flin Flon arc assemblage based on a wider range in $\varepsilon Nd_{(1.9Ga)}$ values ($\varepsilon Nd_{(1.9Ga)}$ = -0.4 to +3.8 for Snow Lake versus +2.1 to +4.8 for Flin Flon: Stern et al. 1992) and the presence of inherited Archean zircons in the Stroud breccia (Machado and David 1992; David et al. 1996). Previous workers have suggested these data may indicate that the Snow Lake arc assemblage evolved as a pericratonic arc, whereas the Flin Flon assemblage evolved as an oceanic arc (Stern et al. 1992, 1995; David et al. 1996; Percival et al. 2004; Corrigan et al. 2007, 2009). These data may also suggest that the Flin Flon arc assemblage represents a more primitive arc than the Snow Lake arc assemblage and is associated with thinner crust and less crustal residence time of the magmas. The two arc assemblages also differ in terms of their VMS deposit distribution. The deposits of the main camp in the Flin Flon block (Flin Flon, 777, Callinan) occur at a single ore interval associated with felsic volcanism in a

sequence dominated by mafic flows and volcaniclastic rocks (Gibson et al. 2011, and references therein). This is similar to the setting for the Anderson deposits but differs significantly from the setting for the Chisel deposits. This contrast in mineralization may be a product of different spreading rates during rifting of the Flin Flon and Snow Lake arcs. In modern systems, fast spreading rates typically occur in thin crust and are associated with voluminous volcanic eruptions, whereas slow spreading rates are more common in thick crust and are associated with longer periods of tectonic activity (Hannington et al. 2010). The Flin Flon arc assemblage is interpreted to have formed in thinner crust, and the hanging wall to its VMS deposits is dominated by flows, whereas the hanging wall to the Anderson VMS deposits of the Snow Lake arc assemblage has a large volume of primary and resedimented volcaniclastic rocks. These differences are consistent with a faster rate of arc rifting in the Flin Flon arc than in the Snow Lake arc. If the Flin Flon arc experienced faster rates of rifting, the Flin Flon VMS deposits would have been displaced from their heat source faster and seafloor spreading may have been initiated sooner than in the Snow Lake arc, where slower rates of rifting may have allowed for the second stage of VMS mineralization to occur (the Chisel VMS deposits).

The Flin Flon arc assemblage has also been compared with modern arc settings, specifically the Tonga-Kermadec-Lau arc-backarc basin system (Syme et al. 1999; DeWolfe et al. 2009). Although the Flin Flon and Snow Lake arc assemblages share similarities with modern arc settings, it is important to consider the relative scales of these systems when making such comparisons. The entire strike length of the Tonga-Kermadec -Lau system is >3,000 km and it is approximately 350 to 625 km wide, whereas the Snow Lake arc assemblage deposits are all located within an area that covers ~250 km^2, and the Flin Flon deposits are located within an area

that covers ~400 km^2. Therefore, the two arc assemblages are not analogous to the entire Tonga-Kermadec-Lau system as a whole, but rather to discrete volcanic and tectonic centres within the larger geodynamic environment. Constraints on the timing and location of VMS districts within their broader tectonic setting are poorly understood and further work to identify these controls on mineralization will be critical for future exploration in ancient volcanic terrains.

4.9 Conclusions

The volcanic reconstruction of the Chisel sequence combined with the whole rock geochemistry and isotopes have contributed to a new understanding of the stratigraphy and petrogenesis of units related to the Chisel ore interval and to controls on selective metal endowment of the VMS deposits.

The LREE enrichment of the Moore Lake basalt, Chisel member of the Powderhouse dacite, Powderhouse rhyolite, and possibly Chisel rhyolite are interpreted to be related to the tectonic environment associated with arc rifting and VMS deposit formation. Light-REE enrichment is attributed to preferential melting of an enriched component in a heterogeneous mantle, either due to decreased fluid addition to the mantle during arc rifting or due to upwelling of deep enriched mantle during crustal thinning associated with arc rifting. Identification of LREE-enriched units in volcanic environments may therefore assist in VMS exploration.

Variations in water depth as reflected by facies changes in the Threehouse unit suggest that the water depth at which the Chisel sequence deposits formed may have also been variable. This is further supported by the extensive synvolcanic faulting and subsidence observed throughout the

ore interval and documented in the Powderhouse dacite unit by Friesen (2018). These water depth variations may have influenced the base metal content of the VMS deposits by influencing the depth in the subseafloor at which the hydrothermal fluids began boiling. This may have contributed to the anomalously high Cu concentrations in the Photo Lake deposit (Stewart et al. 2018b). The Photo Lake and Lalor deposits are also interpreted to have formed at major structures in the Lalor-Chisel cauldron, which may be important for maintaining high fluid temperatures at shallow levels in the subseafloor and for magmatic fluid contributions to their hydrothermal systems, contributing to the Au enrichment of the two deposits.

Voluminous primary and resedimented volcaniclastic rocks and rapid lateral facies changes indicate that intra-arc extension and rifting commenced during emplacement of the Stroud breccia and continued throughout the development of the Chisel sequence. The Chisel sequence represents a localized volcanic subsidence structure built on the primitive Anderson sequence. The Anderson and Chisel VMS deposits are distinct in terms of their stratigraphic positions, volcanic architecture and setting and metal contents, consistent with their formation at different times during the evolution of a rifted arc. The Anderson VMS deposits formed during early widespread arc rifting, whereas the Chisel VMS deposits formed during localized extension above a magma chamber in the extended arc.

4.10 References

Allègre, C.J. and Turcotte, D.L. 1986. Implications of a two-component marble-cake mantle. Nature, **323**(11): 123-127.

Allen, R.L., Lundstrom, I., Ripa, M., Simeonov, A., and Christofferson, H. 1996a. Facies analysis of a 1.0 Ga continental margin, backarc felsic caldera province with diverse Zn-Pb-Ag-(Cu-Au) sulfide and Fe oxide deposits, Bergslagen region, Sweden. Economic Geology, **91**: 979-1008.

Allen, R.L., Weihed, P., and Svenson, S.-A. 1996b. Setting of Zn-Cu-Au-Ag massive sulfide deposits in the evolution and facies architecture of a 1.9 Ga marine volcanic arc, Skellefte District, Sweden. Economic Geology, **91**: 1022-1053.

Ansdell, K.M. 2005. Tectonic evolution of the Manitoba-Saskatchewan segment of the Paleoproterozoic Trans-Hudson orogen, Canada. Canadian Journal of Earth Sciences **42**: 741-759.

Ansdell, K.M., Lucas, S.B., Connors, K., and Stern, R.A. 1995. The Kisseynew Gneiss Belt, Trans-Hudson Orogen, Canada: origin and history of a Paleoproterozoic back-arc sedimentary basin. Geology **23**: 1039-1043.

Bailes, A.H. 1992. Wekusko Lake (north) project (NTS 63J/13SW). *In* Report of Activities 1992. Manitoba Energy and Mines, Minerals Division, p. 55-64.

Bailes, A.H. 1996. Setting of Cu-Zn-Au mineralization at Photo Lake (part of NTS 63K16). *In* Report of Activities 1996. Manitoba Energy and Mines, Minerals Division, p. 66-74.

Bailes, A.H. 1997. Geochemistry of Paleoproterozoic volcanic rocks in the Photo Lake area, Flin Flon Belt (part of NTS 63K16). *In* Report of Activities 1997. Manitoba Energy and Mines, Minerals Division, p. 61-72.

Bailes, A.H. 2014. Regional geological setting of the Zn- and Au-rich Lalor VMS deposit, Snow Lake, Manitoba, Canada. *In* British Columbia Geophysical Society Lalor Symposium

Presentations Listing. Available from http://www.bcgsonline.org/lalor-symposium/ [accessed 10 June 2017].

Bailes, A.H., and Galley, A.G. 1996. Setting of Paleoproterozoic volcanic-hosted massive base metal sulphide deposits, Snow Lake. *In* Bonham-Carter, G.F., Galley, A.G., and Hall, G.E.M., eds., EXTECH 1: A Multidisciplinary Approach to Massive Sulphide Research in the Rusty Lake-Snow Lake Greenstone Belts, Manitoba: Geological Survey of Canada, Bulletin 426, p. 105-138.

Bailes, A.H., and Galley, A.G. 1999. Evolution of the Paleoproterozoic Snow Lake arc assemblage and geodynamic setting for associated volcanic-hosted massive sulphide deposits, Flin Flon Belt, Manitoba, Canada. Canadian Journal of Earth Sciences **36**: 1789-1805.

Bailes, A.H., and Galley, A.G. 2007. Geology of the Chisel-Anderson lakes area, Snow Lake, Manitoba (NTS area 63K16SW and west half of 63J13SE). Manitoba Science, Technology, Energy and Mines, Manitoba Geological Survey, Geoscientific Map MAP2007-1, scale 1:20 000 plus notes.

Bailes, A.H., and Simms, D. 1994. Implications of an unconformity at the base of the Threehouse formation, Snow Lake, Manitoba (NTS 63 K/16). *In* Report of Activities 1994. Manitoba Energy and Mines, Geological Services, p. 85-88.

Bailes, A.H., and Syme, E.C. 1989. Geology of the Flin Flon – White Lake area. Manitoba Energy and Mines, Geological Report GR87-1.

Bailes, A.H., Hunt, P.A., and Gordon, T.M. 1991. U-Pb zircon dating of possible synvolcanic plutons in the Flin Flon belt at Snow Lake, Manitoba. *In* Radiogenic age and isotopic studies report 4. Geological Survey of Canada, p. 35-43.

Bailes, A.H., Chackowsky, L.E., Galley, A.G., and Connors, K.A. 1994. Geology of the Snow Lake – File Lake area, Manitoba (parts of NTS 63 K/16 and 63 J/13). Manitoba Energy and Mines, Open Field Report OF94-4 and Map, 1:50 000 scale.

Bailes, A.H., Galley, A.G., Skirrow, R.G., and Young, J. 1996. Geology of the Chisel volcanic-hosted massive sulphide area, Snow Lake, Manitoba (part of 63K/16SE). Manitoba Energy and Mines, Open File Report OF95-4, annotated 1:5000 colour map.

Bailes, A.H., Simms, D., Galley, A.G., and Young, J. 1997. Geological setting of the Photo Lake volcanic-hosted massive sulphide deposits, Snow Lake, Manitoba (part of 63K/16SE). Manitoba Energy and Mines, Open File Report OF97-5, annotated 1:5000 colour map.

Bailes, A.H., Rubingh, K., Gagné, S., Taylor, C., Galley, A., Bernauer, S., and Simms, D. 2013. Volcanic setting of Paleoproterozoic VMS and gold deposits at Snow Lake, Manitoba. Geological Association of Canada – Mineralogical Association of Canada Joint Annual Meeting, Field Trip Guidebook FT-A2. Manitoba Innovation, Energy and Mines, Manitoba Geological Survey, Open File OF2013-3, 63 p.

Barrett, T.J., and MacLean, W.H., 1994. Chemostratigraphy and hydrothermal alteration in exploration for VHMS deposits in greenstones and younger volcanic rocks. *In* Lentz, D.R., ed., Alteration and alteration processes associated with ore-forming systems. Geological Association of Canada, Short Course Notes 11, pp. 433–467.

Bea, F. 1996. Controls on the trace element composition of crustal melts. Transactions of the Royal Society of Edinburgh, Earth Sciences, **87**: 33-41.

Cabanis, B. and Lecolle, M. 1989. Le diagramme La/10-Y/15-Nb/8 : un outil pour la discrimination des séries volcaniques et la mise en évidence des processus de mélange

et/ou de contamination crustale. Comptes Rendus de l'Académie des Sciences de Paris, Série 2, **309** : 2023-2029.

Cas, R.A.F. Submarine volcanism : eruption styles, products, and relevance to understanding the host-rock successions to volcanic-hosted massive sulfide deposits. Economic Geology, **87:** 511-541.

Cas, R.A.F., and Wright, J.V. 1987. Volcanic successions modern and ancient. Chapman and Hall, London, UK.

Cas, R.A.F., and Wright, J.V. 1991. Subaqueous pyroclastic flows and ignimbrites: an assessment. Bulletin of Volcanology, **53**: 357-380.

Caté, A. 2016. Geology of the Paleoproterozoic Zn-Cu-Au Lalor volcanogenic massive sulphide deposit and its gold-rich lenses, Snow Lake, Manitoba. / Géologie du gisement de sulfures massifs volcanogène Paléoprotérozoïque à Zn-Cu-Au de Lalor et de ses lentilles riches en or, Snow Lake, Manitoba. Ph.D. thesis, Université du Québec, Institut national de la recherche scientifique, Québec, Québec, 430 p.

Caté, A., Mercier-Langevin, P., Ross, P.-S., and Simms, D. 2014. Structural controls on geometry and ore distribution in the Lalor auriferous VMS deposit, Snow Lake, west-central Manitoba (part of NTS 63K16): preliminary results from underground mapping. *In* Report of Activities 2014. Manitoba Mineral Resources, Manitoba Geological Survey, p. 104-155.

Clift, P.D., and Dixon, J.E. 1994. Variations in arc volcanism and sedimentation related to rifting of the Lau basin (southwest Pacific). *In* Proceedings of the Ocean Drilling Program, Scientific Results, **135**: p. 23-49.

Clift, P.D., and ODP Leg 135 Scientific Party. 1994. Volcanism and sedimentation in a rifting island-arc terrain: an example from Tonga, SW Pacific. Geological Society, London, Special Publications, **81**: 29-51.

Connors, K.A., Ansdell, K.M., and Lucas, S.B. 1999. Coeval sedimentation, magmatism, and fold-thrust development in the Trans-Hudson Orogen: propagation of deformation into an active continental arc setting, Wekusko Lake area, Manitoba. Canadian Journal of Earth Sciences **36**: 275-291.

Cooper, L.B., Plank, T., Arculus, R.J., Hauri, E.H., Hall, P.S., and Parman, S.W. 2010. High-Ca boninites from the active Tonga Arc. Journal of Geophysical Research, **115**: B10206.

Corrigan, D., Galley, A.G., and Pehrsson, S. 2007. Tectonic evolution and metallogeny of the southwestern Trans-Hudson Orogen. *In* Mineral Deposits of Canada: A Synthesis of Major Deposit-Types, District Metallogeny, the Evolution of Geological Provinces, and Exploration Methods. Special Publication No. 5. *Edited by* W.D. Goodfellow, W.D. Geological Association of Canada, Mineral Deposits Division. p. 881-902.

Corrigan, D., Pehrsson, S., Wodicka, N., and de Kemp, E. 2009. The Palaeoproterozoic Trans-Hudson Orogen: a prototype of modern accretionary processes. Geological Society, London, Special Publications, **327**: 457-479.

Creaser, R.A., and White, A.J.R. 1991. Yardea dacite: large-volume, high-temperature felsic volcanism from the Middle Proterozoic of South Australia. Geology, **19**: 48-51.

David, J., Bailes, A.H., and Machado, N. 1996. Evolution of the Snow Lake portion of the Palaeoproterozoic Flin Flon and Kisseynew belts, Trans-Hudson Orogen, Manitoba, Canada. Precambrian Research, **80**: 107-124.

DeWolfe, Y.M. and Gibson, H.L. 2016. Volcanic reconstruction of the Paleoproterozoic Stroud Breccia, Snow Lake, Manitoba: Understanding the transition from primitive to mature arc and implications for re-defining the ore-forming environment of the Anderson-Stall-Rod VMS deposits. *In* GAC-MAC 2016 Joint Abstracts Listing.

DeWolfe, Y.M., Gibson, H.L., and Piercey, S.J. 2009. Petrogenesis of the 1.9 Ga mafic hanging wall sequence to the Flin Flon, Callinan, and Triple 7 massive sulphide deposits, Flin Flon, Manitoba, Canada. Canadian Journal of Earth Sciences, **46**: 509-527.

Dinel, E., Saumur, B.M., and Fowler, A.D. 2008. Spherulitic aphyric pillow-lobe metatholeiitic dacite lava of the Timmins area, Ontario, Canada: a new Archean facies formed from superheated melts. Economic Geology, **103**: 1365-1378.

Engelbert, M.S., Friesen, V., Gibson, H.L., and Lafrance, B. 2014. Volcanic reconstruction of the productive VMS ore interval in the Paleoproterozoic Chisel sequence, Snow Lake, Manitoba. *In* Geological Association of Canada – Mineralogical Association of Canada Joint Annual Meeting Abstracts Listing, Fredericton, 2014, Abstract Volume, pp. 83-84.

Falloon, T.J., Danyushevsky, L.V., Crawford, T.J., Maas, R., Woodhead, J.D., Eggins, S.M., Bloomer, S.H., Wright, D.J., Zlobin, S.K., and Stacey, A.R. 2007. Multiple mantle plume components involved in the petrogenesis of subduction-related lavas from the northern termination of the Tonga Arc and northern Lau Basin: evidence from the geochemistry of arc and backarc submarine volcanics. Geochemistry, Geophysics, Geosystems, **8**: Q09003.

Fisher, R.V. 1961. Proposed classification of volcaniclastic sediments and rocks. Geological Society of America Bulletin **72**: 1395-1408.

Fisher, R.V. 1966. Rocks composed of volcanic fragments and their classification. Earth Science Reviews **1**: 287-298.

Franklin, J.M., Gibson, H.L., Jonasson, I.R., and Galley, A.G., 2005, Volcanogenic massive sulfide deposits, in Hedenquist, J.W., Thompson, J.F.H., Goldfarb, R.J., and Richards, J.P., eds., Economic Geology 100th Anniversary Volume, p. 523-560.

Friesen, V.C., Engelbert, M., DeWolfe, Y.M., and Gibson, H.L. 2015. Volcanic reconstruction of the Powderhouse dacite in the Paleoproterozoic VMS hosting Chisel sequence, Snow Lake, Manitoba. *In* AGU-GAC-MAC-CGU 2015 Joint Assembly Abstracts Listing, pp. 276.

Friesen, V.C. 2018. Volcanic Reconstruction of the Powderhouse Formation in the Paleoproterozoic VMS Hosting Chisel Sequence, Snow Lake, Manitoba. M.Sc. thesis in preparation, Department of Earth Sciences, Laurentian University, Sudbury, Ontario.

Froese, E. and Moore, J.M. 1980. Metamorphism in the Snow Lake area, Manitoba. Geological Survey of Canada, Paper 78-27.

Galley, A.G. and Bailes, A.H. 2002. Volcanogenic massive sulphide-related hydrothermal events within the Paleoproterozoic Snow Lake arc assemblage. Geological Association of Canada – Mineralogical Association of Canada Joint Annual Meeting, Saskatoon, Field Trip Guidebook A2, 94 p.

Galley, A.G., Ames, D.E., and Franklin, J.M. 1988. Geological Setting of Gold Mineralization, Snow Lake, Manitoba. Geological Survey of Canada, Open File 1700.

Galley, A.G., Bailes, A.H., and Kitzler, G. 1993. Geological setting and hydrothermal evolution of the Chisel Lake and North Chisel Zn-Pb-Cu-Ag-Au massive sulfide deposits, Snow Lake, Manitoba. Exploration and Mining Geology **2**: 271-295.

Gibson, H.L., Morton, R.L., and Hudak, G.J., 1999. Submarine volcanic processes, deposits, and environments favorable for the location of volcanic-associated massive sulfide deposits. Reviews in Economic Geology, **8**: 13-51.

Gibson, H., Pehrsson, S., Lafrance, B., DeWolfe, M., Syme, R., Bailes, A., Gilmore, K., Devine, C., Simard, R.-L., MacLachlan, K., and Pearson, B. 2011. The volcanological and structural evolution of the Paleoproterozoic Flin Flon and Snow Lake mining districts. Geological Association of Canada – Mineralogical Association of Canada Joint Annual Meeting, Ottawa, Field Trip Guidebook 3B, 76 p.

Gill, J.B. 1981. Orogenic andesites and plate tectonics. Springer-Verlag, New York, Berlin, and Heidelberg, 392 p.

Goldstein, S.L., O'Nions, R.K., and Hamilton, P.J. 1984. A Sm-Nd isotopic study of atmospheric dusts and particulates from major river systems. Earth and Planetary Science Letters, **70**: 221-237.

Hagen, R.A., Shor, A.N., and Fryer, P. 1992. SeaMARC II evidence for the locus of seafloor spreading in the southern Mariana Trough. Marine Geology **103**: 311-322.

Hanchar, J.M., and Watson, E.B. 2003. Zircon saturation thermometry. Reviews in Mineralogy and Geochemistry, **53**: 59-112.

Hannington, M., Jamieson, J., Monecke, T., and Petersen, S. 2010. Modern sea-floor massive sulfides and base metal resources: towards an estimate of global sea-floor massive sulfide potential. Economic Geology Special Publication, **15**: 317-338.

Hart, T.R., Gibson, H.L., and Lesher, C.M. 2004. Trace element geochemistry and petrogenesis of felsic volcanic rocks associated with volcanogenic massive Cu-Zn-Pb sulfide deposits. Economic Geology, **99**: 1003-1013.

Hastie, A.R., Kerr, A.C., Pearce, J.A., and Mitchell, S.F. 2007. Classification of altered volcanic island arc rocks using immobile trace elements: development of the Th-Co discrimination diagram. Journal of Petrology, **48**: 2341-2357.

Hawkesworth, C.J., Gallagher, K., Hergt, J.M., and McDermott, F. 1993. Mantle and slab contributions in arc magmas. Annual Review of Earth and Planetary Science, **21**: 175-204.

Hildreth, W. 1981. Gradients in silicic magma chambers: Implications for lithospheric magmatism. Journal of Geophysical Research: Solid Earth, **86**: 10153-10192.

Huston, D.L., Pehrsson, S., Eglington, B.M., and Zaw, K. 2010. The geology and metallogeny of volcanic-hosted massive sulfide deposits: variations through geologic time and with tectonic setting. Economic Geology, **105**: 571-591.

Jacobsen, S.B. and Wasserburg, G.J. 1980. Sm-Nd isotopic evolution of chondrites. Earth and Planetary Science Letters, **50**: 139-155.

Kelley, K.A., Plank, T., Grove, T.L., Stolper, E.M., Newman, S., and Hauri, E. 2006. Mantle melting as a function of water content beneath back-arc basins. Journal of Geophysical Research, **111**: B09208.

Kokelaar, P. 1986. Magma-water interactions in subaqueous and emergent basaltic volcanism. Bulletin of Volcanology, **48**: 275-289.

Kraus, J. and Williams, P.F. 1993. Structural studies along the northern margin of the Flin Flon-Snow Lake greenstone belt, Snow Lake. *In* Report of Activities 1993. Manitoba Energy and Mines, Minerals Division, p. 117-118.

Kraus, J. and Williams, P.F. 1994. Structure of the Squall Lake area, Snow Lake (NTS 63K/16). *In* Report of Activities 1994. Manitoba Energy and Mines, Minerals Division, p. 189-193.

Kraus, J. and Williams, P.F. 1998. Relationship between foliation development, porphyroblasts growth and large-scale folding in a metaturbidite suite, Snow Lake, Canada. Journal of Structural Geology, **20**: 61-76.

Kraus, J. and Williams, P.F. 1999. Structural development of the Snow Lake Allochthon and its role in the evolution of the southeastern Trans-Hudson Orogen in Manitoba, central Canada. Canadian Journal of Earth Sciences, **36**: 1881-1899.

Lentz, D.R., 1998. Petrogenetic evolution of felsic volcanic sequences associated with Phanerozoic volcanic-hosted massive sulphide systems: The role of extensional geodynamics. Ore Geology Reviews, **12**: 289–327.

Lesher, C.M., Goodwin, A.M., Campbell, I.H., and Gorton, M.P. 1986. Trace element geochemistry of ore-associated and barren felsic metavolcanic rocks in the Superior Province, Canada. Canadian Journal of Earth Sciences, **23**: 222-237.

Lucas, S.B., Stern, R.A., Syme, E.C., Reilly, B.A., and Thomas, D.J. 1996. Intraoceanic tectonics and the development of continental crust: 1.92-1.84 Ga evolution of the Flin Flon Belt, Canada. GSA Bulletin **108**: 602-629.

Machado, N., Zwanzig, H., and Parent, M. 1999. U-Pb ages of plutonism, sedimentation, and metamorphism of the Paleoproterozoic Kisseynew metasedimentary belt, Trans-Hudson Orogen (Manitoba, Canada). Canadian Journal of Earth Sciences **36**: 1829-1842.

MacLean, W.H., 1990. Mass changes in altered rock series: Mineralium Deposita, **25**: 44-49.

McBirney, A.R. 1963. Factors governing the nature of submarine volcanism. Bulletin of Volcanology, **30**: 337-363.

Menard, T., and Gordon, T.M. 1997. Metamorphic P-T paths from the eastern Flin Flon belt and Kisseynew Domain, Snow Lake, Manitoba. The Canadian Mineralogist **35**: 1093-1115.

Meschede, M., 1986. A method of discriminating between different types of mid-ocean ridge basalts and continental tholeiites with the Nb-Zr-Y diagram. Chemical Geology, **56**: 207–218.

Morton, R.L., Walker, J.S., Hudak, G.J., and Franklin, J.M. 1991. The early development of an Archean submarine caldera complex with emphasis on the Mattabi ash-flow tuff and its relationship to the Mattabi massive sulfide deposit. Economic Geology, **86**: 1002-1011.

Ordóñez-Calderón, J.C., Lafrance, B., Gibson, H.L., Schwartz, T., Pehrsson, S.J., and Rayner, N.M. 2016. Petrogenesis and geodynamic evolution of the Paleoproterozoic (~1878 Ma) Trout Lake volcanogenic massive sulfide deposit, Flin Flon, Manitoba, Canada. Economic Geology, **111**: 817-847.

Parson, L.M., and Wright, I.C. 1996. The Lau-Havre-Taupo back-arc basin: a southward-propagating, multi-stage evolution from rifting to spreading. Tectonophysics, **263**: 1-22.

Pearce, J.A. 1996. A user's guide to basalt discrimination diagrams. *In* Trace element geochemistry of volcanic rocks; applications for massive sulphide exploration. Geological Association of Canada, Short Course Notes 12, pp. 79-113.

Pearce, J.A., 2008. Geochemical fingerprinting of oceanic basalts with applications to ophiolite classification and the search for Archean oceanic crust. Lithos, **100**: 14–48.

Pearce, J.A., Harris, N.B.W., and Tindle, A.G., 1984. Trace element discrimination diagrams for the tectonic interpretation of granitic rocks: Journal of Petrology, **25**: 956–983.

Pecover, R.S., Buchanan, D.J., and Ashby, D.E. 1973. Fuel-coolant interaction in submarine volcanism. Nature, **245**: 307-308.

Piercey, S.J., Peter, J.M., Mortensen, J.K., Paradis, S., Murphy, D.C., and Tucker, T.L. 2008. Petrology and U-Pb geochronology of footwall porphyritic rhyolites from the Wolverine volcanogenic massive sulphide deposit, Yukon, Canada: implications for the genesis of massive sulphide deposits in continental margin environments. Economic Geology, **103**: 5-33.

Ross, P-S., and Bédard, J.H., 2009. Magmatic affinity of modern and ancient subalkaline volcanic rocks determined from trace-element discriminant diagrams: Canadian Journal of Earth Sciences, **46**: 823–839.

Rubingh, K.E., Lafrance, B., and Gibson, H.L. 2012. Lithostratigraphy and structural geology of the McLeod Road-Birch Lake thrust panel, Snow Lake, west-central Manitoba (parts of NTS 63K16, 63J13). *In* Report of Activities 2012. Manitoba Innovation, Energy and Mines, Manitoba Geological Survey, p. 104-114.

Rubingh, K.E., Gibson, H.L., and Lafrance, B. 2017. Evidence for voluminous bimodal pyroclastic volcanism during rifting of a Paleoproterozoic arc at Snow Lake, Manitoba: Canadian Journal of Earth Sciences, **54:** 654-676.

Schellart, W.P. 2004. Kinematics of subduction and subduction-induced flow in the upper mantle. Journal of Geophysical Research, **109**: B07401.

Shen, Y. and Forsyth, D.W. 1995. Geochemical constraints on initial and final depth of melting beneath mid-ocean ridges: Journal of Geophysical Research, **100:** 2211-2237.

Smith, R.L. 1979. Ash flow magmatism. Geological Society of America Special Papers, **180**: 5-27.

Smith, R.L. and Bailey, R.A. 1968. Resurgent cauldrons. *In* Coats, R.R., Hay, R.L., and Anderson, C.A., eds., Studies in volcanology: Geological Society of America Memoir 116, p. 613-662.

Spitz, G. and Darling, E. 1978. Major and minor element lithogeochemical anomalies surrounding the Louvern copper deposit, Val d'Or, Quebec. Canadian Journal of Earth Sciences, **15**: 1161-1169.

Stern, R.A., Syme, E.C., Bailes, A.H., Galley, A.G., Thomas, D.J., and Lucas, S.B. 1992. Nd-isotopic stratigraphy of Early Proterozoic Amisk group metavolcanic rocks from the Flin Flon Belt, Manitoba and Saskatchewan. *In* Radiogenic age and isotopic studies report 6. Geological Survey of Canada, p. 73-84.

Stern, R.A., Syme, E.C., Bailes, A.H., and Lucas, S.B. 1995. Paleoproterozoic (1.90-1.86 Ga) arc volcanism in the Flin Flon Belt, Trans-Hudson Orogen, Canada. Contributions to Mineralogy and Petrology **119**: 117-141.

Stewart, M.S., Lafrance, B., and Gibson, H.L. 2018a. Early thrusting and folding in the Snow Lake camp, Manitoba: tectonic implications and their effects on volcanogenic massive sulfide deposits. Canadian Journal of Earth Sciences **55**: 935-957.

Stewart, M.S., Gibson, H., and Lafrance, B. 2018b. The structural and stratigraphic setting, mineralogy, and geochemistry of the Photo Lake VMS deposit, Snow Lake, Manitoba: implications for the timing and source of gold mineralization. Submitted to Economic Geology.

Stolper, E. and Newman, S. 1994. The role of water in the petrogenesis of Mariana trough magmas. Earth and Planetary Science Letters, **121**: 293-325.

Sun, S.-S. and McDonough, W.F. 1989. Chemical and isotopic systematics of oceanic basalts: Implications for mantle composition and processes. Geological Society Special Publication 42, pp. 313-345.

Syme, E.C. and Bailes, A.H. 1993. Stratigraphy and tectonic setting of Early Proterozoic volcanogenic massive sulphide deposits, Flin Flon, Manitoba. Economic Geology, **88**: 566-589.

Syme, E.C., Bailes, A.H., and Lucas, S.B. 1995. Geology of the Reed Lake area (Parts of 63K/9 and 63K/10). *In* Report of Activities 1995. Manitoba Energy and Mines, Minerals Division, p. 42-60.

Syme, E.C., Lucas, S.B., Bailes, A.H., and Stern, R.A. 1999. Contrasting arc and MORB-like assemblages in the Paleoproterozoic Flin Flon Belt, Manitoba, and the role of intra-arc extension in localizing volcanic-hosted massive sulphide deposits. Canadian Journal of Earth Sciences, **36**: 1767-1788.

Tanaka, T., Togashi, S., Kamioka, H., Amakawa, H., Kagami, H., Hamamoto, T., et al. 2000. JNdi-1: A neodymium isotopic reference in consistency with La Jolla neodymium. Chemical Geology, **168**: 279-281.

Tatsumi, Y. and Eggins, S. 1995. Subduction zone magmatism. Blackwell Science, Boston, 211p.

Taylor, R.N., Lapierre, H., Vidal, P., Nesbitt, R.W., and Croudace, I.W. 1992. Igneous geochemistry and petrogenesis of the Izu-Bonin fore-arc basin. *In* Taylor, B. Fukioka, K., et al., eds., Proceedings of the Ocean Drilling Program, Scientific Results, pp. 627-651.

Weis, D., Kieffer, B., Maerschalk, C., Pretorius, W., and Barling, J. 2005. High-precision Pb-Sr-Nd-Hf isotopic characterization of USGS BHVO-1 and BHVO-2 reference materials. Geochemistry Geophysics Geosystems, **6**(2): Q02002.

Weis, D. Kieffer, B., Maerschalk, C., Barling, J., de Jong, J., Williams, G.A., et al. 2006. High-precision isotopic characterization of USGS reference materials by TIMS and MC-ICP-MS. Geochemistry Geophysics Geosystems, **7**(8): Q08006.

Weis, D., Kieffer, B., Hanano, D., Nobre Silva, I., Barling, J., Pretorius, W., Maerschalk, C., and Mattielli, N. 2007. Hf isotope compositions of U.S. Geological Survey reference materials. Geochemistry Geophysics Geosystems, **8**(6): Q06006.

White, J.D.L., and Houghton, B.F. 2006. Primary volcaniclastic rocks. Geology **34**: 677- 680.

Winchester, J.A. and Floyd, P.A. 1977. Geochemical discrimination of different magma series and their differentiation products using immobile elements. Chemical Geology, **20**: 325-343.

Woodhead, J.D., Eggins, S.M., and Johnson, R.W. 1998. Magma genesis in the New Britain island arc: further insights into melting and mass transfer processes. Journal of Petrology, **39**: 1641-1668.

Yoshida, M. 2017. Trench dynamics: effects of dynamically migrating trench on subducting slab morphology and characteristics of subduction zone systems. Physics of the Earth and Planetary Interiors, **268**: 35-53.

Zindler, A., Staudigel, H., and Batiza, R. 1984. Isotope and trace element geochemistry of young Pacific seamounts: Implications for the scale of upper mantle heterogeneity. Earth and Planetary Science Letters, **70**(2): 175-195.

4.11 Appendix A: Isotopic reference materials

During this study, the Japanese basalt (JB-3) reference material yielded the following values: $^{143}Nd/^{144}Nd = 0.513049 \pm 0.000009$ (2SE), $^{176}Hf/^{177}Hf = 0.283239 \pm 0.000005$ (2SE), $^{208}Pb/^{204}Pb = 38.2505 \pm 0.0027$ (2SE), $^{207}Pb/^{204}Pb = 15.5349 \pm 0.0012$ (2SE), $^{206}Pb/^{204}Pb = 18.2939 \pm 0.0011$ (2SE). The USGS granite (G-3) reference material yielded the following values: $^{143}Nd/^{144}Nd = 0.512242 \pm 0.000009$ (2SE), $^{176}Hf/^{177}Hf = 0.282513 \pm 0.000005$ (2SE), $^{208}Pb/^{204}Pb = 38.8570 \pm 0.0038$ (2SE), $^{207}Pb/^{204}Pb = 15.6354 \pm 0.0013$ (2SE), $^{206}Pb/^{204}Pb = 18.3922 \pm 0.0016$ (2SE). Neodymium isotope data are presented relative to a value of $^{143}Nd/^{144}Nd = 0.512083 \pm 0.000008$ (2SE) for the JNdi-1 reference material, which correlates with a value of 0.511826 for the La Jolla standard (Tanaka et al. 2000). The external reference used for lead isotope data is the NIST NBS 981 material, which yielded values of $^{208}Pb/^{204}Pb = 36.7205 \pm 0.0024$ (2SE), $^{207}Pb/^{204}Pb = 15.4990 \pm 0.0010$ (2SE), $^{206}Pb/^{204}Pb = 16.9428 \pm 0.0009$. Hafnium isotope data are presented relative to a value of $^{176}Hf/^{177}Hf = 0.282151 \pm 0.000005$ for the JMC-475 reference material (Weis et al. 2007). Results were corrected for mass fractionation using $^{146}Nd/^{144}Nd = 0.7219$ and $^{179}Hf/^{177}Hf = 0.7325$, and the ^{204}Hg correction was made using natural abundances of $^{202}Hg = 0.29863$ and $^{204}Hg = 0.06865$ (Weis et al. 2005).

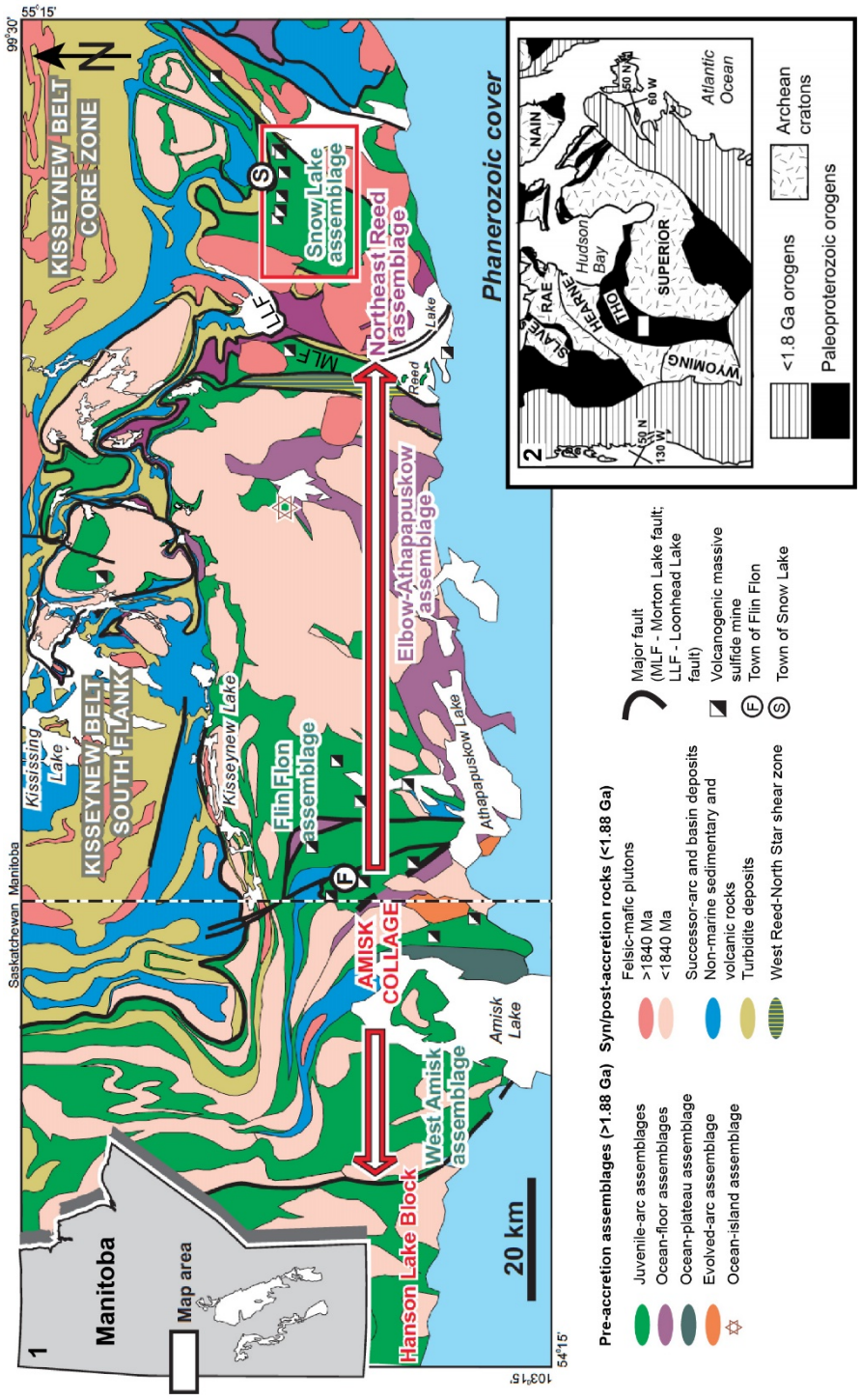

Figure 4-1. Tectono-stratigraphic assemblages of the Flin Flon belt, Manitoba, Canada (modified after Syme et al. 1999). Red box indicates location of the Snow Lake arc assemblage. Inset map 1 shows Manitoba with location of the Flin Flon belt map area. Inset map 2 shows location of Flin Flon belt within the Trans-Hudson Orogen (modified after Syme et al. 1999).

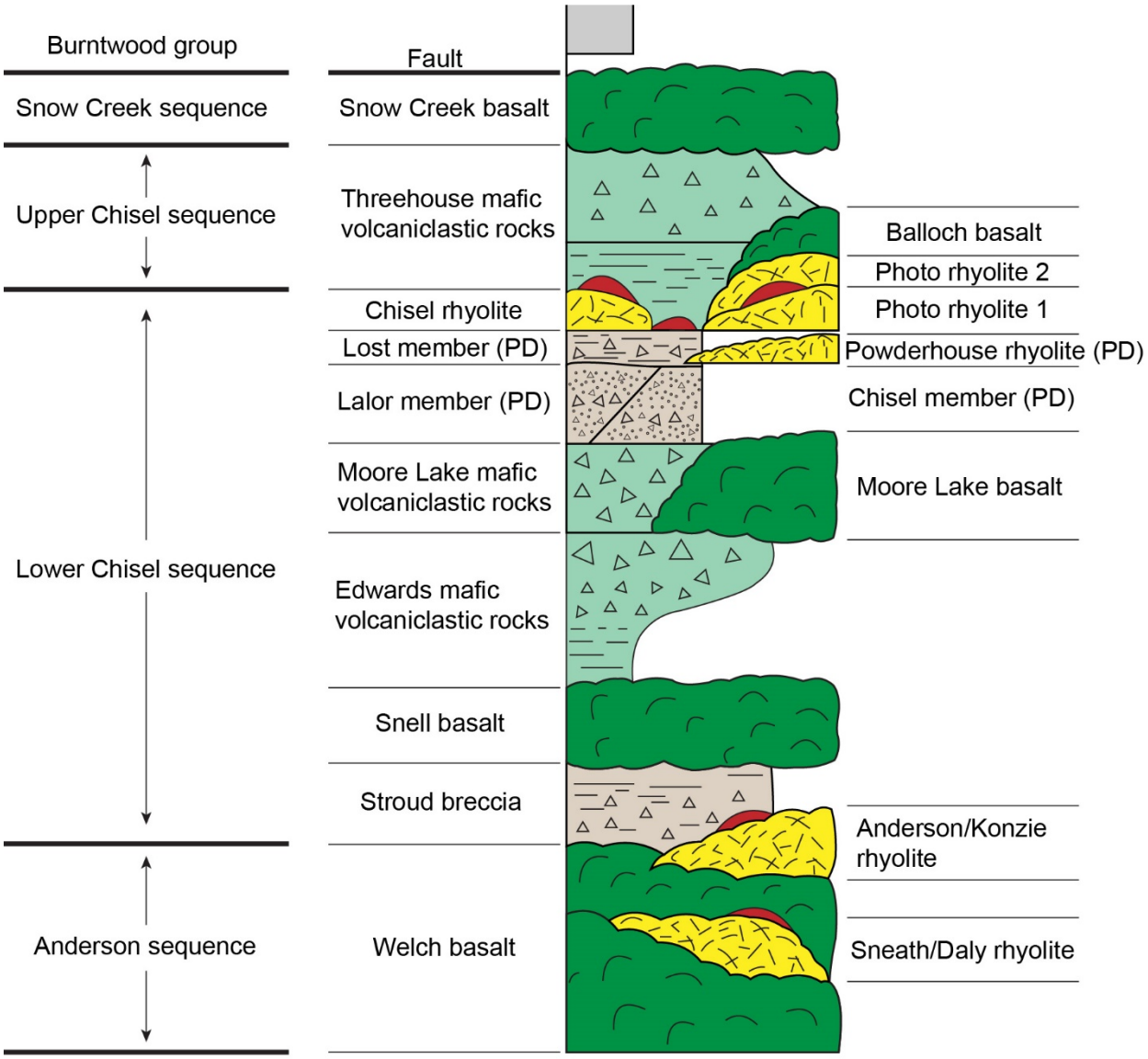

Figure 4-2. Idealized stratigraphic column of the Snow Lake arc assemblage. Stratigraphy modified from Bailes and Galley (2007) and Stewart et al. (2018a). Lithofacies colours: yellow – felsic coherent; dark green – mafic coherent; light green – mafic volcaniclastic; brown – felsic volcaniclastic with a mafic component; red – massive sulfide; grey – turbidite. Symbols: triangles – clasts; circles – crystals; horizontal lines – bedding; half circles – pillows; lines in felsic units – lobes.

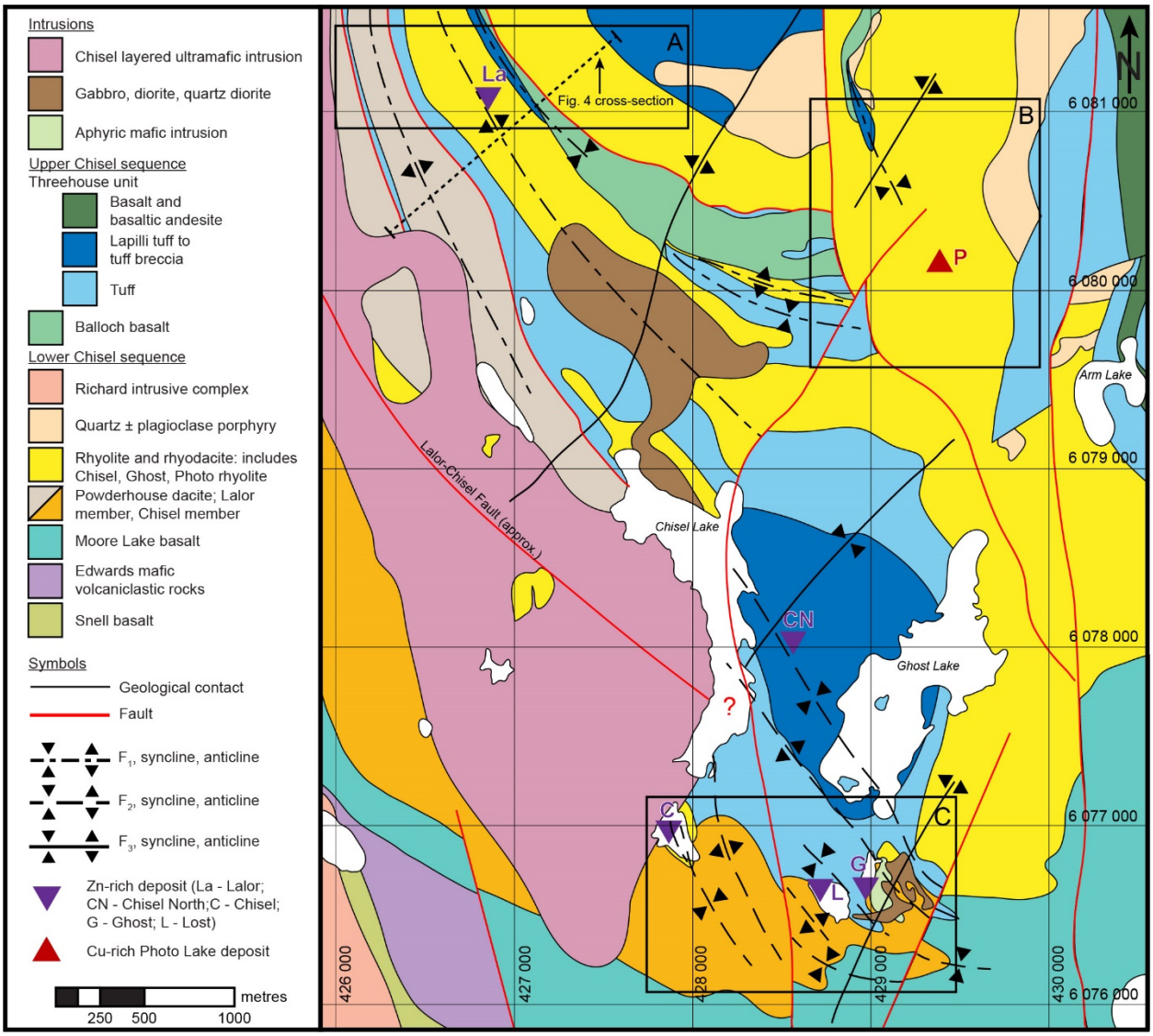

Figure 4-3. Geology of the Chisel sequence (modified from Bailes and Galley 2007). Structural fabrics and minor intrusions not shown. Up-plunge locations of Photo, Chisel, Ghost, and Lost orebodies and vertical projections of Lalor and Chisel North orebodies shown. Boxes show (a) Lalor area; (b) Photo Lake area; and (c) South Chisel basin area. Cross-section line shown for Figure 4.

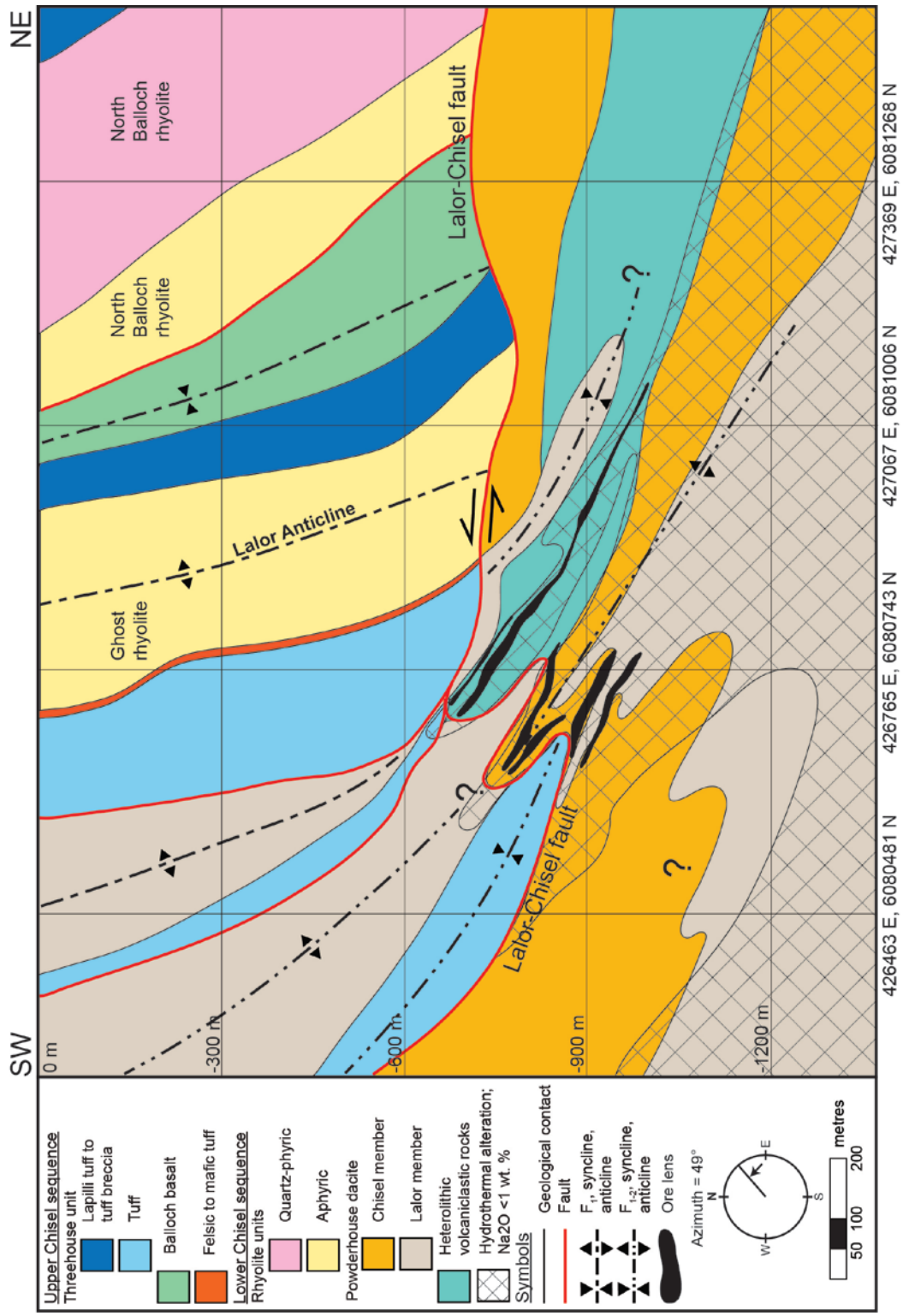

Figure 4-4. Vertical cross-section through the Lalor section stratigraphy. Cross-section line shown in Figure 3. Modified after Stewart et al. (2018a).

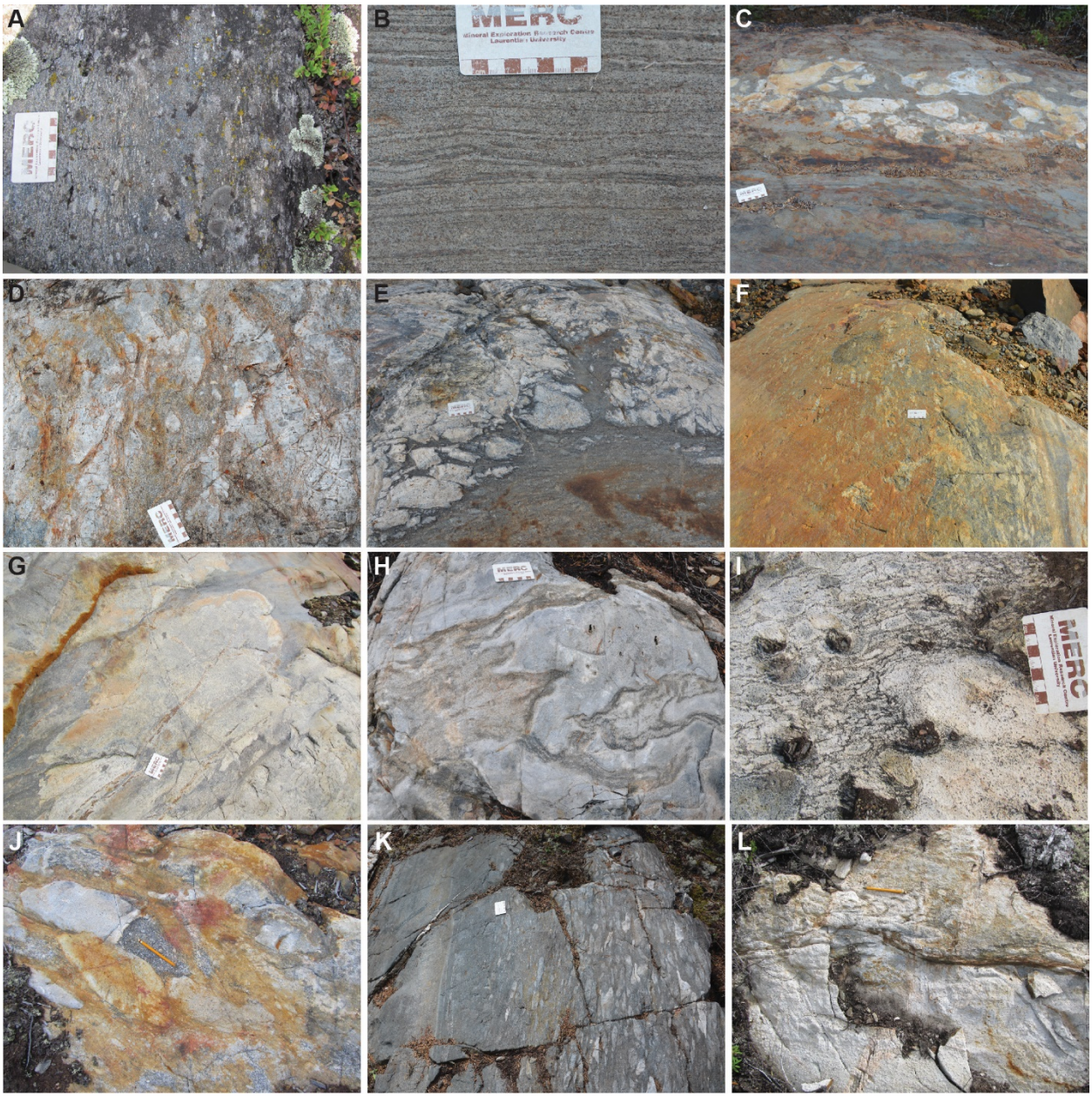

Figure 4-5. Representative photographs of felsic to intermediate coherent and volcaniclastic lithofacies. Scale photo card is 9 cm in length. (a) Bedded lapilli tuff in the Lalor member of the Powderhouse dacite. (b) Bedded tuffs of the Lost member of the Powderhouse dacite. (c) Monolithic felsic tuff breccia bed in the Lost member of the Powderhouse dacite. (d) Lobes in the Powderhouse rhyolite. (e) Altered and least altered Chisel rhyolite and monolithic autobrecciated clasts in the Chisel open pit. (f) Well-bedded felsic lapilli tuff in the Chisel open

pit. (g) Lobes in least altered Chisel rhyolite in the Chisel open pit. (h) Lobes in Photo rhyolite 1. (i) Flow-top breccia at the upper margin of the quartz-feldspar-phyric rhyolite in the North Balloch rhyolite. (j) Altered felsic lapillit tuff to tuff breccia separating aphyric and quartz-feldspar-phyric flows in the North Balloch rhyolite. (k) Heterolithic volcaniclastic rocks at the contact between the Ghost rhyolite and the Threehouse unit in the Lalor area. Rhyolite is not visible in this photograph but is located to the right of this outcrop. Rhyolite clasts are most abundant at this contact and significantly decrease in abundance moving away from the contact. The volcaniclastic rocks exhibit normal grading with respect to clast size and content. (l) Flow-top breccia at the upper margin of the quartz-feldspar-phyric rhyolite in the Photo Lake area.

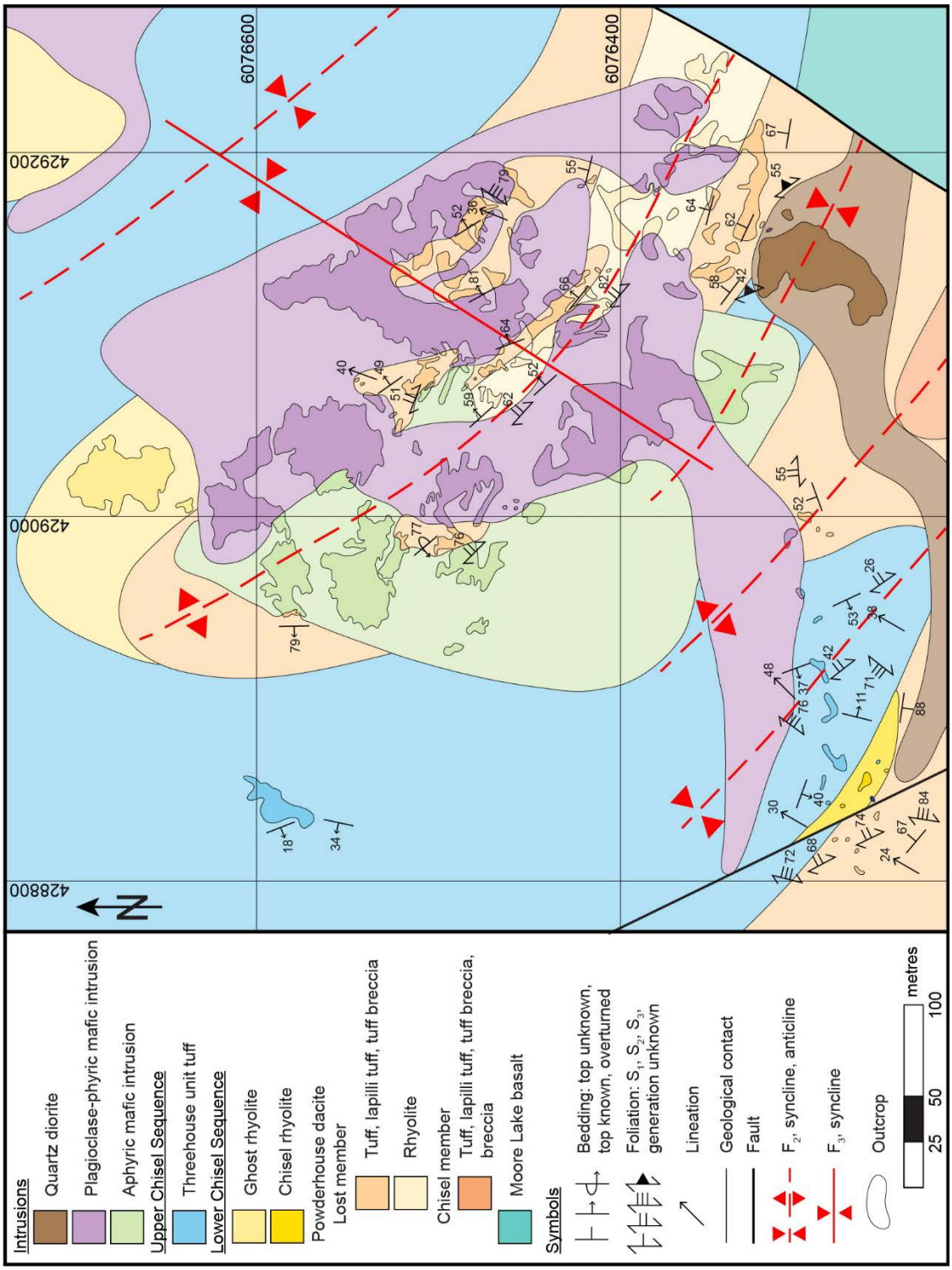

Figure 4-6. Detailed geological map of the eastern extent of the South Chisel basin area. Map datum is NAD83 UTM Zone 14. Modified after Stewart et al. (2018a).

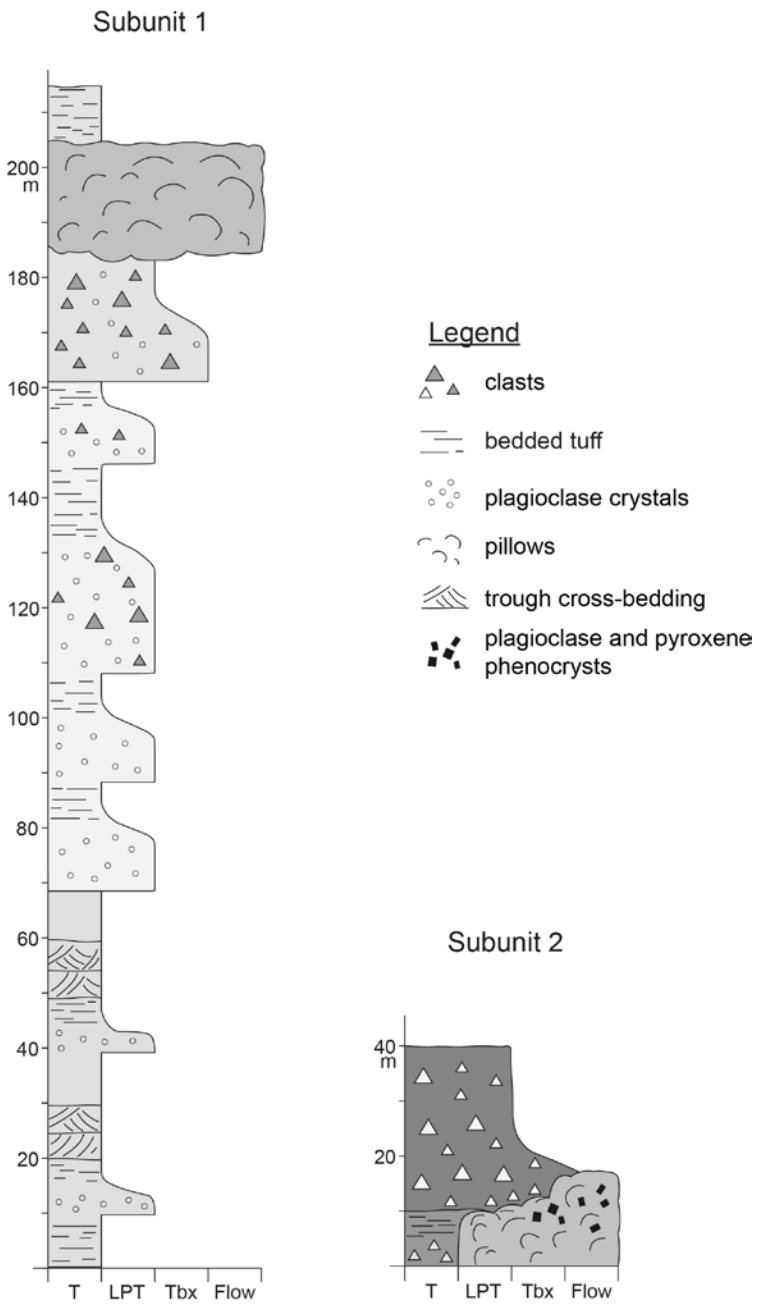

Figure 4-7. Idealized stratigraphic sections through the Threehouse unit showing the two main subunits. T – tuff, LPT – lapilli tuff, Tbx – tuff breccia.

A
B
C
D
E
F
G
H
I

Figure 4-8. Representative photographs of the Threehouse unit and Balloch basalt. Scale photo card is 9 cm in length. (a) Symmetrical ripple marks with mud drapes cut by a scour channel in the Threehouse unit. (b) Trough cross-bedding in the Threehouse unit. (c) Chilled rims on a mafic clast in lapilli tuff of the Threehouse unit (indicated by arrows). (d) Columnar jointing in crystal lapilli tuff of the Threehouse unit. (e) Highly vesicular to scoria blocks with chilled rims in the Threehouse unit. (f) Bedded heterolithic mafic lapilli tuff to tuff breccia in the Threehouse unit. Arrow indicates stratigraphic younging direction. Dashed yellow lines outline a bed of heterolithic clasts. (g) Pillowed and massive flows in the Balloch basalt. Arrow indicates stratigraphic younging direction. Dotted yellow line represents the transition from massive to pillowed flows. Dashed yellow line represents the sharp contact between the pillowed flows and the overlying massive flows. Upper massive flows contain patchy quartz-epidote alteration. (h) Pyrrhotite-rich tuff between the Chisel rhyolite and bedded tuffs of the Threehouse unit. Arrow indicates stratigraphic younging direction. Dashed yellow line represents contact between rhyolite and pyrrhotite-rich tuff. Pencil is 12 cm. (i) Felsic clasts at the base of the Threehouse unit in the Photo Lake map area.

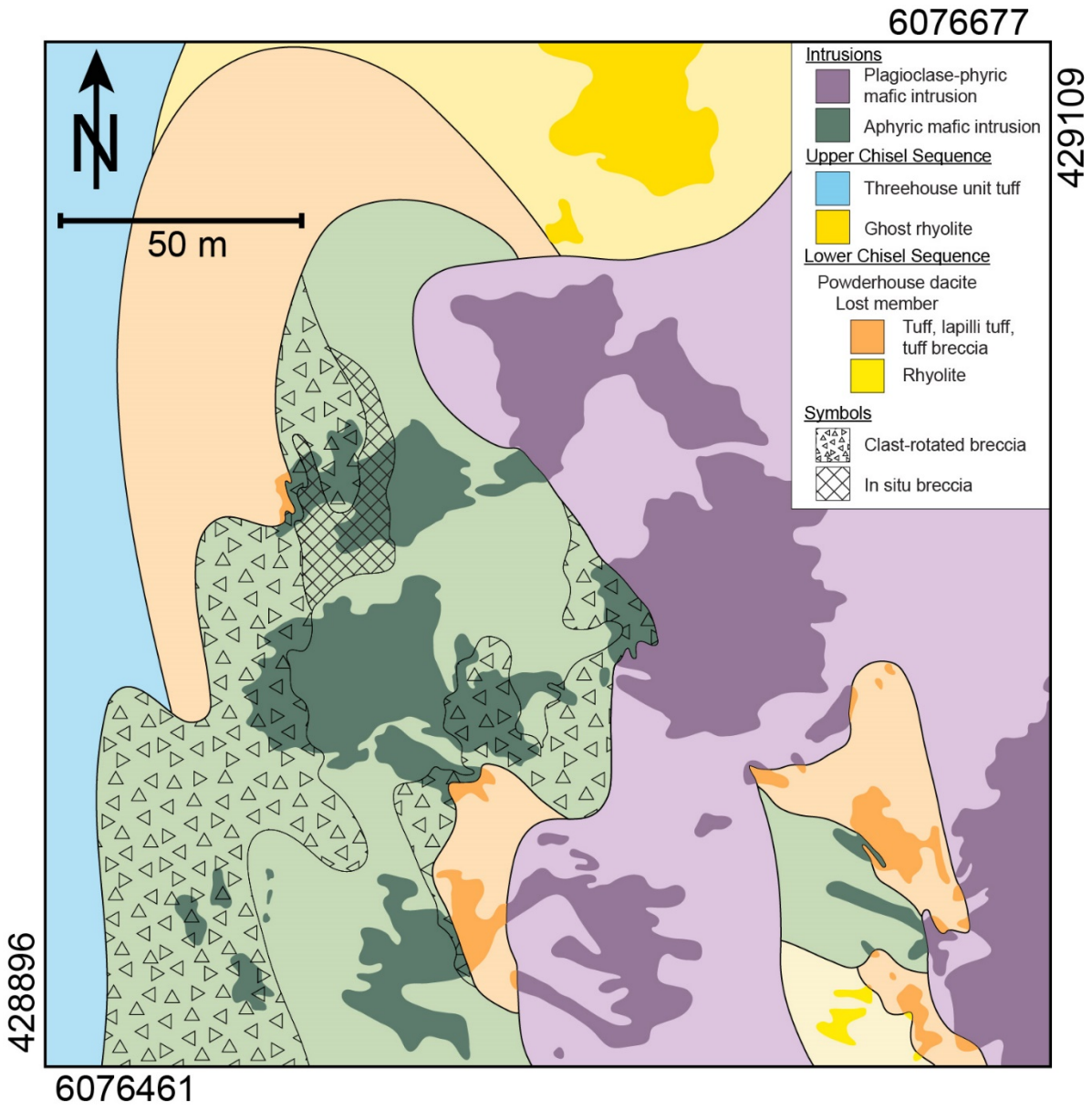

Figure 4-9. Detailed geological map of the South Chisel basin area showing the relationship between aphyric and plagioclase-porphyritic Threehouse intrusions. Map datum is NAD83 UTM Zone 14.

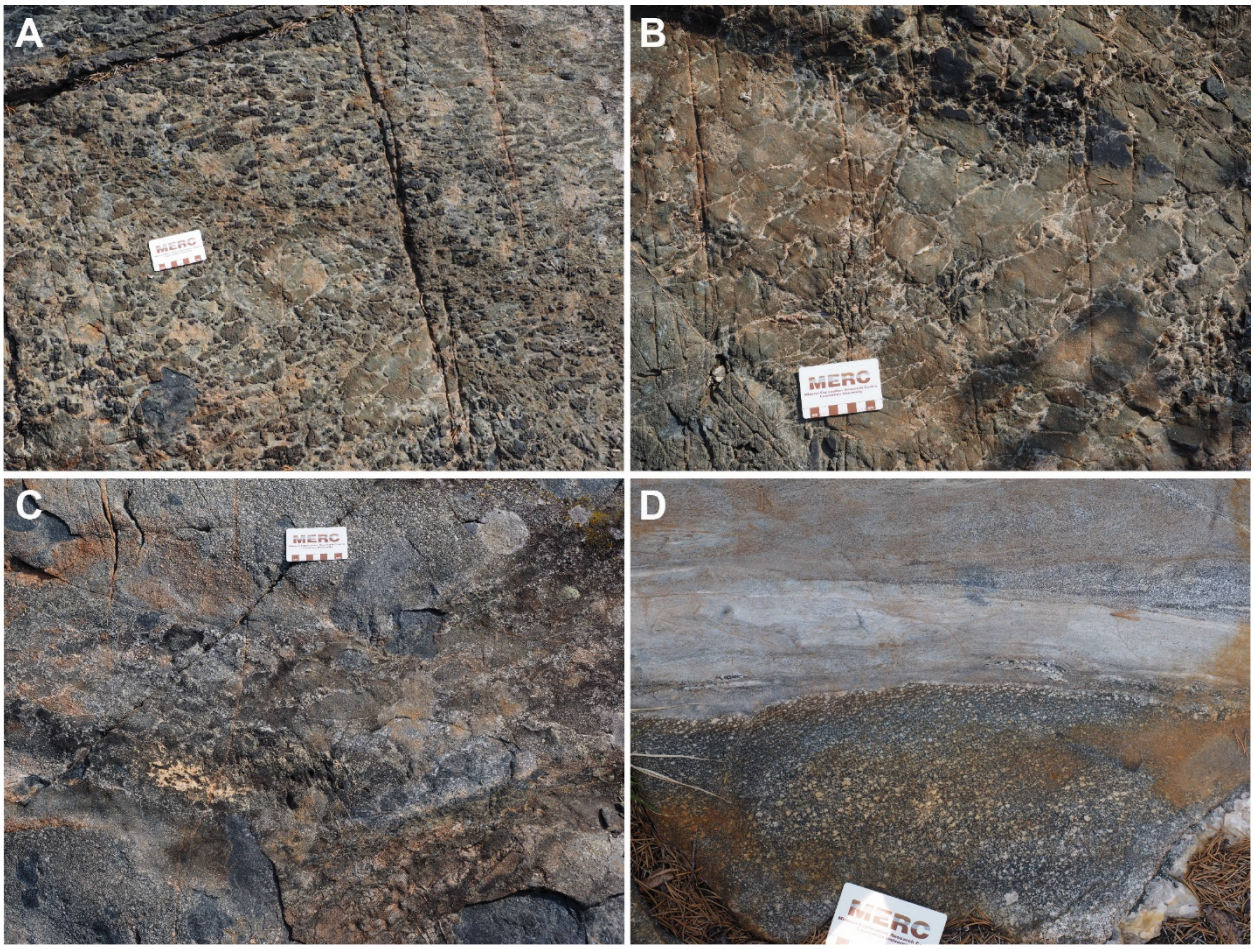

Figure 4-10. Representative photographs of mafic intrusions in the South Chisel basin map area. Scale photo card is 9 cm in length. (a) Peperite developed at the contact between the aphyric mafic intrusion and bedded tuffs of the Lost member of the Powderhouse dacite. (b) In situ breccia and fracturing in the aphyric intrusion proximal to its contact with bedded tuffs of the Lost member. (c) Peperite developed in the plagioclase-phyric intrusion where it is in contact with peperite of the aphyric intrusion. (d) Sharp contact between the plagioclase-phyric intrusion and bedded tuffs of the Lost member.

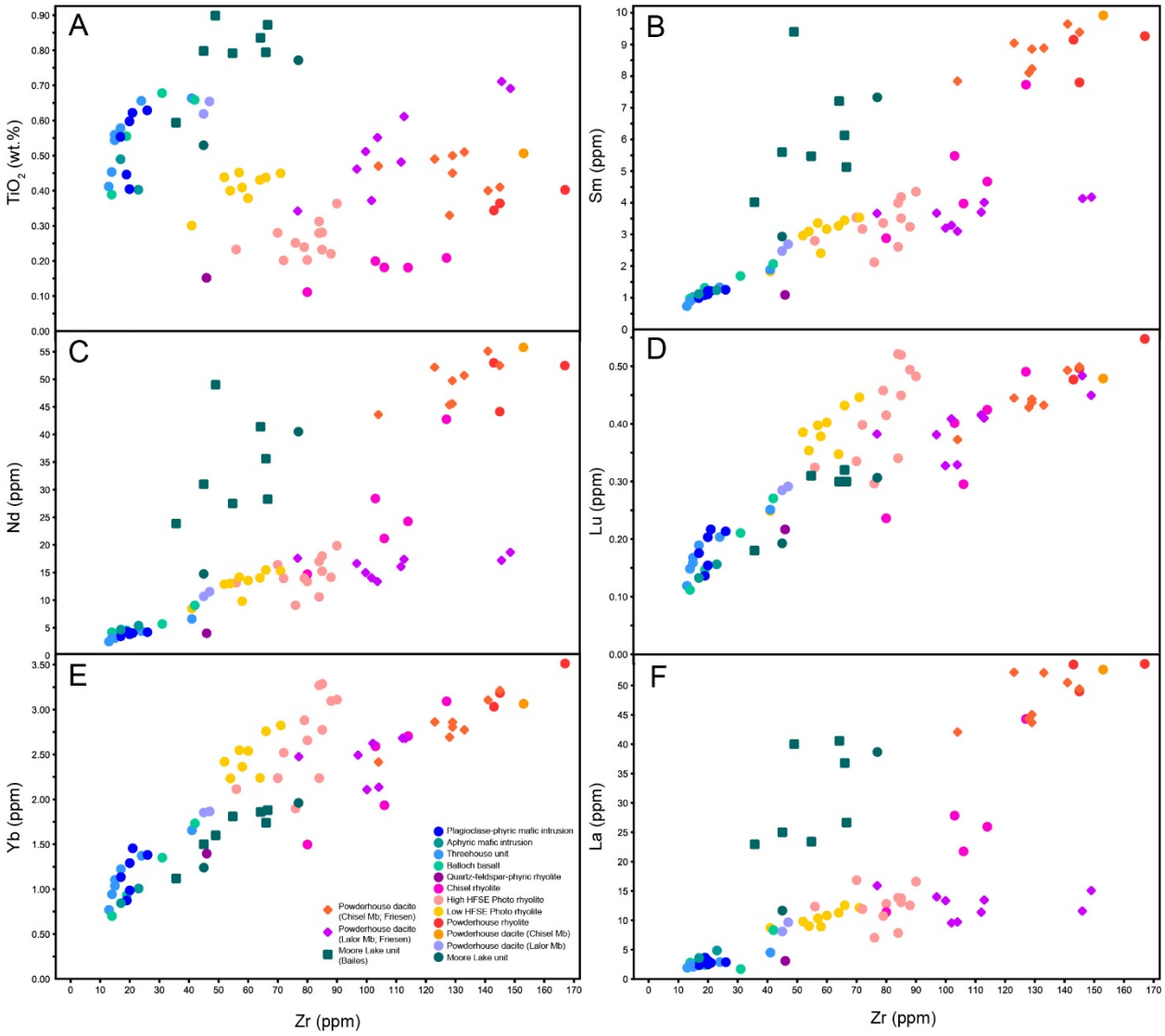

Figure 4-11. Selected binary plots of Zr vs. (a) TiO_2; (b) Sm; (c) Nd; (d) Lu; (e) Yb; (f) La.

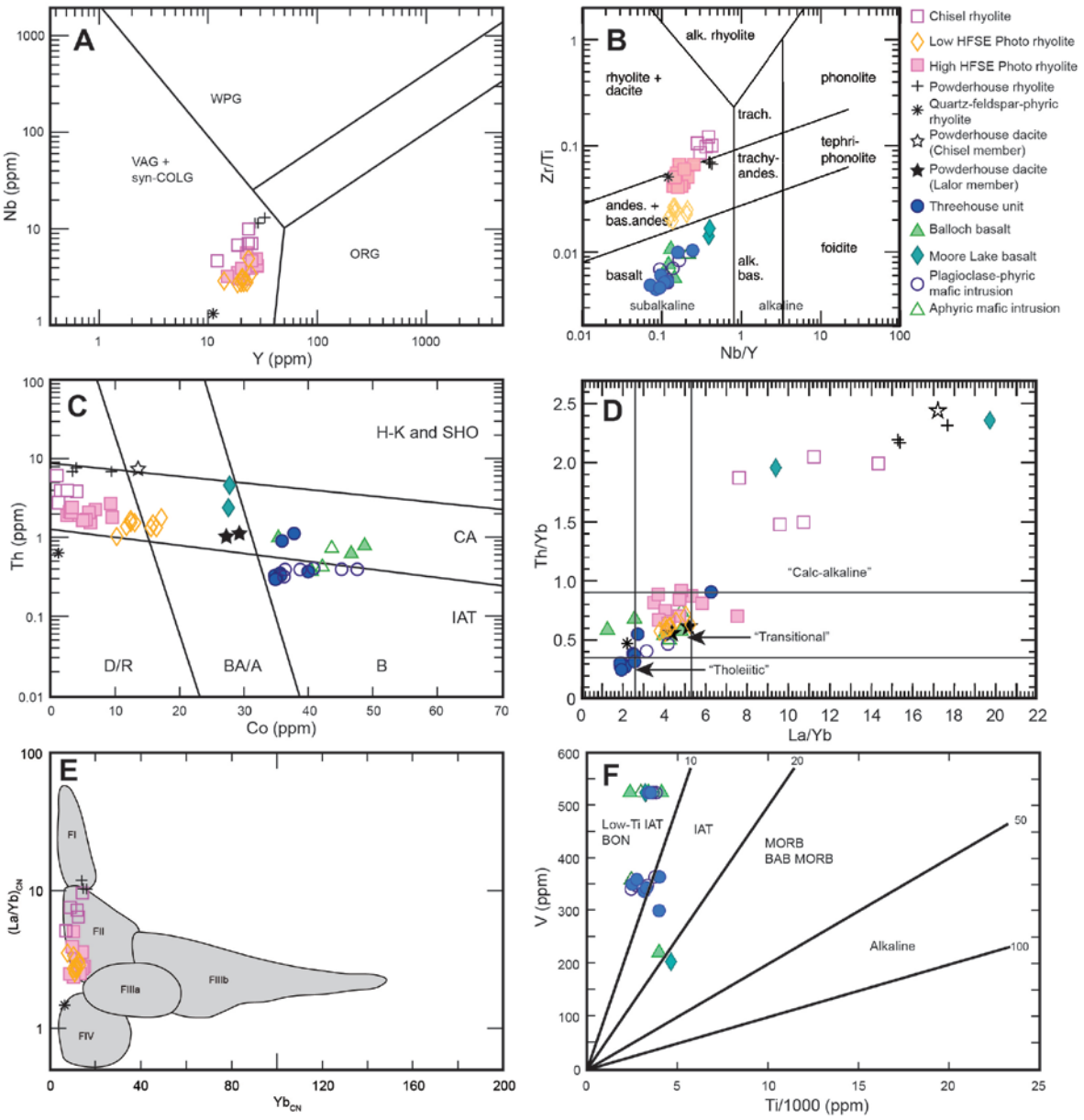

Figure 4-12. Geochemical plots for felsic and mafic units in the Chisel sequence. (a) Y versus Nb plot of Pearce et al. (1984) WPG – within-plate granitoid, VAG + syn-COLG – volcanic arc granitoid and syn-collisional granitoids, ORG – ocean-ridge granitoid. (b) Nb/Y versus Zr/Ti plot of Pearce (1996) modified after Winchester and Floyd (1977). (c) Co versus Th plot of Hastie et al. (2007). D/R – dacite/rhyolite, BA/A – basaltic-andesite/andesite, B – basalt, H-K and SHO – high-potassium and shoshonitic, CA – calc-alkaline, IAT – island-arc tholeiite. (d) La/Yb versus

Th/Yb plot showing the calc-alkaline, transitional and tholeiitic fields of Ross and Bédard (2009). (e) Yb_{CN} versus $(La/Yb)_{CN}$ plot of Hart et al. (2004). (f) Tectonic classification diagram for mafic igneous rocks of Shervais (1982). BAB – back-arc basalt, BON – boninite, IAT – island-arc tholeiite, MORB – mid-ocean ridge basalt. High and low HFSE Photo rhyolite includes Photo-type Ghost and North Balloch rhyolites. Chisel rhyolite includes Chisel-type North Balloch rhyolite.

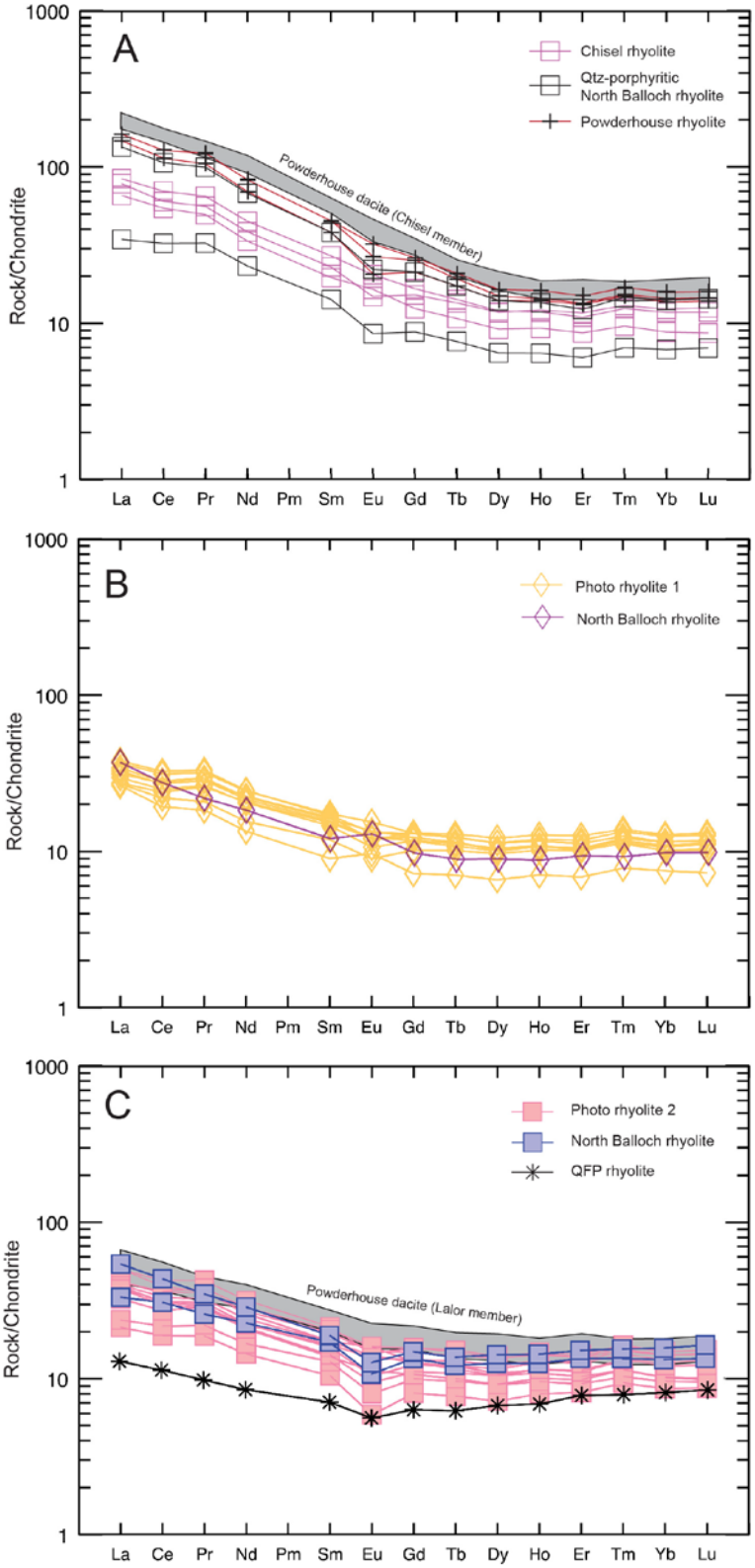
A
Chisel rhyolite
Qtz-porphyritic North Balloch rhyolite
Powderhouse rhyolite
Powderhouse dacite (Chisel member)
Rock/Chondrite
1000
100
10
1
La Ce Pr Nd Pm Sm Eu Gd Tb Dy Ho Er Tm Yb Lu
B
Photo rhyolite 1
North Balloch rhyolite
Rock/Chondrite
1000
100
10
1
La Ce Pr Nd Pm Sm Eu Gd Tb Dy Ho Er Tm Yb Lu
C
Photo rhyolite 2
North Balloch rhyolite
QFP rhyolite
Powderhouse dacite (Lalor member)
Rock/Chondrite
1000
100
10
1
La Ce Pr Nd Pm Sm Eu Gd Tb Dy Ho Er Tm Yb Lu

Figure 4-13. Chondrite-normalized REE plots for the felsic units of the Chisel sequence. Chisel and Lalor members of the Powderhouse dacite included for comparison. (a) Chisel-type chemistry, includes Chisel rhyolite, uppermost quartz-porphyritic flows of the North Balloch rhyolite, and Powderhouse rhyolite. Data for Chisel member of the Powderhouse dacite from Friesen (2018). (b) PR1 subdivision (low HFSE) of Photo-type chemistry. Photo rhyolite 1 includes Ghost rhyolite with low HFSE. (c) PR2 subdivision (high HFSE) of Photo-type chemistry and QFP-type chemistry. Photo rhyolite 2 includes Ghost rhyolite with high HFSE. Data for Lalor member of the Powderhouse dacite from Friesen (2018). PR1 and PR2 shown on separate plots due to large number of data points.

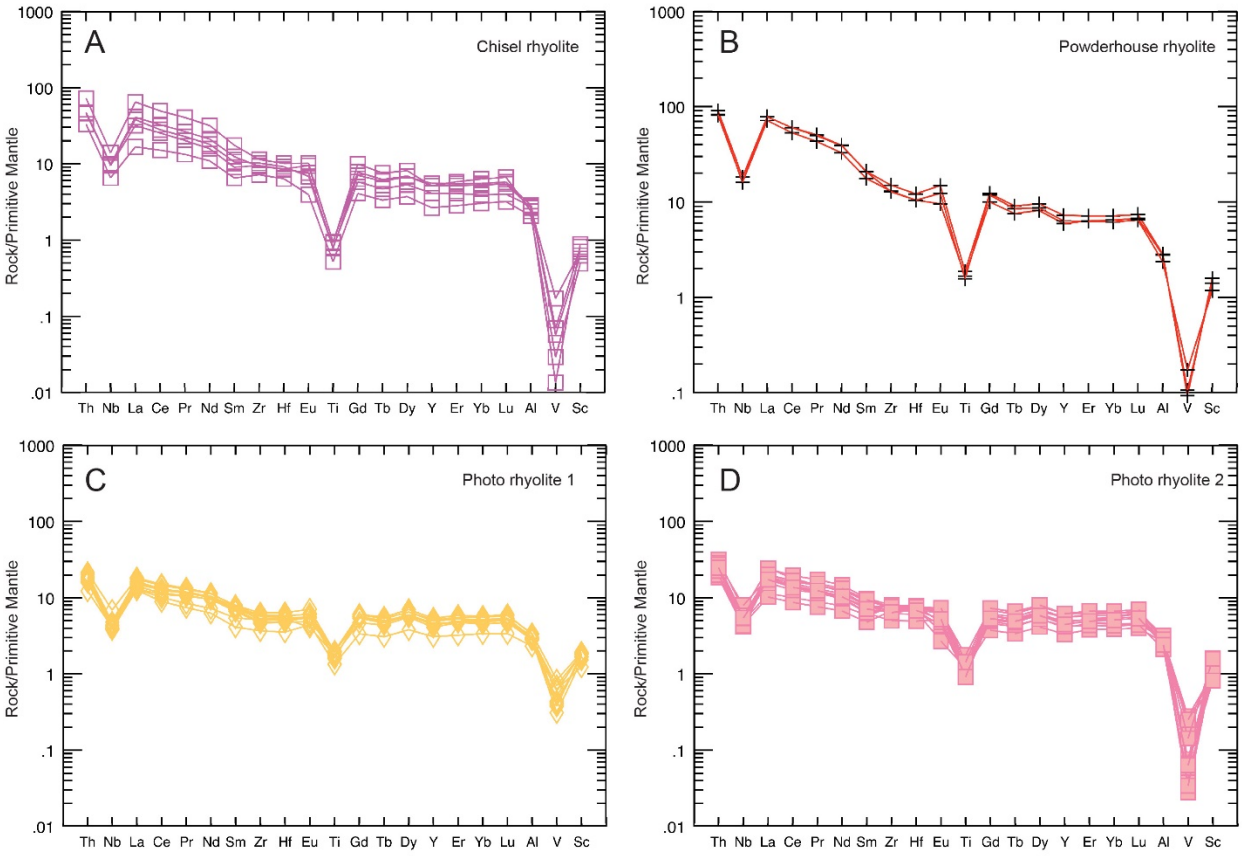

Figure 4-14. Primitive mantle-normalized trace element plots for the felsic units of the Chisel sequence. (a) Chisel rhyolite and uppermost flows of the North Balloch rhyolite. (b) Powderhouse rhyolite. (c) Low HFSE Photo and Ghost rhyolites. (d) High HFSE Photo and Ghost rhyolites.

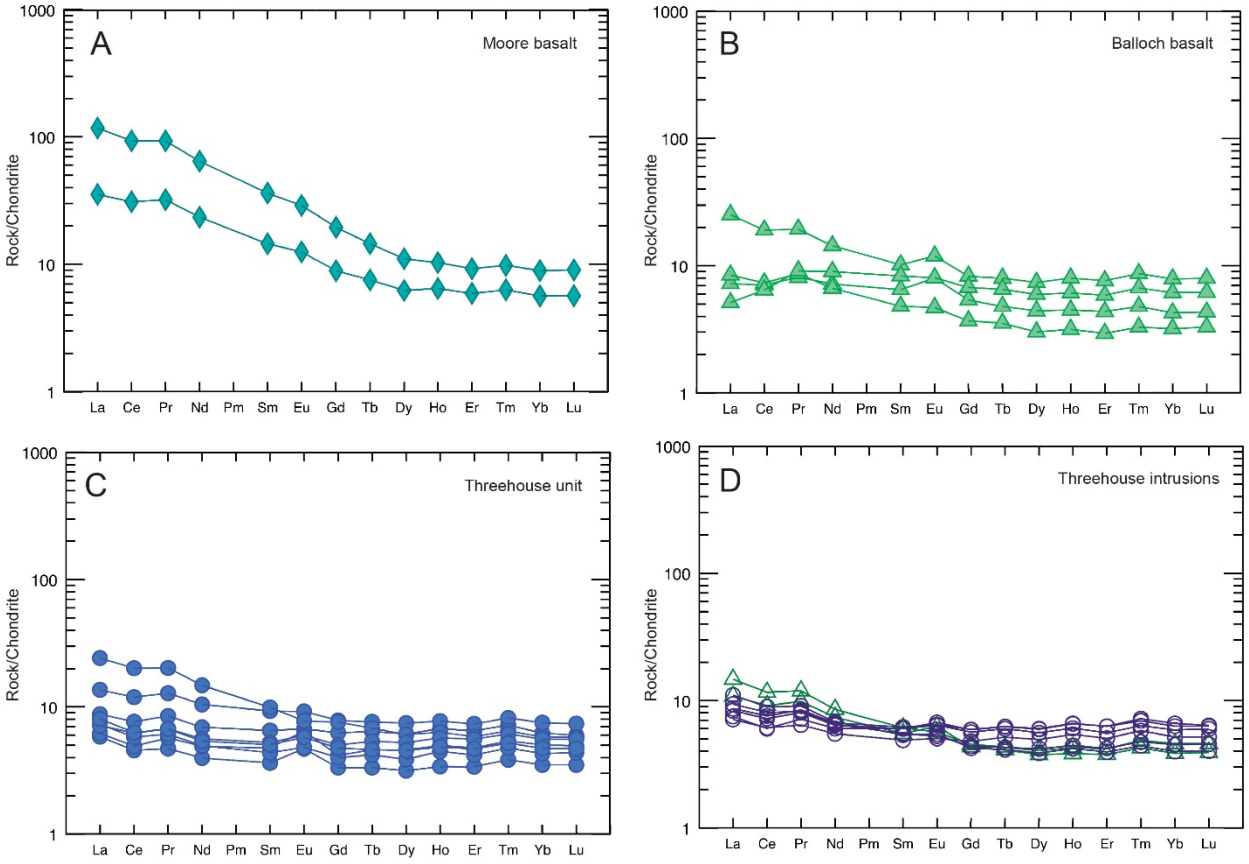

Figure 4-15. Chondrite-normalized REE plots for the mafic units of the Chisel sequence. (a) Moore basalt. (b) Balloch basalt. (c) Threehouse unit. (d) Threehouse intrusions.

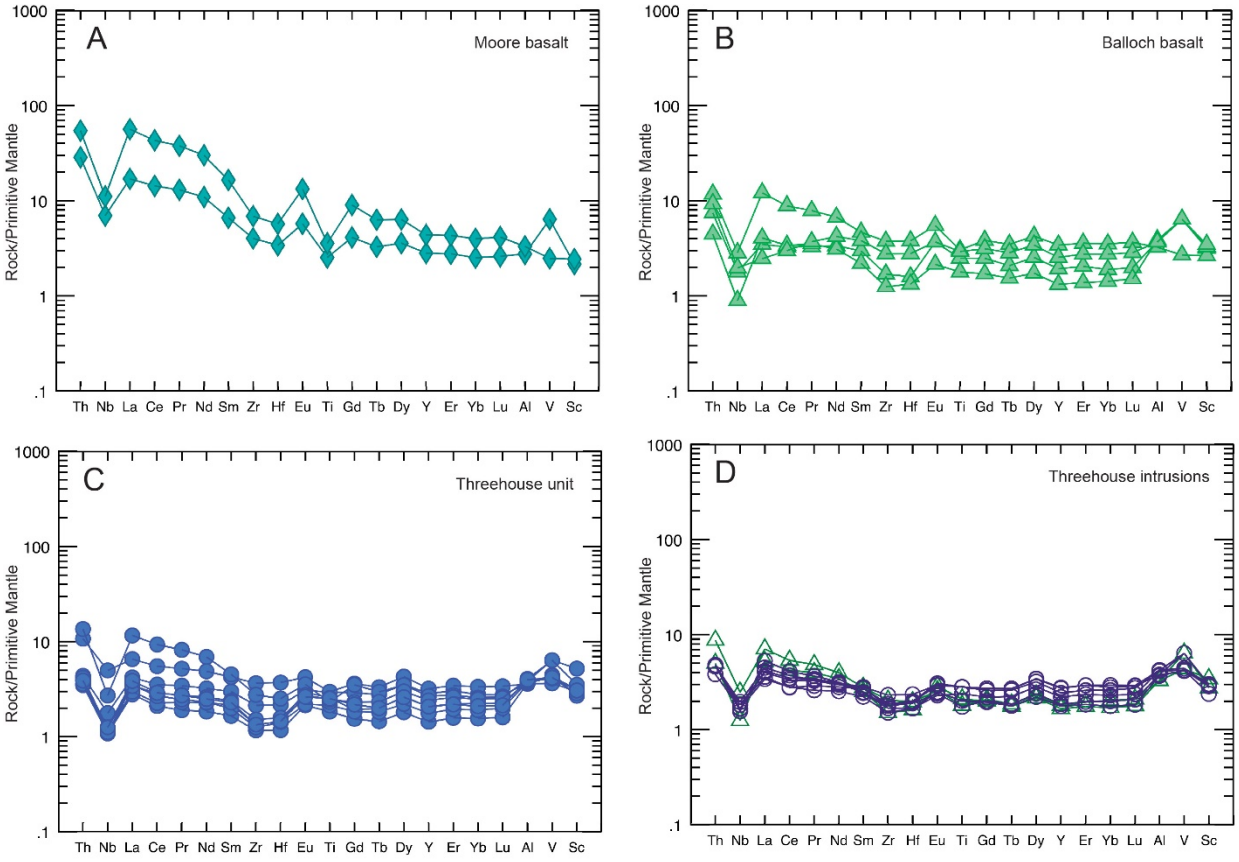

Figure 4-16. Primitive mantle-normalized trace element plots for the mafic units of the Chisel sequence. (a) Moore basalt. (b) Balloch basalt. (c) Threehouse unit. (d) Threehouse intrusions.

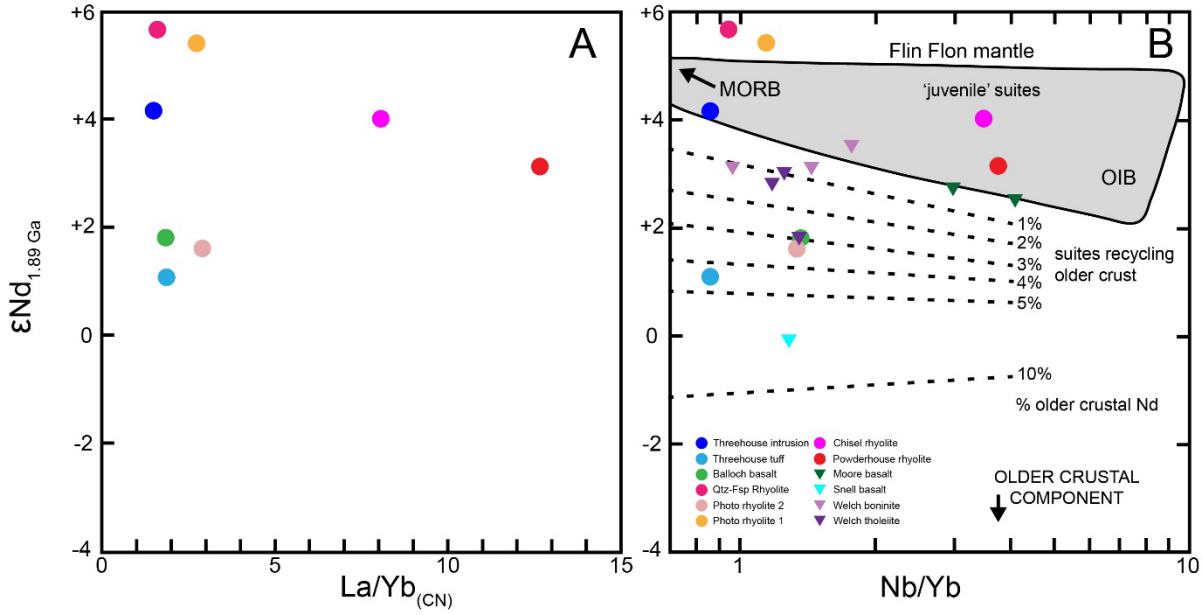

Figure. 4-17. (a) $(La/Yb)_{CN}$ versus εNd and (b) Nb/Yb versus εNd plot of Stern et al. (1995).

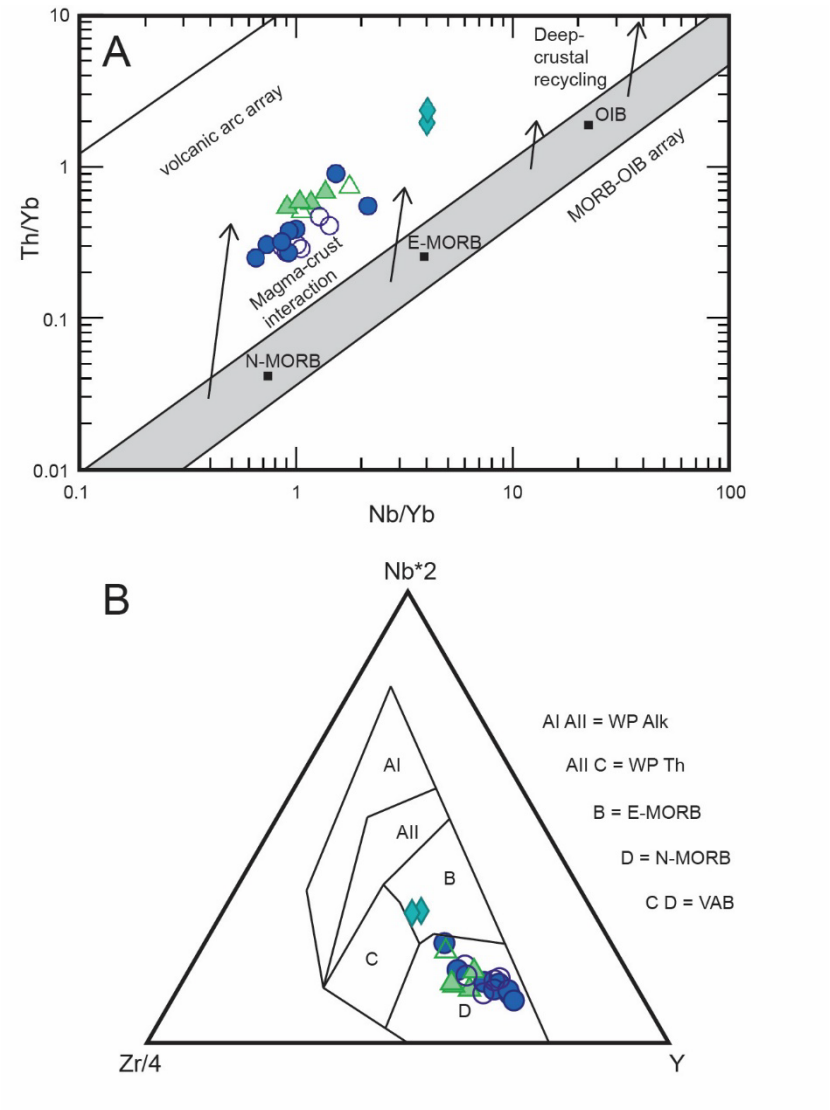

Figure 4-18. (a) Nb/Yb versus Th/Yb basalt discrimination plots of Pearce (2008). (b) Zr-Nb-Y plot of Meschede (1986).

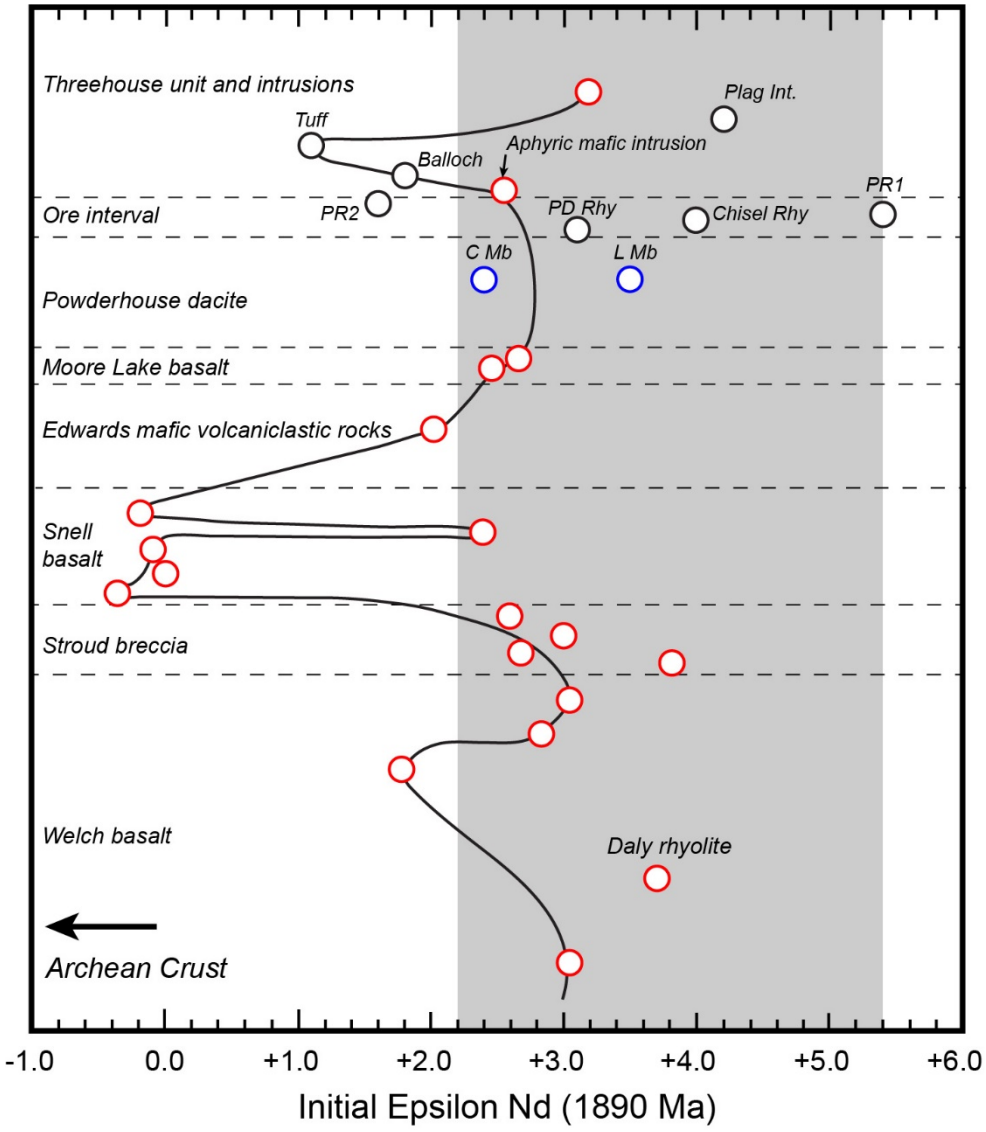
Threehouse unit and intrusions
Tuff
Plag Int.
Balloch
Aphyric mafic intrusion
PR1
Ore interval
PR2
PD Rhy
Chisel Rhy
C Mb
L Mb
Powderhouse dacite
Moore Lake basalt
Edwards mafic volcaniclastic rocks
Snell basalt
Stroud breccia
Welch basalt
Daly rhyolite
Archean Crust
-1.0
0.0
+1.0
+2.0
+3.0
+4.0
+5.0
+6.0
Initial Epsilon Nd (1890 Ma)

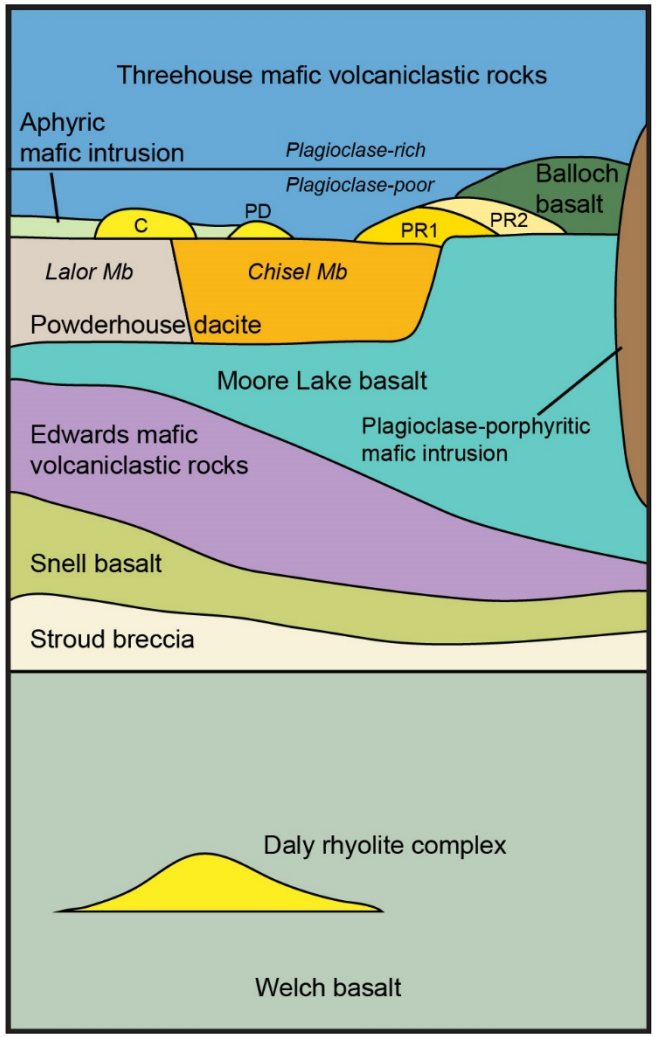
Threehouse mafic volcaniclastic rocks
Aphyric mafic intrusion
Plagioclase-rich
Plagioclase-poor
Balloch basalt
C
PD
PR1
PR2
Lalor Mb
Chisel Mb
Powderhouse dacite
Moore Lake basalt
Plagioclase-porphyritic mafic intrusion
Edwards mafic volcaniclastic rocks
Snell basalt
Stroud breccia
Daly rhyolite complex
Welch basalt

Figure 4-19. Geological and Nd isotopic stratigraphy of the Chisel sequence modified after Stern et al. (1992). Diagram incorporates new stratigraphy, additional epsilon Nd data from this study (black dots), data from Stern et al. (1992; red dots), and Friesen (2018; blue dots). Black line traces mafic samples. Grey box shows range of enriched ($\varepsilon Nd_{(1.9Ga)}$ = +2.2) to depleted ($\varepsilon Nd_{(1.9Ga)}$ = +5.4) mantle values at 1890 Ma from Stern et al. (1995).

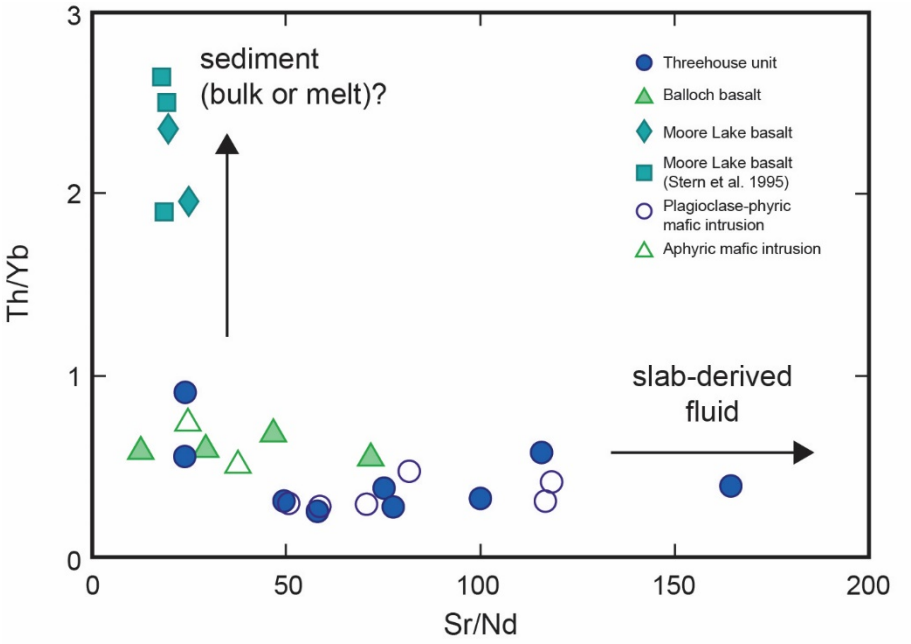

Figure 4-20. Sr/Nd versus Th/Yb plot of Woodhead et al. (1998).

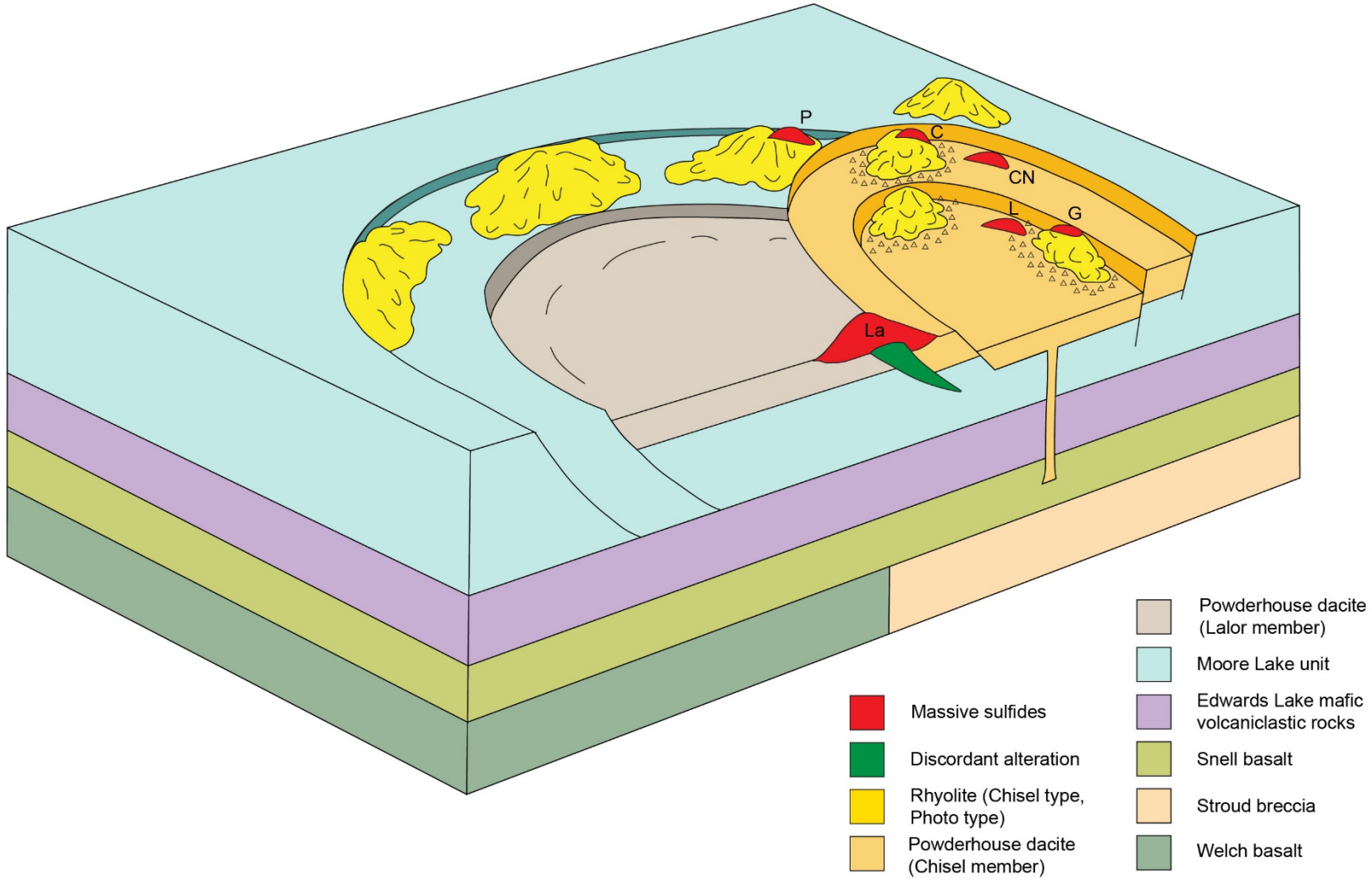
P
C
CN
L
G
La
Massive sulfides
Discordant alteration
Rhyolite (Chisel type, Photo type)
Powderhouse dacite (Chisel member)
Powderhouse dacite (Lalor member)
Moore Lake unit
Edwards Lake mafic volcaniclastic rocks
Snell basalt
Stroud breccia
Welch basalt

Figure 4-21. Schematic diagram illustrating the Chisel sequence ore-forming environment. The Chisel (C), Chisel North (CN), Ghost (G), and Lost (L) deposits formed proximal to small-volume rhyolite domes in a smaller basin within the subsidence structure. The Photo Lake (P) deposit formed at the margin of the subsidence structure along a major crustal-scale fault that served as a conduit for fissure-fed, voluminous rhyolite flows and high-temperature hydrothermal fluids. The Lalor (La) deposit formed at a major structure separating nested basins. The subsidence structure is illustrated here as two circular basins as an example; however, the geometry of the original subsidence structure is unknown due to overprinting deformation.

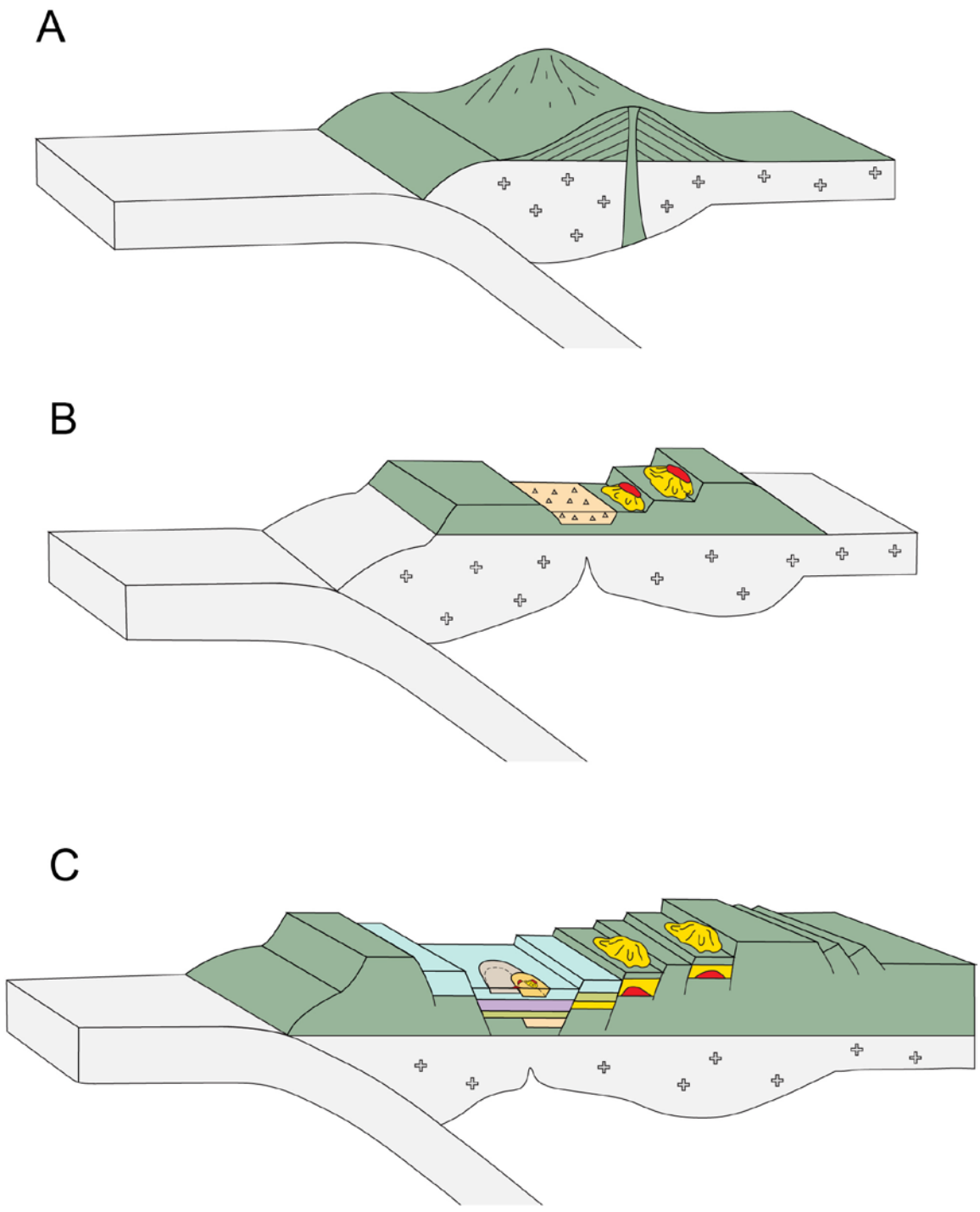
A
B
C

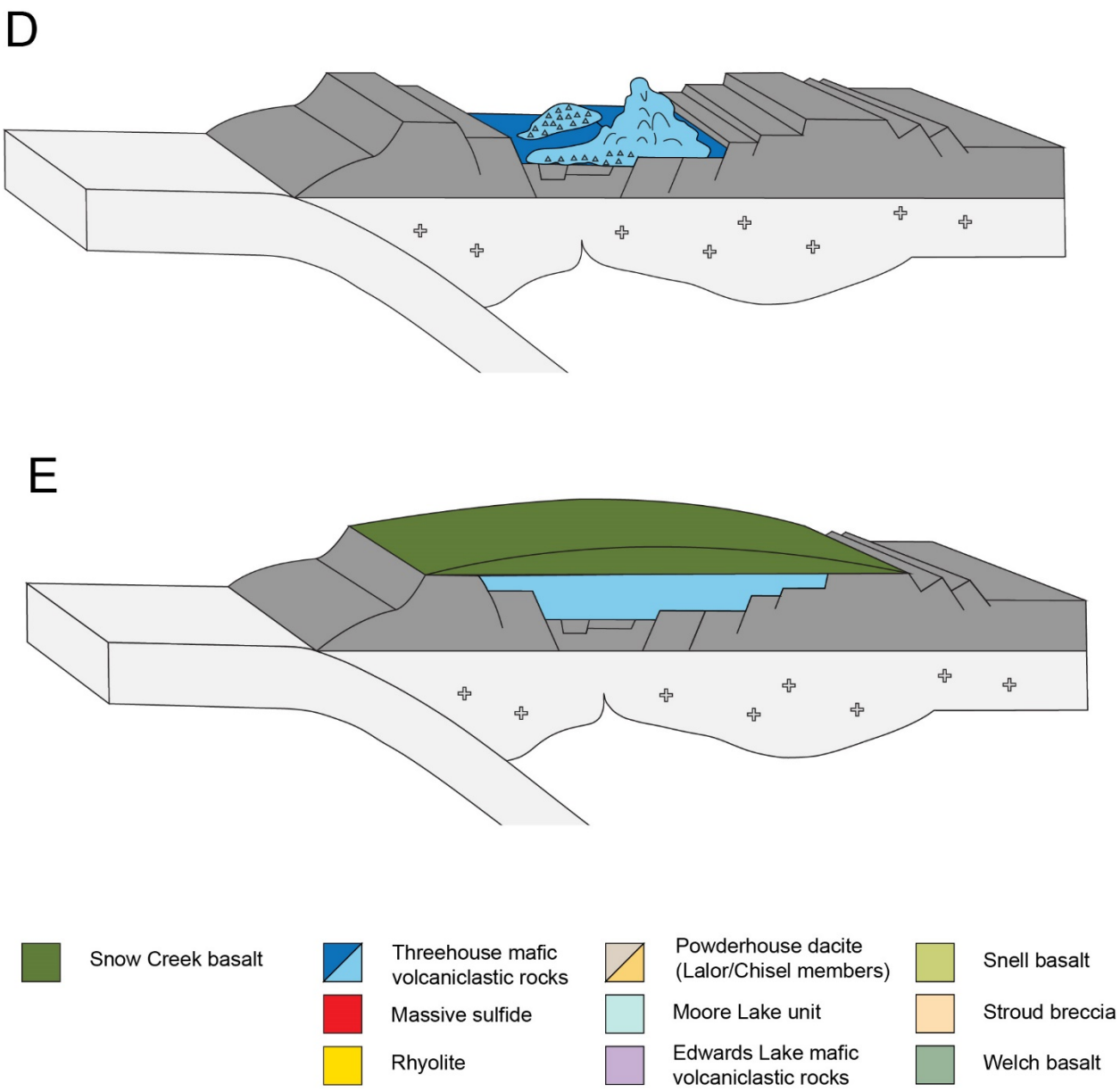

Figure 4-22. Schematic diagram illustrating the evolution of the Snow Lake arc assemblage and the ore-forming environment of the Chisel sequence VMS deposits. Diagram not to scale. (a) Development of the primitive Anderson and extrusion of the Welch basalt. (b) Rifting of the Anderson arc caused crustal thinning, eruption of the Anderson sequence rhyolites, and emplacement of the Stroud breccia. A mineralizing hydrothermal system developed as a result of

high heat flow associated with crustal thinning and the formation of crustal-scale faults associated with rifting, and the Anderson VMS deposits were formed. Welch basalt volcanism likely continued during this interval, resulting in extrusion of Welch basalt flows over the Anderson sequence rhyolites. (c) Continued rifting and localized extension driven by magma chamber collapse led to development of the Lalor-Chisel subsidence structure. Major structures acted as conduits for felsic volcanism and high-temperature fluid flow to form the Chisel VMS deposits. (d) Threehouse effusive and explosive eruptions formed the hanging wall to the Anderson and Chisel VMS deposits. Localized subsidence and mass flow deposition within topographic basins accompanied Threehouse volcanism. (e) Rifting transitioned to seafloor spreading and the Snow Creek basalt flows were erupted. Dark grey in (d) and (e) represents Anderson sequence and Lower Chisel sequence.

TABLE 1. Summary of deformation events in the Snow Lake district (Froese and Moore, 1980; Galley et al., 1988; Kraus and Williams 1993, 1994, 1998, 1999; Rubingh et al., 2012; Stewart et al., 2018a)

D_1	**D_2**	**D_3**	**D_4**
N- to NW-trending isoclinal F_1 folds – Photo syncline, Lost anticline, Lalor anticline; W-directed, NW-striking faults	NW- to NNW-trending isoclinal F_2 folds; axial planar S_2 cleavage defined by orientation of biotite and amphibole, inclusion trails in porphyroblasts, and flattened clasts; S_2 is dominant fabric in volcanic rocks and rare in Burntwood Group rocks; NE-plunging stretching lineation; tightening of NW-trending F_1 folds	NE-trending open to tight F_3 folds – Threehouse synform; N- to NE-trending, steeply E- to SE-dipping axial planar S_3 cleavage	E-W-trending F_4 folds that occur locally in N-S trending domains; development of kink bands in unfavourably oriented domains

TABLE 2. Summary of geochemical characteristics of volcanic rocks of the Chisel sequence.

	Aphyric mafic intrusion		Plagioclase-porphyritic mafic intrusion		Balloch basalt		Powderhouse dacite, Chisel member	Powderhouse dacite, Lalor member		Chisel rhyolite	
	Mean	2σ	Mean	2σ	Mean	2σ		Mean	2σ	Mean	2σ
	n = 2		n = 5		n = 4		n = 1	n = 2		n = 5	
SiO_2 (wt%)	51.43	5.02	48.97	2.06	50.49	8.88	60.16	55.71	4.26	76.57	6.72
Al_2O_3	15.25	0.16	18.21	2.17	16.82	2.53	14.78	14.31	0.07	11.79	3.02
Fe_2O_3(T)	12.97	2.32	13.32	2.51	13.74	2.65	10.67	12.94	0.13	3.05	3.98
MnO	0.22	0.08	0.21	0.04	0.21	0.06	0.20	0.25	0.03	0.08	0.20
MgO	5.66	0.24	4.22	1.02	5.18	3.73	2.47	2.98	0.20	0.67	0.87
CaO	9.66	4.17	10.23	1.97	8.76	1.96	3.71	8.38	2.66	1.45	2.23
Na_2O	2.80	2.80	2.71	1.60	3.29	1.11	1.66	2.48	0.62	3.95	4.08
K_2O	0.27	0.14	0.55	0.82	0.22	0.17	3.53	0.50	0.27	1.31	1.75
TiO_2	0.45	0.13	0.53	0.20	0.57	0.27	0.51	0.64	0.04	0.18	0.08
P_2O_5	0.11	0.07	0.06	0.04	0.13	0.12	0.17	0.17	0.03	0.03	0.02
Cr_2O_3	0.01	0.00	0.01	0.01	0.02	0.01	0.01	0.01	0.00	0.01	0.00
V_2O_5	0.07	0.03	0.06	0.01	0.07	0.04	0.02	0.03	0.01	0.00	0.00
LOI	1.10	1.05	0.92	0.95	0.47	0.33	2.14	1.61	1.91	0.90	0.87
Total	99.97	0.08	100.00	0.04	99.96	0.08	100.01	99.99	0.06	100.00	0.03
Cr (ppm)	31.00	11.31	40.40	42.53	40.75	50.05	11.00	15.50	1.41	27.40	18.14
Ni	17.10	8.20	17.22	5.58	18.03	17.42	3.90	4.60	0.00	3.86	8.34
Co	42.90	2.06	41.21	10.28	42.81	12.19	13.45	28.21	2.88	1.98	2.51
Sc	53.10	16.69	48.90	9.17	53.65	12.08	32.00	40.40	2.55	12.02	5.28
V	440.60	233.06	416.42	194.66	447.30	302.80	115.70	172.10	13.86	5.60	10.18
Cu	150.75	107.34	98.46	137.43	157.20	381.40	32.30	126.60	168.29	7.04	11.32
Pb	2.05	0.14	13.50	32.58	2.43	3.02	6.30	5.45	0.14	57.20	195.24
Zn	83.50	32.53	97.60	31.83	102.00	28.19	182.00	136.50	1.41	777.20	2628.31
In	0.04	0.01	0.05	0.01	0.05	0.02	0.10	0.06	0.00	0.06	0.08
Sn	0.27	0.07	0.26	0.13	0.37	0.39	1.20	0.56	0.13	0.78	0.74
Mo	0.70	0.44	1.00	1.26	1.09	2.11	3.21	1.40	0.47	2.58	3.60
Sb	0.19	0.28	0.31	0.28	0.23	0.10	0.10	0.20	0.11	0.14	0.12
Rb	1.20	0.88	5.67	15.80	1.52	1.70	59.00	6.58	9.08	15.61	22.39
Cs	0.01	0.00	0.08	0.24	0.02	0.05	0.60	0.07	0.08	0.26	0.52
Ba	69.65	108.75	134.90	222.69	51.00	69.21	1553.10	126.60	146.51	296.98	428.51
Sr	153.80	59.11	347.44	239.70	198.83	158.79	145.30	293.00	130.39	84.46	75.77
Tl	0.01	0.02	0.03	0.05	0.01	0.01	0.38	0.03	0.03	0.18	0.41
Ga	13.99	0.93	15.59	2.33	16.54	5.49	17.61	14.00	0.40	11.62	7.17
Ta	0.08	0.08	0.07	0.02	0.07	0.07	0.56	0.22	0.03	0.40	0.16
Nb	1.33	1.24	1.24	0.22	1.33	1.14	12.28	3.85	0.04	7.06	3.75
Hf	0.56	0.16	0.59	0.17	0.73	0.70	3.43	1.28	0.11	2.62	0.84
Zr	20.00	8.49	20.40	6.72	26.50	25.11	153.00	46.00	2.83	106.00	34.50
Y	7.92	0.88	10.09	3.77	10.47	8.15	27.47	17.00	1.39	20.48	10.56
Ti	2551.50	558.61	3073.20	1241.80	3329.00	1479.84	3020.00	3798.00	101.82	1031.20	440.74
Th	0.58	0.45	0.39	0.07	0.70	0.52	7.48	1.09	0.15	4.16	2.45
U	0.24	0.15	0.15	0.05	0.35	0.52	2.51	0.47	0.11	2.57	3.29
La	4.22	1.81	2.89	1.04	3.80	6.10	52.72	8.88	2.19	26.24	23.85
Ce	8.99	3.04	6.35	2.18	8.63	10.50	116.21	19.30	3.82	56.06	46.83
Pr	1.22	0.33	0.88	0.24	1.27	1.21	14.39	2.61	0.38	6.79	5.55
Nd	5.02	1.02	3.97	0.69	5.87	4.43	55.77	11.10	1.23	26.26	20.99
Sm	1.18	0.17	1.13	0.21	1.51	0.94	9.92	2.58	0.30	4.95	3.65
Eu	0.46	0.07	0.44	0.10	0.63	0.46	2.37	0.80	0.07	1.27	0.82
Gd	1.22	0.08	1.38	0.42	1.66	1.08	7.35	2.72	0.37	4.11	2.58
Tb	0.20	0.01	0.24	0.09	0.27	0.18	0.96	0.44	0.02	0.60	0.35
Dy	1.34	0.13	1.68	0.62	1.78	1.30	5.36	2.94	0.32	3.66	1.99
Ho	0.28	0.05	0.37	0.15	0.38	0.29	1.01	0.63	0.05	0.75	0.39
Er	0.89	0.13	1.13	0.43	1.17	0.91	2.98	1.89	0.13	2.24	1.16
Tm	0.14	0.03	0.17	0.06	0.18	0.14	0.45	0.28	0.01	0.34	0.18
Yb	0.93	0.23	1.13	0.42	1.18	0.91	3.06	1.86	0.02	2.36	1.28
Lu	0.14	0.03	0.18	0.06	0.18	0.14	0.48	0.29	0.01	0.37	0.20

TABLE 2 (continued). Summary of geochemical characteristics of volcanic rocks of the Chisel sequence.

	Photo rhyolite 1		Photo rhyolite 2		Moore Lake basalt		Powderhouse rhyolite		Quartz-feldspar rhyolite	Threehouse unit	
	Mean	2σ	Mean	2σ	Mean	2σ	Mean	2σ		Mean	2σ
	n = 12		n = 9		n = 2		n = 3		n = 1	n = 8	
SiO_2 (wt%)	65.25	8.17	72.77	7.03	55.55	1.48	72.41	6.20	85.08	49.03	4.35
Al_2O_3	13.61	2.87	12.32	2.52	14.04	3.61	12.27	2.36	8.07	17.60	1.50
Fe_2O_3(T)	9.51	3.46	5.14	3.64	12.18	3.28	6.40	3.52	1.32	13.89	2.33
MnO	0.15	0.08	0.09	0.11	0.22	0.01	0.12	0.08	0.03	0.25	0.12
MgO	1.77	0.96	0.80	0.55	3.09	0.91	0.87	0.12	0.15	5.05	2.12
CaO	4.49	2.54	2.58	2.81	8.99	2.70	1.94	0.86	0.95	9.61	4.40
Na_2O	2.91	1.61	3.78	2.28	2.62	0.38	3.83	1.38	3.25	2.14	1.80
K_2O	0.92	1.17	1.20	1.05	0.36	0.06	1.00	0.79	0.60	0.60	0.88
TiO_2	0.41	0.10	0.26	0.09	0.65	0.34	0.37	0.06	0.15	0.55	0.18
P_2O_5	0.22	0.14	0.10	0.06	0.32	0.30	0.07	0.01	0.05	0.06	0.07
Cr_2O_3	0.01	0.01	0.01	0.01	0.01	0.00	0.01	0.00	0.01	0.01	0.01
V_2O_5	0.01	0.01	0.00	0.00	0.05	0.05	0.00	0.00	0.00	0.06	0.01
LOI	0.75	1.21	0.95	0.94	1.97	3.89	0.70	0.43	0.34	1.15	1.09
Total	100.00	0.07	100.01	0.04	100.01	0.03	100.00	0.01	100.01	100.00	0.03
Cr (ppm)	16.78	4.77	27.42	26.40	21.50	7.07	32.00	15.87	37.00	26.75	12.50
Ni	2.31	1.31	2.30	1.89	3.65	5.80	1.78	1.14	1.70	12.30	5.04
Co	13.83	4.85	5.21	4.87	27.64	0.27	5.52	6.71	1.13	36.21	3.57
Sc	29.11	7.44	19.54	9.35	39.25	6.65	23.70	6.92	13.50	56.91	27.24
V	42.69	28.54	10.06	15.16	363.00	452.55	10.17	7.07	4.50	387.29	172.03
Cu	20.87	39.76	17.13	18.21	52.65	129.12	209.87	340.05	18.60	115.23	128.16
Pb	2.61	2.79	3.28	3.57	4.95	2.12	5.20	3.17	2.70	7.64	14.50
Zn	95.33	49.42	87.83	56.76	118.50	38.18	97.67	127.58	67.00	142.63	147.26
In	0.06	0.02	0.06	0.03	0.06	0.04	0.09	0.04	0.06	0.05	0.02
Sn	0.69	0.42	0.84	0.41	0.57	0.06	1.35	0.05	0.24	0.29	0.22
Mo	1.12	0.64	1.84	1.67	1.96	0.69	2.96	2.21	1.93	0.68	0.64
Sb	0.09	0.10	0.12	0.24	0.17	0.00	0.26	0.46	0.12	0.53	0.60
Rb	11.69	17.35	16.17	18.77	3.18	3.93	13.54	10.94	8.34	6.49	12.80
Cs	0.61	0.88	0.46	0.73	0.02	0.02	0.20	0.24	0.28	0.16	0.42
Ba	229.90	217.82	296.95	387.28	118.70	74.67	451.07	781.49	70.90	240.50	603.21
Sr	157.14	109.67	138.73	106.38	579.55	600.90	113.20	80.52	51.00	257.58	187.73
Tl	0.05	0.09	0.07	0.12	0.01	0.02	0.11	0.03	0.04	0.07	0.17
Ga	14.19	3.77	12.53	4.31	16.77	1.77	14.97	5.89	5.65	15.86	3.10
Ta	0.17	0.11	0.21	0.11	0.29	0.17	0.54	0.08	0.07	0.07	0.11
Nb	3.15	1.40	3.94	1.55	6.44	4.16	11.92	1.76	1.32	1.36	1.94
Hf	1.61	0.50	2.14	0.51	1.41	1.00	3.40	0.59	1.30	0.60	0.52
Zr	58.11	17.53	79.08	19.00	61.00	45.25	151.67	26.63	46.00	21.25	20.14
Y	20.58	6.16	22.71	8.36	16.36	10.00	29.53	6.08	11.03	10.54	5.36
Ti	2317.00	574.79	1549.58	656.06	3964.00	1909.19	2205.00	407.86	904.00	3221.13	988.42
Th	1.49	0.46	2.04	0.67	3.53	3.11	7.21	0.86	0.66	0.51	0.66
U	0.60	0.21	0.94	0.83	1.28	0.91	2.83	0.29	0.72	0.24	0.24
La	10.40	2.82	12.44	5.86	25.16	38.21	52.08	5.35	3.08	3.35	4.07
Ce	22.72	7.34	27.03	11.55	53.59	75.96	107.73	14.96	6.99	7.30	9.11
Pr	3.02	1.08	3.48	1.48	7.00	9.63	13.15	2.25	0.94	1.00	1.16
Nd	12.96	4.72	14.56	6.03	27.63	36.43	49.86	9.93	4.00	4.49	4.65
Sm	3.01	1.11	3.31	1.32	5.13	6.22	8.74	1.63	1.09	1.24	0.94
Eu	0.92	0.31	0.93	0.50	1.60	1.79	2.06	0.89	0.33	0.49	0.23
Gd	3.20	1.04	3.41	1.29	3.91	4.13	6.77	1.44	1.31	1.48	0.93
Tb	0.52	0.16	0.56	0.21	0.52	0.46	0.90	0.17	0.24	0.25	0.14
Dy	3.52	1.08	3.78	1.39	2.96	2.34	5.23	0.86	1.72	1.76	0.95
Ho	0.75	0.22	0.83	0.29	0.59	0.38	1.05	0.17	0.39	0.39	0.20
Er	2.35	0.71	2.58	0.88	1.70	1.06	3.15	0.47	1.30	1.19	0.58
Tm	0.35	0.10	0.40	0.14	0.24	0.15	0.48	0.06	0.20	0.18	0.08
Yb	2.40	0.69	2.67	0.95	1.60	1.02	3.24	0.49	1.40	1.17	0.55
Lu	0.38	0.12	0.42	0.16	0.25	0.16	0.51	0.07	0.22	0.18	0.08

TABLE 3. Summary of important major and trace element ratios for volcanic rocks of the Chisel sequence.

	Aphyric mafic intrusion		Plagioclase-porphyritic mafic intrusion		Balloch basalt		Powderhouse dacite, Chisel member	Powderhouse dacite, Lalor member		Chisel rhyolite	
	Avg	2σ	Avg	2σ	Avg	2σ		Avg	2σ	Avg	2σ
	n = 2		n = 5		n = 4		n = 1	n = 2		n = 5	
Al_2O_3/Na_2O	6.23	6.29	7.41	6.09	5.25	2.32	8.90	5.81	1.43	3.68	3.65
HASHI-AI	32.26	2.77	26.84	5.93	30.22	12.76	52.77	24.30	3.08	26.75	21.74
CCPI_FeO	85.01	12.42	83.29	10.07	83.15	6.92	69.93	83.10	1.59	38.38	36.05
CCPI_Fe_2O_3	85.89	11.88	84.36	9.50	84.19	6.47	71.69	84.26	1.52	40.18	36.82
Ti/Sc	49.07	25.94	63.37	27.97	63.23	37.87	94.38	94.04	3.40	86.46	25.39
Zr/Y	2.51	0.79	2.05	0.62	2.47	0.53	5.57	2.71	0.05	5.35	1.81
Zr/Sc	0.38	0.04	0.42	0.11	0.51	0.60	4.78	1.14	0.00	8.93	1.49
Zr/Nb	15.99	8.55	16.51	6.32	19.94	6.78	12.46	11.96	0.60	15.35	3.39
Zr/Ti	0.01	0.01	0.01	0.00	0.01	0.00	0.05	0.01	0.00	0.10	0.03
Zr/Hf	35.85	5.24	34.31	3.43	36.22	3.82	44.61	35.95	0.97	40.43	1.43
Nb/Y	0.17	0.14	0.13	0.05	0.13	0.03	0.45	0.23	0.02	0.35	0.12
Nb/Ta	17.15	2.07	18.28	4.14	19.49	2.84	22.08	17.50	1.83	17.53	2.53
Nb/Th	2.25	0.40	3.23	0.76	1.88	0.35	1.64	3.54	0.46	1.71	0.16
Th/Yb	0.62	0.33	0.35	0.16	0.59	0.12	2.44	0.59	0.08	1.78	0.54
Nb/Yb	1.41	0.99	1.13	0.45	1.12	0.39	4.01	2.07	0.00	3.02	0.74
La/Yb_CN	3.25	0.59	1.92	1.39	2.26	2.25	12.34	3.42	0.81	7.68	3.53
Ce/Yb_CN	2.69	0.24	1.63	1.12	2.03	1.38	10.54	2.88	0.54	6.43	2.48
Eu/Eu*	1.16	0.30	1.08	0.08	1.20	0.28	0.81	0.92	0.04	0.85	0.26
Nb/Nb*	0.28	0.10	0.40	0.12	0.28	0.13	0.21	0.42	0.08	0.23	0.04
Zr/Zr*	0.76	0.24	0.75	0.14	0.74	0.25	0.79	0.79	0.05	1.11	0.45
Hf/Hf*	0.76	0.13	0.79	0.10	0.74	0.27	0.64	0.80	0.03	0.99	0.39
Ti/Ti*	0.84	0.28	0.97	0.25	0.85	0.19	0.13	0.56	0.06	0.09	0.03
Sr/Sr*	1.83	1.13	5.41	3.71	2.53	3.04	0.15	1.57	0.50	0.19	0.17

TABLE 3 (continued). Summary of important major and trace element ratios for volcanic rocks of the Chisel sequence.

	Photo rhyolite 1		Photo rhyolite 2		Moore Lake basalt		Powderhouse rhyolite		Quartz-feldspar rhyolite	Threehouse unit	
	Avg	2σ	Avg	2σ	Avg	2σ	Avg	2σ		Avg	2σ
	n = 12		n = 9		n = 2		n = 3		n = 1	n = 8	
Al_2O_3/Na_2O	5.02	2.98	3.78	3.94	5.41	2.17	3.24	0.71	2.48	9.69	9.05
HASHI-AI	26.79	11.73	23.58	15.02	23.09	9.64	24.61	12.54	15.15	32.57	14.26
CCPI_FeO	72.62	10.65	51.68	26.38	82.38	5.57	57.47	7.21	25.82	86.78	10.21
CCPI_Fe_2O_3	74.32	10.25	53.78	26.14	83.55	5.26	59.69	7.21	27.63	87.62	9.61
Ti/Sc	79.67	3.78	81.14	31.33	100.32	31.65	93.59	12.65	66.96	58.85	30.18
Zr/Y	2.83	0.46	3.56	1.30	3.69	0.51	5.14	0.42	4.17	1.96	0.95
Zr/Sc	2.00	0.36	4.21	1.80	1.54	0.89	6.45	1.16	3.41	0.40	0.45
Zr/Nb	18.80	5.82	20.46	5.71	9.40	0.96	12.72	0.37	34.95	17.05	5.79
Zr/Ti	0.03	0.01	0.05	0.02	0.02	0.00	0.07	0.00	0.05	0.01	0.00
Zr/Hf	36.06	1.42	36.89	2.31	43.30	1.26	44.65	0.48	35.38	35.06	4.82
Nb/Y	0.15	0.06	0.18	0.07	0.39	0.01	0.40	0.03	0.12	0.12	0.11
Nb/Ta	18.76	3.84	18.98	2.32	22.02	1.45	22.07	0.81	18.28	21.17	3.40
Nb/Th	2.13	0.68	1.93	0.30	1.88	0.48	1.65	0.06	2.00	2.71	1.34
Th/Yb	0.62	0.09	0.77	0.19	2.16	0.57	2.23	0.16	0.47	0.42	0.43
Nb/Yb	1.32	0.52	1.49	0.49	4.02	0.04	3.67	0.17	0.94	1.09	1.00
La/Yb_CN	3.13	0.71	3.37	1.62	10.44	10.47	11.56	1.94	0.05	2.02	2.06
Ce/Yb_CN	2.64	0.46	2.83	1.09	8.69	7.65	9.26	1.77	0.00	1.69	1.75
Eu/Eu*	0.91	0.25	0.83	0.24	1.05	0.04	0.78	0.21	0.84	1.16	0.34
Nb/Nb*	0.27	0.08	0.26	0.07	0.25	0.15	0.21	0.02	0.30	0.35	0.21
Zr/Zr*	0.86	0.19	1.10	0.45	0.64	0.30	0.88	0.16	1.76	0.70	0.20
Hf/Hf*	0.87	0.18	1.08	0.41	0.54	0.27	0.71	0.12	1.81	0.73	0.20
Ti/Ti*	0.30	0.07	0.19	0.10	0.38	0.27	0.11	0.02	0.30	1.00	0.45
Sr/Sr*	0.71	0.31	0.57	0.34	1.28	0.49	0.13	0.10	1.30	4.46	5.79

TABLE 4. Nd, Hf, and Pb isotopic data for the volcanic rocks of the Chisel sequence.

Unit	$^{143}Nd/^{144}Nd$	$^{147}Sm/^{144}Nd$	$\varepsilon Nd_{(1.9Ga)}$	T_{DM} (Ga)	$^{176}Hf/^{177}Hf$	$^{176}Lu/^{177}Hf$	$\varepsilon Hf_{(1.9Ga)}$	$^{206}Pb/^{204}Pb$	$^{207}Pb/^{204}Pb$	$^{208}Pb/^{204}Pb$
Photo Rhyolite 2	0.512076	0.14492	1.6	2.40	0.282827	0.02893	4.6	20.646	15.737	37.998
Photo Rhyolite 1	0.512242	0.14262	5.4	1.97	0.282982	0.03261	8.7	21.013	15.780	37.946
Balloch Basalt	0.512564	0.18338	1.8	2.99	0.283433	0.04755	5.2	16.308	15.273	35.398
Qtz-Fsp Rhyolite	0.512471	0.16000	5.7	1.96	0.282780	0.02846	6.4	19.564	15.645	35.915
Plag phyric mafic intrusion	0.512515	0.16972	4.2	2.24	0.283379	0.03569	18.4	16.091	15.255	35.471
Threehouse; bedded tuff	0.512563	0.18627	1.1	3.31	0.283696	0.04876	13.0	15.824	15.220	35.235
Powderhouse rhyolite	0.511672	0.10609	3.1	2.10	0.282521	0.02170	5.8	30.625	16.828	44.082
Chisel rhyolite	0.511724	0.10671	4.0	2.04	0.282371	0.01371	10.7	18.629	15.529	35.916

Chapter 5

Concluding statements

5.1 Conclusions

This thesis provides a new interpretation for the deformation history of the Snow Lake arc assemblage. The volcanic rocks of the Snow Lake arc assemblage experienced a period of deformation prior to deposition of the Burntwood Group turbidites. This early deformation event may have resulted from one or a combination of intraoceanic accretion or pre-1.86 Ga accretion of the Snow Lake allochthon to the Amisk collage, which suggests that the Snow Lake allochthon shares a more protracted tectonic history with the rest of the Flin Flon belt than previously thought.

This thesis establishes a new stratigraphic framework for the Chisel sequence, in which the Threehouse unit forms the hanging wall to the Chisel sequence VMS deposits and constitutes the entire Upper Chisel sequence. This new stratigraphy constrains the timing of the Photo Lake VMS deposit and places all six Chisel sequence VMS deposits at the same stratigraphic position. An outcome of this stratigraphic interpretation is that the anomalous enrichment in Au and Cu in the Photo Lake deposit may be attributed to along-strike variations in the Chisel sequence hydrothermal system and water depth. Gold and Cu enrichment is interpreted to be the product of a magmatic input to enrich the hydrothermal fluids in Au and Cu followed by boiling of the hydrothermal fluids to facilitate efficient precipitation of these metals into a Cu-and Au-rich subseafloor stringer zone and Zn- and Au-rich seafloor massive sulfide lens. Variations in water depth, as reflected by lithofacies changes in the Threehouse unit, and variable magmatic fluid

input along the Chisel sequence ore interval may have resulted in the variable Cu and Au metal endowment of the Chisel sequence VMS deposits.

The new understanding of the stratigraphic relationships between VMS deposits and detailed lithofacies descriptions of the volcanic rocks within and immediately above the ore interval provide a framework for the reconstruction of the Chisel sequence ore-forming volcanic environment. The Chisel sequence represents a localized volcanic subsidence structure built on the primitive Anderson sequence. The Anderson and Chisel VMS deposits are distinct in terms of their stratigraphic positions, volcanic architecture and setting and metal contents, consistent with their formation at different times during the evolution of a rifted arc. The Anderson VMS deposits formed during early widespread arc rifting, whereas the Chisel VMS deposits formed during localized extension above a magma chamber in the extended arc.

5.2 Future work

In Chapter 2, the volcanic strata in the structural hanging wall to the Lalor deposit are interpreted to be folded and thrust-repeated Lower Chisel sequence strata. These units extend to the north towards Squall Lake, where their distribution is more complex. A structural and stratigraphic study that builds on previous 1:20,000 scale mapping in this area (Bailes et al. 2011) is needed. Furthermore, the surface expression of the Lalor-Chisel fault has not been identified, and additional work to delineate the extent of this fault at surface and at depth would contribute to a better understanding of the deformation history of the Snow Lake assemblage and the present distribution of its contained VMS deposits.

In Chapter 3, selective Au and Cu enrichment in the Photo Lake deposit is interpreted to be the product of a direct input of magmatic volatiles to enrich the hydrothermal fluids, followed by boiling in the subseafloor to facilitate efficient metal precipitation. This interpretation should be tested by completing a detailed study on the mineralogy and geochemistry of the sulfides in the Chisel, Chisel North, Lost, and Ghost deposits, provided that samples from these deposits are available. Previous studies on the Lalor deposit (Caté 2016; Duff 2016) provide context for a detailed Au study at this deposit.

In Chapter 4, the volcanic environment of the Chisel sequence is compared with that of the Anderson sequence; however, detailed work documenting lithofacies variations in the Anderson sequence has not been done. Deposits in the Anderson sequence exhibit significantly higher Cu/Cu+Zn ratios than the Chisel sequence deposits, suggesting that arc evolution may influence the metal content of VMS deposits. It is possible that the contrasting metal contents are a result of one or a combination of the volcanic environment, water depth, magmatic evolution of the system, or tectonic environment, and these factors must be investigated. A detailed study on the Anderson sequence would improve our understanding of arc evolution and the timing of VMS formation during arc rifting.

5.3 References

Bailes, A.H., Schledewitz, D.C.P., and Gagné, S. 2011. Updated geology of the Squall-Varnson lakes area, west-central Manitoba (part of NTS 63K16). Manitoba Innovation, Energy and Mines, Manitoba Geological Survey, Preliminary Map PMAP2011-2, scale 1:20 000.

Caté, A. 2016. Geology of the Paleoproterozoic Zn-Cu-Au Lalor volcanogenic massive sulfide deposit and its gold-rich lenses, Snow Lake, Manitoba. / Géologie du gisement de sulfures massifs volcanogène Paléoprotérozoïque à Zn-Cu-Au de Lalor et de ses lentilles riches en or, Snow Lake, Manitoba. Unpublished Ph.D. thesis, Université du Québec, Institut national de la recherche scientifique, Québec, Québec, 430 p.

Duff, S. 2016. Ore types of the auriferous Lalor VMS deposit, Snow Lake, Manitoba: implications for genesis and post-depositional processes. Unpublished M.Sc. thesis, Ottawa University, 123 p.